Chemical Probe Design and Development for Assessing Protein Modification and Cross-Linking

BY

Emily N. Pierce

B.S., Benedictine College, 2012

DISSERTATION

Submitted as partial fulfillment of the requirements for the degree of Doctor of Philosophy in Medicinal Chemistry in the Graduate College of the University of Illinois at Chicago, 2018

Chicago, Illinois

Defense Committee:
Gregory R. J. Thatcher, Ph.D, Advisor and Chair
Douglas Thomas, Ph.D.
Terry Moore, Ph.D.
Yue-Ting Wang Ph.D.
Leslie Aldrich Ph.D., Department of Chemistry

AKNOWLEDGEMENTS

ENP

TABLE OF CONTENTS

TABLE OF CONTENTS (continued)

LIST OF TABLES

LIST OF FIGURES

LIST OF FIGURES (continued)

LIST OF FIGURES (continued)

ABBREVIATIONS

ACR   acrolein

ADH   alcohol dehydrogenase

ALDH   aldehyde dehydrogenase

AD   alzheimer's disease

Aβ   amyloid-β

APP   amyloid precursor protein

ALS   amyotrophic lateral scherosis

APOE   apolipoprotein E

CNS   central nervous system

CDNB   1-chloro-2,4-dinitrobenzene

CHD   1,3-cyclohexanedione

DNPH   2,4-dinitrophenylhydrazine

FAD   familial alzheimer's diease

GSH   glutathione

GST-P1   glutathione-S-transferase P1

HH   histidyl-hydrazide

aHH   histidyl-hydrazide alkyne

HD   huntington diseasea

HYD   hydralazine

HNE   4-hydroxynonenal

aHNE   4-hydroxynonenal alkyne

LCS   L-carnosine

LPx   lipid peroxidation products

MDA   malondialdehyde

ABBREVIATIONS (continued)

NAC	N-acetylcysteine
NFTs	neurofibrillary tangles
NOR	novel object recognition
ONE	4-oxononenal
aONE	4-oxononenal alkyne
PD	parkinson's disease
Pin1	peptidyl-prolyl cis-trans isomerase NIMA-interacting 1
PAPs	photoactivatable probes
PSEN	presenilin
PUFAs	polyunsaturated fatty acids
PTM	post-translation modification
ROS	reactive oxygen species
SOD1	superoxide dismutase
TBA	thiobarbituric acid
TBI	traumatic brain injury
TBTA	tris[(1-benzyl-1H-1,2,3-triazol-4-yl)methyl]amine
UPR	unfolded protein response
WT	wild type

SUMMARY

Neurodegenerative diseases are characterized by the progressive loss of neuronal function, a key characteristic of several diseases including: Alzheimer's disease (AD), Parkinson's disease (PD), amyotrophic lateral sclerosis (ALS), and Huntington's disease (HD). More than five million people in the United States suffer from AD today and it is currently the fifth leading cause of death in individuals over 65. The number of individuals diagnosed with AD is projected to increase dramatically in the coming decades as the size of the population over 65 continues to grow. This will place significant strains on the healthcare system which is expected to spend $259 billion in 2017 caring for individuals with some form of neurodegenerative disease. The only drugs currently approved by the FDA for use in AD provide only weak symptomatic relief to patients leaving millions of people without any effective treatment options. A clearer understanding of the mechanisms underlying the development and progression of these diseases is required in order to discover alternative and more effective drug targets.

The cellular mechanisms that drive the development and progression of neurodegenerative disease are not well understood, and a variety of mouse models have been used to further our understanding of these diseases. These transgenic models develop many of the phenotypic markers seen in AD; however, all of these models rely on the expression of genetic risk factors associated with familial AD and do not serve as reliable models for the study of sporadic AD. This is problematic because while there are genetic mutations that lead to the development of familial versions of AD, a majority of cases (>99%) are caused by the development of a sporadic form of disease. For this work we have used an ALDH2$^{-/-}$ mouse model as the starting point for

SUMMARY (continued)

this research in order to better understand the molecular mechanisms underlying the development of sporadic rather than familial AD.

Oxidative stress occurs when the production of reactive oxygen species (ROS) exceeds the capacity of antioxidants in a cell. The CNS is particularly sensitive to oxidative stress and increased oxidative stress is implicated in the development and progression of neurodegenerative diseases. One of the results of increased oxidative stress is the peroxidation of polyunsaturated fatty acids (PUFAs). Lipid peroxides then undergo degradation and produce electrophilic lipid peroxidation products (LPx) which include 4-hydroxynonenal (HNE) and 4-oxononenal (ONE). These LPx contain two reactive functionalities that result in the formation of proteins adducts through different mechanisms. The aldehyde is capable of reacting with the terminal amino group of Lys residues to produce reversible Schiff base protein adducts. Additionally, the reaction of Cys, His, or Lys residues with the α,β-unsaturated aldehyde results in the formation of an irreversible Michael addition adduct. This bivalent reactivity has been shown to promote the formation of protein oligomers, implicated in neurodegenerative diseases, including: Aβ, tau, and α-synuclein. The methods commonly used to detect these protein adducts are chemical derivatization, immunoblotting, or LC-MS/MS analysis. These methods suffer from different limitations; therefore, we have developed a dual color near-IR imaging method that allows for the visualization and quantitation of the Schiff base adducts, Michael addition adducts, and protein crosslinking induced by these LPx. By adapting this method we were also able to enrich these modified proteins and use LC-MS/MS to identify HNE protein adducts in the lysates of neuronal SHSY-5Y cells.

SUMMARY (continued)

Several nucleophilic small molecules have been reported to protect tissues and cells from conditions of increased oxidative stress by behaving as chemical traps of LPx. It has also been reported that the trapping of LPx by these small molecules results in a decreased level of LPx protein adduct formation. We have shown that these trapping agents react with LPx *in vitro* and protect against the death of SHSY-5Y cells induced by the treatment of exogenous LPx. Our imaging method demonstrates that trapping agents containing a free thiol (glutathione, N-acetyl-cysteine) significantly decrease the formation of protein adducts. However, this method shows that the neuroprotective activity observed from certain aldehyde reactive scavengers (histidyl-hydrazide, hydralazine) is a caused by a prevention of protein cross-linking, not an overall decrease in protein adduct formation.

Glutathione (GSH) is the major source of free thiols in biological systems. GSH is necessary for the enzymatic detoxification of electrophiles by glutathione-S- transferases (GSTs) as well as post-translational modification via protein S-glutathionylation. Protein S-glutathionylation is post-translational modification (PTM) that results in the formation of a mixed disulfide bond between a protein cysteine and the cysteine of glutathione (GSH). This PTM is reversible and increases under conditions of oxidation stress. Reversible thiol modifications serve either a protective function, by preventing irreversible oxidative damage, or by modulating protein structure and activity. In order to develop a chemical probe to identify the subset of the proteome that regulate protein S-glutathionylation we evaluated two GSH based photoprobes containing either a diazirine or tetrafluoroazide photophore. Both of these probes were shown to bind to GST-P1 by enzyme activity assays and molecular docking. Proteomic analysis determined that the tetrafluoroazide probe yields selective covalent modification of the

SUMMARY (continued)

residue Tyr108 within the active site of GSTP1. The diazirine probe however yields no protein

modification. We also used a fluorescently tagged analog of the tetrafluoroazide probe that

allowed for the visualization of the several modified proteins in cell lysates.

This work presents two different types of chemical probes that were used to further our

understanding of cell signaling and neurodegenerative disease. The first two chapters discuss the

use of LPx analogs to visualize, quantify, and identify protein adducts in tissue and cells. The

last chapter covers our work to develop a photoprobe that would identify the subset of the

proteins within the proteome that regulate S-glutathionylation.

CHAPTER 1. CHEMOPROTEOMIC ANALYSIS OF PROTEIN CARBONYLATION BY LIPID PEROXIDATION PRODUCTS

1. Introduction

1.1 Neurodegenerative Diseases

At the beginning of the 20th century the average life span was less than 50 years. Today, the average life expectancy exceeds 80 years in several countries.[1] This increase in life expectancy has resulted in a dramatic increase in the size of the population of individuals over the age of 65. In 2010 approximately 500 million people worldwide were over the age of 65 and composed 8% of the world's population. By 2050 this number is projected to exceed two billion.[2] This dramatic increase in life expectancy can be attributed to improved living standards and developments in modern medicine. These developments have caused a shift in the primary causes of death worldwide from communicable diseases to chronic, non-communicable diseases associated with aging, such as cancer, heart disease, and neurodegenerative diseases.[3]

Neurodegenerative disorders encompass a variety of disease including Alzheimer's disease (AD), Parkinson's disease (PD), amyotrophic lateral sclerosis (ALS), and Huntington's disease (HD). AD is the most common neurodegenerative disease and is estimated to effect 5.5 million American in 2017. The number of individuals diagnosed with AD is projected to increase to 13-16 million by 2050. This large increase in the number of individuals diagnosed with AD and other neurodegenerative disease places a substantial burden on the healthcare system. In 2017 the cost of caring for individuals over 65 with AD and other forms of dementia is expected to cost $259 billion in the US alone.[4] This includes not only healthcare costs borne by Medicare and Medicaid, but $56 billion of these costs are out of pocket with an average individual paying

$10,000 out of pocket each year to cover their medical needs. Additionally, these estimates of healthcare costs do not account for the more than 15 million people in the United States who are unpaid caregivers to someone suffering from AD. The estimated contribution of these unpaid caregivers is approximately $230 billion annually.[4] Currently the only therapies available provide weak symptomatic relief and there are currently no treatments available that halt or reverse the progression of these diseases. In order to better understand the progression of these diseases we will study the role of oxidative stress, specifically the role of lipid peroxidation products (LPx) in the progression of neurodegeneration using a mouse model of increased oxidative stress.

Neurodegenerative diseases are characterized by the progressive loss of neuronal function, including the death of neurons. The most common neurodegenerative diseases are AD and PD. Nearly all cases (>99%) of these diseases are caused by the development of a sporadic form of disease associated with aging rather than heritable genetic mutations associated with familial versions of these diseases. A few neurodegenerative disease however, such as HD, are known to be caused by inherited genetic mutations. Despite different underlying causes a majority of neurodegenerative diseases are characterized by protein misfolding and the accumulation of insoluble protein aggregates in the central nervous system (CNS). (**Table 1**) These diseases can be distinguished by the cellular and regional location of accumulated aggregates and the primary protein involved in the formation of these protein aggregates.[5]

Senile plaques and neurofibrillary tangles (NFTs) are the traditional hallmarks of AD and were first described by Alois Alzheimer in 1906.[6] The senile plaques are composed of amyloid-β (Aβ) peptides produced from the proteolytic cleavage of amyloid precursor protein (APP) by β-secretase and γ-secretase. The most abundant Aβ peptides are $A\beta_{40}$ and $A\beta_{42}$. NFTs are

primarily made up of the microtubule-associated protein Tau that has been hyperphosphorylated. Since the description of the two original hallmarks of AD it has also been found that >50% of AD patients also develop Lewy bodies which are commonly associated with PD and are primarily composed of α-synuclein. ALS and HD are also characterized by protein aggregates of polyglutatmine-rich huntingtin protein or super-oxide dismutase (SOD1) respectively.[7]

TABLE I. CHARACTERISTICS OF PROTEIN AGGREGATES IN COMMON NEURODEGENERATIVE DISEASES

Disease	Aggregated Protein	Lesion	Affected Region of brain	References
Alzheimer's Disease	Amyloid-β, Tau, and α-Synuclein	Amyloid plaques, neurofibrillary tangles and Lewy bodies	Hippocampus, cerebral cortex	8, 9
Parkinson's Disease	α-Synuclein	Lewy bodies	Substantia nigra, hypothalamus	10, 11
Amyotrophic lateral sclerosis	Superoxide dismutase	Hyaline inclusions	Motor cortex, brain stem	12, 13
Huntington's Disease	Huntington	Neuronal inclusions	Striatum, cerebral cortex	14

1.2 Mouse Models for the Study of Neurodegeneration

There are a variety of mouse models used to study Alzheimer's disease and other neurodegenerative disorders. The classical hallmarks of AD are Aβ plaques and NFTs. Several known mutations in APP and the components of the γ-secretase protease complex, presenilin 1 (PSEN1) and presenilin 2 (PSEN2), are implicated in the development of familial Alzheimer's disease (FAD). While this form of the disease accounts for about 1% of the total patients these gene mutations have been used universally to develop transgenic mouse models of the familial and sporadic diseases.[15] In addition to WT APP, the following pathogenic APP mutations have

been expressed in transgenic mice: Swedish mutation (K670D/M671L), Arctic mutation (E693G), London mutation (V717I), and Indiana mutation (V717F).[16-20] All of the transgenic mouse models that express mutant APP develop memory deficits and Aβ plaques. Transgenic models expressing mutant human PSEN1 (M146L or A246E) also have increased Aβ plaques.[21-22] The APP(SL)PS1K1 model expresses both mutant APP and PSEN1 leading to increased production of Aβ and neuronal loss at 10 months.[23]

The expression of wild type human tau in mice does not result in the formation NFTs in the brains of these animals, however they do exhibit tau pathology (pre-tangle formaton, hyper-phosphorylation).[24-25] The first transgenic model to express mutant (P301L) tau protein was reported by Lewis, et al in 2000.[26] Since this report, additional transgenic mouse models have been developed that express other tau mutations including, N279K, P301S, and V337M. All of these transgenic mice developed tau pathology, NFTs, and loss of synapses.[27-29] Additionally, the expression of the P301L and P301S tau protein in separate transgenic mouse models resulted in premature lethality. The 3xTg-AD model expresses mutant human tau protein (P301L), APP (Swedish mutation), and PSEN1 (M146V). While this model exhibits amyloid and tau pathology, NFTs, and memory loss, no neuronal loss was reported.[30]

One of the major genetic risk factors for AD is the *APOE4* allele. Apolipoprotein E (APOE) is a polymorphic gene with three alleles: ε2, ε3, and ε4. The risk of developing AD in individuals carrying one ε4 allele is increased by 2-3 fold while in carriers of two ε4 alleles this risk is increased 12-fold. On the other hand the ε2 allele puts carriers at a lower risk for AD.[31] Transgenic APP mice that express APOE4 have increased levels of Aβ production compared to transgenic mice expressing APOE3 or APOE2.[32]

All of the transgenic mouse models described above replicate the hallmark pathology associated with both familial AD and sporadic AD; however, the drivers of disease progression are the genetic mutations only associated with FAD. In an effort to develop an animal model of sporadic AD, an ALDH2$^{-/-}$ mouse model was evaluated by Bennett et al. in 2015. This report showed that these ALDH2$^{-/-}$ mice develop significant memory deficits at 3.5-4 months when compared to WT mice.[33] The ALDH2 loss of function mutations (E504K), prevalent in East Asian populations, is associated with increased risk of AD in males.[34] This loss of function mutation is also found to result in increased levels of HNE protein adducts, age-dependent neurodegeneration and the development of memory deficits.[35] As a potential model of sporadic AD, or mild cognitive impairment (MCI), the Aldh2-/- mouse may allow for a better understanding of the role of HNE and other LPx adducts in the development of memory deficits. This could provide a better understanding of the mechanism driving disease progression and lead to the development new therapeutic approaches.

1.3 Neurodegeneration: The Role of Oxidative Stress

Oxidative stress occurs when the production of reactive molecules derived from molecular oxygen exceeds the capacity of antioxidants within a cell.[36] For several reasons the brain is particularly sensitive to the increased production of reactive oxygen species (ROS). First, the brain consumes a high proportion of O_2 (20%) relative to its overall mass (~2%).[37-38] The brain also contains a higher concentration of transition metals and polyunsaturated fatty acids (PUFAs) as well as a lower level of antioxidants compared to other tissues.[39] A majority of neurodegenerative diseases are progressive diseases, commonly associated with aging, affecting CNS and resulting in decreased neuronal function and neuronal loss.[5] The most common of these diseases are Alzheimer's (AD), Parkinson's (PD), and Huntington's disease (HD). However,

neuronal loss can also be caused by more acute injuries such as ischemic stroke or traumatic brain injury (TBI).[40] While the underlying causes of these diseases are multifactorial, oxidative stress is implicated in the development and progression of neurodegenerative diseases.[38]

ROS are primarily generated in the mitochondria and include both free radicals (superoxide, hydroxyl radicals) and other nonradical byproducts of oxygen metabolism such as hydrogen peroxide.[41-42] Superoxide ($O_2^{\bullet-}$) is produced from the one electron reduction of molecular oxygen. Superoxide can then be converted to hydrogen peroxide (H_2O_2) by SODs.[43] The most reactive ROS is the hydroxyl radical ($OH\bullet$) which is primarily produced from hydrogen peroxide via the Fenton reaction.[42, 44]

An increase in the concentration of these ROS results in oxidative damage to other components of the cells including: nucleic acids, amino acids, and lipids.[42] Guanine is the nucleic acid most susceptible to oxidation and this reaction results in the formation of 8-oxoguanine.[45] There is a significant increase in the levels of oxidative damage to nuclear and mitochondrial DNA in the AD brain compared to age matched controls.[46] For proteins, the oxidation of amino acid side chains results in both reversible and irreversible modifications that impact protein function and cell signaling. Cysteine residues are particularly sensitive to oxidation and several oxidation products (disulfides, sulfenic, sulfinic, or sulfonic acids) are produced from the oxidation of Cys.[47] Although Cys residues are the major site of protein oxidation, oxidative damage can also occur at other amino acid residues.[48] Markesbery et. al. report that increased levels of protein oxidation can be detected in the hippocampal region of post mortem brains from AD patients.[49] Finally, the peroxidation of PUFAs results in the degradation of these lipid peroxides to electrophilic LPx such as 4-hydroxynonenal (HNE) and malondialdehyde (MDA). Damage to other macromolecules can also result from the production

of these secondary reactive species which have their own chemical reactivity and downstream effects. These different forms of oxidative damage to important biomolecules can result in the disruption and alteration of important signaling pathways.[50] As a result, oxidative stress is implicated in several diseases including: cancer, neurodegeneration, and inflammation.[51-52]

Figure 1. Downstream effects of ROS and lipid peroxidation.
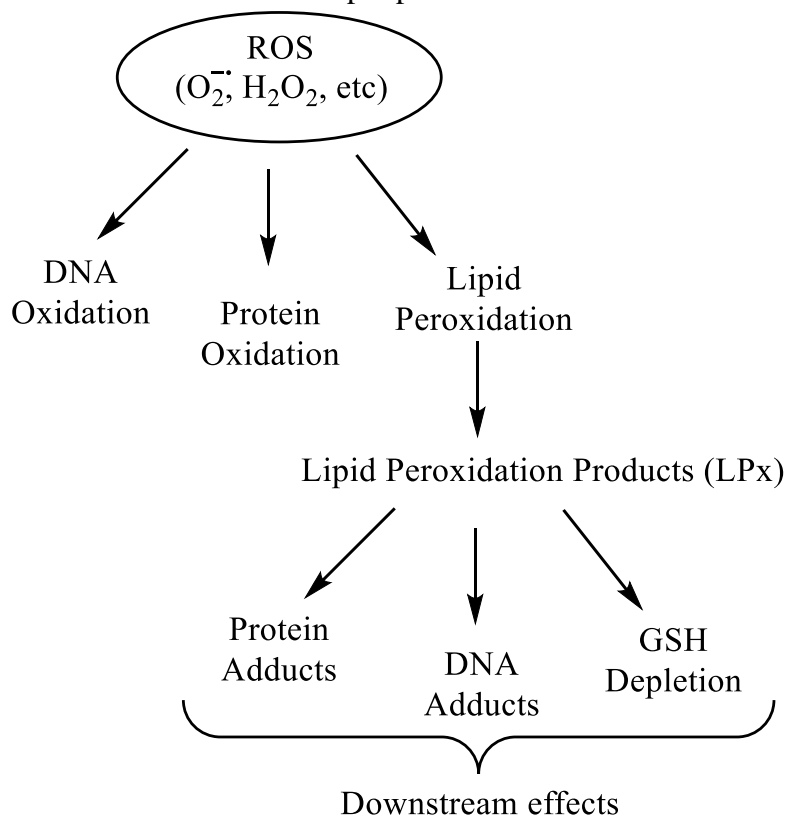
Figure 1. The increased production of ROS results in DNA oxidation, protein oxidation, and lipid peroxidation. The downstream effects of lipid peroxidation leads to the production of lipid peroxidation products that are also capable of forming protein, DNA adducts and causinging in the depletion of cellular GSH.

LPx display a range of reactivity in the presence of nucleophiles; however, they are more stable than the initial ROS that initiated the production of these LPx.[53] The reactions of LPx with different biomolecules are also often reversible which allows for the diffusion of these reactive aldehydes far from the site of production allowing for the formation of various covalent DNA, RNA and protein adducts.[54] The formation of LPx protein adducts has been shown to affect key signaling pathways such as Keap1-Nrf2, the unfolded protein response (UPR) and the heat shock response.[55-58] The production of LPx during oxidative stress may be implicated in neurodegenerative disease because the concentration of LPx is increased in the CSF and the postmortem brains of AD patients.[59] The bivalent reactivity of several LPx has also been shown to play a role in the formation of protein oligomers implicated in neurodegenerative disease such as Aβ, tau, and α-synuclein.[60-62] An increase in the level of oxidative DNA and RNA damage is also reported in individuals with early AD.[39, 63]

Oxidative damage to DNA or RNA is primarily measured by HPLC with electrochemical detection, LC-MS/MS, or immunodetection. These methods were used to analyze samples from brain tissues obtained at autopsy from confirmed cases of AD or from age matched control patients. The results from these studies show that oxidative damage to DNA and RNA occurs early in disease progression and that in AD patients there is significantly more oxidative damage to mitochondrial DNA rather than nuclear DNA in regions of the cortex and the cerebellum.[46, 64] The levels of free HNE in the CSF and postmortem brains of AD and control patients were measured by 1,3-cyclohexanedione derivatization and HPLC detection. These results show a two-fold increase in the amount of HNE in the CSF of AD patients and a significant increase in the level of HNE in the amygdala and hippocampal regions of AD subjects.[65-66] Early analysis of HNE protein adducts in AD brains was conducted by Markesbery et. al. by derivatizing HNE

protein adducts with 2,4-dinitrophenylhydrazine (DNPH) followed by immunohistochemistry or 2D western blot detection of adducts using an anti-DNPH antibody. These results show a significant increase in HNE proteins adducts in the cortex and hippocampus of AD samples compared to control samples.[49]

1.4 Lipid Peroxidation Products

LPx are divided into primary and secondary LPx. Primary LPx include lipid hydroperoxides that result from the peroxidation of unsaturated fatty acids, phospholipids, and glycolipids.[67] This oxidation occurs via both enzymatic and non-enzymatic mechanisms. This oxidation can be catalyzed by lipoxygenases, cyclooxygenases, or cytochrome P450s.[68] The PUFAs most readily oxidized to lipid peroxides are the n-3 (α-linolenic acid, docosahexaenoic acid) and n-6 PUFAs (linoleic acid and arachidonic acid). The formation of lipid peroxides occurs via a three step chemical mechanism: initiation, propagation, and termination (**Figure 2**). This reaction is initiated by the abstraction the allylic hydrogen in the PUFAs by a radical species, generating a radical in the PUFA. This lipid radical then reacts with molecular oxygen resulting in the formation of a lipid peroxy radical. This lipid peroxy radical is then capable of generating new lipid radicals via hydrogen abstraction of a neighboring PUFA generating a lipid peroxide and a new lipid radical. This cycle, a free radical reaction, is then repeated until the termination step.[69]

Secondary LPx products are also produced by both enzymatic and non-enzymatic mechanisms. The enzymes responsible for the generation of specific LPx are detailed below but the general non-enzymatic mechanism occurs from the breakdown of lipid peroxides producing a wide variety of compounds.[70] The structure of the product is dictated both by the structure of the original lipid peroxide as well as the mechanism following the reduction of the peroxide. This

reduction occurs in the presence of transition metals, such as iron, followed by a secondary mechanism such as β-scission.[71] Several different classes of compounds are produced from the breakdown of lipid peroxides, including alkanes, ketones and alcohols, however the aldehyde secondary products have been the focus of the most study because of the chemical activity and toxicity observed by this class of LPx. Some of the most well studied aldehyde LPx are 4-hydroxynonenal (HNE), 4-oxononenal (ONE), malondialdehyde (MDA), and acrolein (**Figure 3**).[72]

Figure 2. Mechanism of arachidonic acid peroxidation
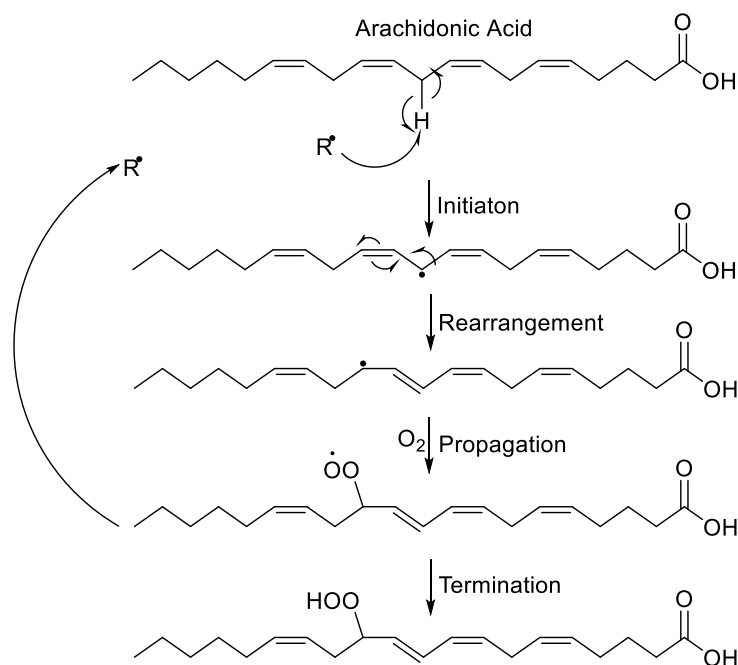
Figure 2. The production of lipid peroxides are initiated by the allylic hydrogen abstraction and this radical is propagated by repeated hydrogen abstraction from other PUFAs. This mechanism is repeated until the termination step.

Figure 3. Secondary lipid peroxidation products

4-Hydroxynonenal
(4-HNE)

Malondialdehyde
(MDA)

4-Oxononenal
(4-ONE)
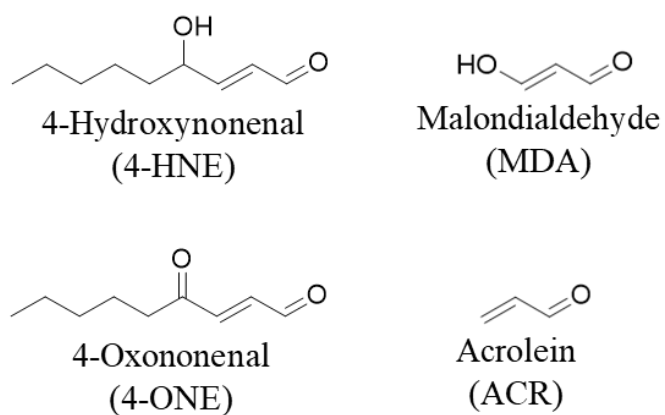
Acrolein
(ACR)

Figure 3. Chemical structures of the secondary lipid peroxidation products: 4-hydroxynonenal,

malondialdehyde, 3-oxononenal, and acrolein.

1.4.1 Secondary LPx Production and Metabolism

MDA is a secondary LPx that exists in a pH-dependent equilibrium. This equilibrium is shifted towards the enolate ion at neutral pH resulting in a decrease in the chemical reactivity of MDA. As the pH decreases the concentration of the more reactive species β-hydroxyacrolein increases (**Figure 4**).[73]

Figure 4. Equilibrium of MDA at acidic pH
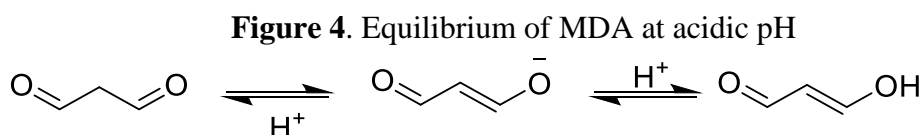
This LPx is generated by enzymatic and non-enzymatic mechanisms. MDA produced during thromboxane A2 biosynthesis as a byproduct of thromboxane A2 synthase.[74] MDA is also produced from the non-enzymatic degradation of ω3 and ω6 PUFAs.[73] The primary mechanisms of MDA metabolism are oxidation by aldehyde dehydrogenase (ALDH) or the ultimate conversion to D-lactate by multiple enzymes in the glyoxalase system initiated by the conversion of MDA to methylglyoxal by phosphoglycose isomerase (**Figure 5**).[69] Acrolein (acrylaldehyde, ACR) is produced from PUFA peroxidation or the enzymatic oxidation of polyamine metabolites. ACR is the most reactive of the α,β-unsaturated aldehyde LPx produced from the degradation of PUFAs and the oxidation of polyamines. It is metabolized by ALDH2 in the liver or glutathione (GSH) conjugation (**Figure 6**).[73]

Figure 5. MDA production and metabolism.
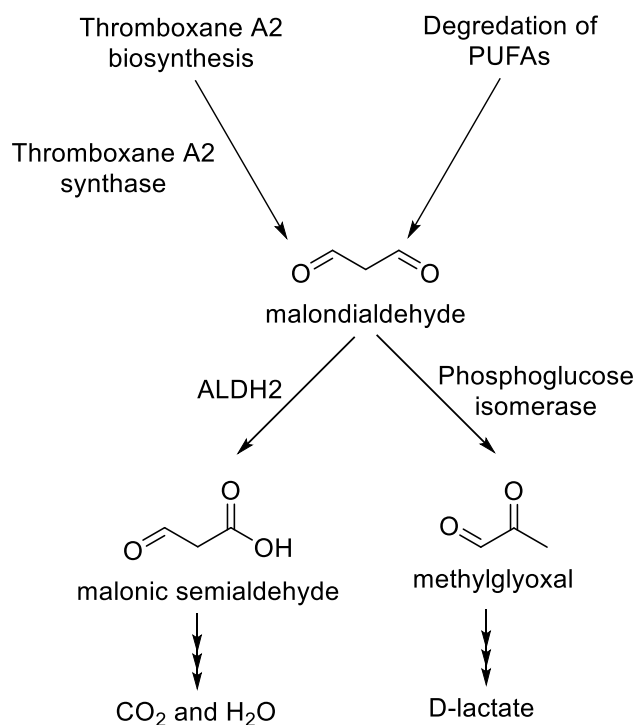
Figure 5. Malondialdehyde (MDA) is produced from the degradation of PUFAs and during thromboxane A2 biosynthesis. The pathways of MDA metabolism are oxidation of ALDH to malonic semialdehyde or the production of D-lactate where one of the steps is the conversion of MDA to methylglyoxal by phosphoglucose isomerase.

Figure 6. Acrolein production and metabolism
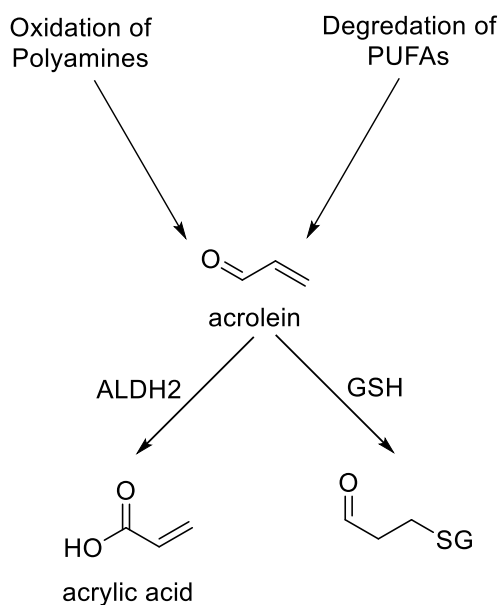
Figure 6. Acrolein (ACR) is produced from the degradation of PUFAs and the oxidation of polyamines. This LPx is metabolized by ALDH2 to acrylic acid or via conjugation to glutathione.

HNE is perhaps the most well studied α,β-unsaturated aldehyde and is produced from the peroxidation of the *n*-6 PUFAs linoleic acid and arachidonic acid.[75-76] It can also be generated enzymatically by 15-lipoxygenases that catalyze the oxidation of *n*-6 PUFAs. At low physiological concentrations of HNE the primary mechanism of HNE metabolism is GSH conjugation. With increasing concentrations of HNE, ALDH2 catalyzes the oxidation of HNE to 4-hydroxynonenoic acid and the reduction of HNE to 1,4 dihydroxy-2-nonene is catalyzed by alcohol dehydrogenase (ADH).[69] ONE is also produced from the peroxidation of *n*-6 PUFAs.

The metabolism of ONE occurs via reduction at the C-1 position by aldo-keto reductase to 4-oxo-2-nonen-1-ol or oxidation by ALDH2 to 4-oxo-2-nonenoic acid (**Figure 7**).[77]

Figure 7. HNE and ONE production and metabolism
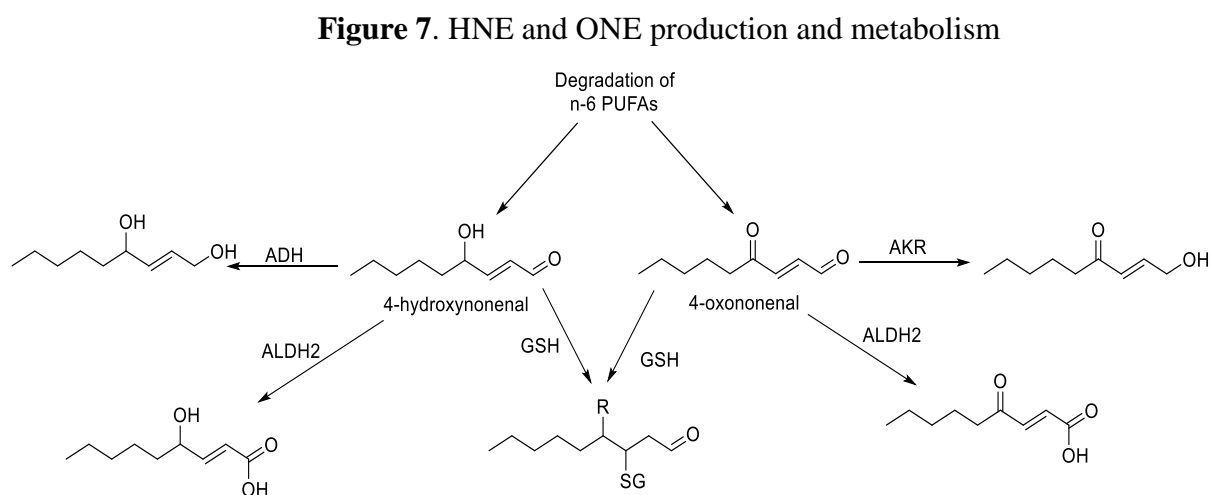
Figure 7. Both HNE and ONE are produced from the degradation of n-6 lipid peroxides. HNE and ONE are metabolized by conjugation to GSH and oxidation by ALDH2. Alcohol dehydrogenase and aldo-keto reductase catalyze the reduction of HNE and ONE respectively.

1.4.2 Biomolecule Adduction by LPx

All of these aldehyde LPx contain two reactive functional groups: the α,β-unsaturated aldehyde and the free aldehyde. These reactive functionalities account for the formation of both LPx-DNA and LPx-protein adducts that have been implicated in the observed toxicity of these compounds. The modification of these biomolecules can occur far from the site of production

due to the decreased reactivity of these molecules relative to the original ROS.[78] LPx have been reported to react with nucleosides that result in DNA damage. The most common site of nucleoside adduct formation is deoxyguanosine (dG). However some LPx form DNA adducts at deoxycytidine (dC) and deoxyadenosine (dA) nucleosides. For MDA the most abundant adduct occurs from the reaction of MDA with the N^2 of dG producing a cyclic adduct, N^2-deoxyguanosine pyrimidopurinone (M$_1$dG). The adduction of dA and dC by MDA forms the non-cyclic adducts M$_1$dC and M$_1$dA.[79-80] Acrolein adducts occur most commonly from the reaction of acrolein with dG in CpG islands. The reaction of acrolein with dG occurs through a multistep mechanism producing regioisomeric cyclic adducts or causing crosslinking with a second DNA stand or proteins.[80-81] These adducts have been shown to be mutagenic.[82] The primary HNE-nucleic acid adducts are four cyclic guanine diastereomers.[83] Finally, ONE forms adducts with dG, dC, and dA that have been characterized in human tissues.[84]

The modification of proteins by LPx occurs primarily at cysteine, histidine, and lysine residues. LPx adducts can form via two different chemical mechanisms. 1,4-conjugates or Michael addition adducts are produced by the attack of a nucleophilic amino acid at the 3-carbon of the α,β-unsaturated aldehyde. The formation of this adduct is irreversible and occurs primarily at Cys residues but these adducts can also form at reactive Lys or His residues. The second mechanism of adduct formation occurs via Schiff base formation. This type of adduct forms from the reaction of the terminal amino group of a lysine residue with the free aldehyde ultimately resulting in the loss of a water molecule. This type of adduct differs from the Michael addition in that the formation of the Schiff base is reversible. The bifunctionality of many LPx also implicates these α,β-unsaturated aldehydes in the promotion of protein crosslinking and the formation of cross-linked protein adducts (**Figure 8**).[72] The order of reactivity for the other LPx

is acrolein> ONE > HNE > MDA. Acrolein is the most reactive LPx with Cys, His, and Lys

residues while ONE is the LPx most likely to form cross-linked protein adducts and cause

protein crosslinking.[85-86]

Figure 8. Mechanisms of LPx protein adduct formation
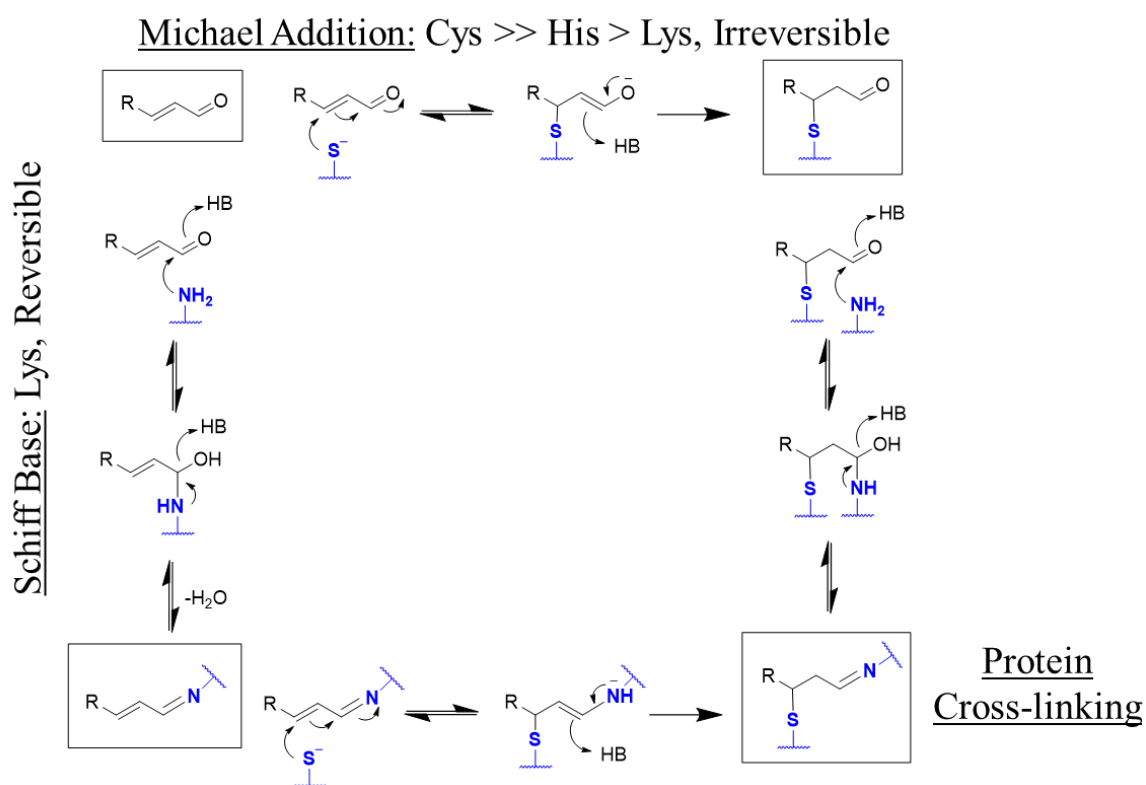
Figure 8. LPx contain two reactive functionalities: an aldehyde capable of forming a Schiff base

protein adduct, and an α,β-unsaturated aldehyde that reacts primarily with Cys residues to form

Michael Addition protein adduct. Due to the presence of two reactive functionalities, LPx can

promote the formation of intra- or inter-molecular protein crosslinked adducts.

1.4.3 Methods for LPx Adduct Detection

LPx products have an absorbance in the UV range of approximately 220nm; however, the direct detection of LPx in complex biological samples requires the use of a chemical derivatization method due to the limited selectivity or sensitivity of methods that directly measure free LPx. A variety of chemical derivatization methods have been reported to increase the sensitivity to LPx detection (**Figure 9**). Thiobarbituric acid (TBA) has been used for the derivatization of MDA. The reaction of two TBA molecules with the free aldehyde groups of MDA forms a conjugate with an absorbance at 535 nm.[87] Other chemical derivatization methods for LPx also require the presence of a free aldehyde. For example the reaction of an LPx with two molecules 1,3-cyclohexanedione (CHD) and an ammonium ion produces a fluorescent cyclic molecule with excitation and emission wavelengths at 395 nm and 460 nm.[88] 2,4-dinitrophenylhydrazine (DNPH) undergoes a Schiff base reaction with the free aldehyde under acidic conditions resulting in a product with an absorbance of 360 nm. Because the formation of a Schiff base is reversible, this reaction can be made irreversible by reduction with sodium cyanoborohydride.[89] These chemical derivatization methods suffer from the limitation of being unable to detect any Schiff base or cross-linked adducts due to the absence of a free aldehyde group and therefore provide a method for the detection of Michael adducts only.

Figure 9. Chemical derivatization of LPx

Figure 9. Chemical reactions for the derivatization of LPx. The thiobarbituric acid derivatization is specific for the derivatization of MDA and produces a product with an absorbance at 535 nm. The 1,3-cyclohexanedione and 2,4-dinitrophenylhydrazine derivatization methods are nonspecific methods that react with any free aldehyde. The CHD derivatization results in the formation of a fluorescent product with excitation and emission wavelength at 395 and 460 nm. The use of DNPH produces an aldehyde derivative with an absorbance at 360 nm.
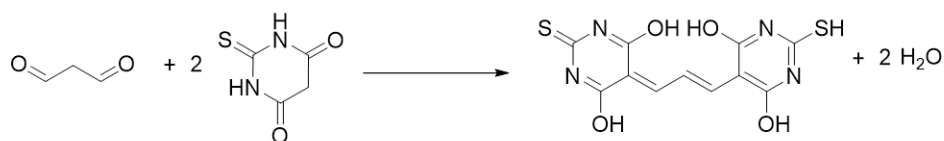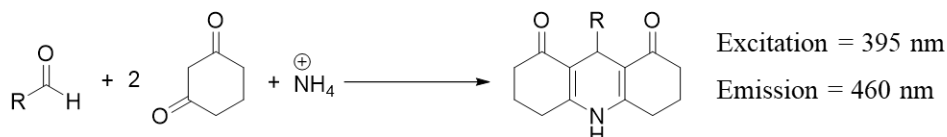
These chemical derivatization methods can be applied to the detection of LPx protein adducts provided that the protein adduct occurs via Michael addition and a free aldehyde remains present. Following the chemical derivatization of the protein adducts both 1D or 2D gel electrophoresis can be used to separate a complex protein mixture followed by western blot analysis using an anti-DNPH antibody.[49] Commercial antibodies for certain LPx are also available and antibodies have been used for both Western blot and ELISA analysis.[90] However, these antibodies also have limitations; for example, the HNE antibodies currently available were raised against reduced HNE-lysine adducts or HNE-histidine adducts.[91] Due to the fact that a majority of HNE-protein adducts are formed at Cys residues these antibodies have limited applications for the measurement of HNE-protein adducts.

There are also several methods that allow for the enrichment of LPx protein adducts followed by LC-MS/MS proteomic analysis in order to identify and quantify LPx adducts (**Table 2**). These methods commonly use chemical derivatization, with similar chemistry as the methods described above, but biotin derivatives (biotin hydrazide) are primarily used because the use of biotin allows for the enrichment of LPx protein adducts using solid phase streptavidin beads.[92] Other research groups have used solid phase hydrazide beads, which react directly with the free aldehyde groups of the LPx-protein adducts therefore bypassing the need for an initial chemical derivatization step.[93-94] Both of these methods also rely on the presence of a free aldehyde in the LPx adduct meaning that these methods suffer from the same limitations as the chemical derivatization methods. Finally, the utilization of exogenous alkyne-LPx analogs, such as alkyne-HNE or alkyne-ONE have been used and these analogs allow for the addition of azide tags to the resulting adducts using click chemistry. These azide containing tags can either contain biotin for affinity enrichment followed by LC-MS/MS analysis, or the tag may contain a fluorescent or UV

active functional group for quantitation and visualization.[95-96] This method allows for the

quantitation of all three types of adducts formed by this exogenous LPx analog but this method is

not applicable to the study of LPx adducts formed from endogenous LPx.

TABLE II. ENRICHMENT AND LC-MS/MS METHODS FOR IDENTIFICATION OF

LPX PROTEIN ADDUCTS

Cell or Tissue Type	Treatments	Enrichment Method	MS Instrument	# of Proteins Identified	Ref.
RKO cells	1-50 µM alkynyl-HNE or azido-HNE	Streptavidin bead enrichment after click reaction	LTQ linear ion trap	41-118	95
MDA-MB-231 and Ramos cells	5-500 µM HNE followed by alkynyl-iodoacetamide	Streptavidin bead enrichment after click reaction	LTQ-Orbitrap	~700 cysteines	115
HEK293T cells	25-100 µM HNE followed by aminooxy-alkyne	Streptavidin bead enrichment after click reaction	LTQ-Orbitrap	398	116
THP-1 and RKO cells	10-50 µM alkynyl-HNE or alkynyl-ONE	Streptavidin bead enrichment after click reaction	LTQ linear ion trap	847-1396	97
Rat liver mitochondria	10-2000 µM HNE followed by aldehyde reactive biotin	Streptavidin bead enrichment	LTQ-FT	217	98
Rat heart mitochondria	None	Affi-Gel hydrazide beads	MALDI	54	93
Liver from liver disease mouse model	None	Streptavidin bead enrichment after biotin hydrazide derivatization	Ion trap	414	92
Brain homogenates from EAD subjects and age matched controls	None	Excision of protein from 2D gels	MALDI-Tof	6	99
Frontal Cortex from subjects with Down syndrome, Down syndrome with AD, and age matched controls	None	Excision of proteinss from 2D gels	MALDI-ToF	24	90

2. Results

2.1 Validation of ALDH2$^{(-/-)}$ Mouse Model

The ALDH2$^{(-/-)}$ mice were previously reported to develop memory deficits at the age of 3.5-4 months.[33] To replicate these data the novel object recognition (NOR) behavioral test was conducted using WT and *ALDH2$^{-/-}$* mice, ages 3 to 9.5 months. This test measures an animal's ability to recognize and distinguish a familiar object from a novel one. The NOR test has two phases: exposure and testing. During the exposure phase a mouse is placed in an enclosure with two identical objects. The mouse is then removed from the enclosure and one of the objects replaced with a novel object.[100] The mouse is then returned to the enclosure and the time each animal spends with the novel object (T_N) and the familiar object (T_F) is recorded and used to calculate the discrimination index for each animal (DI, DI (%) = [(T_N - T_F)/(T_N + T_F) x 100]).[101] This behavioral test showed that there was no significant decline in the ability of the WT mice to discriminate between the novel and familiar objects from 3-9.5 months. However, as early as 3.5-4 months the ALDH2 knockout mice began losing the ability to differentiate between the novel and familiar object and this decline plateaued after 4.5 months (**Figure 10**).

The brain homogenates from both WT and ALDH2$^{(-/-)}$ mice, ages 3 and 6 months, were prepared after the animals were sacrificed and half of the brain from each animal was homogenized. In order to determine the level of LPx protein adducts in these homogenates, these samples were subjected to chemical derivatization using a hydrazide fluorescent tag (Alexa Flur488 hydrazide, **Figure 11**) or a near-IR hydrazide tag (Cyanine7.0 hydrazide, **Figure 12**) . After incubating the brain homogenates with one of the hydrazide tags for two hours in phosphate buffer (pH 5.5), SDS-PAGE gel electrophoresis was used to resolve the LPx protein adducts and the incorporation of the hydrazide tag was measured by in-gel imaging using a

Typhoon Fluorescent Imager or the LICOR Sa imaging system. The images collected using both

methods show that there is increased incorporation of the fluorescent or near-IR hydrazide tags

in the brain homogenates of the knockout animals compared to the WT animals. This indicates

that there is a higher level of LPx protein adducts in the ALDH2 knockout animals; however, in

the brains of the knockout mice there is no significant increase in the level of LPx protein

adducts from 3 to 6 months. The Alexa Flur488 hydrazide was primarily incorporated into

proteins with a molecular weight below 70 kDa while the Cyanine7.0 hydrazide showed greater

reactivity with LPx protein adducts over 70 kDa. This difference can be explained by the

presence of the sulfate and amine groups in the Alexa Flur488 dye which makes this dye much

more hydrophilic than the Cyanine7.0 hydrazide dye.

Figure 10. NOR behavioral test of ALDH2$^{(-/-)}$ and WT mice
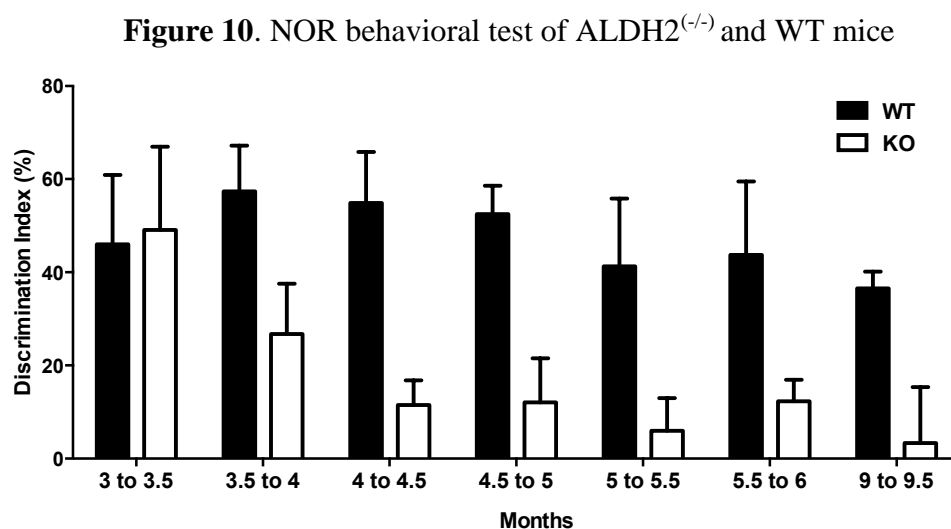
Figure 10. The discrimination index for WT and ALDH2$^{(-/-)}$ mice were measured by NOR. A

decrease in the ability of ALDH2$^{(-/-)}$ to distinguish a novel object from a familiar object

developed at 3.5-4 months.

Figure 11. Detection of LPx Adducts in Mouse Brain using Alexa488 Hydrazide
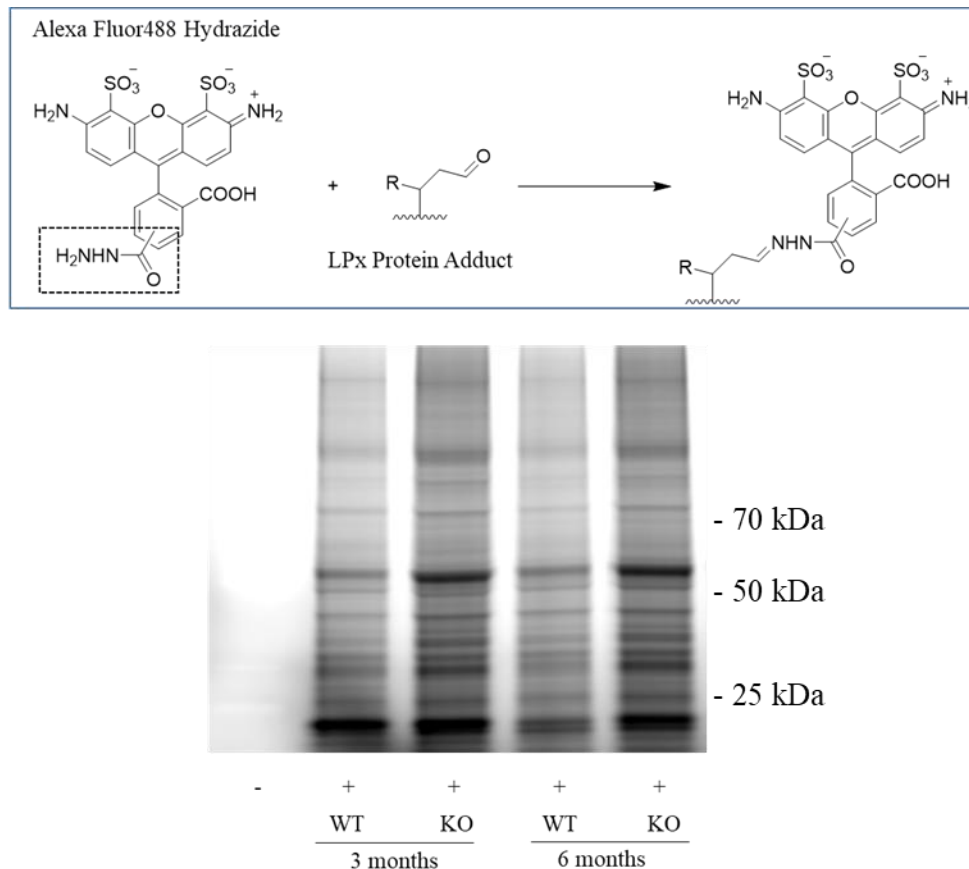
Figure 11. Top: Structure of Alexa Fluor488 hydrazide and the resulting LPx protein adduct after the derivatization reaction. Bottom: The proteins from whole brain homogenates from ALDH2$^{(-/-)}$ and WT mice at ages 3 and 6 months were derivatized by adding 500 µM Alexa 488 hydrazide to each sample ([protein] = 2 µg/µL) in 0.1 M phosphate buffer (pH=5.5). After incubating these samples at room temperature for 2 hours the proteins were separated by SDS-PAGE gel electrophoresis (30 µg/lane) and imaged by a Typhoon Trio Fluorescent Imager (Ex/Em, 488/520 nm). This image is representative of two independent experiments.

Figure 12. Detection of LPx adducts in mouse brain homogenates using cyanine7.0 hydrazide
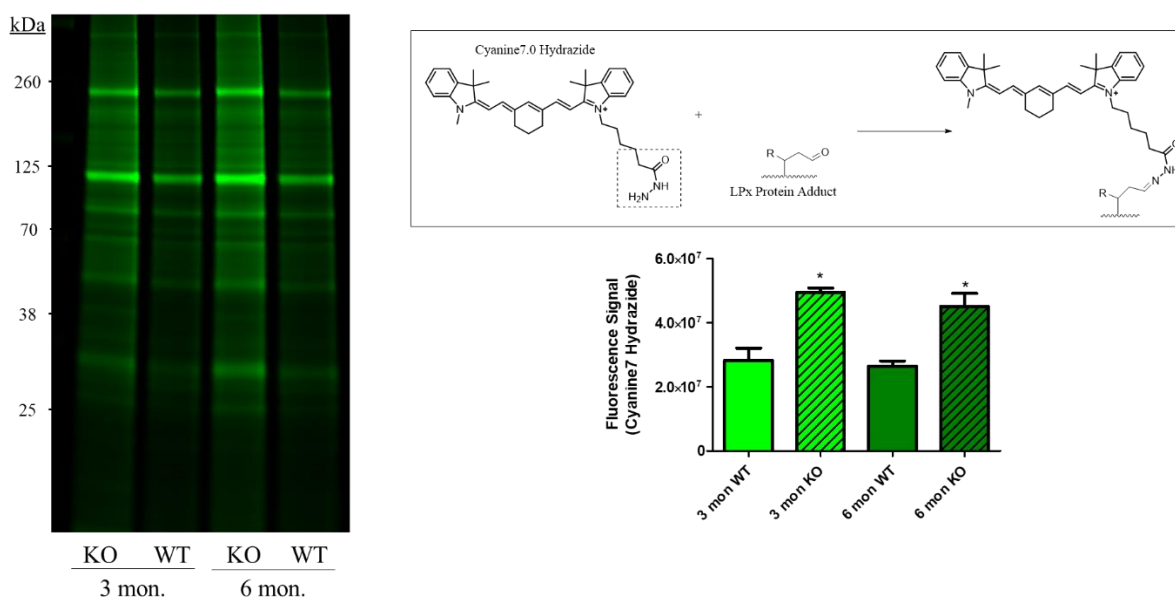
Figure 12. Left: The proteins from whole brain homogenates from ALDH2[(-/-)] and WT mice at ages 3 and 6 months were derivatized by adding 50 µM Alexa 488 hydrazide to each sample ([protein] = 0.5 µg/µL) in 0.1 M phosphate buffer (pH=5.5). After incubating these samples at room temperature for 2 hours the proteins were separated by SDS-PAGE gel electrophoresis (3.75 µg/lane) and imaged using a LICOR Sa imaging system. Top Right: Structure of Cyanine7.0 hydrazide and the resulting LPx protein adduct after the derivatization reaction. Bottom Right: The signals from the hydrazide dye were quantified for all samples. This data represents the results of three separate experiments (mean ± SEM) and significant difference from WT and KO samples was determined by one-way ANOVA with Tukey's post-test. (*$P<0.05$).

2.3 LPx Toxicity and the Role of ALDH2 in LPx Metabolism

SHSY-5Y cells are a neuronal cell line that originate from a human neuroblastoma. In order to evaluate if LPx are neurotoxic SHSY-5Y cells were treated with EtOH, 1 or 5 µM ONE, and 5 or 10 µM HNE for 24 hours prior to measuring cell viability (**Figure 13**). The treatment of SHSY-5Y cells with 10 µM HNE or 5 µM ONE induces ~50% cell death after 24 hours. These results are consistent with previous publications which report that ONE is more toxic than HNE.[102]

Figure 13. Treatment of SHSY-5Y cells with LPx
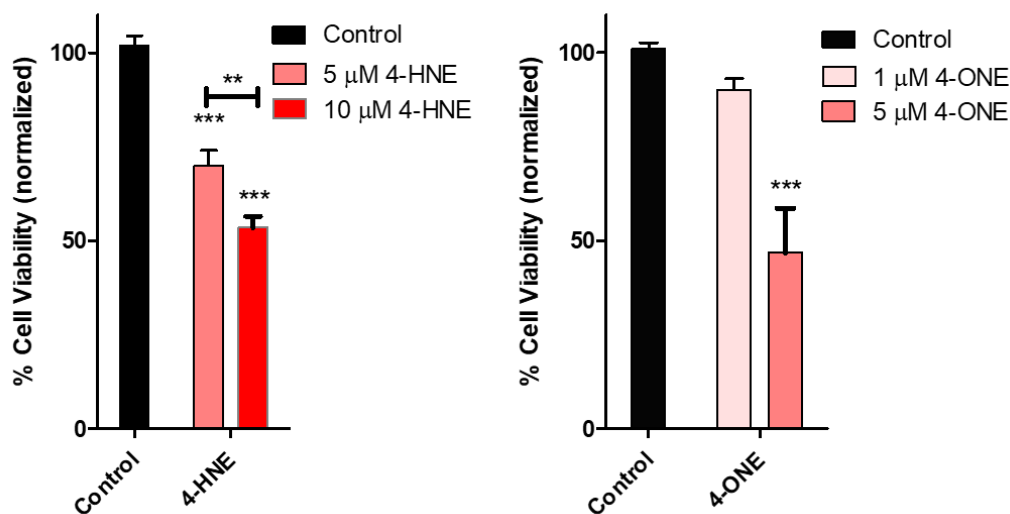
Figure 13. Left: The treatment of SHSY-5Y cells with EtOH, 5 µM HNE, or 10 µM HNE for 24 hours prior to measuring cell viability by MTT. Right: The treatment of SHSY-5Y cells with EtOH, 1 µM ONE, or 5 µM ONE for 24 hours prior to measuring cell viability by MTT. Data represents the mean ± SEM of at least ten independent readings. The data was analyzed by one-way ANOVA with Tukey's post-test (**P<0.01, ***P<0.001).

HNE and ONE have been reported to act both as substrates and inhibitors of ALDH2. Human ALDH2 demonstrated enzyme activity with 5-100 µM ONE but the preincubation of ALDH2 with 50 µM ONE also prevented the oxidation of propionaldehyde by ALDH2.[103] This enzyme inhibition was not observed when the same experiment was conducted with 50 µM HNE. The treatment of ALDH2 with 50 µM ONE results in the modification of Cys302, located within the active site of ALDH2.[103] HNE has been reported as a substrate of rat ALDH with a K_M of 14 µM and an inhibitor of acetaldehyde oxidation with a K_I of 0.5 µM.[104] We measured ALDH2 activity by monitoring the reduction of NADPH by recombinant human ALDH2 in the presence of HNE and ONE with or without the addition of acetaldehyde. (**Figure 14**).

These reactions were initiated by the addition of substrate, and the reactions were monitored for 10 minutes. The activity of ALDH2 was monitored in the presence and absence of the substrate acetaldehyde (1 mM) and a range of HNE and ONE concentrations (0-100 µM). This data are reported as the percent of ALDH2 activity normalized to 1 mM acetaldehyde alone as 100%. The incubation of 10 µM HNE alone with ALDH2 produced 10% of the enzyme activity observed with 1 mM acetaldehyde. However, the coincubation of 10 µM HNE and 1 mM acetaldehyde resulted in a 55% inhibition of ALDH2 turnover of acetaldehyde. Enzyme activity towards acetaldehyde was entirely inhibited in the presence of 100 µM HNE. In both the presence and absence of acetaldehyde, 1 µM ONE resulted in nearly complete inhibition of ALDH2 activity showing that ONE is more reactive with the cysteine residue within the active site of ALDH2 than HNE.

Figure 14. ALDH2 enzyme activity assay with acetaldehyde, HNE and ONE
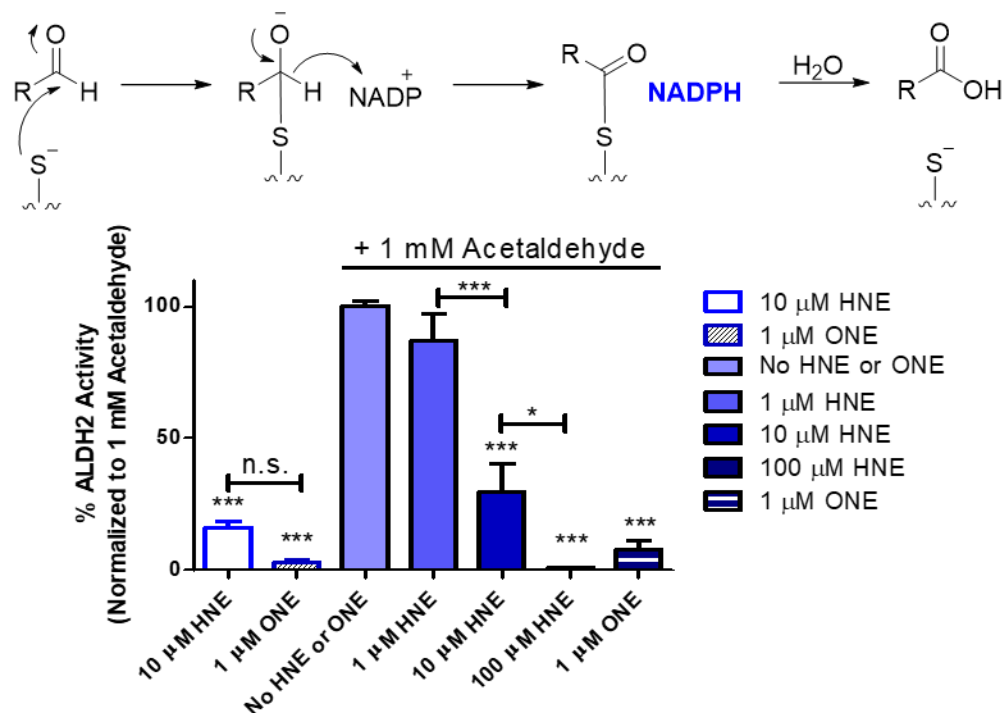
Figure 14. Top: Enzyme reaction mechanism of ALDH2. Bottom: ALDH2 activity measured using recombinant human ALDH2 (180 nM) which was preincubated with EtOH, 1 µM ONE or 1, 10 or 100 µM HNE and 500 µM NADP$^+$ in an assay buffer (50 mM sodium pyrophosphate, pH = 8.8) for 5 min at 25°C. 1 mM of acetaldehyde was then added and the production of NADPH (340 nm) was monitored for 10 minutes. The rate of the reaction was then normalized to the rate of the reaction without HNE or ONE. Data represents the mean ± SEM of at least four independent readings. Significant difference from the enzyme activity measure without HNE and ONE, unless indicated, was analyzed by one-way ANOVA with Tukey's post-test. (*P<0.05, ***P<0.001).

PC12 cells are a neuronal cell line that originates from a pheochromocytoma in the rat adrenal medulla. This cell line was used to evaluate the role of ALDH2 in the protection of these cells from LPx-induced cell death and the prevention of LPx protein adduct formation. Both WT and *ALDH2*$^{-/-}$ PC12 cells were treated with 100 µM HNE for 2 hours before measuring cell viability. These results show that the treatment of *ALDH2*$^{-/-}$ PC12 cells with HNE results in 50% cell death while the treatment of WT PC12 cells results in only 20% cell death (**Figure 15**). The role of ALDH2 in regulating the formation of LPx protein adducts was also investigated using WT and *ALDH2*$^{-/-}$ PC12 cells. Both variants of PC12 cells were treated with HNE (0 or 5 µM) for 24 hours, lysed, and the LPx protein adducts were derivatized using cyanine7.0 hydrazide. This derivatization reaction was carried out by adding 5 µM cyanine7.0 hydrazide to a sample of these cell lysates ([protein] = 2 mg/mL) in 0.1 M phosphate buffer (pH 5.5) and these samples were incubated at room temperature for two hours. Half of each sample was then subjected to reduction by 50 µM sodium cyanoborohydride (NaCNBH$_3$) in order to optimize the in gel visualization for the HNE adducts. NaCNBH$_3$ selectively reduces the Schiff base formed from the derivatization of LPx protein adducts by cyanine7.0 hydrazide and this reduction prevents the reversal of the Schiff base reaction. The HNE protein adducts were then separated by SDS-PAGE gel electrophoresis and the gels were then visualized using a LICOR Sa imaging system.

Figure 16 shows that the treatment of WT PC12 cells with HNE does not result in any increase in the level of HNE protein adducts. On the other hand the treatment of ALDH2$^{-/-}$ PC12 cells with HNE resulted in a significant increase in the formation of HNE protein adducts. Finally, the addition of NaCNBH$_3$ following the incubation of these samples with the hydrazide dye resulted in the decrease of the background signal in each lane.

Figure 15. Toxicity of HNE in native and ALDH2$^{(-/-)}$ PC12 cells
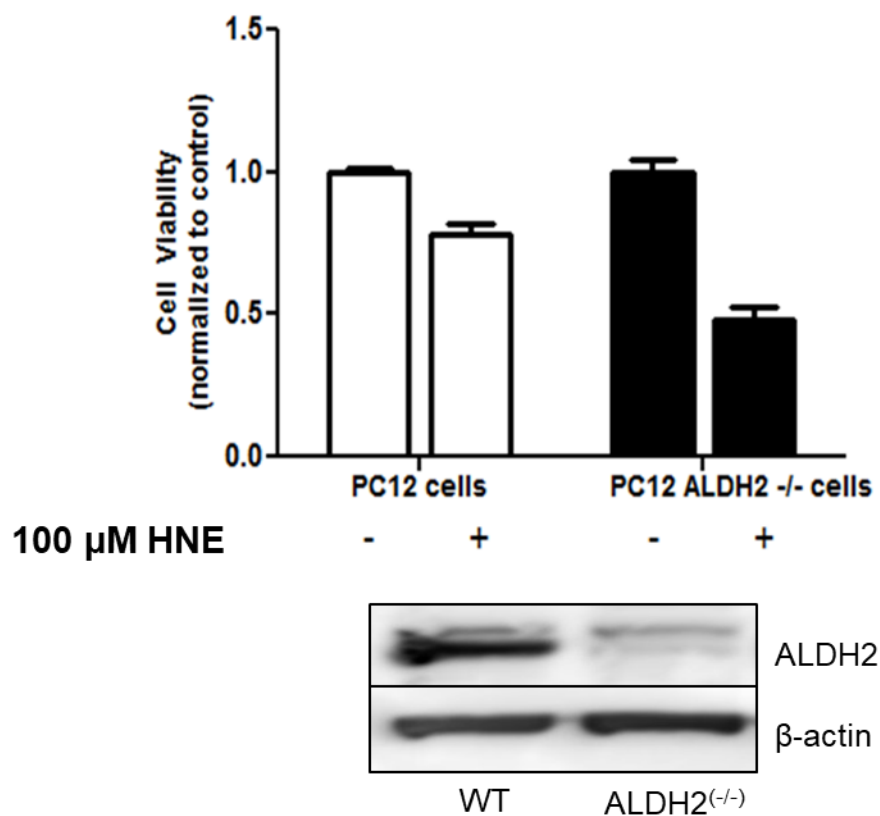
Figure 15. ALDH2$^{(-/-)}$ PC12 cells were generated by infection of PC12 cells with ALDH2 shRNA. These cells were then treated with EtOH or 100 μM HNE for 2 hours before measuring cell viability by MTT. The treatment of native PC12 cells resulted in 20% cells death and the treatment of the ALDH2$^{(-/-)}$ PC12 cells resulted in 50% cell death.

Figure 16. Detection of LPx protein adducts in WT and *ALDH2*[(-/-)] PC12 cells
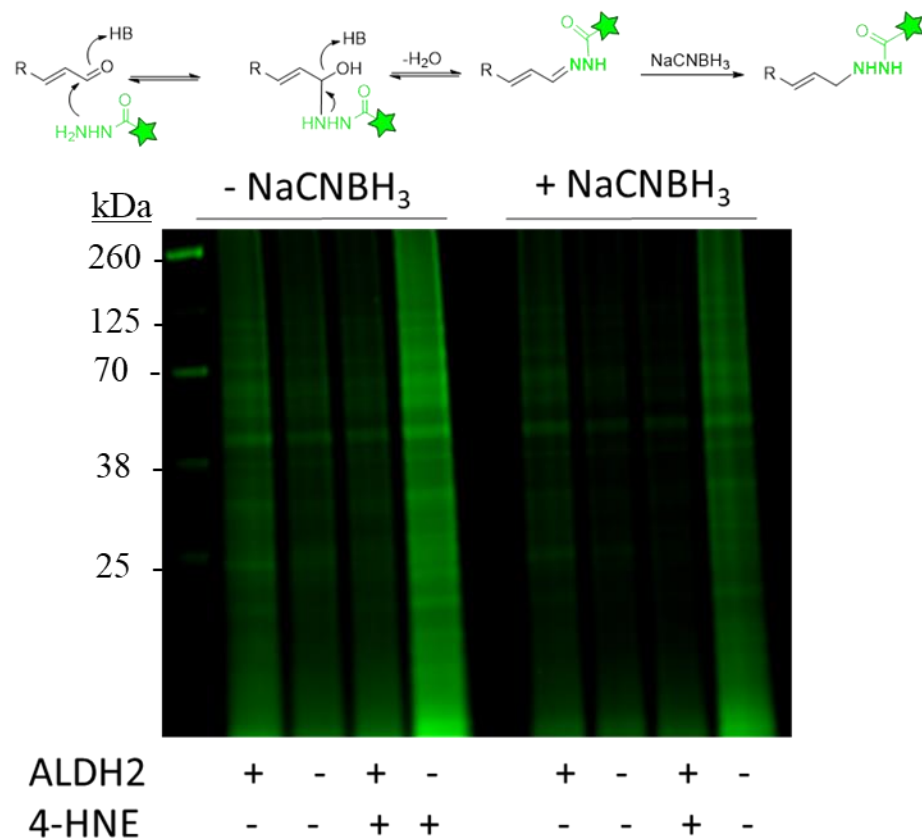
Figure 16. Cell lysates were collected from native PC12 or ALDH2[(-/-)] PC12 cells treated with 25 µM HNE for 8 hours. The lysates were collected, and LPx protein adducts were derivatized with 50 µM cyanine7.0 hydrazide in 0.1 M phosphate buffer (pH=5.5). After incubating these samples at 37 °C for 2 hours, 25 mM NaCNBH$_3$ was added to half of the samples to evaluate the effect of reducing any Schiff bases on the in-gel imaging. This image represents the results of three independent experiments. The HNE treated ALDH2[(-/-)] PC12 cells contained significantly more LPx protein adducts than the HNE treated native PC12 cells.

2.3 Development of In-gel Imaging Method

2.3.1 Method Development

Due to the limitations of previously reported methods for the detection of LPx proteins adducts, we have developed a new imaging technique that would allow for the detection and quantitation of Michael addition, Schiff base, and cross-linked protein adducts. For this method we utilized the alkyne-containing analogs of HNE (aHNE) and ONE (aONE) along with two near-IR dyes. A cyanine5.5 azide dye can react with the terminal alkyne of aHNE and aONE using 'click' chemistry and the cyanine7.0 hydrazide dye forms a Schiff base with the free aldehyde of any Michael addition LPx protein adduct. In order to optimize this method glutathione S-transferase P1 (GST-P1) that contains reactive Cys residue was used as a model protein. A low concentration of aONE was also used for this initial method development because it had previously been reported that ONE is more reactive than HNE.[105]

GSTs are a family of enzymes that catalyze the conjugation of glutathione (GSH) with endogenous and xenobiotic electrophiles.[106] Glutathione-S-transferase P1 (hGST-P1) is a 23 kDa protein that is ubiquitously expressed in human tissues. GST-P1 was used as a model protein for the development of this method because this enzyme contains four cysteine residues (Cys14, Cys47, Cys101, Cys169), none of which are required for the catalytic activity of GST-P1.[107] GST-P1 has been previously used to develop methods for the measurement of protein oxidation, nitrosation, and electrophilic modification by electrophilic quinones.[108-111] These studies of cysteine oxidation, nitrosation, and carbonylation show that Cys47 is the most reactive cysteine residue in GST-P1 with C101 being the second most reactive thiol group.[108, 110] In addition to direct modification of cysteine residues, the incubation of GST-P1 with 4-hydroxy-equilenin (4-OHEN) caused intramolecular and intermolecular disulfide bond formation induced by the redox

cycling of 4-OHEN.[111] GST-P1 is a redox sensitive protein that also plays a role in the

metabolism of HNE making it a useful model protein for the development of this in-gel imaging

method.[112]

     To validate the use of both dyes, aONE (0, or 1 µM) was added to GST-P1 (0.1 µg/µL) in

phosphate buffer (0.1 M, pH=7.4), and these samples were incubated at 37 °C for one hour.

These samples were then divided in half and subjected to two different chemical reactions for

derivatization. To the first half of the reaction the Cyanine5.5 azide (5 µM) was added with the

components required for the copper-catalyzed click reaction (1 mM CuSO4, 1 mM TCEP). The

buffer of the second half of the GST-P1 and aONE incubations was then exchanged for a

phosphate buffer (pH 5.5) prior to the addition of the Cyanine7.0 hydrazide (5 µM). These

samples were then incubated at 37 °C for two hours prior to subjecting these samples to SDS-

PAGE gel electrophoresis. These gels were then immediately imaged using a LICOR Sa imaging

instrument.

     Figure 17A shows that the incubation of GST-P1 with 1 µM aONE results in the

increased incorporation of both the Cyanine5.5 azide (red) and Cyanine7.0 hydrazide (green)

dyes compared to the control treated samples. This image shows a high level of background from

the untreated GST-P1 samples at the 25 kDa region of the gel, indicating the need for further

method optimization in order to decrease this background. The increased incorporation of both

dyes at 50 kDa results from the formation of GST-P1 dimer caused by aONE induced

crosslinking. This image also shows that a greater amount of azide dye (red) is incorporated into

the cross-linked adduct because many of the free aldehyde groups from aONE, required for

reaction with the hydrazide dye (green), are occupied in the formation of the cross-linked adduct.

In order to optimized these reaction conditions reported catalysts for the click reaction and the formation of the Schiff base, required for the addition of the hydrazide dye, were evaluated during the method development. Tris[(1-benzyl-1H-1,2,3-triazol-4-yl)methyl]amine (TBTA) is a reported catalyst for the click reaction and after incubation of GST-P1 with 1 µM aONE, the click reaction was carried out in the presence and absence of 100 µM TBTA.[113] The results show that in the presence of TBTA the signal from the azide dye is greater than the signal from the samples without TBTA. This triazole improves the incorporation of the azide dye by stabilizing the Cu(I) required for the catalysis of the azide-alkyne cycloaddition (**Figure 17B**), therefore TBTA was added as a component of the click reaction in all future experiments.[114] Aniline is a reported catalyst of the aldehyde-hydrazide reaction, and, following the incubation of GST-P1 with aONE, the hydrazide dye was added with or without 1 mM aniline. However, **Figure 17C** shows that the use of aniline with the hydrazide dye does not result in an increased incorporation of the hydrazide dye. Therefore, aniline was not utilized in any further experiments.

Figure 17. Method development for near-IR imaging technique
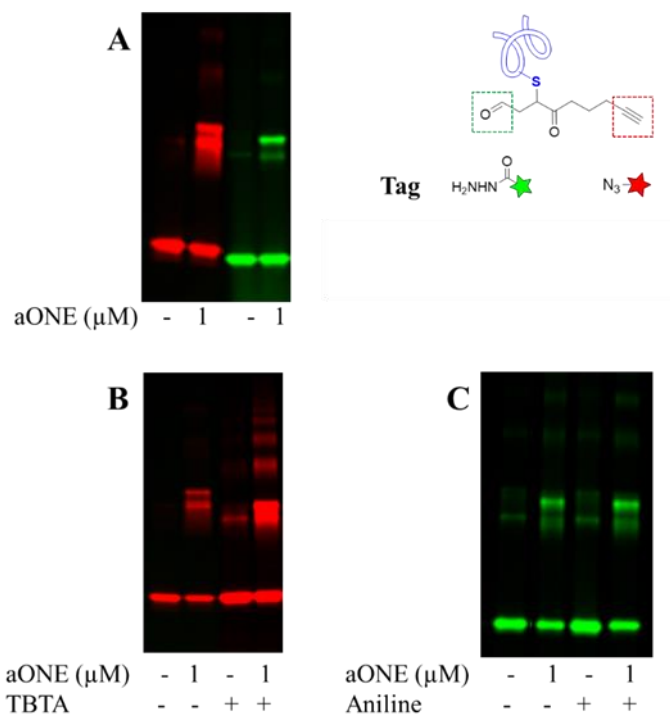
Figure 17. A: Recombinant hGST-P1 (0.1 µg/µL) was incubated with EtOH or 1 µM aONE for 1 hour. These samples were then divided in half and 50 µM cyanine5.5 azide and other click reaction components (1 mM TCEP, 1 mM CuSO4) were added to one half of the sample. The buffer of the second half of the sample was then exchanged for 0.1 M phosphate buffer (pH=5.5) followed by the addition 50 µM cyanine7.0 hydrazide. After incubating these samples at 37°C for two hours the samples were subjected to SDS-PAGE gel electrophoresis (1 µg protein/lane) and imaged using LICOR Sa imaging system. B: The reported click reaction catalyst TBTA was evaluated by detecting the encorporatin of the cyanine5.5 azide dye in samples subjected to the click reaction with or without the addition of 100 µM TBTA. C: The reported catalyst of Schiff base formation, aniline (1 mM), was added to the samples in order to evaluate the effect of the reported catalyst on the incorporation of cyanine7.0 hydrazide to the samples.

2.3.2 Method Validation

Here we demonstrate that after further optimization this method is capable of detecting

Michael addition adducts, Schiff base adducts, and both inter- or intra-molecular cross-linked

LPx protein adducts. This was demonstrated using dose dependent treatment of the recombinant

proteins, GST-P1 and Peptidyl-prolyl cis-trans isomerase NIMA-interacting 1 (Pin1), with aHNE

and aONE. Pin1 is an enzyme with a role in regulating the dephosphorylation of p-Ser/p-Thr

residues by catalyzing the isomerization of these p-Ser/p-Thr-Pro residues from the cis to trans

conformation (**Figure 18**).[115]

Figure 18. Pin1 isomerization reaction
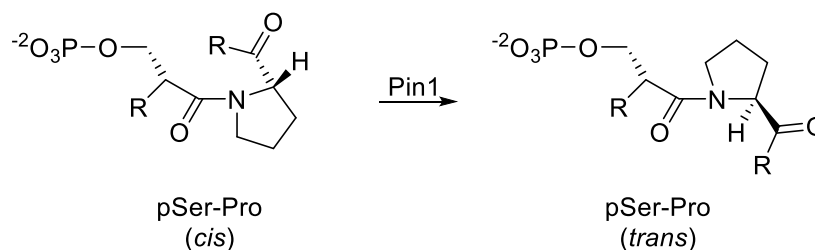
Figure 18. Pin1 catalyzes the isomerization of pSer-Pro from the cis to trans conformations.

This enzyme has been implicated in the regulation of Tau phosphorylation and the inhibition of

this enzyme upon HNE modification could play a role in the buildup of hyperphosphorylated

Tau in Alzheimer's disease.[116] Pin1^{-/-} transgenic mice have been shown to develop Aβ plaques,

NFTs, memory deficits, and neuronal loss.[117-118] The active site of this enzyme also contains both

a Cys and Lys residue. The Cys residue is modified by HNE to form a Michael addition adduct, and ONE produces a cross-linked adduct within the active site reacting with the Cys and Lys residues in the active site.[119-120]

These recombinant enzymes (0.1 µg/µL) were incubated with aHNE and aONE (0, 1, 5, 10, 25 µM) for one hour. These samples were then divided in half. The components for the click reaction (1 mM CuSO4, 1 mM TCEP, 100 µM TBTA, 250 µM Cy5.5 azide) were added to the first half of the reaction. HCl was used to adjust the pH of the second half of these sample from 7.4 to 5.5 before adding the Cy7.0 hydrazide dye (2.5 mM). After incubating both sets of samples at 37 °C for two hours, NaBH$_3$CN (25 mM) was added to all the samples and the reduction reaction which was carried out for one hour at 37 °C. These samples were then recombined, separated by SDS-PAGE gel electrophoresis, and imaged using the LICOR Sa imaging system (**Figure 19**).

Figure 19. Optimized sample preparation protocol for near-IR imaging method
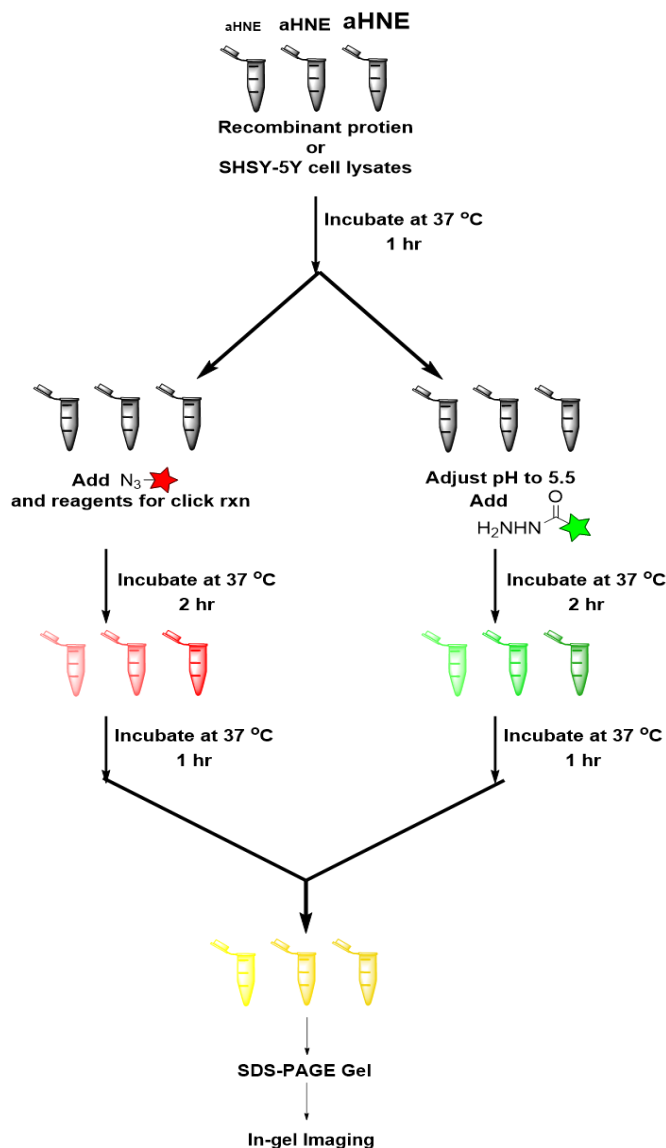
Figure 19. Samples containing recombinant protein or SHSY-5Y cell lysates were treated with EtOH or 1-25 μM of aHNE or aONE. After incubating these samples at 37 °C for 1 hour these samples were divided in half. The components for the click reaction (CuSO$_4$, TCEP, TBTA, and N$_3$-Cy5.5) were added to the first half of each sample and the second half of the reaction was derivatized using Cy7.0 hydrazide. These samples were then reduced, recombined and subjected to SDS-PAGE gel electrophoresis prior to in-gel imaging.

Figure 20 shows that for GST-P1 the addition of aHNE results in a concentration dependent increase in the signals for both the Cy5.5 azide and Cy 7.0 hydrazide dyes at the 25 kDa region of the gel, indicating that the addition of aHNE to GST-P1 results primarily in the formation of Michael addition adducts with the GST-P1 monomer. The incubation of GST-P1 with aHNE causes only a slight increase in the azide dye signal at 50 kDa indicating that only a small amount of cross-linking is caused by the addition of aHNE to GST-P1. The incubation of aONE with GST-P1 results in the formation of cross-linked protein adducts even at the lowest concentration of 1 µM aONE (**Figure 21**). A significant increase in the signal from the azide dye above 25 kDa is observed for all concentrations of aONE. At the 50 kDa region there is still signal from the hydrazide dye because GST-P1 contains multiple reactive Cys residues allowing for the addition of multiple aONE molecules to a single GST-P1 monomer. However, in the region of the gel above 50 kDa there is an increase in the azide dye signal but no appearance of the hydrazide dye because all the free aldehyde groups from the LPx are occupied by the formation of the intermolecular cross-linked aONE adducts. The addition of increasing concentrations of aONE also results small decrease in the molecular weight and broadening of the GST-P1 dimer band at ~50 kDa. This decrease in the molecular weight and the broadening of the dimer band indicates that the GST-P1 dimer becomes more disordered and is composed of multiple conformations dimer that move through the gel at different rates. Some of these conformations may be more compact due to the formation additional cross-linked adducts within the original GST-P1 dimer causing these adducts to move through the gel more quickly than the dimer formed at lower concentrations of aONE.

The results from the incubation of Pin1 with 1-25 µM of aHNE and aONE are shown in **Figure 22**. When comparing the reactivity of aHNE and aONE with Pin1, 25 µM aONE results

in an eight fold increase in the signal from the azide dye and a twofold signal increase from the

same dye from the incubation of Pin1 with 25 µM aHNE. Indicating that ONE is more reactive

than HNE with the Cys residue with the active site of Pin1. When Pin1 was incubated with

increasing concentrations of aONE there is a significant increase in the signal from the azide dye

(red) but a decrease in the hydrazide dye signal (green) without a significant increase in the

formation of dimer adducts. This indicates that the incubation of aONE with Pin1 results in the

formation of an intramolecular cross-linked protein adduct (**Figure 23**). This accounts for the

observed increased incorporation of the azide dye and the decrease in hydrazide dye signal.

Figure 20. Method validation using GST-P1

Figure 20. GST-P1 (0.1 µg/µL in 0.1 M phosphate buffer, pH =7.4) was incubated with 1-25

µM alkyne-HNE or alkyne-ONE for 1 hour before adding the click reaction components (1mM

TCEP, 1 mM CuSO₄, 100 µM TBTA, 250 µM N₃-cyanine5.5) to half of the sample. The second

half of the samples were derivatized with 2.5 mM cyanine7.0 hydrazide after adjust the pH of the

samples to 5.5 with 1 M HCl. To reduce all Schiff bases 25 mM NaCNBH₃ was added. These

samples were then separated by SDS-PAGE gel electrophoresis (1.5 µg protein/lane) and imaged

using the LICOR Sa imaging system. The signals from the azide dye (red) and hydrazide dye

(green) were then quantified. These results show that there is a dose dependent increase in the

signals from both dyes with the aHNE treatments. However with the treatment of aONE there a

significant increase in the signal from the azide dye was observed without an equal increase in

the fold signal from the hydrazide dye. The images are representative of at least four independent experiments and data represents the mean ± SEM of these replicates

Figure 21. Measurement of GST-P1 cross-linking induced by LPx
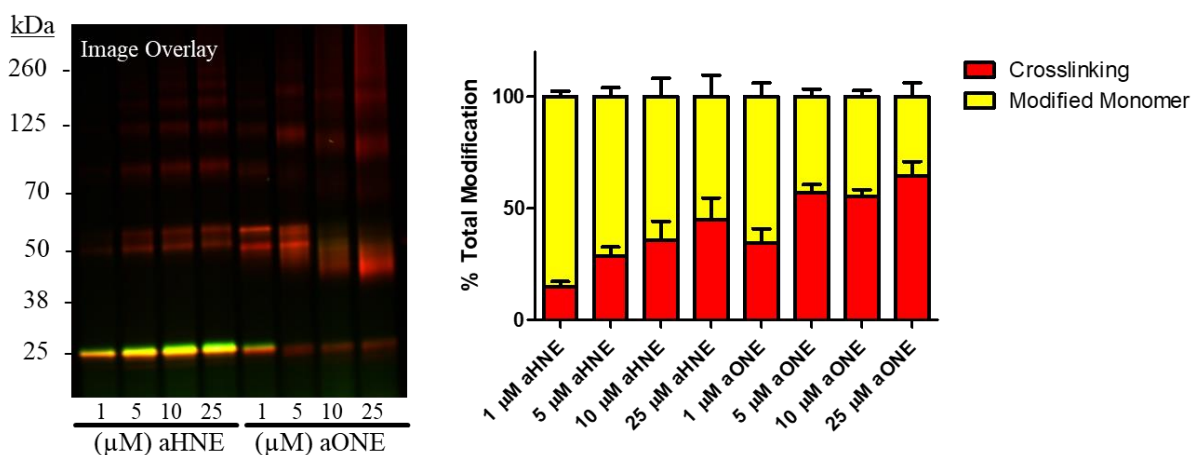
Figure 21. Left: The overlay of the two dye channels from the incubation of GST-P1 with 1-25 µM aHNE and aONE. Right: The total signal for both dyes from each lane was quantified. The red signal (azide dye) measures all GST-P1 aHNE or aONE protein adducts while the green signal (hydrazide dye) measures all Michael addition protein adducts. When the singal from the hydrazide dye was subtracted from the azide dye, the remaining signal from the azide dye is attributed to intermolecular crosslinking inducted by aHNE or aONE. The images are representative of at least four independent experiments and data represents the mean ± SEM of these replicates.

Figure 22. Method validation using Pin-1

Figure 22. Pin1 (0.1 µg/µL in 0.1 M phosphate buffer, pH =7.4) was incubated with 1-25 µM

alkyne-HNE or alkyne-ONE for 1 hour before adding the click reaction components (1mM

TCEP, 1 mM CuSO$_4$, 100 µM TBTA, 250 µM N$_3$-cyanine5.5) to half of the sample. The second

half of the samples were derivatized with 2.5 mM cyanine7.0 hydrazide after adjust the pH of the

samples to 5.5 with 1 M HCl. To reduce all Schiff bases 25 mM NaCNBH$_3$ was added. These

samples were then separated by SDS-PAGE gel electrophoresis (1.5 µg protein/lane) and imaged

using the LICOR Sa imaging system. The signals from the azide dye (red) and hydrazide dye

(green) were then quantified. The treatment of Pin1 with increasing concentrations of aHNE

results in low level of adduct formation. However aONE results in dose dependent increase in

the signal from that azide dye only. Because this increase in the red signal is observed at the 15

kDa can be attributed to the formation of an intramolecular crosslinked adduct. The images are

representative of four independent experiments and data represents the mean ± SEM of these

replicates.

Figure 23. Measurement of Pin-1 cross-linking induced by LPx
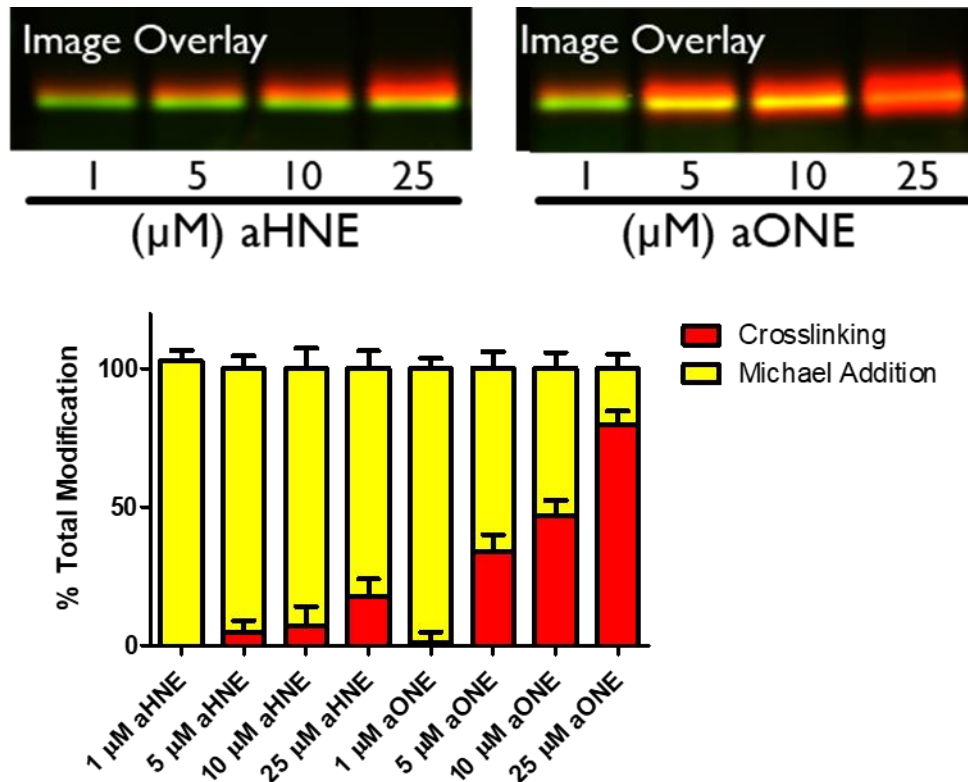
Figure 23. Top: Image overlay of 700 nm (red, azide dye) and 800 nm (green, hydrazide dye) from Pin1 incubated with 1-25 µM aHNE or aONE. Bottom: The total signal for both dyes from each lane was quantified. The red signal (azide dye) measures all GST-P1 aHNE or aONE protein adducts while the green signal (hydrazide dye) measures all Michael addition protein adducts. When the singal from the hydrazide dye was subtracted from the azide dye, the remaining signal from the azide dye is attributed to intramolecular crosslinking inducted by aHNE or aONE. The images are representative of four independent experiments and data represents the mean ± SEM of these replicates.

The same in-gel imaging method was then used to visualize alkyne-LPx protein adducts across the whole proteome from SHSY-5Y cell lysates (**Figure 24**). For these experiments 1-25 µM of each alkyne-LPx was added to whole cell SHSY-5Y cell lysates. The images resulting from these experiments show that in whole cell lysates there is a high background from the Cy7.0 hydrazide dye (green) in the control samples due to the fact that this dye is not selective for the LPx adducts formed from the exogenously added alkyne-LPx, but this dye reacts with all proteins containing a free aldehyde or a hydrazide reactive group. The azide dye in these experiments reacts selectively with alkyne-LPx adducts. When SHSY-5Y cell lysates were incubated with increasing concentrations of the alkyne-LPx there is a dose dependent increase in the Cy5.5 azide signal for both alkyne-LPx. At the highest concentration of aHNE clear and distinct bands still appear in the 700 nm channel (red). This indicates that the amount of protein crosslinking is limited and does not interfere with the resolution of aHNE-protein adducts. However, when the same lysates are treated with 25 µM aONE the clear resolution of proteins adducts into distinct bands by SDS-PAGE gel is lost indicating a high level of protein crosslinking catalyzed by aONE.

LPx protein adducts can also be evaluated in isolated protein fractions. Histones are an important group of proteins with a role in the organization of DNA into chromatin and histone PTMs are involved in the epigenetic regulation of gene expression. This group of proteins can be enriched by the isolation of nuclei from tissues or cell followed by acid extraction. ONE was previously reported to induce intramolecular crosslinking in histone H4 by modifying His75 and Lys77.[121] The nuclei of SHSY-5Y cells were isolated and the histones were then extracted using trichloroacetic acid. Isolated histones were then treated with the alkyne analogs of HNE and ONE and subjected to the same sample preparation described above. This imaging method was

used to visualize the LPx histone adducts (**Figure 25**). The results show that aHNE causes dose

dependent increase in both dye signals suggesting that the primary adducts are formed via

Michael addition. However the treatment of isolated histones with aONE resulted in a significant

loss in the hydrazide dye at all concentrations of aONE treatment. Therefore the dose dependent

increase of the signal resulting from the incorporation of the azide dye caused by the formation

of intramolecular crosslinked ONE histone adducts. The broadening of the histone band in

samples treated with higher concentrations of aONE indicates that the histone adducts become

more disordered and is composed of multiple conformations that move through the gel at

different rates. Some of these conformations may be more compact due to the formation

additional intra-molecular cross-linked adducts causing these adducts to move through the gel

more quickly than the adducts formed at lower concentrations of aONE.

Figure 24. Imaging of LPx protein adducts in SHSY-5Y cell lysates.
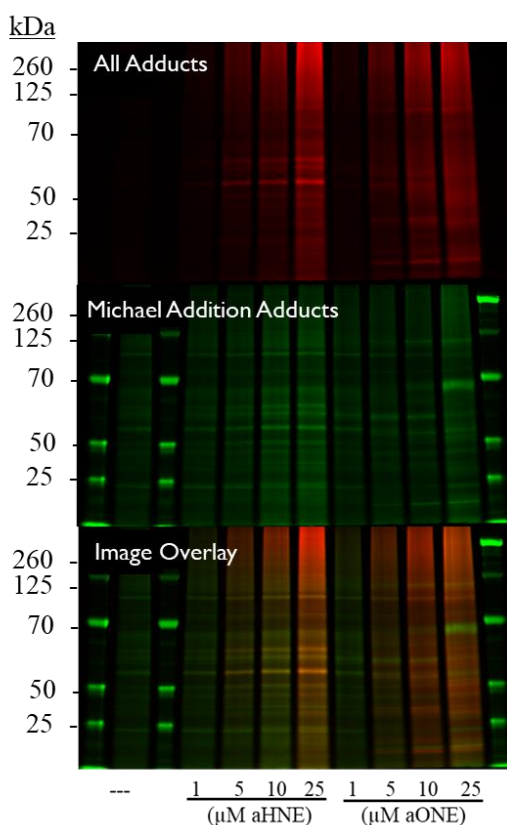
Figure 24. SHSY-5Y lysates (0.5 µg/µL) were treated with EtOH, 1-25 µM aHNE or aONE.

Each lane of the gel contains 30 µg of protein. Top: Image from 700 nm channel (azide dye).

Middle: Image from 800 nm channel (hydrazide dye). Bottom: Image overlay of both channel.

The images are representative of four independent experiments and data represents the mean ±

SEM of these replicates.

Figure 25. Detection of histone LPx adducts
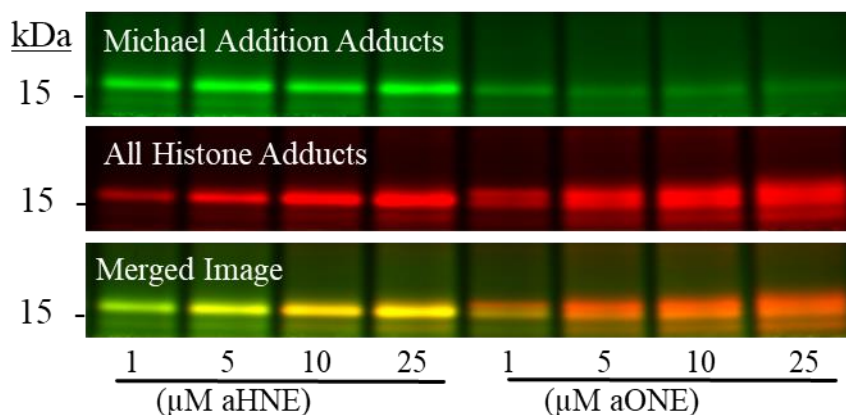
Figure 25. Isolated histones (0.1 µg/µL) were treated with 1-25 µM aHNE or aONE. Sample preparation was conducted using identical conditions as outlined previously. Top: Image from 800 nm channel (hydrazide dye) shows that aHNE causes slight increase in signal with increasing concentrations but with aONE the 800 nm signal is lost. Middle: Image from 700 nm channel (azide dye) shows increase in the signal from this dye with increasing concentrations of both aHNE and aONE. However, aONE is more reactive towards histones than aHNE. Bottom: Overlay of both 700 nm and 800 nm channels. Yellow signal indicates that theses adducts are Michael addition adducts while the signals from the aONE treatment that remain red in the overlay indicate the formation of intramolecular crosslinked adducts. The images are representative of three independent experiments.

2.4 Proteomic Analysis of LPx Modified Proteins

Whole cell SHSY-5Y lysates were treated with EtOH vehicle, 1 µM or 25 µM aHNE in order to develop a method for the enrichment of LPx protein adducts. After incubating the cell lysates (1 mg/mL) with aHNE, azido-biotin and the other components of the click reaction were added to these lysates in order to conjugate the azido-biotin to the LPx protein adducts. Affinity enrichment using magnetic streptavidin beads was then conducted to wash out unmodified proteins and isolate aHNE adducts. The work flow for this method is depicted in **Figure 25**. The elution fractions from the affinity enrichment were subjected to SDS-PAGE gel electrophoresis and any proteins were visualized by Coomassie Blue stain. The elution fraction from the control (EtOH, lane 1) treatment of the SHSY-5Y cells contains a low molecular weight band resulting from the loss of streptavidin from the magnetic beads during the elution step. The other proteins seen from the Coomassie Blue staining in the elution fractions from 1 µM aHNE (lane 2) and 25 µM aHNE (lane 3) treatments are the result of the biotin-streptavidin enrichment of aHNE protein adducts.

This method was then used to enrich aHNE protein adducts for protein identification by LC-MS/MS. SHSY-5Y cell lysates were treated with 25 µM aHNE and subjected to the sample work flow described above. The elution fractions collected from the biotin-streptavidin enrichment were reduced using TCEP (25 mM), and all cysteine residues were capped using iodoacetamide (20 mM). These samples were then loaded on the stacking gel of an SDS-PAGE gel, and that stacking gel was stained with Coomassie blue dye. The resulting band was excised from the gel, and subjected to in-gel trypsin digestion overnight. The peptides were collected after overnight digestion, desalted, dried, and analyzed by LC-MS/MS. The data were collected

using an OrbiTrap Velos MS and analyzed by the Mascot search engine against the Uniprot-

human database.

Figure 26. Biotin-streptavidin enrichment of aHNE protein adducts in SHSY-5Y cell lysates
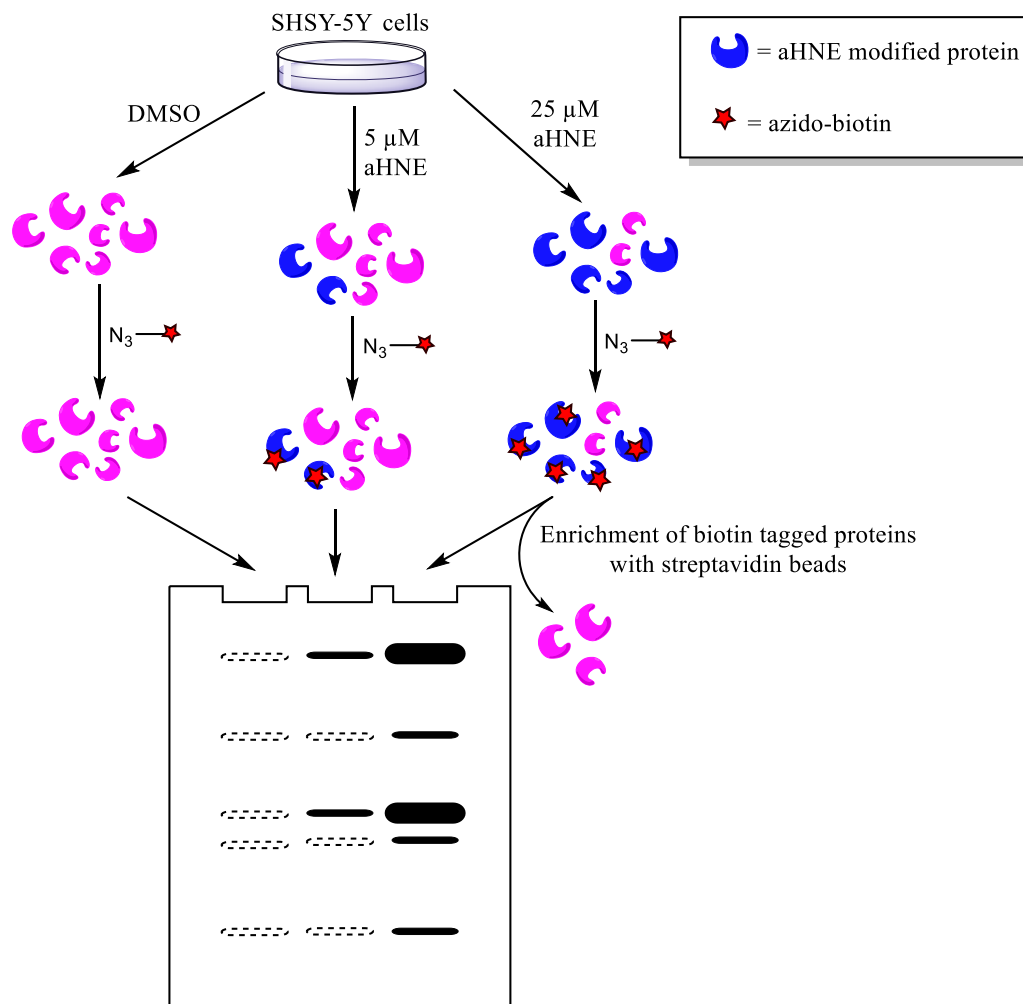
Figure 26. SHSY-5Y cell lysates (1 mg/mL) were treated with EtOH, 5 µM aHNE, or 25 µM aHNE. The aHNE modified proteins were then conjugated to biotin using click chemistry. The proteins collected from this enrichment step were separated by SDS-PAGE gel electrophoresis and the resulting gels were stained with Comassie Blue dye.

The proteomic analysis from duplicate samples identified 403 proteins from the enrichment of aHNE treated SHSY-5Y lysates (**Appendix A**). Some of the proteins identified include several heat shock proteins, cysteine proteases such as calpain-1, epigenetic regulators such as HDAC2, and histone H2B, important protein involved in cell redox homeostasis including protein disulfide-isomerase. These results were compared to previously reported proteomic analyses that were conducted in order to identify LPx protein adducts in the brain homogenates from subjects diagnosed with AD. One report utilized frontal cortex homogenates taken from subjects with Down syndrome, Down syndrome with AD pathology, or age matched controls. This analysis identified 24 HNE modified proteins, including α-enolase, fructose-bisphosphate aldolase A, and glyceraldehyde-3-phosphate dehydrogenase. The level of HNE modification for several of these proteins was also increased in the subjects with Down syndrome and Down syndrome with AD pathology relative to the age matched controls.[90] A similar analysis was conducted using brain homogenates form subjects with early AD and the results were compared to age matched controls. This analysis identified six proteins (MnSOD, α-enolase, F1 ATPase α-subunit, dihydropyrimidinase-related protein 2, triose phosphate isomerase, and malate dehydrogenase) that were modified by HNE in these samples. There was a significant increase in the HNE modification of dihydropyrimidinase-related protein 2, triose phosphate isomerase, and malate dehydrogenase in early AD samples compared to the age matched controls.[99] Our analysis identified 15 out of the 28 unique proteins identified in these previous reports as aHNE modified proteins in SHSY-5Y cell lysates.

The proteins identified from our LC-MS/MS analysis were further analyzed by Gene Ontology which classifies the functions of gene products into three categories: molecular function, cellular component, and biological process. The molecular function classification is

used to describe the general biochemical activity of a specific gene product (**Figure 27**). The

cellular component classification describes where a gene product is located within a specific

organelle or gene product group (proteasome, ribosome) (**Figure 29**). Finally, the biological

process refers to a specific biological process to which a gene product contributes and is broader

than the molecular function classification (**Figure 28**).[122]

Figure 27. Molecular Functions of aHNE modified proteins
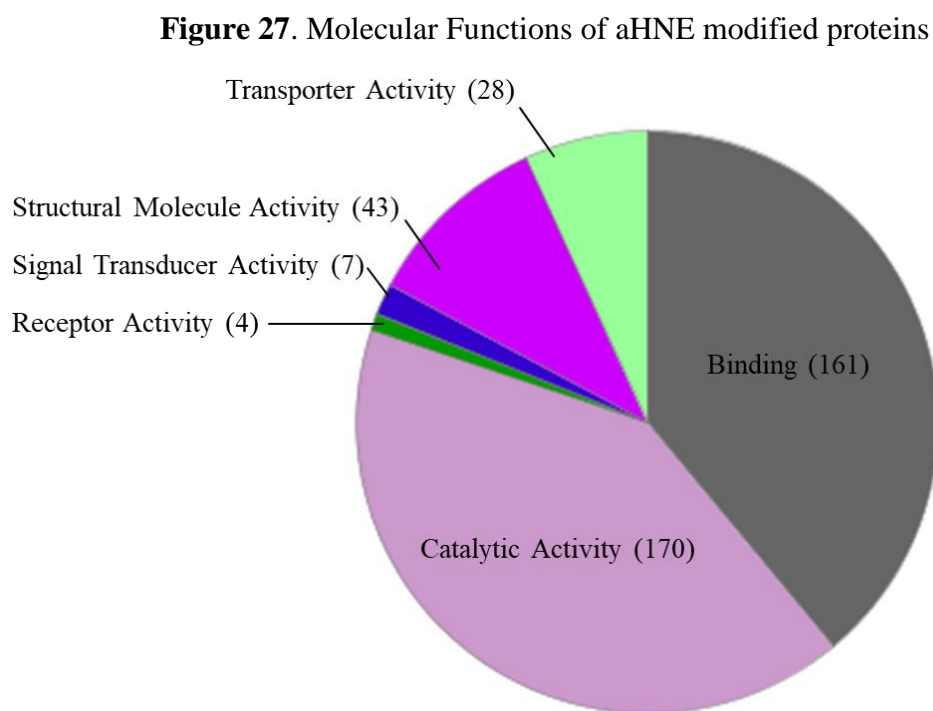
Figure 27. The molecular function classifies the identified aHNE modified proteins by the

biochemical activity of the gene products. This analysis shows that 331 of the identified proteins

are involved in catalytic activity or binding. The remainder of the proteins are classified by

transporter, structural molecule, signal transducer, or receptor activity.

Figure 28. Biological Processes of aHNE modified proteins
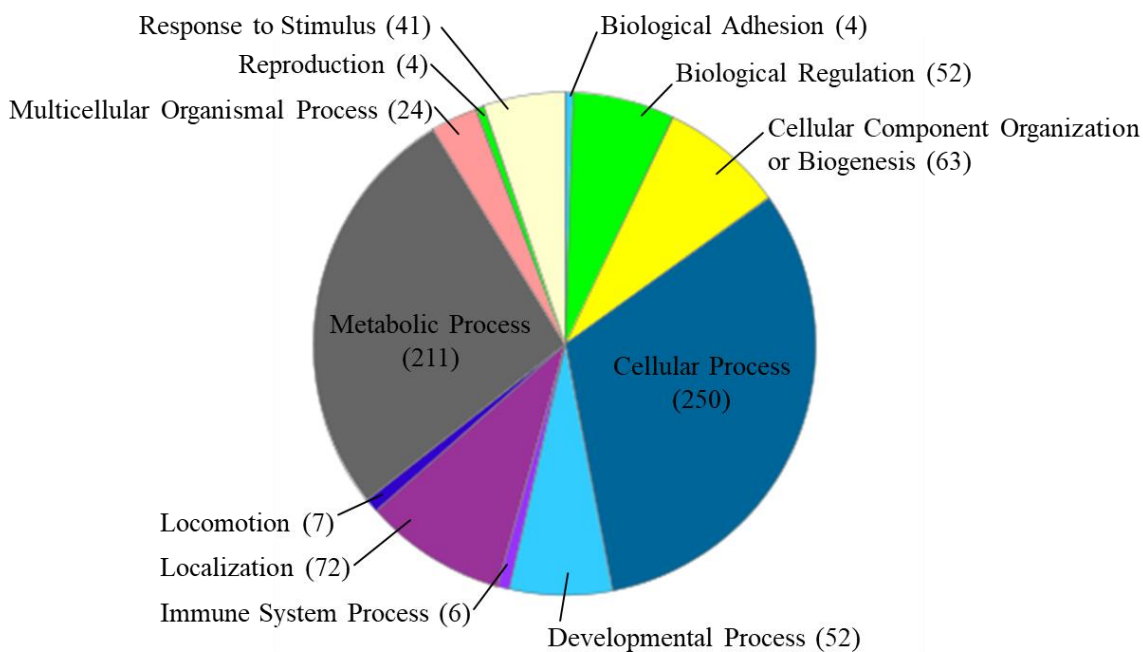
Figure 28. The biological process of aHNE modified proteins classifies the biological function of the gene product. A majority of the proteins identified contribute to metabolic or cellular processes. The processes of localization, development, biological regulation, cellular component organization, and response to stimulus all contain more than 40 proteins. Finally the processes of reproduction, biological adhesion, multicellular organismal, locomotion, and immune system contain less than 25 aHNE modified proteins

Figure 29. Cellular components of aHNE modified proteins
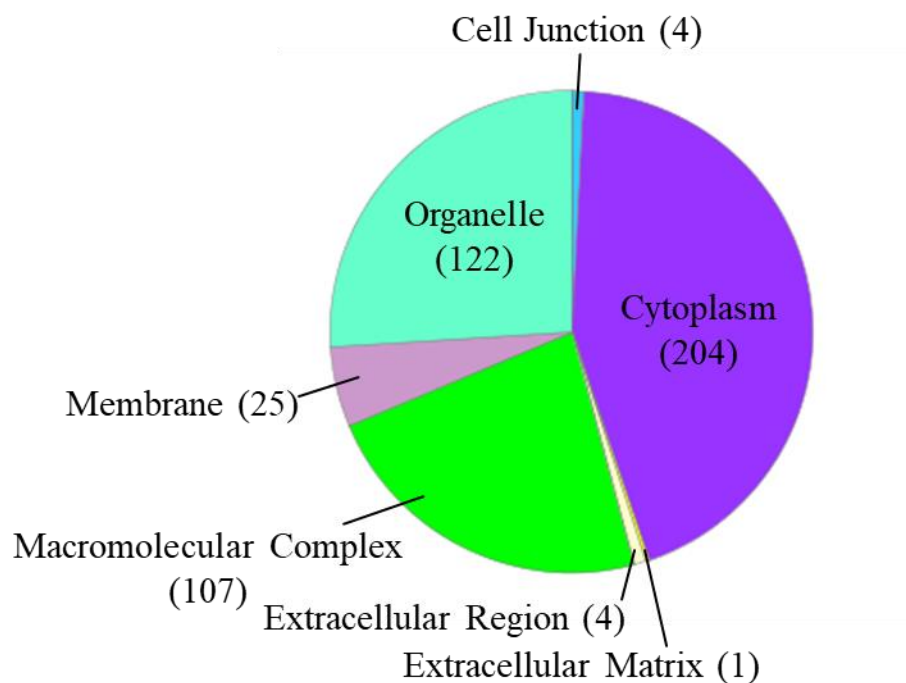
Figure 29. The cellular components of the aHNE classifies these proteins based on the cell location where the protein is active. Nearly all of the identified proteins are active in the cytoplasm, a macromolecular complex, or an organelle. A small number of the identified proteins are active in the membrane, extracellular matrix, extracellular region, or at a cell junction.

3. Discussion

3.1 Near-IR In-gel Imaging Method

The current methods for the detection and quantitation of LPx protein adducts include chemical derivatization (DNPH, CHD, TBA) and the use of anti-HNE antibodies, however, both of these methods suffer from limitations that prevent the detection of all LPx protein adducts (**Figure 30**). A free aldehyde group is required for all chemical derivatization methods and is therefore only capable of detecting Michael addition protein adducts. The reported anti-HNE antibodies were raised against reduced Lys, non-reduced Lys, or His HNE adducts and have demonstrated limited cross reactivity with adducts at other amino acids.[91]

Figure 30. Methods for the detection of HNE protein adducts
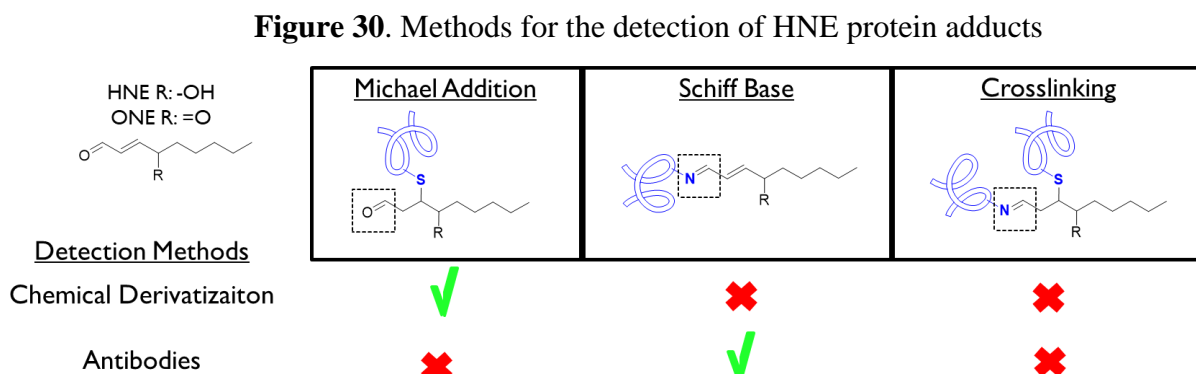
Figure 30. The chemical derivatization methods are capable of detecting Michael addition adducts, but are incapable of detecting Schiff base and cross-linked adducts due to the lack of a free aldehyde group. Certain commercially available anti-HNE antibodies can detect Schiff base adducts and show limited reactivity against Michael addition and cross-linked LPx protein adducts.

Two near-IR chemical tags and alkyne derivatives of HNE and ONE were used for the development of an in-gel imaging method for the detection of aHNE and aONE protein adducts (**Figure 31**). The use of these components allows for the detection of all Michael addition, Schiff base, and cross-linked protein adducts. The azide dye (cyanine5.5 azide, red) used in this method reacts with the terminal alkyne of the aHNE and aONE and is therefore capable of detecting all possible protein adducts formed by the addition of exogenous alkyne-LPx. The hydrazide dye (cyanine7 hydrazide, green) is only able to detect Michael addition protein adducts. These adducts can then be distinguished from the other types of adducts because the incorporation of both the hydrazide and alkyne dyes will result in the appearance of a yellow signal in the overlay image of the two near-IR channels while the other types of adducts will only appear in the red channel. Additionally, the use of SDS-PAGE gel electrophoresis allows for the separation of monomeric LPx protein adducts, from dimers and high molecular weight oligomers formed as a result of LPx cross-linked protein adducts for recombinant protein experiments.

Figure 31. The use of two near-IR dyes for the detection of alkyne-LPx protein adducts.
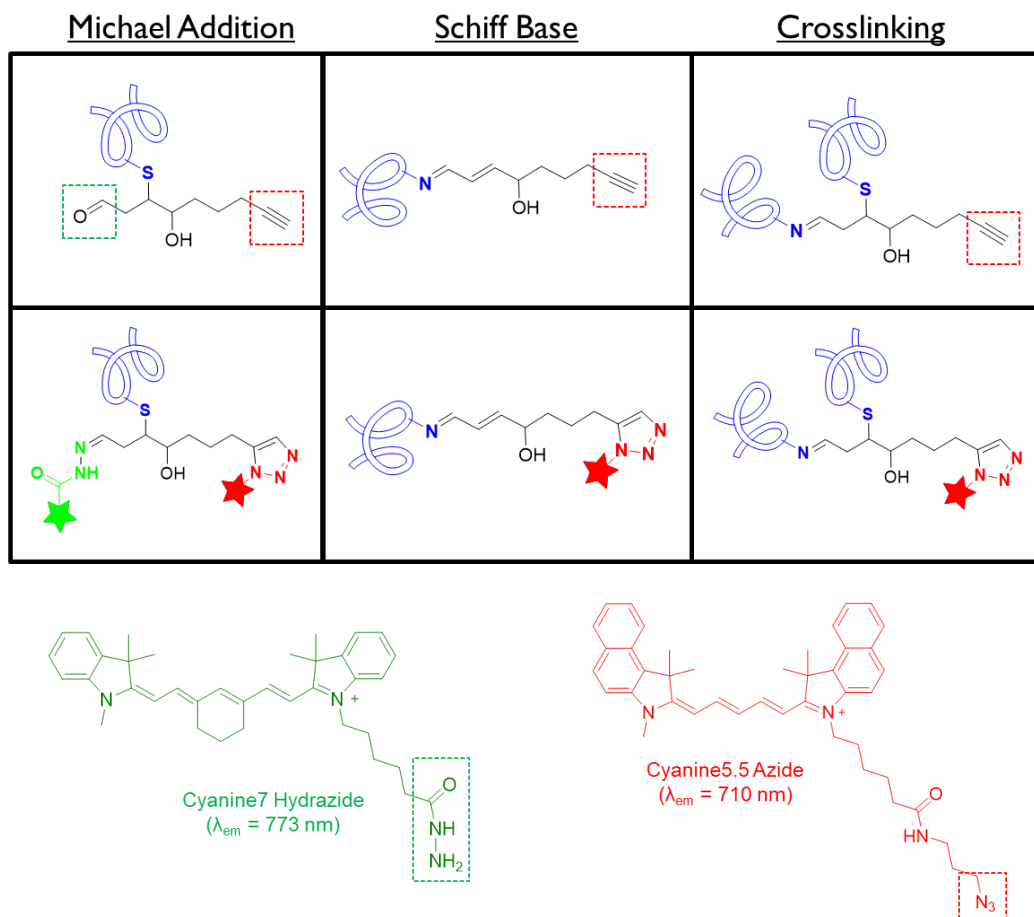
Figure 31. Cyanine5.5 azide reacts with the terminal alkyne of aHNE or aONE that is present in all types of adducts. Cyanine7 hydrazide however only reacts with the Michael addition adducts where a free aldehyde is available for reaction with the hydrazide dye.

3.2 Detection of Intra- and Inter-molecular Cross-linked Adducts

The Pin1 intramolecular cross-linked adducts has previously been detected by LC-MS/MS analysis of recombinant Pin1 and RKO cells treated with ONE.[120] The active site of Pin1 contains both Cys113 and Lys117 that both react with a single ONE molecule (**Figure 32**). When recombinant Pin1 was treated with increasing concentrations of aONE, the resulting in-gel images in **Figure 22** show a concentration-dependent increase in the signal from the azide dye but a decrease in the hydrazide signal. These results are consistent with the formation of an intra-molecular cross-linked adduct and demonstrate that this method is capable of detecting both Michael addition adducts and intramolecular cross-linked adducts.

GST-P1 contains multiple reactive Cys residues (Cys47 and Cys101) allowing for the formation of multiple HNE or ONE Michael addition adducts in a single GST-P1 monomer. The formation of intermolecular cross-linked adducts can then result not only in the formation of covalently linked dimers, but also the formation of high molecular weight oligomers. The results from the in-gel imaging method (**Figure 21**) demonstrated that the use of SDS-PAGE gel electrophoresis allows for the separation of intermolecular cross-linked protein adducts with different molecular weights. Although a majority of the cross-linked adducts were dimers, with a molecular weight of 50 kDa, the treatment of recombinant GST-P1 with aHNE and aONE also caused the formation of larger oligomers with a molecular weight greater than 50 kDa (**Figure 33**).

Figure 32. Formation of an intra-molecular cross-linked ONE adduct in Pin1 active site.
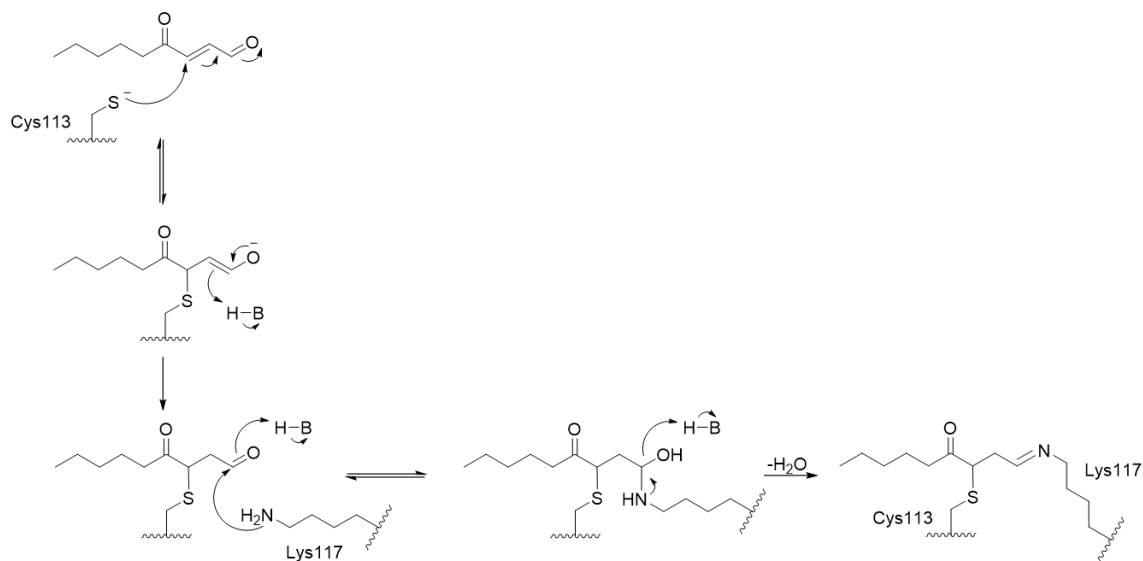
Figure 32. The α,β-unsaturated aldehyde of ONE reacts with the thiol of Cys113 via a Michael addition reaction. The remaining free aldehyde then reacts with the terminal amino group of the Lys117 residue to form a Schiff base and resulting in the formation of an intra-molecular cross-linked adduct.

Figure 33. Formation of inter-molecular cross-linked adducts by treating GST-P1 with ONE
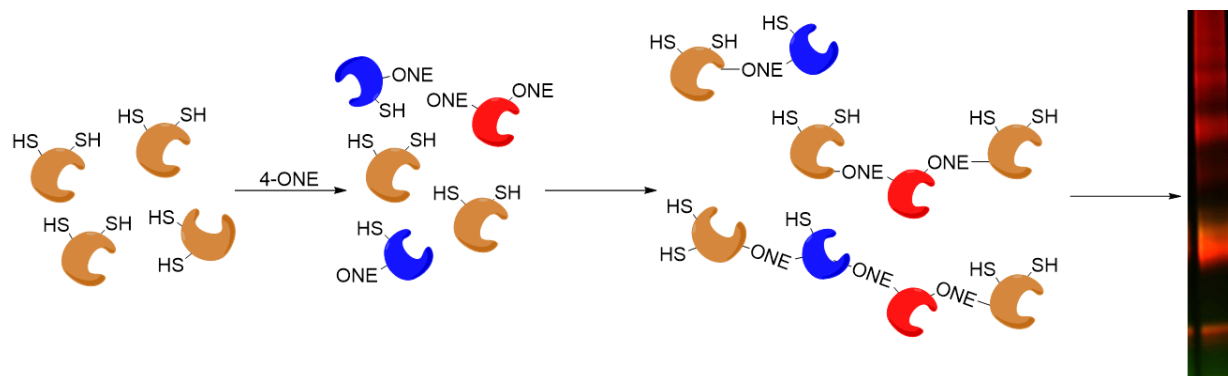
Figure 33. The treatment of GST-P1 with ONE can result in the formation of single ONE adducts (blue) or multiple ONE adducts (red) in a single GST-P1 monomer. This results in the formation of cross-linked dimers and oligomers that can be separated during the in-gel imaging method by SDS-PAGE gel electrophoresis.

The increase in the level of protein cross-linking induced by aONE compared to aHNE can be explained by the chemical reactivity of the aHNE and aONE protein adducts. (**Figure 34**) Upon the formation of a Michael addition protein adduct by aHNE the LPx no longer retains its original cis-trans stereochemistry. This allows the hydroxyl group at the C4 position to undergo an intramolecular reaction with the carbon in the aldehyde resulting in the formation of a five-membered ring acetal product. The acetal formed reversibly from HNE is unreactive to Schiff base formation and is unable to cross-link, in contrast to ONE; resulting in relatively low amounts of protein crosslinking even at higher concentration of HNE. Two other factors also contribute to the increased reactivity of ONE: 1) statistically, there are double the number of

electrophilic carbon; and 2) the second keto group is electron-withdrawing and enhances the reactivity of ONE.

Figure 34. Mechanism of HNE and ONE Michael addition reaction

4-HNE

4-ONE
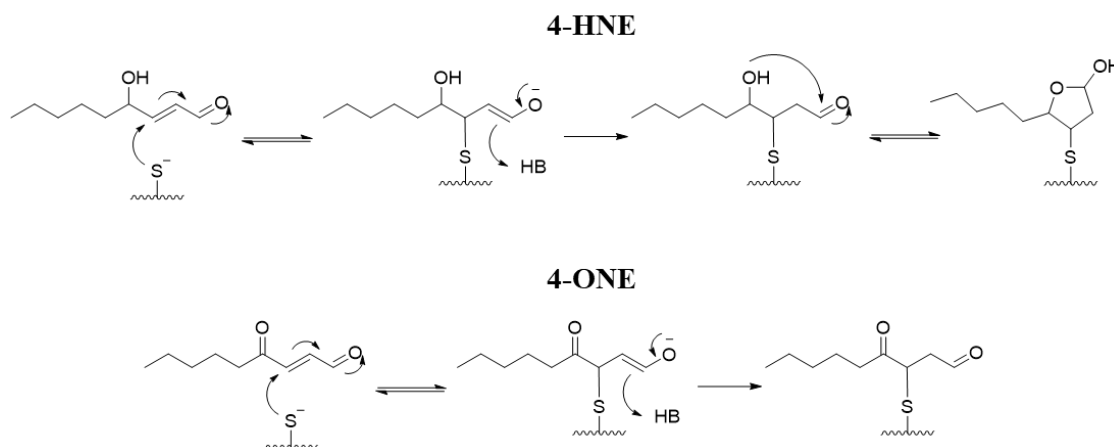
Figure 34. Top: The formation of a HNE Michael addition adduct can result in the formation of a five-membered ring aldol product. Bottom: The lack of an alcohol group at the 4 position of ONE prevents the formation of a cyclic aldol product.

4. Conclusion

ALDH2 is a key enzyme in the metabolism of LPx. We have validated that knocking out this enzyme in mice results in the development of age-dependent memory deficits that were not observed in the age matched WT mice. When the brain homogenates from WT and ALDH2 KO mice were subjected to chemical derivatization by hydrazide dyes, a significant increase in

protein carbonylation was observed in the brains of KO compared to the WT animals. Similar results were observed when WT and ALDH2$^{-/-}$ PC12 cells were treated with exogenous HNE. Additionally, enzyme activity assay showed that both HNE and ONE are inhibitors of ALDH2. These results demonstrate the fact that ALDH2 is a key enzyme in the metabolism of LPx, including HNE, and protects tissues or cells from the toxic effects of these molecules by reducing the modification of biomolecules by LPx.

The use of HNE and ONE alkyne derivatives, along with two near-IR dyes, allowed for the development of an in-gel imaging technique that allows for the detection and quantitation of all aHNE and aONE protein adducts. This method was optimized using recombinant GST-P1 and the most abundant protein adducts this method detected were Michael addition and inter-molecular cross-linked adducts. However, when this method was used to analyze the protein adducts formed in the presence of recombinant Pin1 or isolated histones treatment with aHNE resulted in the formation of Michael addition adducts while aONE primarily caused the formation of intra-molecular cross-linked adducts. Finally, LC-MS/MS analysis of aHNE treated SHSY-5Y cell lysates resulted in the identification of 403 proteins that were modified by aHNE. This method does suffer from certain limitations including that it relies on the addition of exogenous aHNE or aONE to cells or a protein samples. Our method cannot be used to measure adducts formed by endogenous LPx. However, this method can be particularly useful when investigating LPx protein adducts to a specific protein or subset of proteins. One example of this was shown above in the use of this method to detect histone aHNE and aONE adducts.

5. Methods

All chemicals and reagents were purchased from Sigma-Aldrich (St. Louis, MO), ThermoFisher Scientific or Cayman Chemicals (Ann Arbor, MI) unless stated otherwise.

5.1 Animal Behavioral Test: Novel Object Recognition

The two phases to the NOR are habituation and testing. During habituation, the mice are exposed to two identical objects for 5 min and returned back to their home cage for 1 min. During testing, mice are exposed to a familiar object and a novel object and the time spent with each object is measured and the percentage of discrimination index is calculated (% discrimination index = (time spent with novel object/total time spent with objects)*100).

5.2 General hydrazide derivatization method

Alexa488 hydrazide: Whole brain homogenates (2 mg/mL) were incubated with 500 µM Alexa488 hydrazide (ThermoFisher) in 0.1 M phosphate buffer (pH=5.5) for 2 hours at room temperature. These proteins were then separated on a 4-12% Bis-Tris, 10 well, 1.5 mm SDS-PAGE gel with 30 µg of protein loaded in each lane with NuPAGE LDS sample buffer (1x, 10% β-mercaptoethanol). These gels were run at 150V with 1x MOPS buffer and the gels were immediately imaged using a GE Typhoon Trio imager.

Cy7 hydrazide: Whole brain homogenates (0.5 mg/mL) or PC12 cell lysates (0.5 mg/mL) were incubated with 50 µM Cy7.0 hydrazide (Lumirobe) in 0.1 M phosphate buffer (pH=5.5) for 2 hours at room temperature. Half of the PC12 cells lysate samples were then reduced by incubated 25 mM NaCNBH$_3$ at 37°C for 2 hours. These proteins were then separated on a 4-12% Bis-Tris, 12 well, 1.0 mm SDS-PAGE gel with 3.75 µg of protein loaded in each lane. These gels were run at 150V with 1x MOPS buffer and gels were immediately imaged using a LICOR Sa Imaging System.

5.3 ALDH2 enzyme kinetics

Recombinant human ALDH2 (180 nM, Abnova) was preincubated with EtOH or 1, 10 or 100 µM ONE or HNE and 500 µM NAD^+ in an assay buffer (50 mM sodium pyrophosphate, pH = 8.8) for 5 min at 25°C. 1 mM of acetaldehyde was then added and the production of NADPH (340 nm) was monitored for 10 minutes. The rate of the reaction was then normalized to the rate of the reaction without ONE or HNE.

5.4 Histone Isolation

Histones were isolated from SHSY-5Y cells according to a previously published protocol Garcia, et, al.[123] The SHSY-5Y cell pellet were was resuspended in nuclei isolation buffer (15 mM Tris-HCl, 60 mM KCl, 15 mM NaCl, 5 mM $MgCl_2$, 250 mM sucrose, 1 mM DTT, pH=7.5) with 10% NP-40 and incubated on ice for 5 minutes. This cell suspension was then centrifuged for 5 minutes at 1000x g and 4°C. This resulting supernatant was then removed and the remaining cell pellet was washed three times by repeating this process using nuclei isolation buffer without NP-40. A solution of 0.4N H_2SO_4 was then slowly added to the washed pellet until five times the volume of the cell pellet was added. After gentle vortexing the cell pellets were incubated at 4°C with rotation for 4 hours. These pellets were then centrifuged at 3400x g for 5 minutes and the resulting supernatant was collected. TCA was gently added to the collected supernatant until the final concentration of TCA reached 20% and incubated on ice overnight. After centrifugation at 3400x g for 5 minutes the resulting supernatant was removed and the protein washed with acetone + 0.1% HCl. The centrifugation was repeated and the protein was washed with acetone two more times. After the acetone was evaporated, the resulting film was resuspended in dH_2O.

5.5 In-gel imaging method

The recombinant enzymes GST-P1 and Pin1 (0.1 µg/µL), in 0.1 M sodium phosphate buffer, pH = 7.4), isolated histones (0.1 µg/µL) or SHSY-5Y cell lysates (0.5 µg/µL) were incubated with EtOH, aHNE, and aONE (1, 5, 10, 25 µM) for one hour at 37°C. These samples were then divided in half. The components for the click reaction (1 mM CuSO4, 1 mM TCEP, 100 µM TBTA, 250 µM Cy5.5 azide) were added to the first half of the reaction. 1 M HCl was used to adjust the pH of the second half of these sample from 7.4 to 5.5 before adding the Cy7.0 hydrazide dye (2.5 mM). After incubating both sets of samples at 37 °C for two hours the reduction reaction was carried out for one hour after the addition of $NaBH_3CN$ (25 mM) to all samples. These samples were then recombined and NuPAGE LDS loading buffer with 10% β-mercaptoethanol was added to each sample and heated to 70 °C for 15 min. These samples were on a 12% Bis-Tris, 12 well, 1.0 mm SDS-PAGE gel. For the recombinant enzymes and histones 1.5 µg of protein was loaded in each land and 7.5 µg of protein from SHSY-5Y lysates. These gels were run at 150V with 1x MOPS buffer and gels were immediately imaged using the LICOR Sa imager.

5.6 Biotin-streptavidin enrichment of LPx protein adducts

SHSY-5Y cell lysates (1 mg/mL) in 0.1 M phosphate buffer (pH=7.4) were treated with EtOH, 5 µM, or 25 µM aHNE and these samples were incubated at 37°C for 1 hour. The components for the click reaction were then added: 1 mM $CuSO_4$, 1 mM TCEP, 100 µM TBTA, 500 µM N_3-biotin and incubated for another hour at 37°C. The excess N_3-biotin was then removed using molecular weight cutoff filters (10 kDa) and the samples were diluted 3x the original sample volume with 0.1 mM phosphate buffer (pH=7.4) and incubated with washed Pierce streptavidin magnetic beads (1/10th of sample volume) at room temperature with rotation.

The supernatant was then removed and the magnetic beads were washed sequentially using, 0.1

M phosphate buffer (10x original sample volume), 1 M NaCl (2x original sample volume), twice

with 0.1 M phosphate buffer (2x original sample volume). Finally the elution was conducted

using 1% SDS and heating the samples to 90°C for 15 minutes. The resulting elution fractions

were either separated by SDS-PAGE gel or prepared for LC-MS/MS analysis. The SDS-PAGE

gel separation was done using a 4-12% Bis-Tris, 10 well, 1.5 mm SDS-PAGE gel with 30 µg of

protein loaded in each lane.

For the LC-MS/MS analysis the protein concentration of the elution fractions was

determined using a Pierce^{TM} BCA protein assay kit (Thermo Scientific). The cysteines were

alkylated by adding 50 mM TCEP that was incubated at 60°C for 10 minutes followed by the

addition of 50 mM IAA. After a 1 hour incubation at room temperature the whole sample was

loaded into an SDS-PAGE gel, however the gel was only run for ~10 minutes to run the samples

into the stacking gel. After staining the gel with Coommassie Blue dye the resulting band was

excised was subjected to in-gel trypsin digestion using the Pierce in-gel trypsin digestion kit

(Thermo Scientific). The resulting peptides from the protein digests were desalted using Amika

(Harvard Apparatus), Nest Part # SS18V, UltraMicroSpin Columns, 2-100µl (3-30µg) and dried

using a SpeedVac.

5.7 LC-MS/ MS Analysis

The protein digests with 1% formic acid were analyzed using LTQ Velos Pro-Orbitrap

high resolution mass spectrometer (Thermo Electron Corp., Bremen, Germany) equipped with a

nanospray ESI source and nano-HPLC system (Agilent Technologies, Inc., Santa Clara, CA).

The trapping cartridge and the capillary column used for separation were Zorbax 300 SB-C18 (5

x 0.3 mm, 5 µm, Agilent Technologies) and Zorbax 300 SB-C18 (150 mm x 75 µm , 3.5 µm,

Agilent Technologies), respectively. Peptides were loaded onto the column with mobile phase A

(5% acetonitrile, 0.1% formic acid) and separated at a flow rate of 250 nL/min through a 60 min

gradient where mobile phase B (95% acetonitrile, 0.1% formic acid) increases from 5% to

40%. Higher energy collisional dissociation fragmentation was performed for the top-10 peaks

in each MS scan. Resolution of the MS scans was 30,000 and 7500 for the MS/MS scans. The

raw MS/MS data files were converted to MGF files and searched in Mascot search engine

(Matrix Science, London, UK; version 2.2.07 http://www.matrixscience.com) against the

Uniprot-human_20170926 database with the appropriate (deamidation, oxidation) variable

modifications. Mascot was searched with a fragment ion mass tolerance of 0.60 Da and a parent

ion tolerance of 15.0 ppm. For protein identification (ID) Scaffold (version Scaffold_4.8.4,

Proteome Software Inc., Portland, OR) was used to validate MS/MS based peptide and protein

identifications. Peptide identifications were accepted if they could be established at greater than

95.0% probability by the Peptide Prophet algorithm. Protein identifications were accepted if they

could be established at greater than 99.0% probability and contained at least 2 identified

peptides. Protein probabilities were assigned by the Protein Prophet algorithm. For gene

ontology (GO) interpretations, UniProt IDs of the identified proteins submitted to GORetriever

were categorized using CateGOrizer.

CHAPTER 2. CHEMICAL SCAVENGERS OF REACTIVE ALDEHYDES PREVENT PROTEIN CROSS-LINKING

1. Introduction

1.1 Chemical Scavengers of LPx

Different classes of nucleophilic small molecules have been explored as small molecule scavengers of LPx. The bifunctional reactivity of LPx allows for small molecule scavengers to react with LPx by two different mechanisms. Thiol containing small molecules such as glutathione (GSH), and N-acetylcysteine (NAC) react with LPx via Michael addition. A second class of small molecule scavengers react primarily via the Schiff base reaction and include carnosine, histidyl-hydrazide, and hydralazine.[124]

Figure 35. Structures of LPx scavengers.
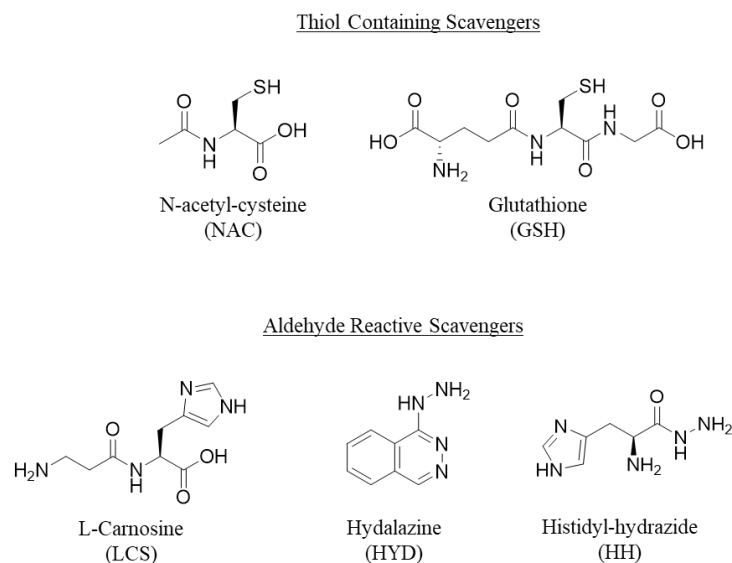
Figure 35. Top: Chemical structures of the thiol containing scavengers NAC and GSH. Bottom: Chemical structure of aldehyde reactive scavengers LCS, HYD, and HH.

1.1.1 Glutathione

Glutathione (GSH) is an endogenous tripeptide composed of γ-glutamate, cysteine, and glycine residues. GSH is the most abundant non-protein thiol found in cells, with intracellular concentrations in the millimolar range, that has important antioxidant activity and a role in xenobiotic metabolism.[125] The conjugation of HNE and GSH accounts for 20%-50% of HNE metabolism in rat hepatocytes treated with 50- 250 µM HNE.[126] The reaction of LPx with GSH occurs spontaneously but the rate of this conjugation reaction is accelerated by glutathione-S-transferases (GSTs).[127-128] There are 22 human isoforms of GSTs and the A4-4 isoform of GST has the highest specific activity for the conjugation of HNE with GSH.[128-129] The treatment of rat hepatoma or PC12 cells with LPx has also been shown to induce the expression of GSTA1-1 and GSTA4-4.[130-131] The crystal structure of GSH-HNE bound to mGSTA4-4 has also been reported.[132]

1.1.2 N-Acetylcysteine

N-acetylcysteine (NAC) is a precursor of L-cysteine required for glutathione synthesis.[133] NAC has been shown to decrease levels of protein carbonylation in the hepatic tissue of acetaminophen treated mice, methamphetamine treated N27 cells, the muscle tissue of a mouse model of Duchenne muscular dystrophy, and spermine treated human aortic smooth muscle cells.[134-137]

1.1.3 L-Carnosine

L-Carnosine (β-alanyl-L-hystidine) is an endogenous dipeptide synthesized by carnosine synthase from β-alanine and histidine.[138] L-Carnosine contains two nucleophilic sites, an imidazole ring and an amino group, both of which are capable of forming conjugates with LPx although the terminal amino group from β-alanine is not reactive at physiological pH. Carnosine

was first demonstrated to have potential scavenging activity by Hipkiss, et al. in 1997 when they reported that carnosine (20 mM) reduced cell death in rat brain endothelial cells treated with MDA (4 mM).[139] The addition of L-carnosine to liposomes was reported to trap 40% of the free MDA produced from the lipid peroxidation induced by $FeSO_4$ and ascorbic acid.[140] The incubation of α-crystallin (1 mg/mL) with MDA (100 mM) for 1-8 hours produced inter-molecular protein cross-linking that was observed when these samples were separated by SDS-PAGE gel electrophoresis and stained by Coomassie blue dye. This crosslinking was decreased when carnosine (200 mM) was added to the incubation of MDA and α-crystallin.[141]

The structure of carnosine-acrolein adducts have been identified by LC-MS/MS, and this analysis reported that a single carnosine molecule is also capable of reacting with one to three acrolein molecules (**Figure 36**).[142] The most abundant carnosine-acrolein adduct identified from human urine samples is produced from the sequential reaction of the amino group from the β-alanine with two acrolein molecules followed by the cyclization and dehydration of the two acrolein molecules to form a β-picolinium ring (**Figure 37**).[143] However, other reports that monitored free acrolein by HPLC showed that after 30 minutes only ~40% of 0.5 mM acrolein was scavenged by 0.5 mM carnosine, classifying carnosine a poor scavenger of acrolein.[124] The incubation of RNase (1 mM) with HNE (7.5 mM) for 72 hours in pH 7.4 phosphate buffer resulted in the intermolecular cross-linking of RNase that was visualized after these samples were separated by SDS-PAGE gel electrophoresis and stained by GelCode Blue Stain. The coincubation of RNase, HNE and carnosine (1-200 mM) was shown to prevent the HNE induced cross-linking of RNase *in vitro* at concentrations greater than 10 mM.[144] However, carnosine is not effective at preventing protein crosslinking caused by ONE when similar experiments were conducted using β-lactoglobulin, ONE (0.5-2 mM), and carnosine (1 mM).[145]

L-Carnosine was evaluated as a scavenger of HNE by Guiotto, et. al., by monitoring the loss of the L-carnosine and other scavengers (28 mM) in the presence of HNE (1.4 mM). The results from these experiments report that 80% of L-carnosine is lost after a two hour incubation with HNE.[146] It has been shown that L-carnosine is nearly five time more effective at trapping HNE than N-acetyl-carnosine in phosphate buffer (pH 7.4) over 24 hours. This indicates that the mechanism of HNE scavenging by carnosine is faster when both nucleophilic sites are available. These results are supported by both NMR and LC-MS/MS analysis that reported the formation of a cyclic conjugate upon the reaction of carnosine with HNE.[147-148]

Figure 36. Chemical structures of carnosine acrolein adducts
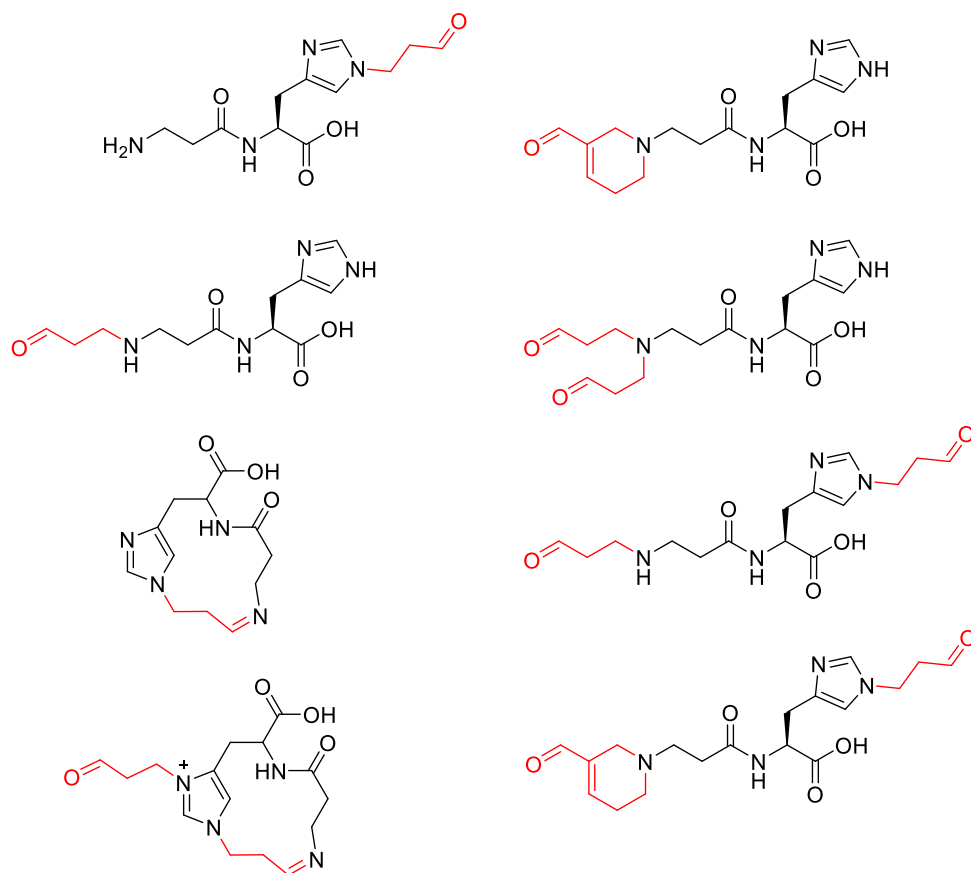
Figure 36. The chemical structures of carnosine-acrolein adducts formed *in vitro* and identified by LC-MS/MS analysis. The atoms colored in red are from one, two, or three acrolein molecules.

Figure 37. Structure and mechanism of carnosine acrolein adduct detected in human urine.
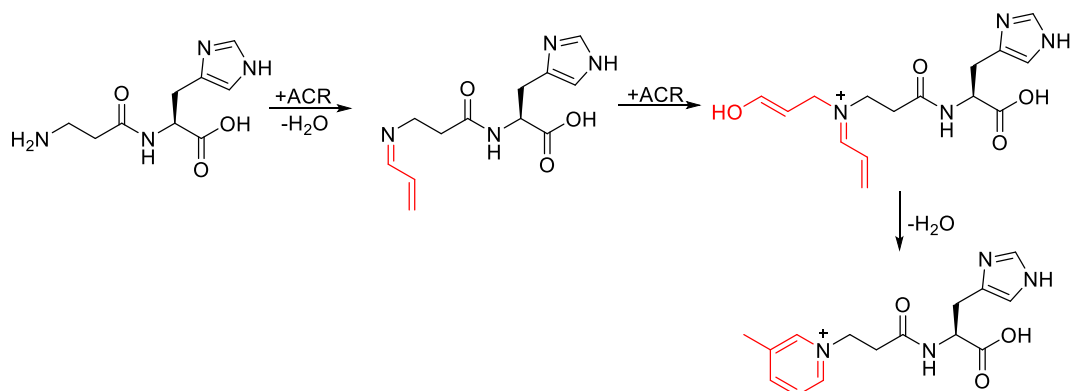
Figure 37. The proposed mechanism for the formation of carnosine-acrolein adduct containing two acrolein molecules resulting in the formation of a β-picolinium ring. These carnosine-acrolein adducts were detected in human urine samples. The atoms colored in red are from two acrolein molecules.

1.1.4 Histidyl-Hydrazide

The exploration of histidyl-hydrazide as a scavenger of HNE was first reported by Guiotto, et al. when evaluating analogs of carnosine.[146] The reactivity of these analogs was measured *in vitro* by incubating HNE (28 mM) with each carnosine analog (1.4 mM) in phosphate buffer (pH=7.4) for 1-24 hours. The amount of free scavenger was then determined by HPLC. This experiment reported that histidyl-hydrazide was the most effective scavenger of HNE with only 10% of histidyl-hydrazide remaining after one hour. In this same report histidyl-hydrazide demonstrated concentration dependent (20-600 µM) protection of SHSY-5Y cells from HNE induced cell death (10 or 20 µM).[146] In a second report Guiotto, et al. evaluated a

second generation group of analogs which were shown to be effective scavengers of MDA.[140]

HH was reported to protect primary neurons from cell death induced by HNE (10 µM) or

glucose deprivation (12 hr). In the same report HH was also evaluated in a mouse model of

ischemic stroke to determine if the ability of histidyl-hydrazide to scavenge LPx produced

neuroprotective activity *in vivo*. This study showed that both the pre-treatment and post-

treatment (1 or 3 hr) of these mice with histidyl-hydrazide (20 mg/kg) reduced the volume of

infarct resulting from ischemic stroke. Histidyl-hydrazide was also suggested to penetrate the

blood-brain barrier, based on one LC-MS trace, without pharmacokinetics.[149]

1.1.5 Hydralazine

Hydrazine protects PC12 cells from cell death induced by acrolein and has been reported

to prevent RNase A crosslinking induced by acrolein, demonstrated by incubating RNase A (2.1

mg/mL) with acrolein (3.2 mM) and hydralazine (0.3-3 mM) prior to separating these sample by

SDS-PAGE gel electrophoresis and staining by Coomassie blue dye.[150-151] Hydralazine was

evaluated in a rat model of spinal cord injury and was shown to decrease the level of acrolein

protein adducts in the spinal cord compared to the untreated animals. The treatment of these

animals with hydrazide immediately following the delivery of the spinal cord injury resulted in

significant protection from tissue damage caused by this injury, which was evaluated by

measuring acrolein protein adducts using immunoblotting and an anti-acrolein antibody.[152-154]

Similar results were observed in animal models of diabetic neuropathy, neuroinflammation, and

hepatotoxicity.[154-156] Hydralazine was reported to prevent the formation of amyloid β (Aβ) fibrils

caused by the incubation of Aβ with HNE *in vitro* and measured by western blot using anti-Aβ

and anti-HNE antibodies.[157]

A small library of hydrazine derivatives were evaluated as LPx scavengers and for antiatherogenic activity. In this small library all the derivatives, with the exception of isoniazid and pargyline, were shown to decrease the production of thiobarbituric acid reactive substances (TBARS), and protected HMEC-1 cells from the cell death induced by oxidized LDL. Compounds from this library also prevented the formation of atherosclerosis lesions in apoE-/- mice, and as shown by Western Blot analysis (anti-HNE and anti-acrolein antibodies), to prevent the formation of HNE protein adducts and acrolein protein adducts.[158]

2. Results

2.1 Chemical Reactivity of LPx Scavengers

The reactivity of hydralazine, histidyl-hydrazide, L-carnosine, N-acetylcysteine, and glutathione with equimolar 4-hydroxynonenal and 4-oxononenal was monitored using UV-HPLC analysis. HNE or ONE (500 µM) were incubated at room temperature with each scavenger (500 µM) in 0.1 M phosphate buffer (pH=7.4) for 0-6 hours. The reaction of HNE or ONE with each scavenger was monitored by measuring the area under the curve corresponding to free HNE or ONE. These measurements were taken every 1.25 hours in order to determine the amount of free LPx remaining in the presence of each scavenger. Control samples, without any scavenger, were also monitored over time and showed that there was no significant change in the level of free HNE or ONE in the control samples.

The most effective scavengers of HNE were the thiol containing scavengers: GSH and NAC. The level of free HNE reached a steady state of 100 µM and 125 µM of the free HNE remaining after 2.5 hours in the presence of GSH or NAC respectively. Of the aldehyde reactive scavengers, HYD was the most efficient aldehyde reactive scavenger of HNE with 250 µM of

the HNE remaining after two hours, and decreasing to 125 µM after six hours. At neutral pH more than 350 µM of HNE remained after incubation with HH and LCS (**Figure 38**).

These scavengers all showed greater reactivity with ONE than HNE. The incubation of ONE with GSH, NAC, and HYD resulted in nearly complete loss of free ONE within a few minutes of initiating the reaction. After 2.5 hours of incubation with HH, 200 µM ONE remained, decreasing to 100 µM after six hours. In the presence of L-carnosine the concentration of ONE decreased linearly, with 220 µM of ONE remaining after six hours (**Figure 39**).

Figure 38. Reactivity of HNE with aldehyde reactive and thiol containing scavengers.
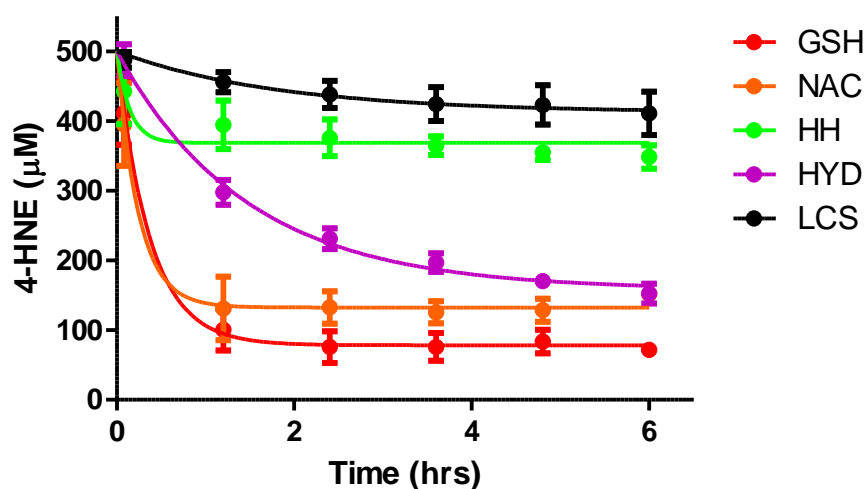
Figure 38. The concentration of free HNE was monitored by UV-HPLC. 500 µM HNE was incubated in 0.1 M phosphate buffer (pH=7.4) with 500 µM of each scavenger: glutathione (GSH), N-acetylcysteine (NAC), histidyl-hydrazide (HH), hydralazine (HYD), and L-carnosine (LCS). These reactions were incubated at room temperature and monitored at six time points from 0-6 hours. Each data point represents the mean ± SEM of triplicate experiments.

Figure 39. Reactivity of ONE with aldehyde reactive and thiol containing scavengers.
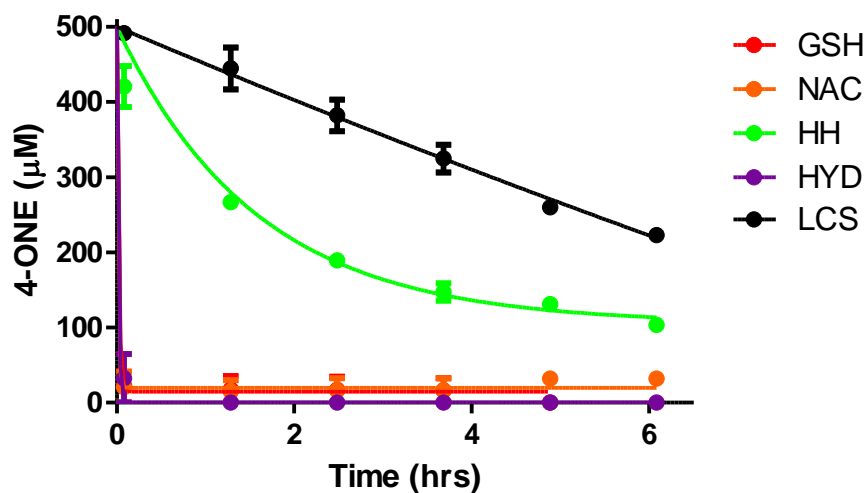
Figure 39. The concentration of free ONE was monitored by UV-HPLC. 500 µM HNE was incubated in 0.1 M phosphate buffer (pH=7.4) with 500 µM of each scavenger: glutathione (GSH), N-acetylcysteine (NAC), histidyl-hydrazide (HH), hydralazine (HYD), and L-carnosine (LCS). These reactions were incubated at room temperature and monitored at six time points from 0-6 hours. Each data point represents the mean ± SEM of duplicate experiments.

The effect of increasing concentrations of HH and acidic pH on the reaction of HH with HNE and ONE was evaluated in order to better understand the reactivity of HNE and ONE with HH. The reaction of 500 µM HNE or ONE was monitored in the presence of 0.5-5 mM HH. After 2.5 hours, and at the lowest concentration of HH, 375 µM of free HNE remained in the sample. With increasing concentrations of HH the level of free HNE decreased to 280 µM, 160 µM, and 30 µM at the same time point in the samples with 1, 2, and 5 mM HH (**Figure 40**). The increased reactivity of ONE with HH resulted in the rapid scavenging of ONE at higher concentrations of HH with the amount of free ONE decreasing to less than 100 µM in the presence of 1 mM HH after 2.5 hours and nearly complete scavenging of ONE after the same period time when the concentration of HH was increased to 2 and 5 mM (**Figure 41**).

Figure 40. Concentration dependent reactivity of HNE with histidyl-hydrazide
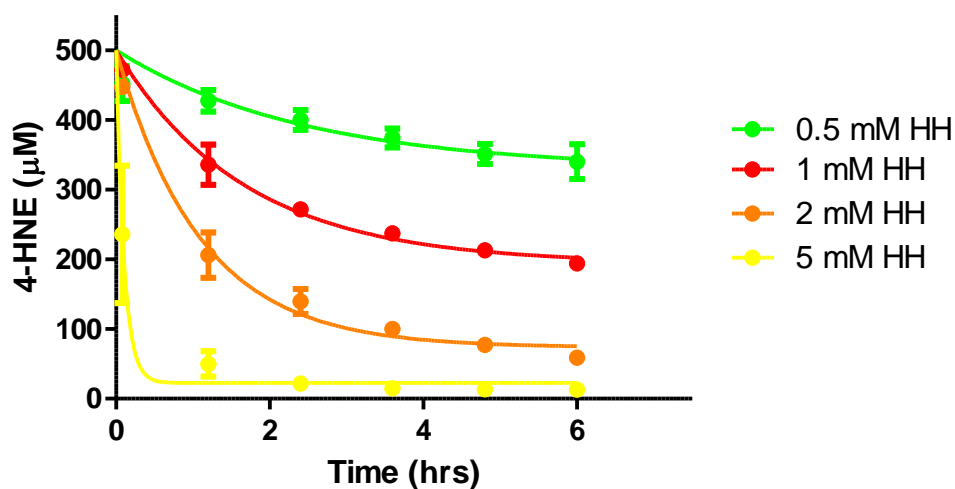
Figure 40. The concentration of free HNE was monitored by UV-HPLC. 500 µM HNE was incubated in 0.1 M phosphate buffer (pH=7.4) with 0.5, 1, 2, 5 mM of histidyl-hydrazide (HH). These reactions were incubated at room temperature and monitored at six time points from 0-6 hours. Each data point represents the mean ± SEM of duplicate experiments.

Figure 41. Concentration dependent reactivity of ONE with histidyl-hydrazide
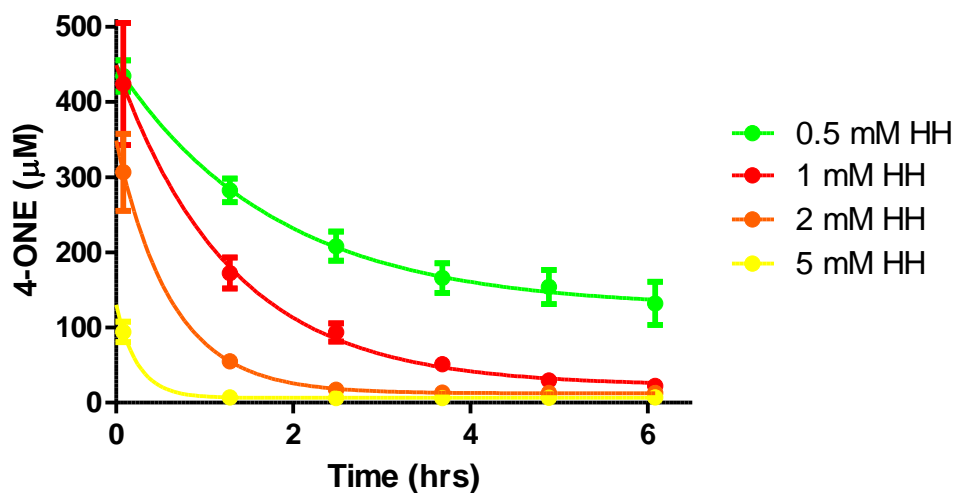
Figure 41. The concentration of free ONE was monitored by UV-HPLC. 500 µM HNE was incubated in 0.1 M phosphate buffer (pH=7.4) with 0.5, 1, 2, 5 mM of histidyl-hydrazide (HH). These reactions were incubated at room temperature and monitored at six time points from 0-6 hours. Each data point represents the mean ± SEM of duplicate experiments.

'

Decreasing the pH of the phosphate buffer from pH=7.4 to pH=5.5 resulted in an increased rate of reactivity with HNE at higher concentrations of HH (**Figure 42**). When 500 µM HNE was incubated with equimolar HH no significant change in the scavenging of HNE by HH was observed with a change in the pH. A five-fold increase in the concentration of HH to 2.5 mM resulted in a significant increase in the rate of the reaction of HH with HNE in the pH 5.5 phosphate buffer compared to when the reaction conducted at neutral pH.

Figure 42. Reactivity of HNE with histidyl-hydrazide at pH 7.4 and pH 5.5
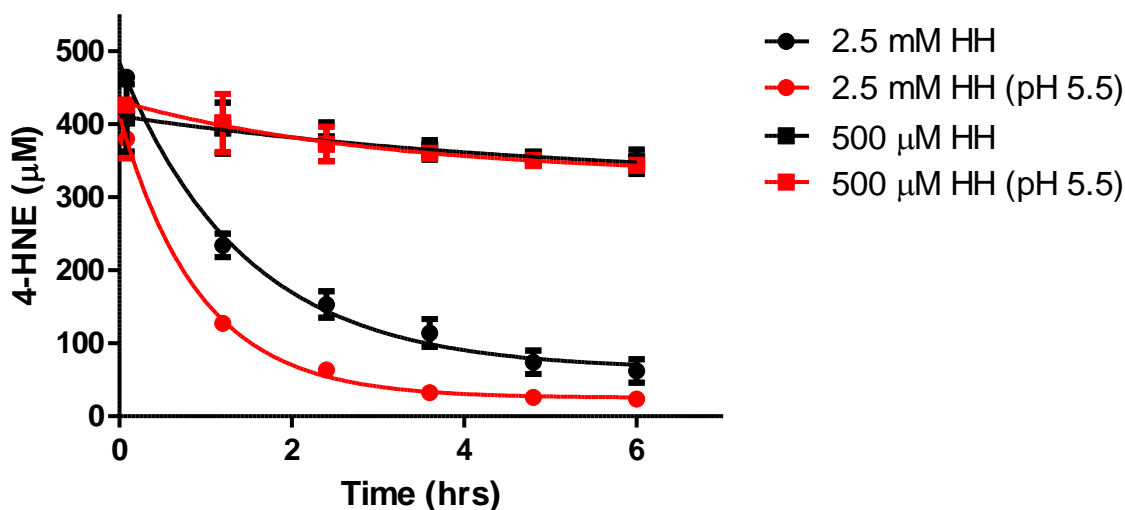
Figure 42. The concentration of free HNE was monitored by UV-HPLC. 500 µM HNE was incubated in 0.1 M phosphate buffer (pH=7.4 or pH=5.5) with 500 µM or 2.5 mM of histidyl-hydrazide (HH). These reactions were incubated at room temperature and monitored at six time points from 0-6 hours. Each data point represents the mean ± SEM of duplicate experiments.

2.2 Neuroprotection

The treatment of SHSY-5Y cells with 10 µM HNE resulted in 50% cell death after 24 hours. When these cells were co-treated with 10 µM HNE and 50-500 µM LCS, HYD, HH, and NAC all of the scavengers were shown to be protective. NAC prevented any HNE induced cell death at 50 µM but showed slight cell toxicity at the highest concentrations. The co-treatment of SHSY-5Y with HYD resulted in only ~25% cell death at all the concentrations tested. Finally, both LCS and HH showed dose dependent neuroprotective activity with HH being the more neuroprotective scavenger of HNE at the highest concentration tested in this cell line.

Figure 43. Cell viability of SHSY-5Y cells treated with HNE and LPx scavengers.
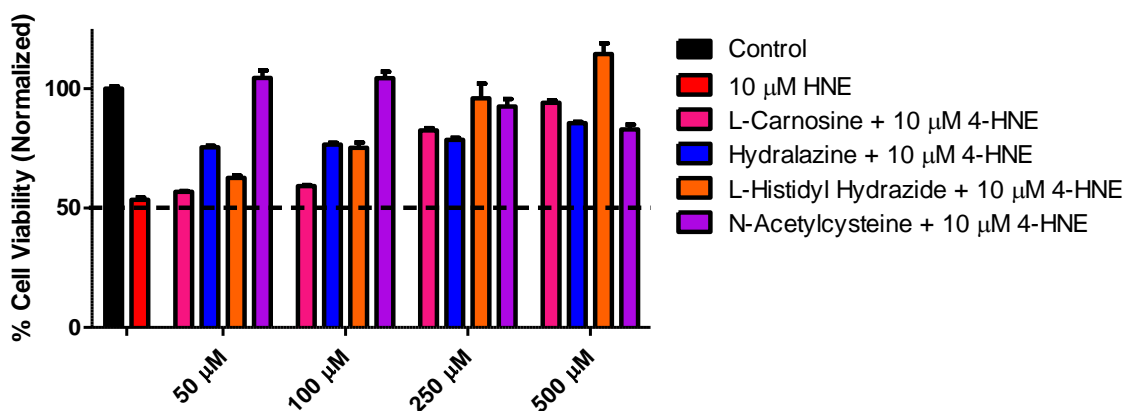
Figure 43. SHSY-5Y cells were treated with EtOH, 10 µM HNE, or cotreated with 10 µM HNE and 50-500 µM of L-carnosine, hydralazine, histidyl-hydrazide, or N-acetylcysteine for 24 hours prior to measuring cell viability by MTT.

SHSY-5Y cells were also treated with 5 µM ONE resulting in 50% cell death after 24 hours. Only the cotreatment of these cells with 50-500 µM NAC and 500 µM HH were observed to completely protect SHSY-5Y cells from the cell toxicity induced by 5 µM ONE. Similar to the results reported with the treatment of HNE, NAC was the most neuroprotective scavenger, preventing any significant cell death at 50 µM. The co-treatment of SHSY-5Y cells with 50-500 µM HH showed concentration dependent neuroprotective activity. However, the cotreatment of these cells with both LCS and HYD resulted in only low levels of neuroprotective activity at all tested concentrations with the treatment with 5 µM ONE.

2.3 Prevention of LPx protein adducts by GSH and NAC

The thiol containing scavengers GSH or NAC (25-250 µM) were pre-incubated with aHNE (25 µM) for one hour at 37°C prior to adding this mixture to SHSY cell lysates (0.5 µg/µL). After a second one hour incubation was completed the sample preparation for the dual color nearIR imaging technique was then used in order to measure the ability of these scavengers to prevent the formation of aHNE-protein adducts. **Figures 44** and **45** show that the addition of increasing concentrations of GSH and NAC resulted in the concentration dependent decrease in the formation of aHNE protein adducts in the SHSY cell lysates. An equal decrease in both the red and green dye signals indicates that both of these thiol containing scavengers prevent the formation of Michael addition aHNE-protein adducts. The level of aHNE protein adducts in SHSY-5Y cell lysates was quantified by selecting two protein bands (40 and 55 kDa) in the 250 µM NAC or GSH samples and the signals for both dyes were normalized to the intensities of each signal from the same bands of the aHNE treated sample alone. The treatment of cell lysates with 250 µM GSH or NAC resulted in ~50% or ~40% decrease in the signals from both dyes, respectively.

GST-P1 was used as a model system in order to further investigate and quantify the ability of the thiol-containing scavengers to inhibit the formation of aHNE protein adducts. However, only NAC could be evaluated in this model system, because GSH is a substrate for GST-P1 which complicated the interpretation of the results of these experiments. The pre-incubation of NAC (25-250 µM) with aHNE (25 µM) prior to the addition of GST-P1 resulted in a dose dependent decrease in the signals from both the azide and hydrazide dyes in the presence of 50-250 µM NAC and a ~50% decrease in the signal from both dyes was observed at the highest concentration of NAC (**Figure 46**).

Figure 44. Co-treatment of SHSY-5Y cells with aHNE and GSH.
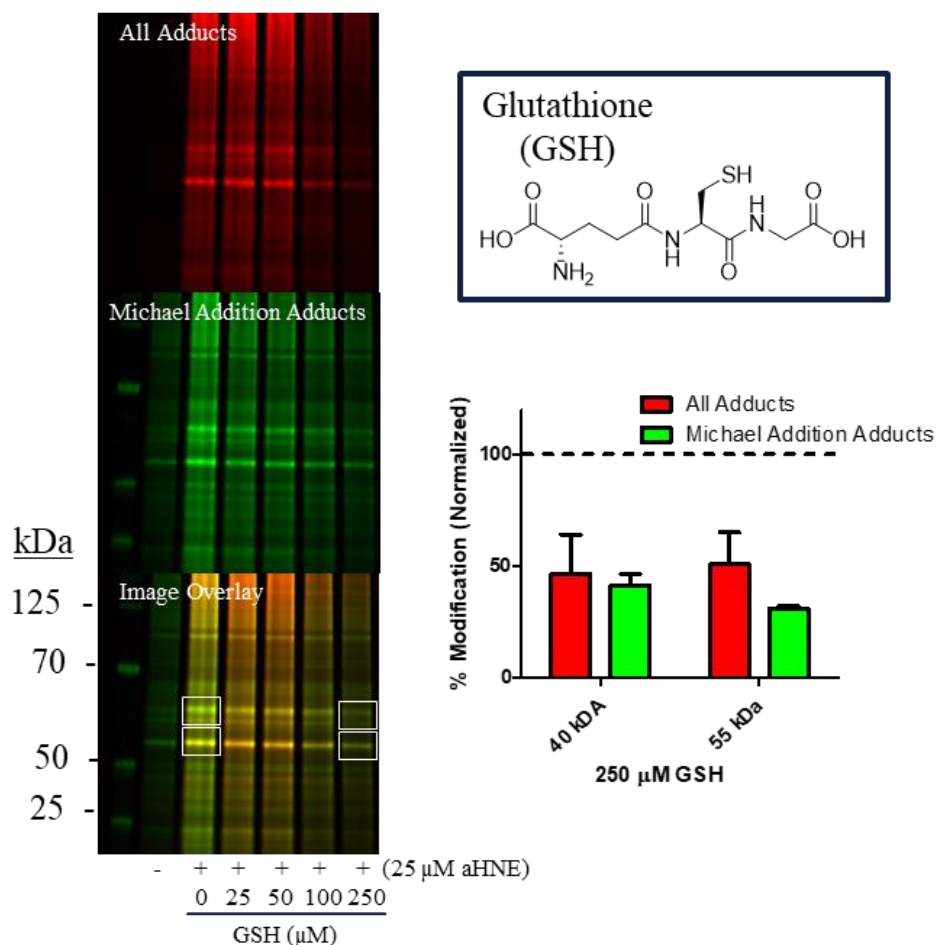
Figure 44. Left: SHSY-5Y lysates (0.5 µg/µL) were treated with EtOH, 25 µM aHNE, or cotreated with 25 µM aHNE and 25-250 µM GSH. Each lane of the gel contains 30 µg of protein. The white rectangles in the image overlay indicate the two regions of the gel that were quantified in order to measure the aHNE-protein adducts. Right: The signals from the azide dye (red) and hydrazide dye (green) in the aHNE only and aHNE plus 250 µM GSH samples were quantified at the 40 and 55 kDa gel regions, and the data were normalized to the aHNE only treated samples. Each image is representative of two independent experiments and the data represents the mean ± SEM of these experiments.

Figure 45. Co-treatment of SHSY-5Y cells with aHNE and NAC.
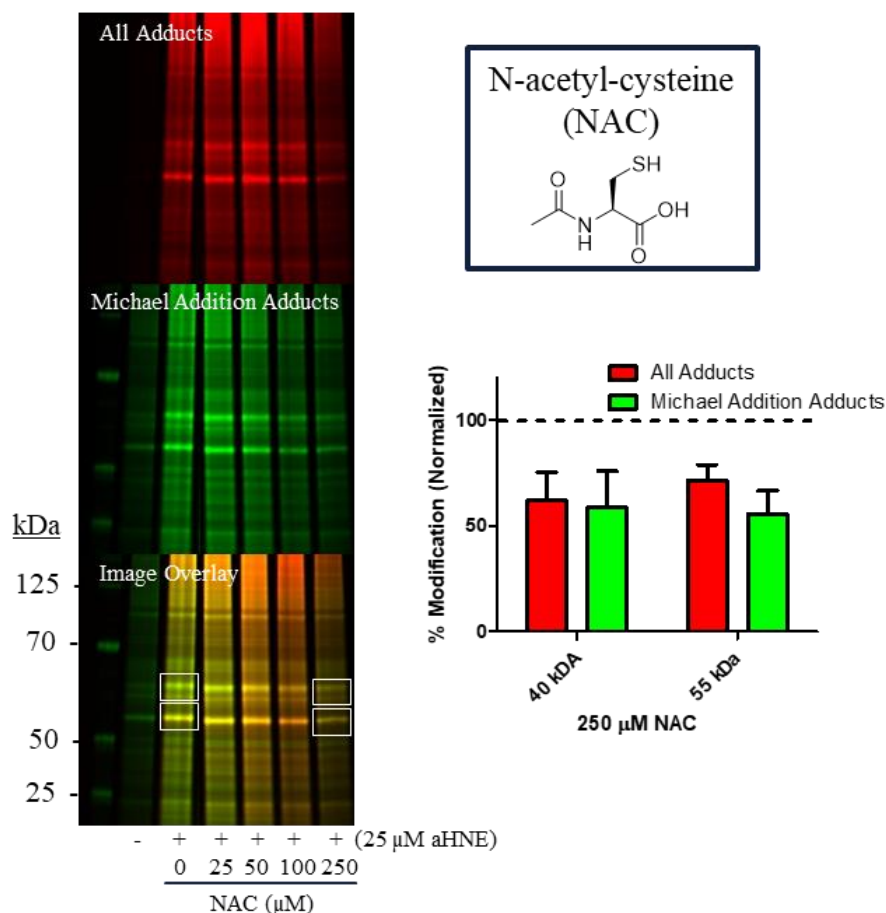
Figure 45. Left: SHSY-5Y lysates (0.5 µg/µL) were treated with EtOH, 25 µM aHNE, or

cotreated with 25 µM aHNE and 25-250 µM NAC. Each lane of the gel contains 30 µg of

protein. The white rectangles in the image overlay indicate the two regions of the gel that were

quantified in order to measure the aHNE-protein adducts. Right: The signals from the azide dye

(red) and hydrazide dye (green) in the aHNE only and aHNE plus 250 µM NAC samples were

quantified at the 40 and 55 kDa gel regions, and the data were normalized to the aHNE only

treated samples. Each image is representative of two independent experiments and the data

represents the mean ± SEM of these experiments.

Figure 46. NAC prevents formation of aHNE GST-P1 WT protein adducts.
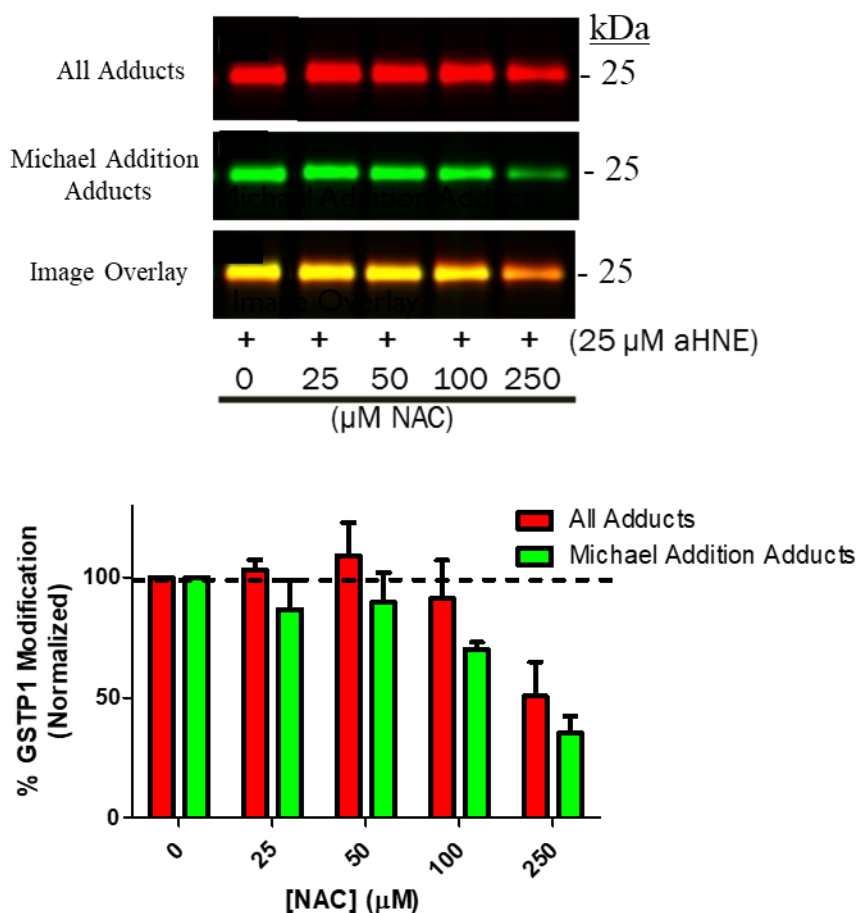
Figure 46. Top: GST-P1 WT (0.1 µg/µL) was treated with EtOH, 25 µM aHNE, or cotreated

with 25 µM aHNE and 25-250 µM NAC. Each lane of the gel contains 1.5 µg of protein.

Bottom: The signals from the azide dye (red) and hydrazide dye (green) were then quantified.

These results show that there is a dose dependent decrease in the signals from both dyes with an

increasing concentration of NAC. Each image is representative of three independent experiments

and the data represents the mean ± SEM of these experiments.

In order to address if these thiol containing scavengers prevent protein crosslinking, aONE (25 µM) was pre-incubated with NAC (25-250 µM) for one hour prior to the addition of GST-P1. These samples were then incubated for one hour prior to the addition of the cyanine5.5-azide dye and other click reaction components. These samples were then separated by SDS-PAGE gel electrophoresis and imaged using the LICOR Sa imager. The results from this experiment show that the preincubation of NAC with ONE causes a concentration dependent increase of the signal from azide dye at the 25 kDa molecular weight region of the gel, the molecular weight of the GST-P1 monomer. There is also a significant decrease in the signal from the azide dye at the 50 kDa region of the gel with increasing concentrations of NAC (**Figure 47**). This indicates that this thiol-containing scavenger prevents the formation of aONE intermolecular cross-linked GST-P1 adducts.

Figure 47. Prevention of aONE inducted GST-P1 crosslinking by NAC

Figure 47. Top: GST-P1 WT (0.1 µg/µL) was treated with EtOH, 25 µM aONE, or cotreated

with 25 µM aONE and 25-250 µM NAC. Each lane of the gel contains 1.5 µg of protein.

Bottom: The signals from the azide dye (red) at the 25 and 50 kDa region of the gel were then

quantified. These results show that there is a dose dependent increase in the 700 nm signal at the

monomer (25 kDa) region of the gel and a decrease at the dimer (50 kDa) region of the gel with

an increasing concentration of NAC. Each image is representative of three independent

experiments and the data represents the mean ± SEM of these experiments.

2.4 Aldehyde Reactive Scavengers Prevent LPx Induced Protein Cross-linking

The aldehyde reactive scavengers HH and HYD (25-250 µM) were pre-incubated with aHNE (25 µM) prior to adding this mixture to SHSY cell lysates (0.5 µg/µL) and completing the sample preparation for our in-gel imaging method. The final images show that with an increasing concentration of these scavengers there was a significant increase in the incorporation of the azide dye (red) without any significant increase in the signal from the hydrazide dye (green). This indicates that these scavengers actually result in the increased formation of aHNE protein adducts in SHSY-5Y cell lysates. However there is no observable increase in the green (800 nm) signal from the hydrazide dye because the aldehyde of aHNE has formed a Schiff base with the aldehyde reactive scavengers preventing any reaction with the hydrazide dye (**Figures 48** and **50**).

The GST-P1 model system was then used in order to validate and more accurately quantify this observed increase of aHNE protein adducts in SHSY-5Y cells. Using this model system the preincubation of aHNE with HH and HYD resulted in an increase in the signal of the 700 nm channel (red) without any change or a decrease in the signal from the 800 nm signal (green) for both HYD and HH. At 250 µM HYD there is a 40% increase in the 700 nm signal and a >50% decrease in the 800 nm channel. Although HYD was the most effective scavenger of HNE in the HPLC experiments, the lack of significant signal increase in the 700 nm channel from 250 µM HYD compared to 100 µM HYD may be attributed to the limited solubility of HYD-HNE conjugates that was also observed during the HPLC reactivity experiments (**Figure 51**). For HH there is a dose dependent increase in the signal from the azide dye with a 75% increase in this signal at the highest concentration of histidyl-hydrazide. However there is no significant change in the 800 nm channel with the increased concentration of HH (**Figure 49**).

This observed increase in signal from the azide dye in the sample treated with higher concentrations of HYD and HH is due to the increase in the signal from the monomer band. We hypothesize that this increase in the signal from the treatment with the aldehyde-reactive dyes occurs due to the prevention of protein cross-linking induced by the treatment of aHNE resulting in an increase in the amount of Michael addition monomer adducts.

Figure 48. Co-treatment of SHSY-5Y cells with aHNE and HH.
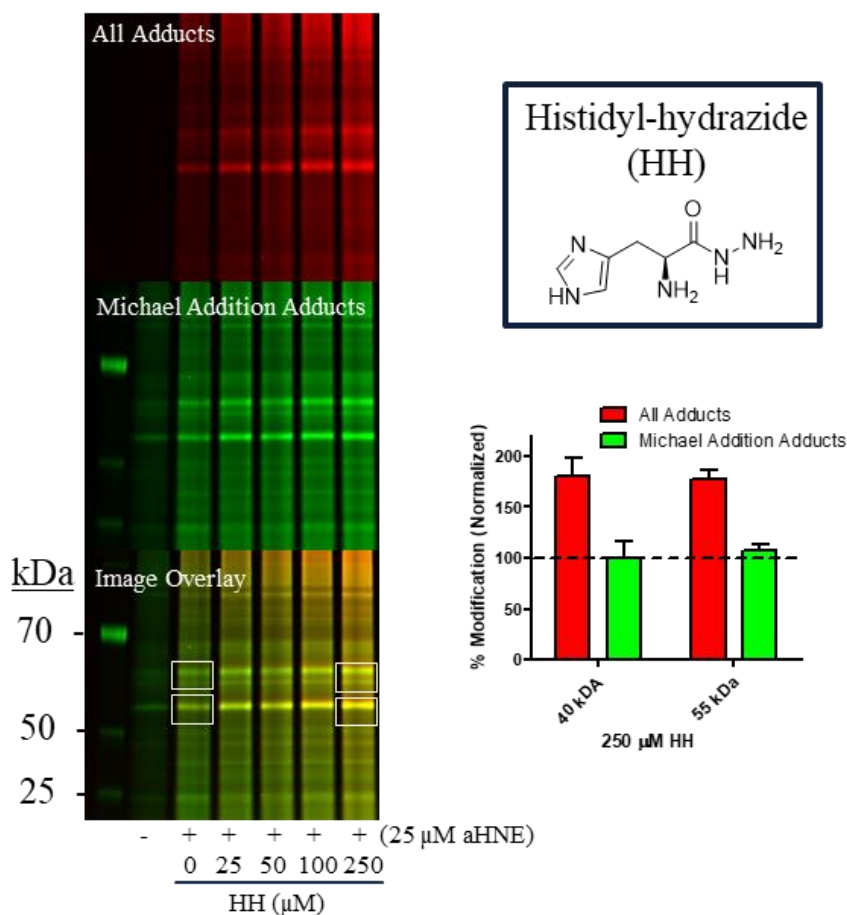
Figure 48. Left: SHSY-5Y lysates (0.5 µg/µL) was treated with EtOH, 25 µM aHNE, or cotreated with 25 µM aHNE and 25-250 µM HH. Each lane of the gel contains 30 µg of protein. The white rectangles in the image overlay indicate the two regions of the gel that were quantified in order to measure the aHNE-protein adducts. Right: The signals from the azide dye (red) and hydrazide dye (green) in the aHNE only and aHNE plus 250 µM HH samples were quantified at the 40 and 55 kDa gel regions and the data was normalized to the aHNE only treated samples. Each image is representative of two independent experiments and the data represents the mean ± SEM of these experiments.

Figure 49. HH increases the formation of aHNE GST-P1 WT protein adducts.
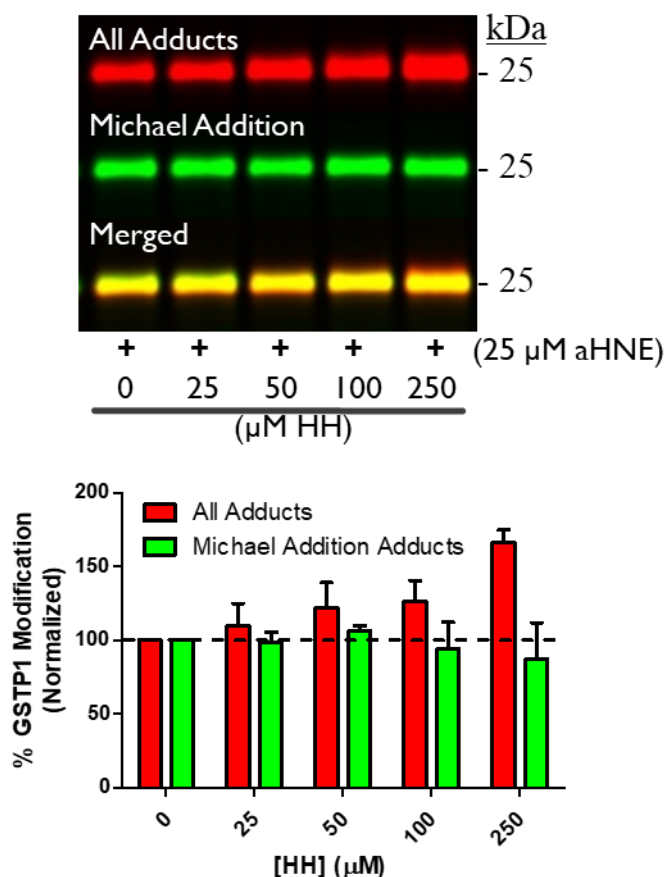
Figure 49. Top: GST-P1 WT (0.1 µg/µL) was treated with EtOH, 25 µM aHNE, or cotreated with 25 µM aHNE and 25-250 µM HH. Each lane of the gel contains 1.5 µg of protein. Bottom: The signals from the azide dye (red) and hydrazide dye (green) were then quantified. These results show that there is a dose dependent increase in the signals from the hydrazide dye, but no significant increase in the signal from the hydrazide dye with the increasing concentration of HH. Each image is representative of four independent experiments and the data represents the mean ± SEM of these experiments.

Figure 50. Co-treatment of SHSY-5Y cells with aHNE and HYD.
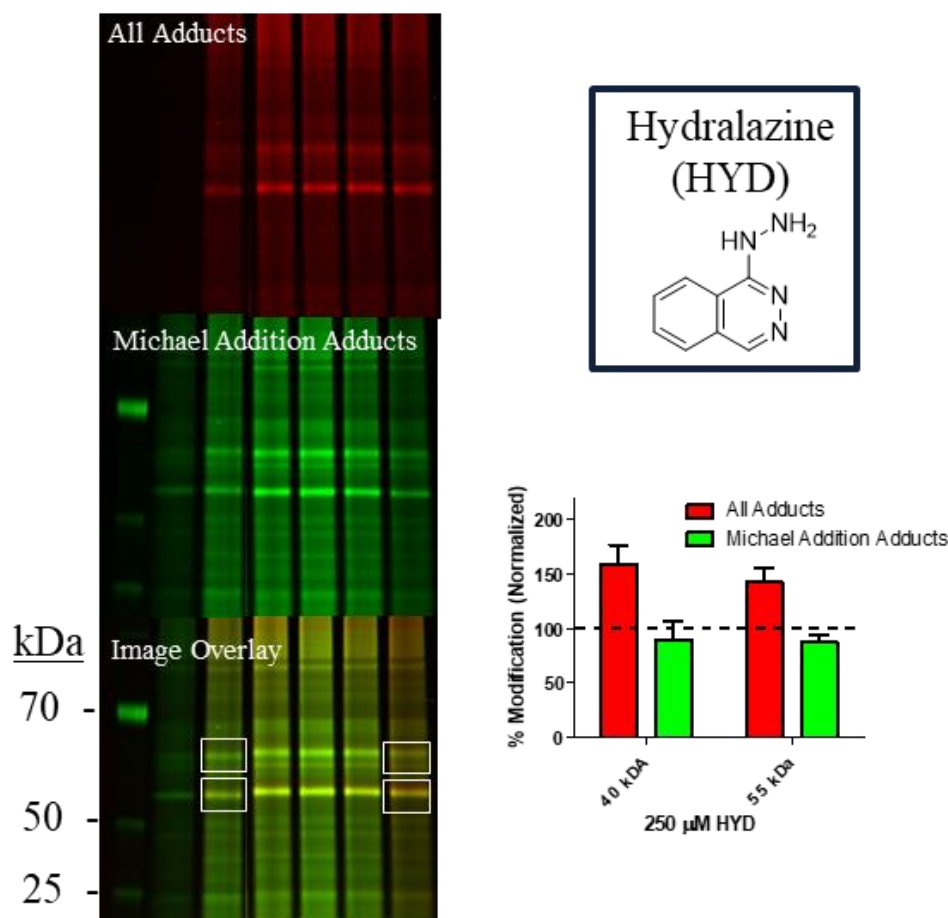
Figure 50. Left: SHSY-5Y lysates (0.5 µg/µL) was treated with EtOH, 25 µM aHNE, or

cotreated with 25 µM aHNE and 25-250 µM HYD. Each lane of the gel contains 30 µg of

protein. The white rectangles in the image overlay indicate the two regions of the gel that were

quantified in order to measure the aHNE-protein adducts. Right: The signals from the azide dye

(red) and hydrazide dye (green) in the aHNE only and aHNE plus 250 µM HYD samples were

quantified at the 40 and 55 kDa gel regions and the data was normalized to the aHNE only

treated samples. Each image is representative of two independent experiments and the data

represents the mean ± SEM of these experiments.

Figure 51. HYD increases the formation of aHNE GST-P1 WT protein adducts.
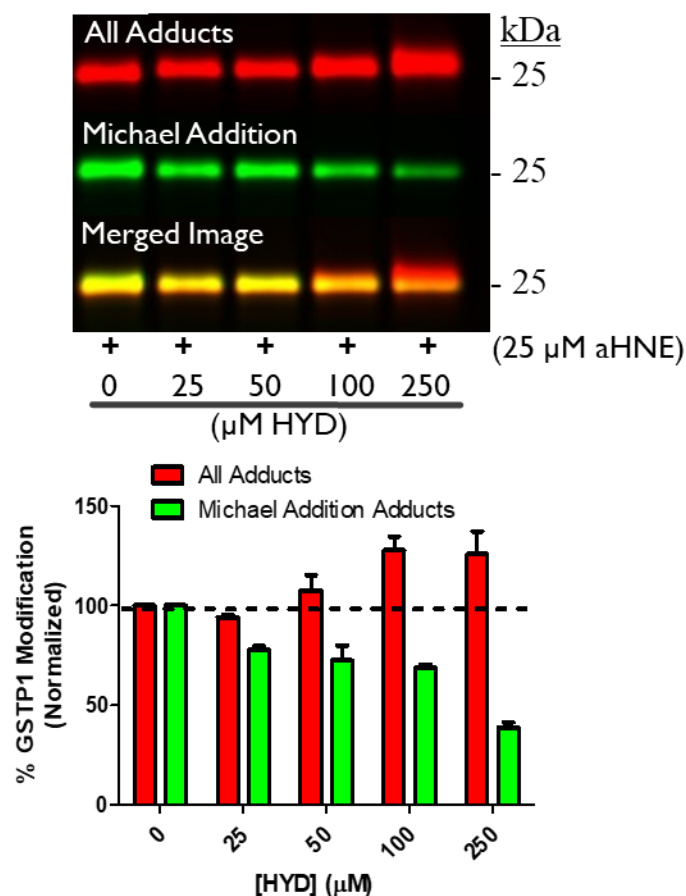
Figure 51. Top: GST-P1 WT (0.1 µg/µL) was treated with EtOH, 25 µM aHNE, or cotreated with 25 µM aHNE and 25-250 µM HYD. Each lane of the gel contains 1.5 µg of protein. Bottom: The signals from the azide dye (red) and hydrazide dye (green) were then quantified. These results show that there is a dose dependent increase in the signals from the hydrazide dye, but a significant decrease in the signal from the hydrazide dye with the increasing concentration of HYD. Each image is representative of four independent experiments and the data represents the mean ± SEM of these experiments.

In order to validate this prevention of protein cross-linking by the aldehyde reactive scavengers we also investigated if these aldehyde reactive scavengers prevent the formation of cross-linked LPx adducts induced by the treatment of GST-P1 with aONE. GST-P1 was incubated with 25 µM aONE in the presence or absence of the aldehyde-reactive scavengers. When HYD (25-250 µM) was pre-incubated with aONE for one hours the cross-linking caused by 25 µM aONE was inhibited by 50 uM HYD. This can be seen in the quantitation of the 25 kDa region of the gel which contains the GST-P1-aONE adducts that have incorporated a hydralazine molecule at the aldehyde position of aONE and therefore preventing the formation of protein crosslinked adducts. The protein adducts quantified at the 50 kDa region on the other hand consist primarily of aONE adducts where the aldehyde group is involved to the formation of a protein cross-linked adduct (**Figure 52**). Therefore the efficient scavenge of aONE by HYD, as observed in the HPLC data reported above, prevent GST-P1 cross-linking induced by aONE and results in a significant increase in the signal from the azide dye at the monomer region (25 kDa) of the gel and nearly a complete loss of the azide dye signal at the dimer (50 kDa) region of the gel.

The conditions for the preincubation of HH with aONE were adjusted slightly due to the lower reactivity of HH with aONE seen in the HPLC reactivity data reported in **Figure 41**. The same conditions as the concentration dependent HPLC reactivity analysis were used; therefore HH (0.5-5 mM) was incubated with aONE (0.5 mM) for two hours at room temperature in 0.1 M phosphate buffer (pH=7.4). These samples were then diluted to a final concentration of 25-250 µM HH and 25 µM aONE and incubationed with GST-P1 (0.1 µg/µL) at 37°C for one hour. The gel images from this experiment show that HH prevents GST-P1 crosslinking at 100 µM HH (**Figure 53**). This can be seen by the increase in the signal at the monomer region (25 kDa) of the

gel, however there is also an increase in the dye signal from the dimer region (50 kDa) which can be attributed to HH preventing of the formation of high molecular weight GST-P1 oligomers. The same experimental conditions were used to detect aONE induced cross-linking in SHSY-5Y cell lysates. The results from this experiment shows that the treatment of SHSY-5Y (0.5 µg/µL) with 25 µM aONE caused a high level of protein cross-linking whith explains the lack of clearly resolved proteins adducts into distinct bands by SDS-PAGE gel electrophoresis. The pre-incubation of aONE with increasing concentrations of HH (25-250 µM) resulted in the reappearance of distinctive bands in the 38-70 kDa region of the gel indicating that HH prevents aONE induced cross-linking in SHSY-5Y cell lysates (**Figure 55**).

Figure 52. HYD prevents aONE induced GST-P1 cross-linking
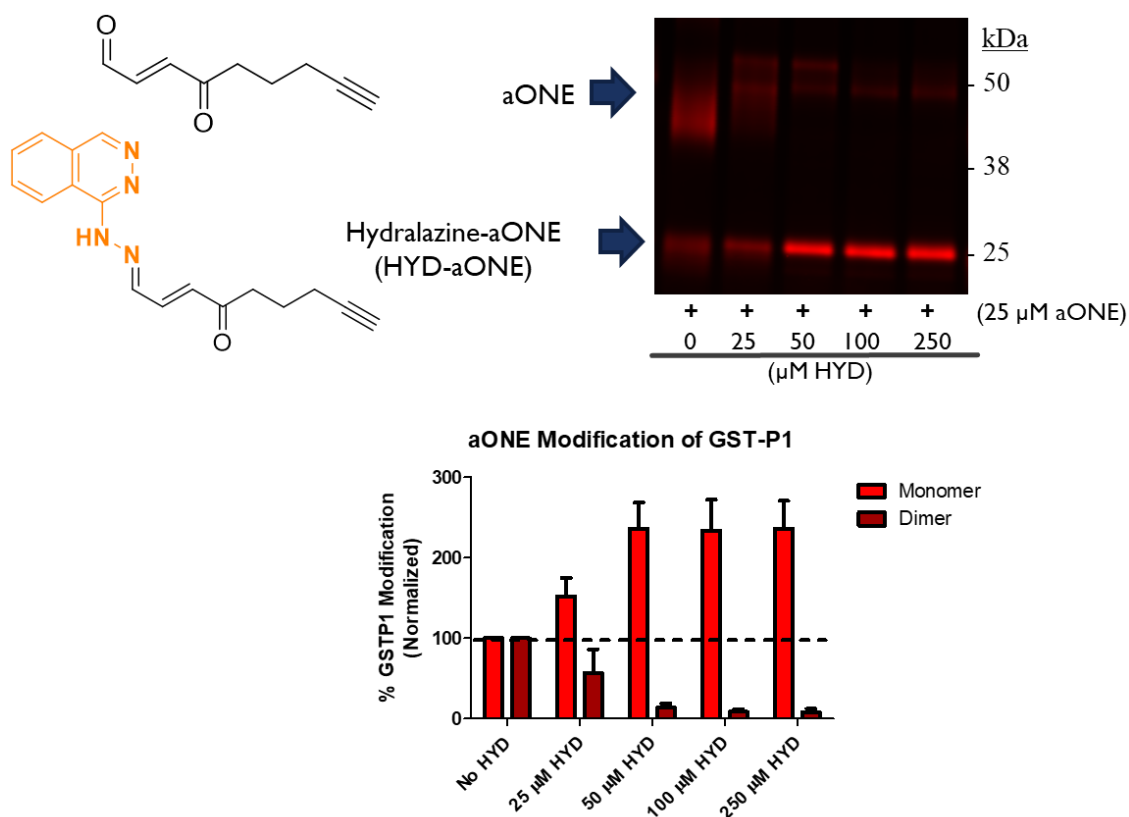
Figure 52. Top: GST-P1 WT (0.1 µg/µL) was treated with EtOH, 25 µM aONE, or cotreated with 25 µM aONE and 25-250 µM HYD. Each lane of the gel contains 1.5 µg of protein. Bottom: The signals from the azide dye (red) at the 25 and 50 kDa region of the gel was then quantified. These results show that there is a dose dependent increase in the 700 nm signal at the monomer (25 kDa) region of the gel and a decrease at the dimer (50 kDa) region of the gel with the increasing concentration of HYD. Each image is representative of four independent experiments and the data represents the mean ± SEM of these experiments.

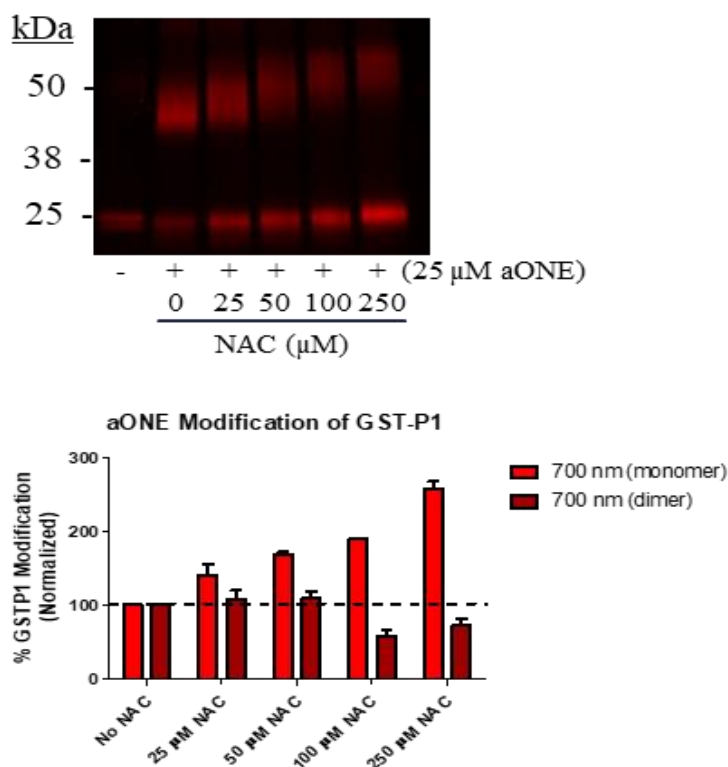**Figure 53**. HH prevents aONE induced GST-P1 cross-linking
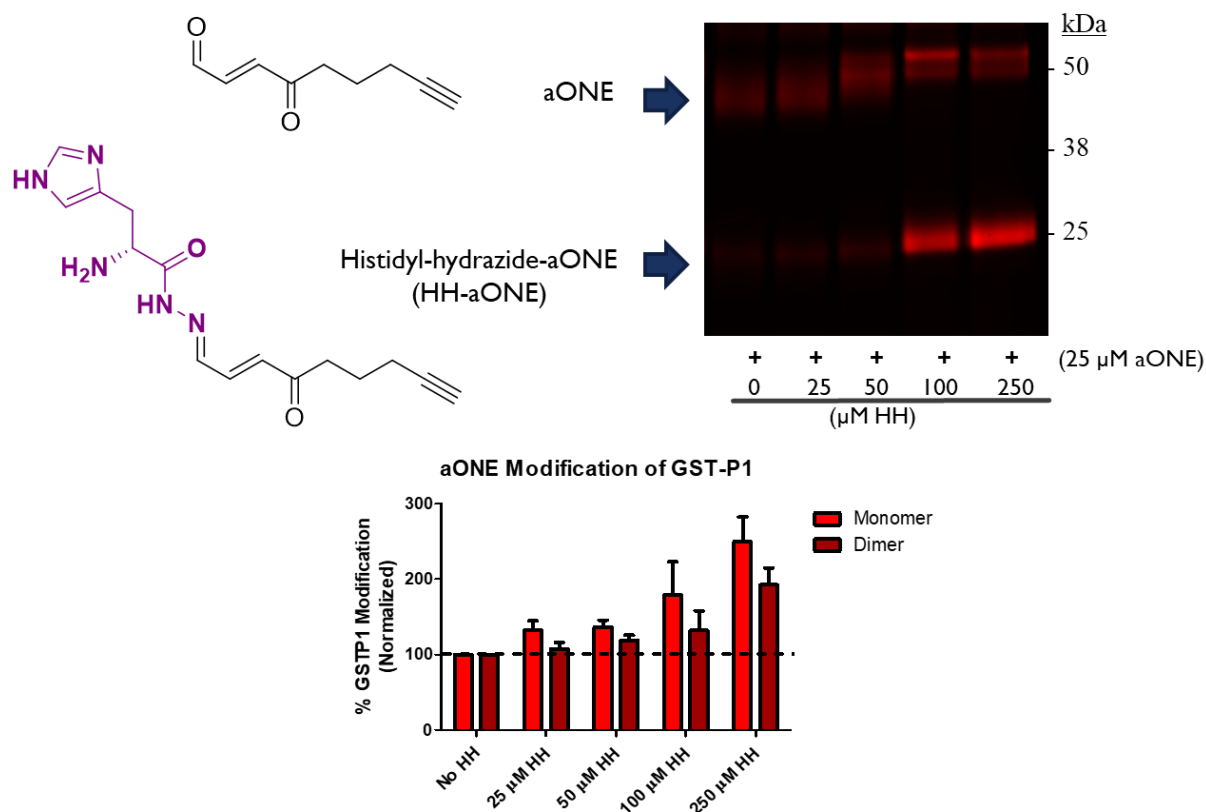
Figure 53. Top: GST-P1 WT (0.1 µg/µL) was treated with EtOH, 25 µM aONE, or cotreated with 25 µM aONE and 25-250 µM HH. Each lane of the gel contains 1.5 µg of protein. Bottom: The signals from the azide dye (red) at the 25 and 50 kDa region of the gel was then quantified. These results show that there is a dose dependent increase in the 700 nm signal at the monomer (25 kDa) region of the gel and an increase at the dimer (50 kDa) region of the gel with the increasing concentration of HH. Each image is representative of four independent experiments and the data represents the mean ± SEM of these experiments.

Figure 54. HH prevents aONE induced cross-linking in SHSY-5Y cells lysates.
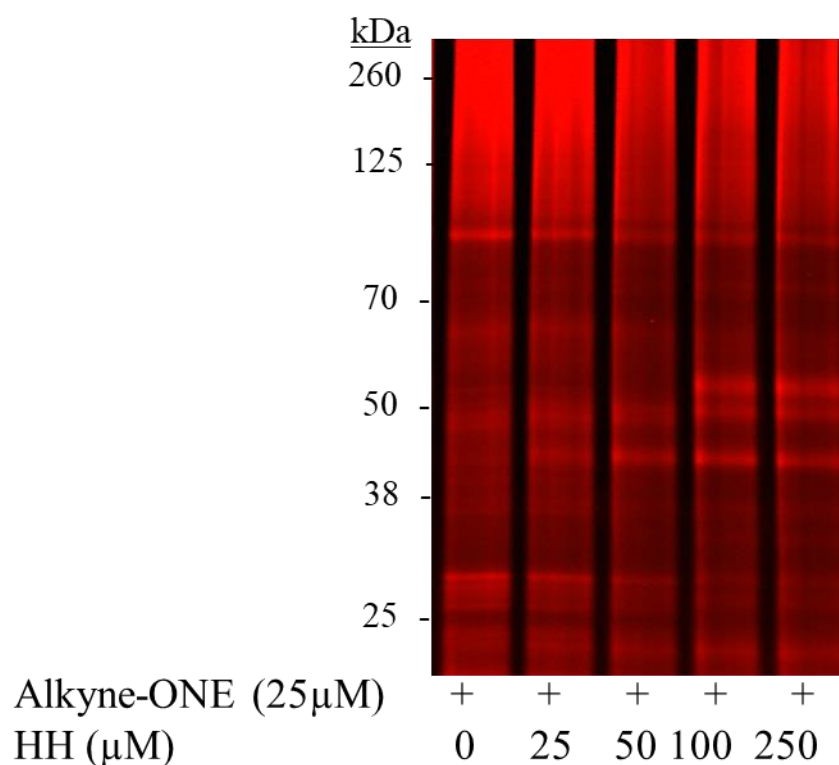
Figure 54. SHSY-5Y cell lysates (0.5 µg/µL) was treated with EtOH, 25 µM aONE, or co-treated with 25 µM aONE and 25-250 µM HH. Each lane of the gel contains 3.75 µg of protein. All distinct bands are lost in the sample treated with 25 µM aONE indicating a high level of protein crosslinking. The addition of increasing concentrations of HH causes the reappearance of distinct bands due to a blocking of aONE induced cross-linking.

2.5 Alkyne-histidyl-hydrazide Validates HH Prevention of Protein Cross-linking

In order to validate that HH is incorporated into the LPx protein adducts and accounts for both the increase in aHNE protein adducts and the prevention of aONE induced crosslinking an alkyne containing histidyl-hydrazide probe (aHH) was synthesized. The same HPLC method used to evaluate the reactivity of the LPx scavengers with HNE and ONE was used to validate that this aHH probe has the same reactivity with LPx as HH. This aHH probe (5 mM) was then preincubated with HNE or ONE (0.5 mM) for two hours prior to dilution of these samples with the GST-P1 (0.1 µg/µL) containing buffer. After incubating these samples at 37°C for one hour all of the components of the click reaction were added. After the click reaction the samples were reduced with NaCNBH$_3$ in order to prevent any loss of the aHH by the reversal of the Schiff base reaction. These protein adducts were than separated by SDS-PAGE gel electrophoresis and the resulting gels were imaged using the LICOR Sa imaging system. In these imagines any signal detected in the 700 nm channel is due to the incorporation the cyanine5.5-azide dye clicked to alkyne functional group within the aHH. The results from these experiments show an increased incorporation of the azide dye when GST-P1 was incubated with HNE or ONE and increasing concentrations of aHH (**Figure 56**). There is also a significant increase in the signal from the azide dye at the 25 kDa region of the gel in the ONE treated samples indicating that the incorporation of the aHH probe accounts for the prevention of GST-P1 induced protein crosslinking by ONE.

Figure 55. Reactive of aHH with HNE and ONE.
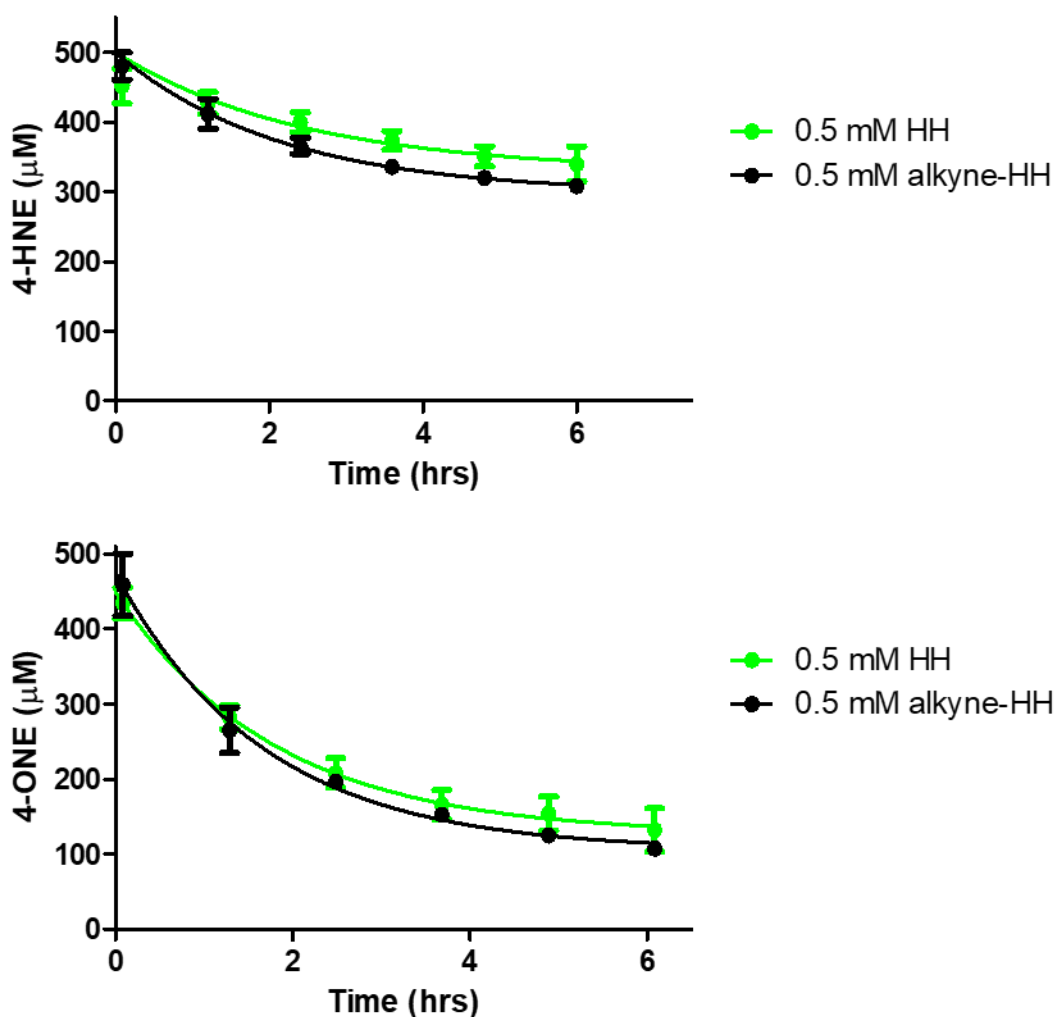
Figure 55. The concentration of free HNE or ONE was monitored by UV-HPLC. 500 µM HNE or ONE was incubated in 0.1 M phosphate buffer (pH=7.4) with 500 µM of alkyne-histidyl-hydrazide (aHH). These reactions were incubated at room temperature and monitored at six time points from 0-6 hours. Each data point represents the mean ± SEM of duplicate experiments.

Figure 56. Alkyne-HH validates that HH prevents GST-P1 cross-linking.
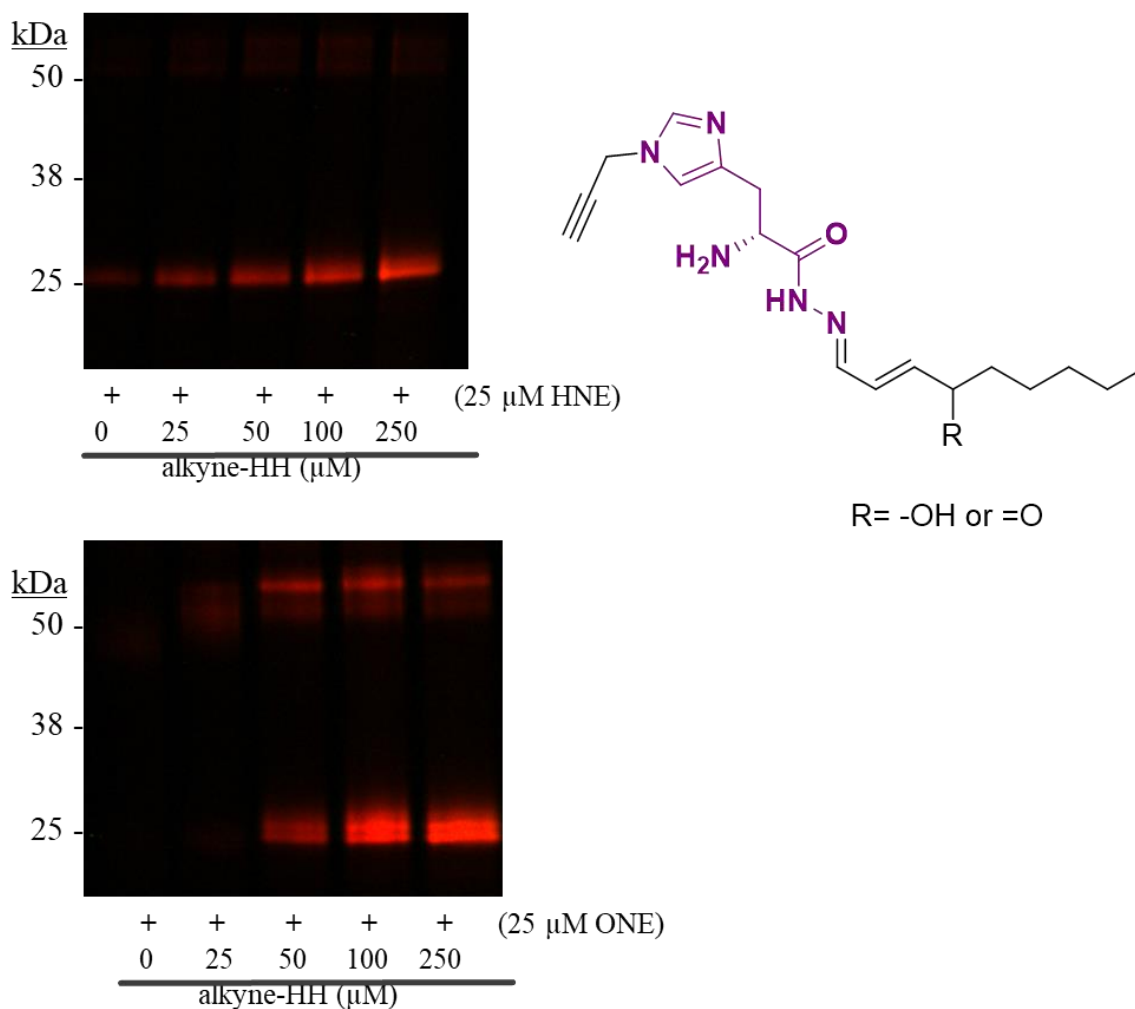
Figure 56. Top: GST-P1 WT (0.1 µg/µL) was treated with 25 µM HNE, or cotreated with 25 µM HNE and 25-250 µM alkyne-HH. Each lane of the gel contains 1.5 µg of protein. Bottom: GST-P1 WT (0.1 µg/µL) were treated with 25 µM ONE, or cotreated with 25 µM ONE and 25-250 µM alkyne-HH. Each lane of the gel contains 1.5 µg of protein. Each image is representative of three independent experiments and the data represents the mean ± SEM of these experiments.

3. Discussion

Aldehyde reactive scavengers have been reported to protect against the formation of protein adducts with LPx.[158-163] These reports utilized anti-HNE or anti-ACR antibodies to measure HNE or ACR protein adducts or chemical derivatization by DNPH to measure total protein carbonylation. The results from all of these studies report that the formation of LPx protein adducts is reduced by the treatment of HH, carnosine derivatives, and hydralazine analogs in a variety of tissues including: isolated mitochondria, mesangial cells, arterial smooth muscle cells, and mouse or rat aorta homogenates.[158-163] It was previously hypothesized that the reported ability of scavengers to prevent the formation of LPx protein adducts can be linked to the observed protective activity of these compounds to in cells or tissues against LPx induced cell death.[159, 161-162] However, using our dual color near-IR imaging methodwe have shown that the more reactive aldehyde reactive scavengers, HYD and HH, caused an increase in the formation of LPx protein adducts in both SHSY-5Y whole cell lysates and in the model GST-P1 system. This can be explained by the fact that the LPx-scavenger conjugates, resulting from the preincubation of HYD and HH with aONE or aHNE, still contain a functional group which can serve as a Michael acceptor (**Figure 57**). The previous reports cited above could have reported the decrease in LPx protein adduct formation by these aldehyde reactive scavengers because the formation of the scavenger-LPx conjugate results in the masking of the resulting scavenger-LPx-protein adduct from the commonly used methods for the detection LPx protein adducts (**Figure 58**).

Even though the aldehyde scavengers HH and HYD do not decrease the level of total aHNE or aONE adducts, the formation of a Schiff base conjugate by HYD or HH does prevent the protein crosslinking caused by the addition of aONE to GST-P1 and SHSY-5Y cell lysates.

The prevention of protein cross-linking by the aldehyde reactive scavengers could account for the observed neuroprotective activity of these scavengers in SHSY-5Y cells. The aggregation of glyceraldehyde-3-phosphate dehydrogenase (GAPDH) has been reported to form protein aggregates under conditions of oxidative stress. GAPDH contains three Cys residues (Cys152, Cys156, Cys 247) but only the mutation of Cys152 to Ala152 prevented the aggregation of GAPDH after treatment with the nitric oxide donors 1-(±)-4-ethyl-2[(*E*)-hydroxyimino]-5-nitro-2-hexenamide or 2,2'-(hydroxynitrosohydrazino)*bis*-ethanamine (NOC-18). The doxcycline-induced expression of C152A GAPDH in SHSY-5Y cells protected these cells against dopamine or NOC-18 toxicity.[164-165] Proteomic LC-MS/MS analysis has shown that HNE and acrolein covalently modify GAPDH, with acrolein specifically forming an adduct at Cys152.[166-167] Our own proteomic analysis identified GAPDH as one of the proteins modified by aHNE in SHSY-5Y cell lysates. Therefore, the prevention of GAPDH cross-linking by HNE or ONE is one potential mechanism that accounts for the neuroprotective activity of these aldehyde reactive scavengers (**Figure 59**).

The mechanism by which HH and HYD prevent protein cross-linking is also relevant to neurodegenerative diseases due to the fact that immunohistochemical analysis of post mortem brain slices from patients with AD has shown that HNE and other forms of protein carbonylation are co-localized with NFTs and amyloid plaques.[168-170] HNE is also reported to directly modify $A\beta_{1-40}$ and promote the aggregation of $A\beta_{1-40}$, $A\beta_{1-42}$, and phosphorylated tau *in vitro*.[170-173] Additionally, GAPDH was identified as a protein associated NFTs by proteomic analysis of NFTs from the hippocampus of AD patients.[174] An additional report shows that GAPDH aggregates were also shown to increase the rate of $A\beta_{1-40}$ aggregation.[175]

Figure 57. Mechanism of protein modification by HH or HYD-LPx conjugates
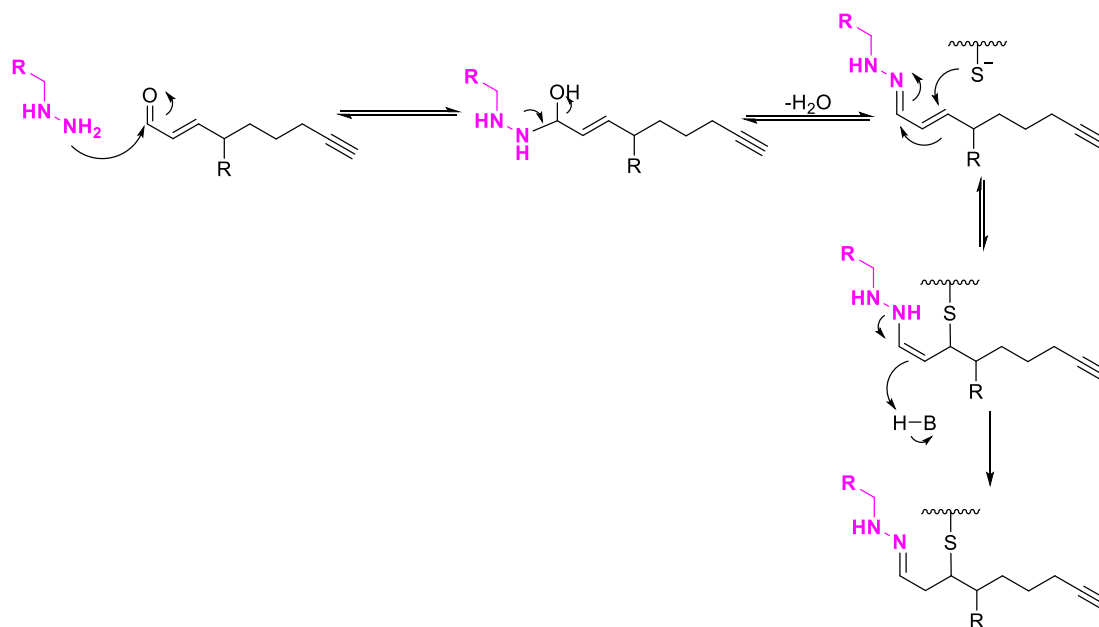
Figure 57. The formation of a Schiff base conjugate between HNE or ONE and aldehyde reactive scavengers maintains a functional group that is still capable of forming a Michael addition protein adduct.

Figure 58. Aldehyde reactive scavengers mask LPx protein adducts
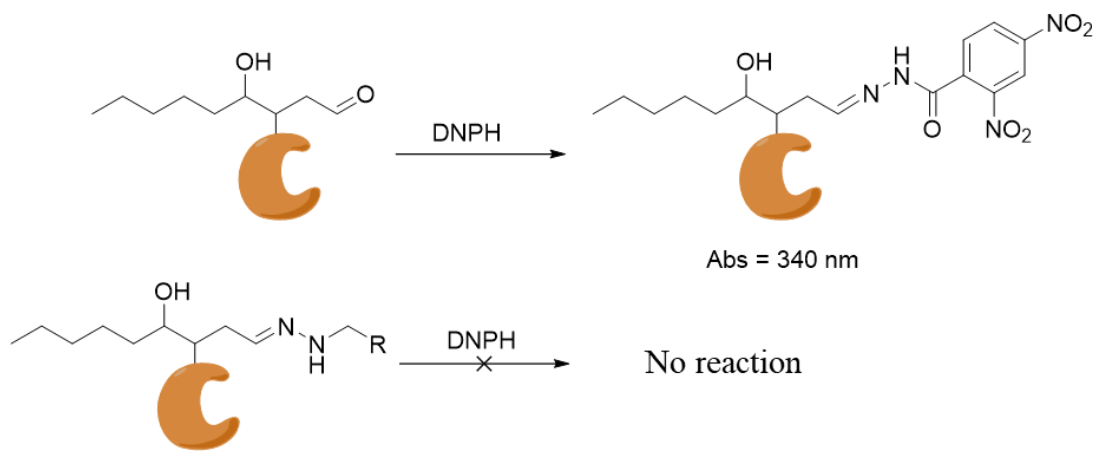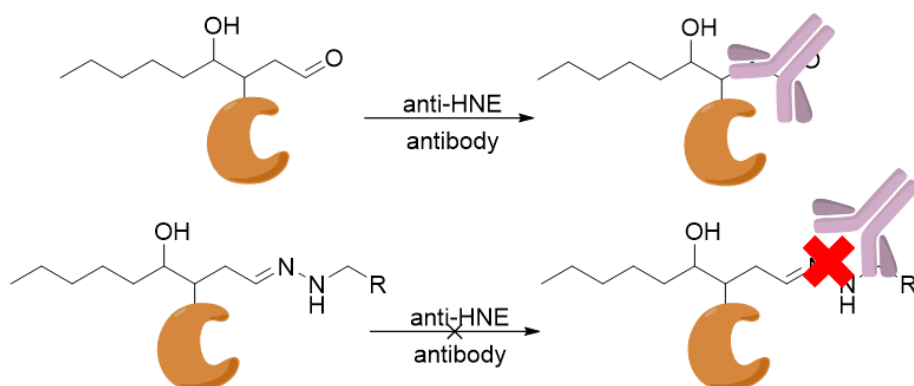
Figure 58. The aldehyde reactive scavenger conjugates with HNE prevents the detection of the HNE protein adducts by replacing the free aldehyde group required for chemical derivatization methods (Top) and interfere with the epitope required for the recognition of these adducts by anti-HNE antibodies (Bottom).

Figure 59. A proposed mechanism of HH neuroprotective activity.
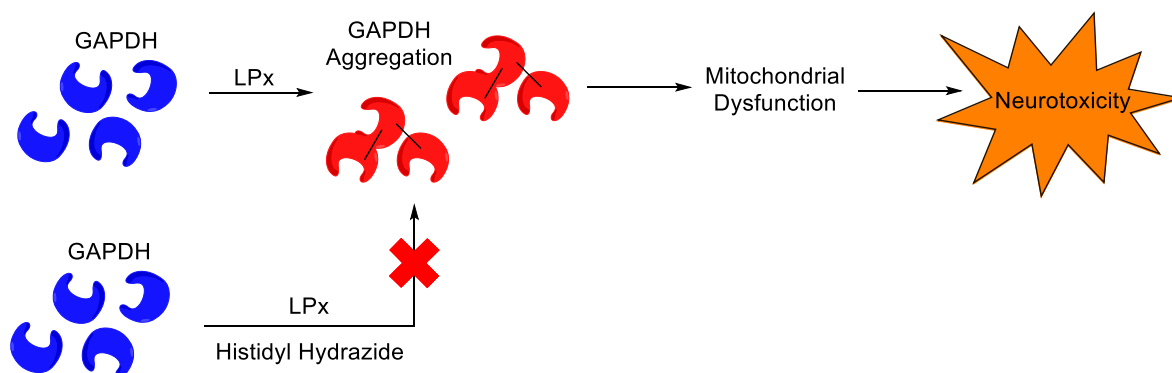
Figure 59. GAPDH aggregation causes mitochondrial dysfuncion, the release of cytochrome c, and the nuclear translocation of apoptosis-inducting factor in SHSY-5Y cells.[165] HH blocks protein cross-linking and therefore preventing LPx neurotoxicity.

4. Conclusion

In order to evaluate thiol containing and aldehyde reactive scavengers of LPx we measured the chemical reactivity of GSH, NAC, HH, HYD and LCS with HNE and ONE by HPLC. The near-IR in-gel imaging method was also modified to determine if each of these scavengers prevent LPx protein adduct formation or protein cross-linking. We showed that the thiol containing scavengers reacted readily with both HNE and ONE and prevented the formation of aHNE protein adducts in the GST-P1 model system and in SHSY-5Y cell lysates. HH and HYD were effective scavengers of ONE while only HYD reacted with >50% of HNE after 6 hours. Both of these aldehyde reactive scavengers increased the level of aHNE protein adducts detected by our in-gel imaging technique but were shown to prevent aONE induced

protein cross-linking. Finally, an alkyne-histidyl hydrazide probe was synthesized and used to validate that this scavenger is responsible for the decrease in ONE protein cross-linking.

This alkyne-histidyl hydrazide probe can now be used to treat the ALDH2$^{(-/-)}$ mouse model and evaluated for its neuroprotective activity. The presence of this alkyne tag will then allow for the enrichment of proteins modified by this probe in the brain homogenates of the treated animals. These proteins can then be identified by LC-MS/MS analysis and may provide insights into the mechanisms that account for the neuroprotective activity of these aldehyde-reactive scavengers.

5. Methods

5.1 HPLC Measurement of HNE and ONE

HNE and ONE reactivity with the LPx scavengers was monitored by HPLC. 500 µM HNE or ONE was incubated with 500 µM of each scavenger or 0.5-5 mM of HH in 0.1 M phosphate buffer (pH=7.4) at room temperature and reaction progress monitored via 10 µL injections every hour for 6 hours. This method utilized a Phenomenex Aqua C18 reverse phase column (3 μm, 150 mm, 2.00 mm); mobile phase ACN/water.

5.2 Modification to Near-IR Imaging Technique

For the experiments using GSH, NAC, or HYD 25 µM aHNE or aONE was preincubated with 25-250 µM of each scavenger for 1 hour prior to that addition of GST-P1 (0.1 µg/µL) or SHSY-5Y cell lysates (0.5 µg/µL) in 0.1 M sodium phosphate buffer, pH = 7.4). The procedure was modified for HH where 0.5-5 mM of HH or aHH was preincuated for 2 hours at room temperature with aHNE and aONE or HNE and ONE respectively. This mixture was then diluted with 0.1 M phosphate buffer (pH=7.4) containing GST-P1 (0.1 µg/µL) or SHSY-5Y cell lysates (0.5 µg/µL) to a final concentration of 25-250 µM for HH and aHH and 25 µM of the LPx.

CHAPTER 3. EVALUATION OF GLUTATHIONE BASED PHOTOPROBES FOR THE STUDY OF PROTEIN GLUTATHIONYLATION

1. Introduction

1.1 Protein S-Glutathionylation

Cysteine residues make up 3% of the human proteome and have an important role in the regulation of protein conformation and enzyme catalysis due to the chemical reactivity of the free thiol group.[176-177] This thiol group is also a target for oxidative modification.[178-179] A variety of products result from oxidative modifications of cysteine thiols, some of which are reversible/labile (sulfenic acid, intra- or intermolecular disulfide formation, S-nitrosation, S-glutathionylation) while other modifications are irreversible (sulfinic and sulfonic acids).[180-181] Reversible thiol modifications serve either a protective function, by preventing irreversible oxidative damage, or modulate protein structure and activity.[182-186] In addition to playing a role in redox signaling, irreversible oxidative Cys modifications can result in the loss of protein function and can lead to protein misfolding and aggregation.[187-188]

The concentration of GSH within many mammalian cells is in the low millimolar range and is a major source of non-protein thiols.[180, 189] Under normoxic conditions the intracellular GSH/GSSG ratio is high (>99% reduced GSH) and this ratio is maintained by glutathione reductase.[190] Glutathione disulfide (GSSG) is produced by the spontaneous reaction of glutathione with ROS or is catalyzed by glutathione peroxidases.[191-192] Under conditions of oxidative stress protein S-glutathionylation is also increased.[193] Protein S-glutathionylation is a form of S-thiolation that results in the formation of a mixed disulfide bond between a protein cysteine and the cysteine of glutathione (GSH). The formation of S-glutathionylation PTMs

occurs via two different mechanisms. The first mechanism is the reaction of GSH with activated thiol intermediates (sulfenic acid, thiyl radical) and the second occurs through thiol/disulfide exchange.[194]

(1) $PSH + GSH + H_2O_2 \rightarrow PSSG + 2\ H_2O$

(2) $PSH + GSSG \leftrightarrow PSSG + GSH$
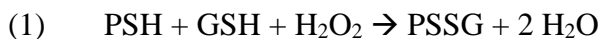
Several enzymes also play a role in the regulation of protein glutathionylation by catalyzing glutathionylation or deglutathionylation. Glutathione S-transferase P (GST-P) is proposed to catalyze S-glutathionylation by lowing the pK_a of the GSH thiol with in the active site of the enzyme to produce a thiolate anion.[195] Proteins such as glutaredoxin (Grx) and thioredoxin (Trx) have been shown to catalyze both glutathionylation and deglutathionylation depending on if there are local reducing or oxidative conditions.[196-197] Other enzymes including flavoprotein sulfhydryl oxidase, sulfiredoxin, protein disulfide isomerase, and other GST isoforms are also implicated in the regulation of protein glutathionylation.[198]

The most commonly reported result of protein S-glutathionylation is loss of enzyme activity.[197] However, there are reports of S-glutathionylation causing increased enzyme activity, altereing DNA binding by transcription factors and protein stabilization. Glutathionylation has been reported to regulate actin polymerization, increase Ras activity, activate Hsp70, and to inhibit a variety of proteins including, caspase 3, GAPDH, PTP1B, and Na^+-K^+ pumps.[199-205]

1.2 Photoactivatable Probes

Photoactivatable probes (PAPs) were first developed in 1962 and describe small molecules that contain a functional group which generates a highly reactive intermediate upon the absorption of photonic energy.[206] In an ideal scenario this reactive intermediate then reacts with amino acid residues of target proteins to form a covalent bond with the target proteins.

Many PAPs also include a functional group that allows for the detection and/or identification of a PAPs protein targets, such as biorthogonal tags or a flurophore.[207] PAPs are categorized by the photoactivatable group incorporated in the small molecule of interest: phenylazides, diazirines, and benzophenones.

1.2.1 Phenylazide

Phenylazide PAPs are the most commonly used class of PAPs. Upon photo-irradiaiton the phenylazide group generates a highly reactive singlet nitrene generated by the loss of N_2. Phenylazides are also relatively stable and the azide group is often easily incorporated into small molecules with an existing phenyl group. Some of the disadvantages of phenylazides include the wavelength that is required for photoactivation (<300 nm), which can damage biomolecule and cell compnents.[208] Additionally, the generated nitrene can undergo rearrangement resulting in the expansion of the phenyl ring, loss of specific photolabeling and variable photoligated product structures. A common strategy used to prevent this nitrene rearrangement is to utilize a substituted tetrafluorophenylazide group rather that an unsubstituted phenylazide.[209]

Figure 60. Nitrene production from photoactivation of phenylazides.
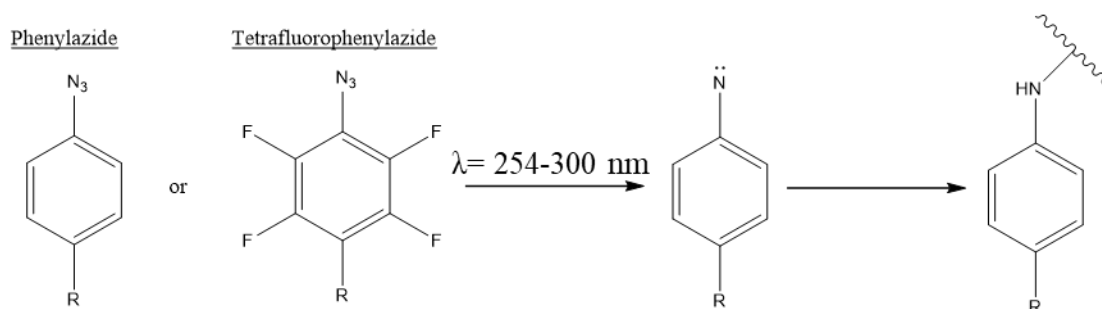
1.2.2 Diazirine

Diazirine PAPs can include either an aryl- or alkyl-diazirine and produce a carbene following photoirradiation at 350-380nm. This higher wavelength range required for photoactivation reduces any protein damage caused by UV irradiation. A majority of diazirine PAPs contain a trifluoromethylaryldiazirine functional group which exhibits favorable photochemical properties and is chemically stable. The main disadvantage of the diazirine PAPs is the rapid quenching of the carbene intermediate by water molecules.[210]

Figure 61. Carbene production from photoactivation of dizirines.
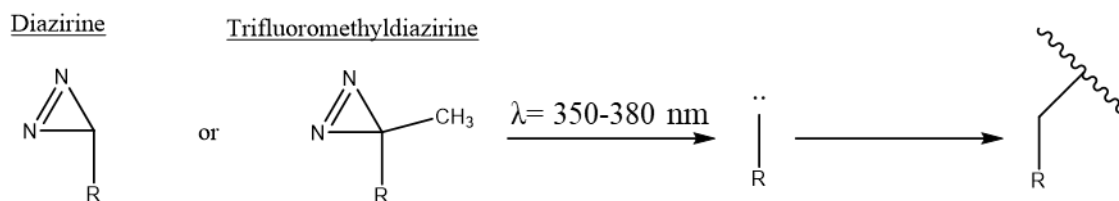
1.2.3 Benzophenone

Benzophenones are activated by photoirradiation at 350-360 nm and generate a triplet diradical at the carbonyl position. In addition to the higher wavelength for photoactivation the diradical intermediate is able to regenerate the benzophenone if the diradical species does not react with an adjacent molecule. This can result in increased labeling efficiency by these PAPs. The major drawback of benzophenones is size of the photoactivatable group which can prevent

high affinity binding of the probe to its protein targets or cause binding to off-target proteins.[209,][211]

Figure 62. Diradical formation from photoactivation of benzophenones.
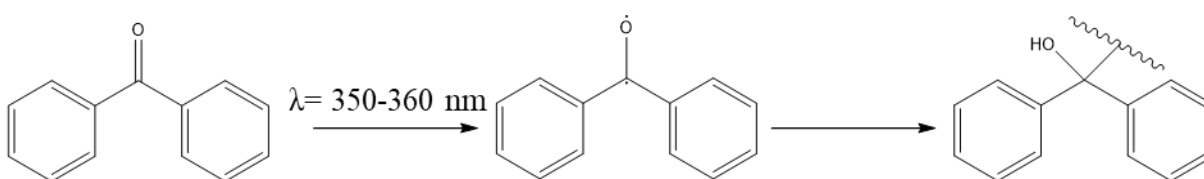
2. Results

2.1. Evaluation of Glutathione Photoprobes

In order to develop a glutathione based photoprobe three glutathione based compounds were evaluated as inhibitors of human GST-P1. Initially two different photoactivatable groups were evaluated: a tetrafluoroazide photoactivatable group (KB-1-013) and a trifluoromethylaryldiazirine photoprobe (KB-1-022). Additionally, KB-1-010 which contains no photoactivatable group was evaluated as a control compound. The initial evaluation was done using molecular docking and a GST-P1 enzyme activity assay to determine the IC_{50} and K_I of these compounds.

Figure 63. Structures of glutathione based photoprobes.
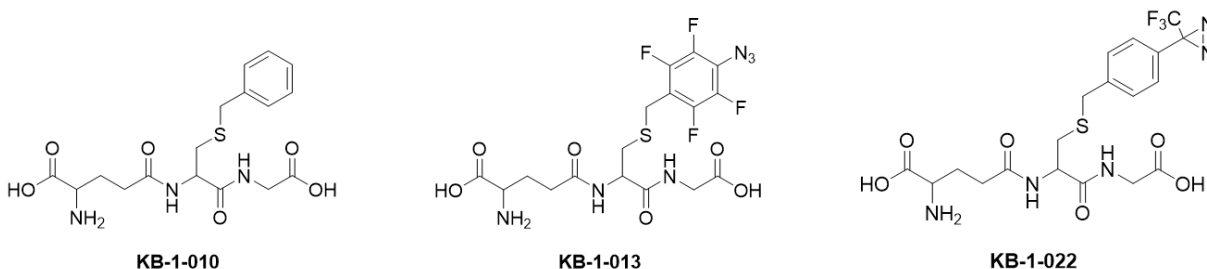
The IC_{50} values of these compounds was measured by monitoring the conjugation of 1-chloro-2,4-dinitrobenzne (CDNB) to glutathione (GSH) by recombinant human GST-P1. Each compound (1-100 µM) was incubated with rhGST-P1 (4 µg/mL) for five minutes prior to the addition of 1 mM GSH and 1 mM CDNB. The production of GS-DNB conjugate was monitored spectrophotometrically (340 nm) for 3.6 minutes. The IC50 values for these compounds ranged from 13-58 µM with KB-1-022 being the most potent inhibitor of GST-P1.

The K_I values for these compounds were also determined using the same assay as described above. For the K_I determination 10-100 µM of each compound was used, depending on the potency of each compound and the concentrations of GSH (0.1-2 mM) were varied while the concentration of CDNB (1 mM) remained constant. KB-1-022 was the most potent inhibitor of GST-P1 with a K_I value of 3 µM. The other compounds, KB-1-013 and KB-1-010, produced K_I values of 7.5 µM and 35 µM respectively.

The crystal structure of human GST-P1 (3GSS), co-crystalized with the glutathione conjugate of ethacrynic acid, was used for the docking analysis of the glutathione photoprobes. The active site of this crystal structure was defined as all protein atoms within 6 Å of the ligand. The docking analysis was conducted using GOLD and the scoring function used to rank the dockings was Chem-PLP. The binding modes for all the probes were influenced by the pi-pi stacking interactions of the aromatic ring on the probes and one of the three aromatic residues in the active site of GST-P1 (Phe8, Tyr108, Trp38). The best docking pose generated for KB-1-022 shows that the diazirine group is oriented towards the solvent while for KB-1-013 the azide group is oriented toward Tyr108.

Figure 64. IC50 values for KB-1-010, KB-1-013, and KB-1-022

Photoactive group	Compound	IC$_{50}$ (µM)
N/A	KB-1-010	57.77 ± 0.02
Azide	KB-1-013	36.26 ± 0.04
Diazirine	KB-1-022	13.20 ± 0.03
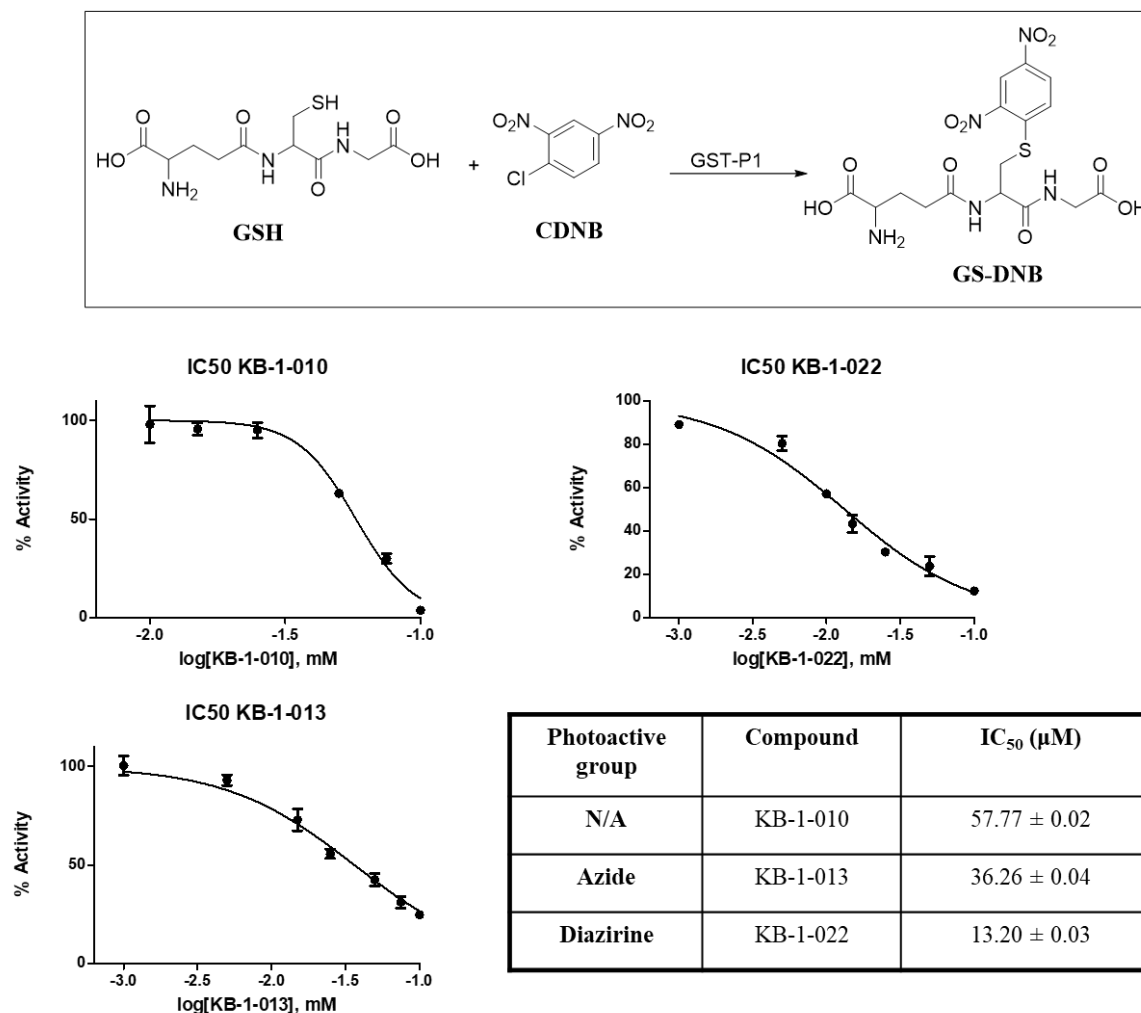
Figure 64. Top: Enzyme reaction mechanism of GST-P1. Bottom: GST-P1 activity measured using recombinant human GST-P1 (4 µg/mL) which was preincubated with EtOH or 1-100 µM of each compound in an assay buffer (0.1 M potassium phosphate, 1 mM EDTA, pH = 6.5) for 5 min at 25°C. 1 mM GSH and 1 mM CDNB was then added and the production of GS-DNB (340 nm) was monitored for 3.6 minutes. The rate of the reaction was then normalized to the rate of the reaction without any inhibitor and the data is represented as the log[inhibitor] vs % enzyme activity. Table: IC50 values for KB-1-010, KB-1-013, and KB-1-022. Each data point represents the mean ± SEM of triplicate experiments.

Figure 65. K_I determination for KB-1-010, KB-1-013, and KB-1-022

Photoactive group	Compound	Km/KI (µM)
N/A	KB-1-010	35.1 ± 3.24
Azide	KB-1-013	7.51 ± 0.74
Diazirine	KB-1-022	3.06 ± 0.56
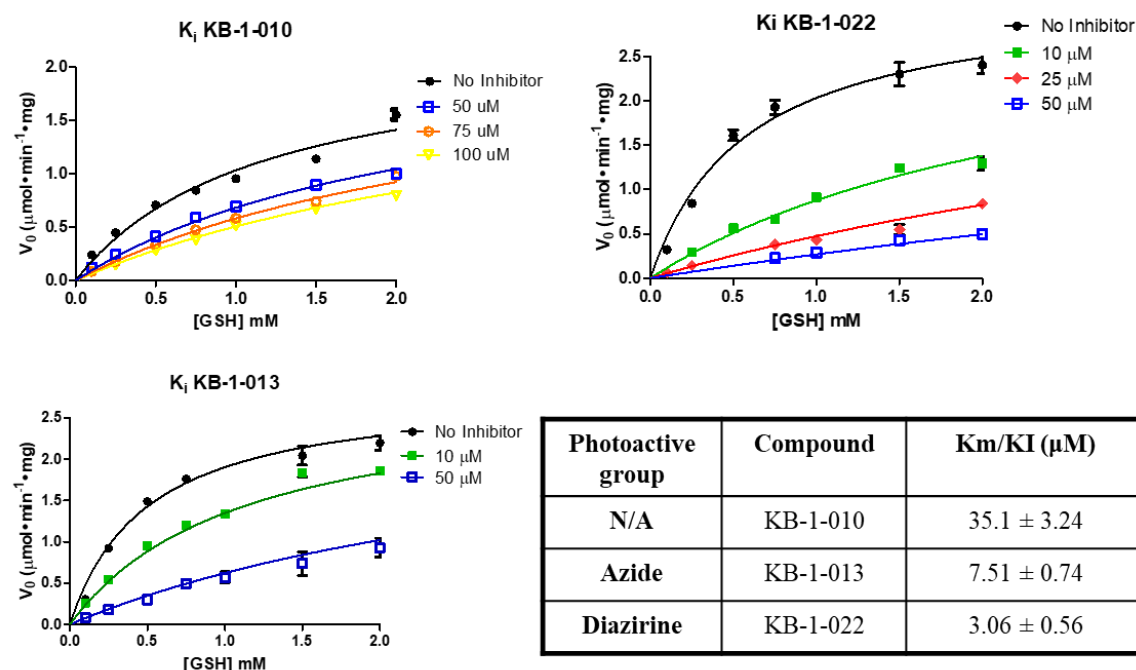
Figure 65. GST-P1 activity measured using recombinant human GST-P1 (4 µg/mL) which was preincubated with EtOH or 10-100 µM of each compound in an assay buffer (0.1 M potassium phosphate, 1 mM EDTA, pH = 6.5) for 5 min at 25°C. 0.1-2 mM GSH and 1 mM CDNB was then added and the production of GS-DNB (340 nm) was monitored for 3.6 minutes. The data is represented as the initial enzyme rate (V_0) vs [GSH] and fit to nonlinear regression for competitive inhibition. Table: K_I values for KB-1-010, KB-1-013, and KB-1-022. Each data point represents the mean ± SEM of triplicate experiments.

Figure 66. Docking scores for KB-1-010, KB-1-022, KB-1-013
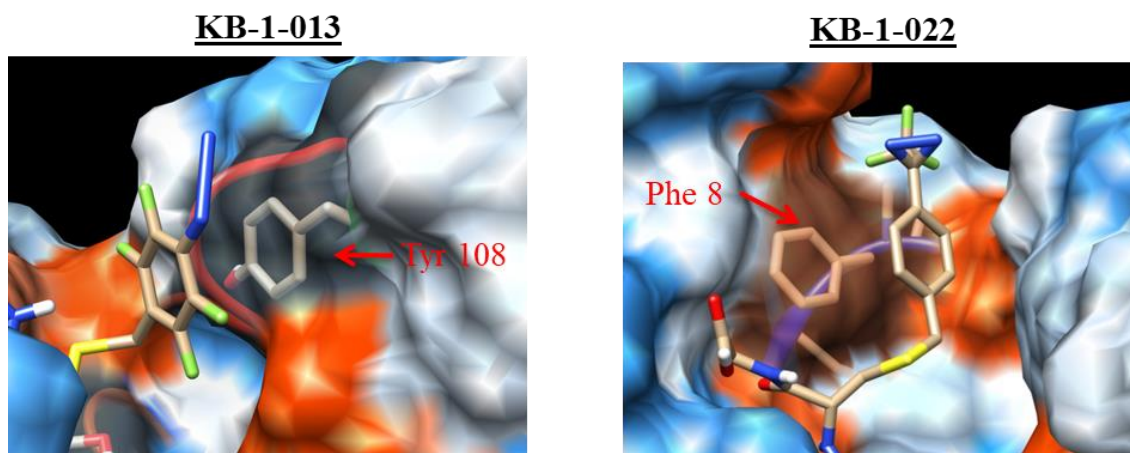
<u>**KB-1-013**</u>   <u>**KB-1-022**</u>

Photoactive group	Compound	Docking Score
N/A	KB-1-010	79.52
Azide	KB-1-013	87.71
Diazirine	KB-1-022	93.13

Figure 66. Top: Images for the highest scoring docking poses of KB-1-013 and KB-1-022.

Table: Docking scores for KB-1-010, KB-1-013, and KB-1-022.

2.2 Proteomic Analysis of Photoprobes

Recombinant GST-P1 (10 µM) was incubated with DMSO or 50 µM of each photoprobe for five minutes at room temperature. Samples containing the azide probe (KB-1-013) were irradiated at 302 nm for four minutes at room temperature. After photoirradiation, TCEP (50 mM) and 0.1% formic acid was added to each sample and these samples were analyzed using a hybrid LTQ-FT linear ion trap mass spectrometer (LTQ-FT). The intact protein analysis of GST-P1 resulted in a signal with a molecular weight of 25,629 Da. The photoirradation of GST-P1 in the presence of KB-1-013 resulted in the addition of 482 Da. This addition corresponds the molecular weight of KB-1-013 (510 Da) after the loss of N_2 (482 Da) that results from photoactivation.

Figure 65. Intact protein analysis of GST-P1.
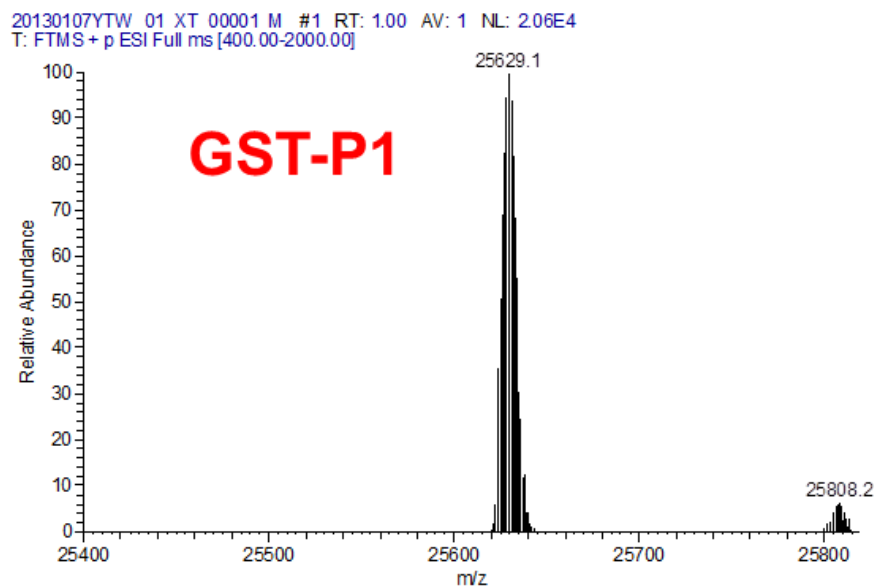
Figure 67. Intact analysis of recombinant human GST-P1 (10 µM) by a hybrid LTQ-FT linear

ion trap mass spectrometer (LTQ-FT).

Figure 68. Intact protein analysis of detect the modification of GST-P1 by KB-1-013
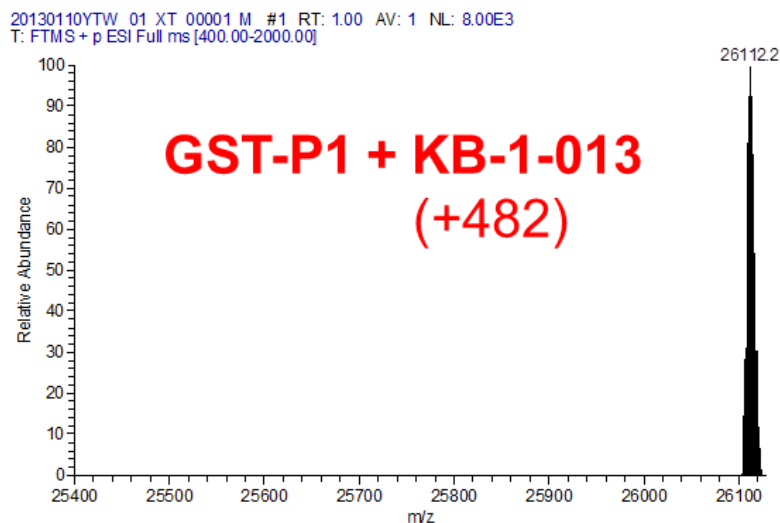
Figure 68. Intact analysis of recombinant human GST-P1 (10 µM) after photoirradiation (302 nm) in the presence of 50 µM KB-1-013. The protein analysis was done using a hybrid LTQ-FT linear ion trap mass spectrometer (LTQ-FT).

The same analysis was done in the presence of KB-1-022, with the photoirradiation conducted at 365 nm; however both LTQ-FT and MALDI analysis showed that no incorporation of KB-1-022 was observed. In order to validate that the diazirine group was activated by photoirradation, KB-1-022 was photo-irradiated for five minutes in methanol and LC-MS/MS analysis was used to measure the incorporation of a –OCH_3 at the site of carbene formation. This analysis shows that the carbene intermediate is generated upon photoirradiation at 365 nm even though no protein modification of GST-P1 was observed by KB-1-022. Due to the lack of protein modification by KB-1-022 no further analysis was conducted using this photoprobe.

Figure 69. Validate the photoactivation of KB-1-022 in methanol.
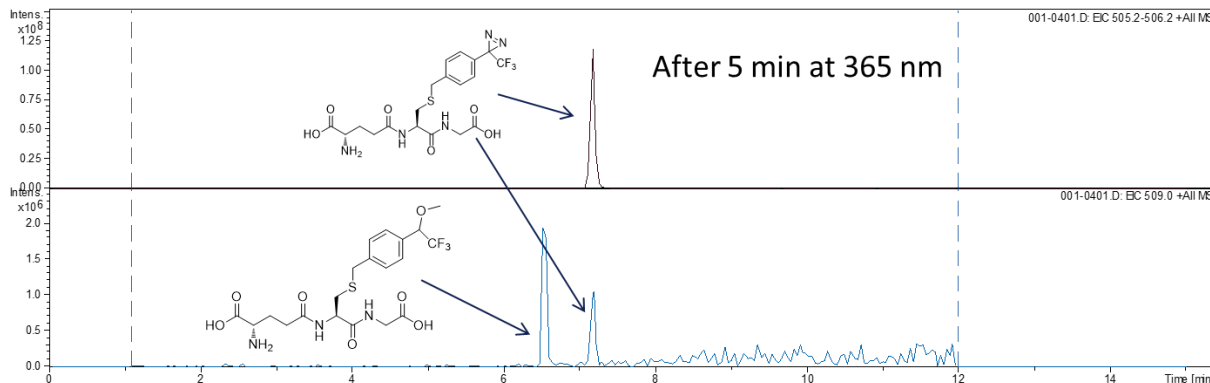
Figure 69. KB-1-022 was irradiated 365 nm for five minutes in methanol. LC-MS/MS analysis was used to measure the incorporation of $–OCH_3$ at the site of carbene formation after photoactivation.

In order to identify the site of GST-P1 modification by KB-1-013, bottom up proteomic analysis was conducted. GST-P1 (10 µM) was incubated with DMSO or 50 µM KB-1-013 for five minutes prior to photo-irradiation of the samples at 302 nm for three minutes. The protein was then reduced by the addition of TCEP and all cysteines were alkylated by the addition of NEM. These samples were then separated by SDS-PAGE gel and the 25 kDa region was excised and subjected to in-gel trypsin digestion. These samples were then analyzed using LC-MS/MS (Agilent Ion Trap). The mass peptide containing Tyr108 is 719.02^{3+} and after the incorporation of KB-1-013 the mass of the modified peptide is 880^{3+} or 660^{4+} ($[719 + (510.1 - 28) + 3H^+]/3 = 880$). The MS/MS spectra for these peptides were then matched to the predicted masses of the b and y ions for this modified peptide. We were able to determine that Tyr108 was the site of GST-P1 modification by KB-1-13

Figure 70. Identified the modification of Tyr108 by KB-1-013.
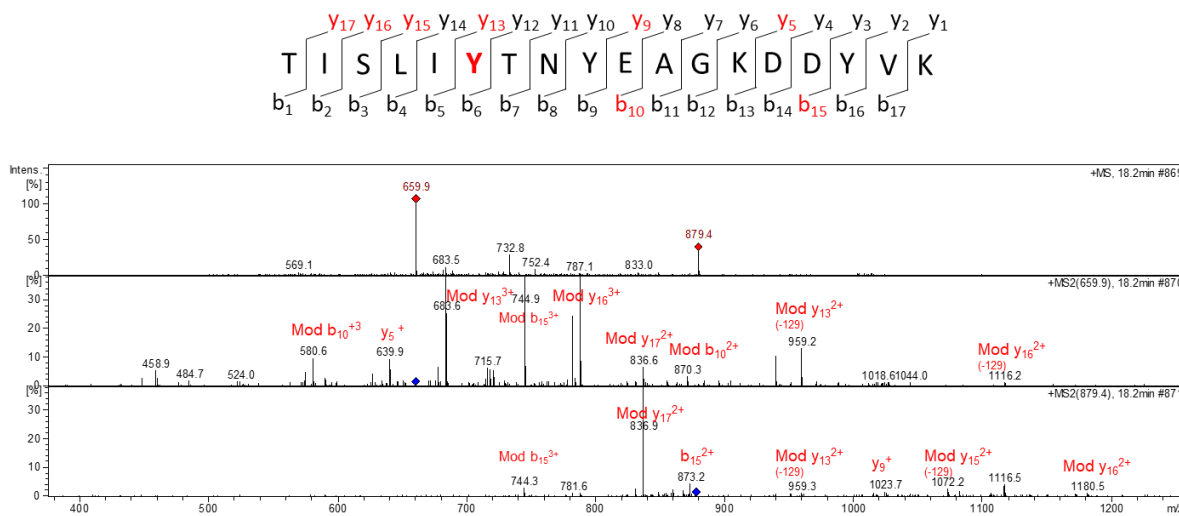
Figure 70. GST-P1 (10 µM) was incubated with 50 µM KB-1-013 at room temperature for 5 minutes prior to photoirradiation at 302 nm for 3 minutes. The protein was then reduced and all cysteine residues were alkylated by the addition of TCEP (10 mM) and NEM (10 mM). After SDS-PAGE gel electrophoresis the 25 kDa region of the gel was excised and subjected to trypsin digestion. The digested protein samples were analyzed with an Agilent 6310 ion trap mass spectrometer (Agilent Technologies, Santa Clara, CA) coupled to Agilent 1100 series high-performance liquid chromatography (HPLC) system with electrospray ionization (ESI). The predicted b and y ions of the modified peptide was matched to the MS^2 spectra of the MS^1 corresponding the predicted mass of the modified peptide. The matching b and y ions are labeled in the MS^2 and highlighted in red in the representative peptide above.

2.3 Evaluation of Fluorescent Derivative of KB-1-013

A fluorescent derivative of the tetrafluoroazide probe was synthesized by conjugating tetramethylrhodamine-5-(and-6)-isothiocyanate (5(6)-TRITC) to KB-1-013. The activity of this fluorescent probe (KB-1-090) as an inhibitor of GST-P1 was evaluated by HPLC analysis in order to determine if this probe had similar activity to KB-1-013. GST-P1 (160 nm) was preincubated with DMSO, or KB-1-090 (50 µM, or 100 µM) for 5 minutes at room temperature prior to the addition of 1 mM CDNB and 0.1-2 mM GSH. These samples were then incubated at 25 °C for 0.5-2 min. The reaction were stopped at 0.5, 1, 1.5, and 2 minutes by the addition of cold MeCN containing 50 µM p-NO$_2$-phenol which is used as an internal standard for the HPLC analysis. After centrifugation, used to remove GST-P1 from the samples, the supernatant was removed and this fraction was analyzed by HPLC.

The peak area for the GS-DNB at each time point and reaction condition was normalized to the peak are of p-NO$_2$-phenol within the same spectra. For each reaction condition the rate of GS-DNB formation was determined by graphing the change in peak area vs. time. The slope of these linear plots were then graphed against the concentration of GSH and fit to nonlinear regression for competitive inhibition. This method resulted in a K$_I$ value of 46 µM for KB-1-090.

Figure 71. K_I determination for KB-1-090

KB-1-090

K_i **KB-1-090**

$Ki = 46.3 \pm 13.8 \; \mu M$

- No Inhibitor
- 100 uM KB-1-090
- 50 uM KB-1-090
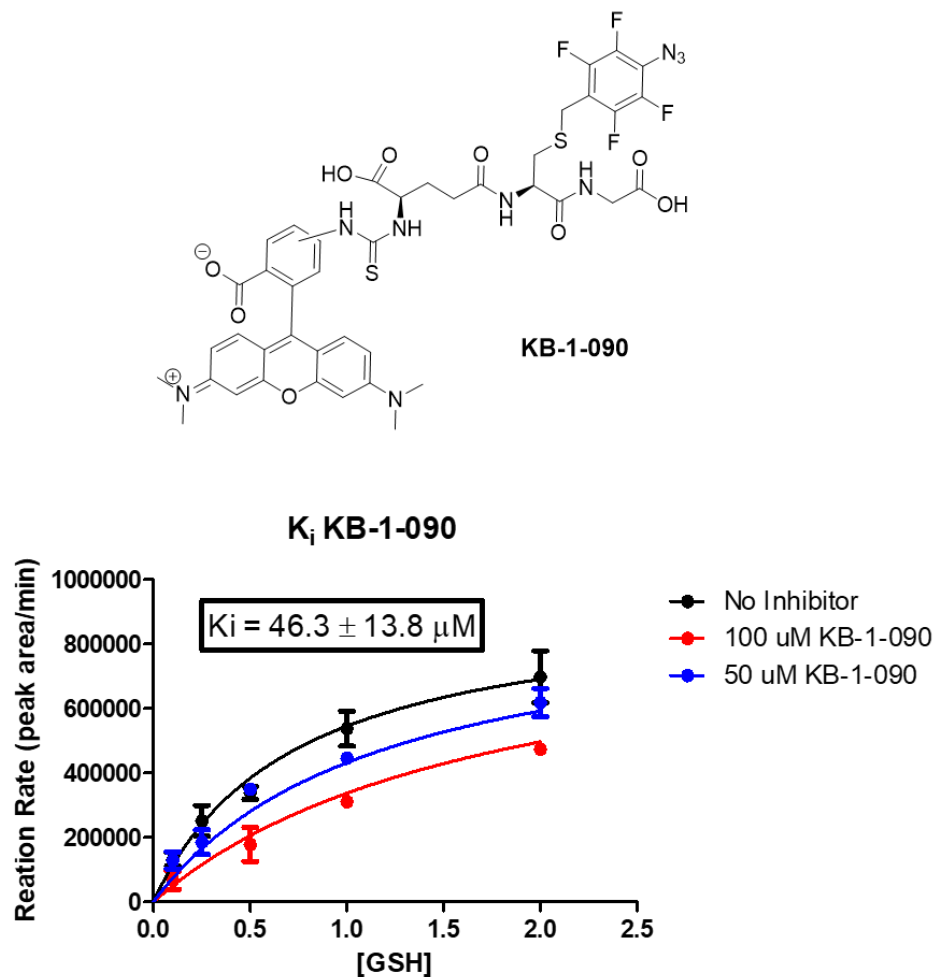
Figure 71. Top: Structure of KB-1-090. Bottom: GST-P1 activity measured using recombinant human GST-P1 (160 nm) which was preincubated with DMSO, 50 µM, or 100 µM of KB-1-090 in an assay buffer (0.1 M potassium phosphate, 1 mM EDTA, pH = 6.5) for 5 min at room temperature. 0.1-2 mM GSH and 1 mM CDNB was then added and the reactions were incubated for 0.5-2 min at 25°C. GST-P1 removed from the samples by precipitation and centrifugation after the addition of ACN. The supernatant was then removed and analyzed by HPLC where production of GS-DNB was measure. The data is represented as the initial enzyme rate (peak

area/min) vs [GSH] and fit to nonlinear regression for competitive inhibition. Each data point represents the mean ± SEM of duplicate experiments.

The fluorescent photoprobe was then used to visualize the modification of recombinant GST-P1 and of proteins in SHSY-5Y cell lysates. GST-P1 was incubated with 1-100 µM of KB-1-090 for 5 minutes prior to photoirradiation at 302 nm for 5 minutes. These samples were then separated by SDS-PAGE gel electrophoresis and the resulting gels were immediately visualized by in-gel fluorescence using the GE Typhoon Trio imager (Ex/Em, 532/582 nm). The same gel was then stained with Coomasie Brilliant Blue to measure the total protein in each well. These results show a dose dependent increase in the intensity of the fluorescent signal with increasing concentrations of KB-1-090, indicating an increased modification of GST-P1 by this fluorescent photoprobe.

The same method described above was used to visualize proteins modified in SHSY-5Y cell lysates. The samples contained 1 µg/µL of protein and were incubated with DMSO or 1-25 µM KB-1-090. A concentration dependent increase in the fluorescence signal was observed with an increased concentration of KB-1-090. The region from 10-70 kDa show the most significant increase in the amount of protein modification by KB-1-090. In order to validate that the modification of these proteins was due to specific interactions of KB-1-090 with these proteins 5 µM KB-1-090 was incubated with SHSY-5Y cell lysates in the presence of 50 or 500 µM GSH or 50 µM KB-1-013. These resulting gel shows that the protein modification observed on by the incubation of KB-1-090 alone was decreased by the competition of 500 µM GSH and 50 µM KB-1-013. Although KB-1-013 is a more effective inhibitor of protein modification by KB-1-090 than GSH. This can most likely be attributed to the covalent modification of proteins by KB-1-013 resulting in irreversible competitive inhibition of KB-1-090 binding.

Figure 72. Concentration dependent modification of GST-P1 by KB-1-090
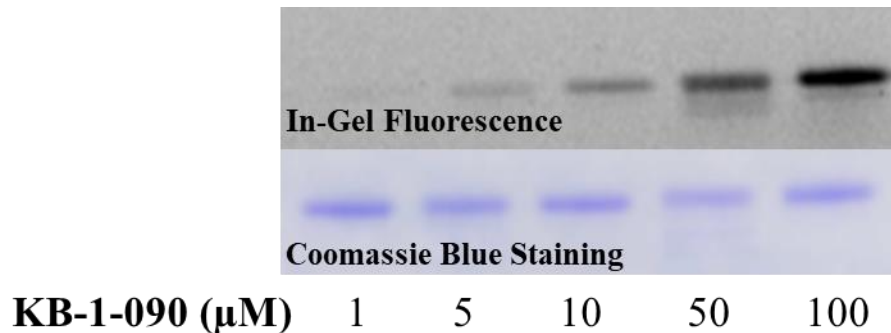
Figure 72. GST-P1 (2 µg/µL) was incubated with 1-100 µM KB-1-090 in 0.5 M sodium phosphate buffer (pH=7.4) for 5 minutes at room temperature before irradiating samples at 302 nm for 5 minutes. These samples were then separated by SDS-PAGE gel electrophoresis (30 µg protein/lane) and gel were immediately imaged using the GE Typhoon Trio imager (Ex/Em, 532/582 nm). The same gels were then stained with Coomasie Brilliant Blue and destained in order to measure the total amount of protein in each well. This image represents the results of two independent experiments.

Figure 73. Modification of proteins from SHSY-5Y cell lysates by KB-1-090.

Figure 73. SHSY-5Y cell lysates (1 µg/µL) was incubated with 1-25 µM KB-1-090 in 0.5 M sodium phosphate buffer (pH=7.4) for 5 minutes at room temperature before irradiating samples at 302 nm for 5 minutes. These samples were then separated by SDS-PAGE gel electrophoresis (30 µg protein/lane) and gel were immediately imaged using the GE Typhoon Trio imager (Ex/Em, 532/582 nm). The same gels were then stained with Coomasie Brilliant Blue and destained in order to measure the total amount of protein in each well. This image represents the results of three independent experiments.

Figure 74. Decreased protein modification by KB-1-090 by GSH and KB-1-013

| In-Gel Fluorescence | Coomassie Blue Staining |

- 250 kDa
- 130 kDa
- 100 kDa
- 70 kDa
- 55 kDa
- 35 kDa
- 25 kDa
- 15 kDa

KB-1-090 (5 µM) + + + + +
Lysate +   + + + +
KB-1-013 (µM)   50
GSH (µM)   50 500
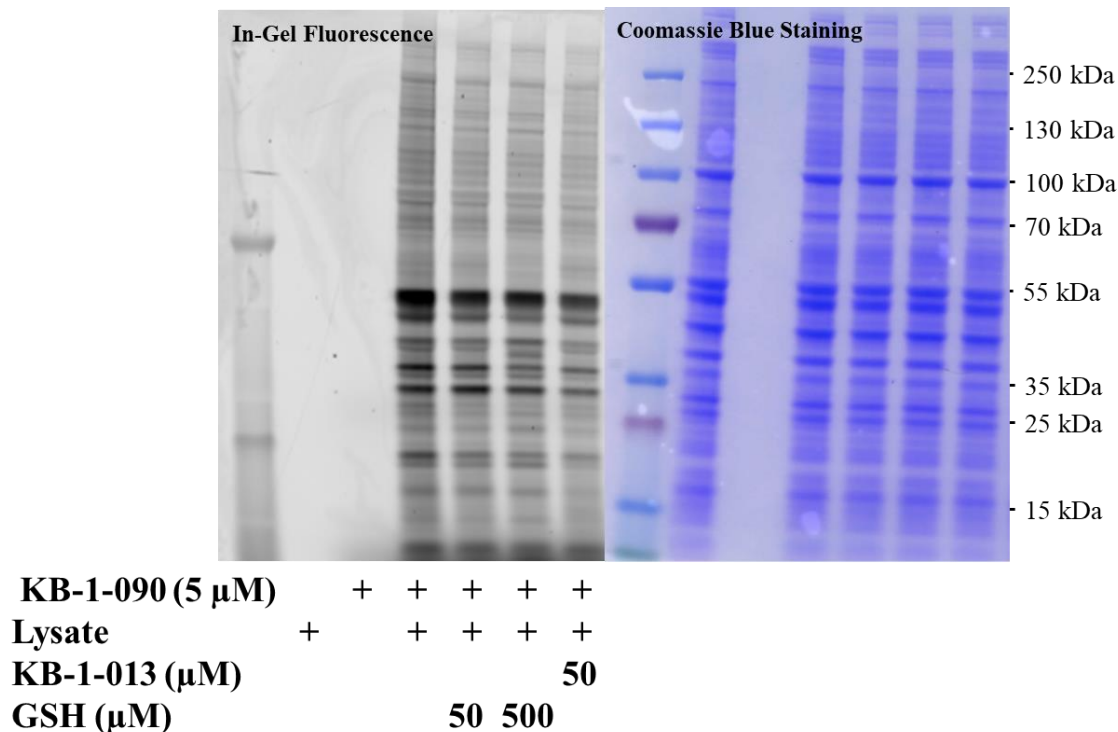
Figure 74. SHSY-5Y cell lysates (1 µg/µL) was incubated with 5 µM KB-1-090 and 50 µM, 500 µM GSH or 50 µM KB-1-013 in 0.5 M sodium phosphate buffer (pH=7.4) for 5 minutes at room temperature before irradiating samples at 302 nm for 5 minutes. These samples were then separated by SDS-PAGE gel electrophoresis (30 µg protein/lane) and gel were immediately imaged using the GE Typhoon Trio imager (Ex/Em, 532/582 nm). The same gels were then stained with Coomasie Brilliant Blue and destained in order to measure the total amount of protein in each well. This image represents the results of three independent experiments.

2.4 Identification of KB-1-013 Modified Proteins in SHSY-5Y Cell Lysates

SHSY-5Y cell lysates were treated with 50 µM, 100 µM or 200 µM KB-1-013 and after photoirradiation, reduction and cysteine alkylation, the proteins were separated by SDS-PAGE gel electrophoresis. After staining these gels with Coomasie Brilliant Blue dye, the regions for each sample from 25-50 kDa were excised and divided into approximately 5 kDa sections. These sections were subjected to trypsin digestion and the resulting peptides were analyzed using a hybrid LTQ-FT linear ion trap mass spectrometer (LTQ-FT). The resulting data files were searched by the MassMatrix search engine with NEM as fixed modification and KB-1-013 ($-N_2$) as a variable modification.

This data analysis resulted in the identification of modified GST-P1 by KB-1-013 and the site of this modification occurs within the peptide containing Tyr108. The modification of GST-P1 was observed in the samples treated with all of the concentration of KB-1-013. From this analysis a short list of seven additional proteins with sequence coverage >40% were also reportedly modified by KB-1-013. A list protein crystal structures from the RCSB Protein Data Bank with GSH or GSH conjugate ligands was compiled (**Appendix B**), however there was no overlap between this list of proteins and the proteins identified by our own LC-MS/MS analysis.

TABLE III. PROTEINS MODIFIED BY KB-1-013 IN SHSY-5Y CELLS

#	Identified Protein	Site of Modification	Sequence Coverage (%)
1	GST-P1	Y108	70%
2	Adenine Phosphoribosyltransferase	R88, I87	72%
3	Rab-1b	K154	52%
4	Rab-1a	K157	51%
5	Crk-like protein	K181	59%
6	Kcrb Human B-Ck	H297, H306	67%
7	Brain acyl-Coa hydrolase	R13	40%
8	Multicatalytic endopeptidase complex subunit C3	I233	44%

3. Discussion

3.1 Orientation of Photoactivatable Group Determines Effectiveness of Photoprobe

GST-P1 contains two different ligand binding sites, the GSH binding site (G-site) and the hydrophobic substrate binding site (H-site).[212-213] Two tyrosine residue are located within the active sites of GST-P1. Tyr7, located between the G-site and the H-site, is required for the abstraction of the proton from the thiol group of GSH to produce a thiolate ion.[214] Tyr108 is located within the H-site and the mutation of this residue to a phenylalanine has different effects depending on the electrophilic substrate.[215] This residue is also the site of modification for multiple covalent inhibitors of GST-P1.[213, 216] The orientation of the phenylazide group of KB-1-013 toward this Try108 residue accounts for the effective modification of GST-P1 by this photoprobe. The orientation of the diazirine group in KB-1-022 toward the solvent accounts for the lack of protein modification by the photoprobe despite this compound being a more potent inhibitor of GST-P1 and a carbene being generated after photoactivation.

3.2 Further Improvements of GSH Photoprobes

The proteomic analysis of proteins modified by KB-1-013 resulted in the identification of very few proteins modified by the photoprobe. The current analysis requires the direct detection of the modified peptide, therefore the due to the low efficiency of photoprobe incorporation, low expression levels of target proteins, and the modified peptides may have poor characteristics for LC-MS/MS detections. This limitation could be addressed through the addition of an alkyne or azide handle that would allow for conjugation and enrichment of all proteins modified by this photoprobe.

4. Conclusion

We have evaluated two glutathione based PAPs using an enzyme activity assay and molecular docking analysis. The results from both of these methods showed that the diazirine photoprobe (KB-1-022) had higher binding affinity and was a more potent inhibitor of GST-P1 compared to the tetrafluoroazide probe (KB-1-013). Despite this higher binding affinity both intact and bottom up proteomic analysis was unable to identify the formation of any protein adducts after irradiation KB-1-022 in the presence of rhGST-P1. We were able to identify the modification of Tyr108 in GST-P1 by KB-1-013 using recombinant protein and after treating SHSY-5Y cell lysates with this photoprobe.

5. Methods

5.1 Expression and purification of GST-P1

GST-P1 was expressed from *Esherichia coli* and purified as previously described.[111, 217]

5.2 Enzyme Activity Assays

For the 96 well plate assay the initial rates of GST-catalyzed conjugation of chlorodinitrobenzene (CDNB) and reduced glutathione (GSH) was measured using a previously described method.[218] Reactions were conducted using a Falcon black/clear 96-well plate with each well containing GST-P1 (4 µg/mL), GSH (0.1-2 mM), CDNB (1 mM) in a total volume of 200 µL of assay buffer (0.1 M KH_2PO_4/K_2HPO_4, 1 mM EDTA, pH 6.5). Change in absorbance was measure by Synergy H4 Hybrid Reader UV/Vis spectrophotometer (BioTek, VT) at 340 nm at 25 °C. The reaction was initiated by the addition of GST-P1. Data was collected at 11 second intervals with a lag time of 15 seconds for a total period of 3 min 40 sec.

For the HPLC analysis GST-P1 activity measured using recombinant human GST-P1 (160 nm) which was preincubated with DMSO, 50 µM, or 100 µM of KB-1-090 in an assay buffer (0.1 M KH_2PO_4/K_2HPO_4, 1 mM EDTA, pH = 6.5) for 5 min at room temperature. The reactions were initiated by the addition of 0.1-2 mM GSH and 1 mM CDNB and the samples were incubated for 0.5-2 min at 25°C. GST-P1 removed from the samples by the addition cold ACN with 50 µM p-nitrophenol followed by centrifugation at 14000 rpm and 4°C for 15 minutes. The supernatant was then removed and analyzed by HPLC-UV absorbance where the production of GS-DNB was measured. The data is represented as the initial enzyme rate (peak area/min) vs [GSH] and fit to nonlinear regression for competitive inhibition.

5.3 Determination of IC$_{50}$ and K$_I$

The IC$_{50}$ and K$_I$ values for all compounds were determined using the assay described above. For the determination of IC$_{50}$ values the reactions contained the inhibitor (1-100 μM), CDNB (1 mM), and GSH (1 mM). The reactions for the determination of K$_I$ contained the inhibitor (10, 25, 50 μM), CDNB (1 mM), and GSH (0.1-2 mM). GST-P1 was incubated with the inhibitor for 5 min. at 25°C prior to initiation of the reaction. All collected data was analyzed using GraphPad Prism. The IC$_{50}$ data was fit with the log[inhibitor] vs. normalized response nonlinear regression, and K$_I$ data was fit with the competitive inhibition nonlinear regression.

5.4 Photo-affinity labeling of GST-P1 and SHSY-5Y cell lysates

GST-P1 (10 μg/mL) was incubated with KB-1-013 (50 or 500 μM) in phosphate buffer (0.1 mM, 1 mM EDTA, pH 6.5) and this mixture was irradiated at 254 nm or 302 nm using a Ultra-Violet Products 3-UV-38 UV Lamp for various amounts of time ranging from 3-10 min at room temperature or on ice. The reaction was then quenched by the addition of TCEP (800 μM). Cys residues were then blocked by incubation with *N*-ethylmaleimide (NEM) (20 mM) for 1 hr at 30 °C. Prepared samples were then run on SDS-PAGE gel and the protein bands were stained with Coomasie Brilliant Blue. Finally, bands containing GST-P1 were excised, destained, and digested using trypsin or chymotrypsin according to the manufacturer's (Thermo, Pierce, IL) instructions.

For the intact proteomic analysis recombinant GST-P1 (10 µM) was incubated with DMSO or 50 µM of each photoprobe for five minutes at room temperature. Samples containing the azide probe (KB-1-013) were irradiated at 302 nm for four minutes at room temperature. Samples containing the diazirine probe were irradiation as 365 nm After photoirradiation, TCEP

(50 mM) and 0.1% formic acid was added to each sample and these samples were analyzed using a hybrid LTQ-FT linear ion trap mass spectrometer (LTQ-FT).

5.5 In-gel fluorescence imaging

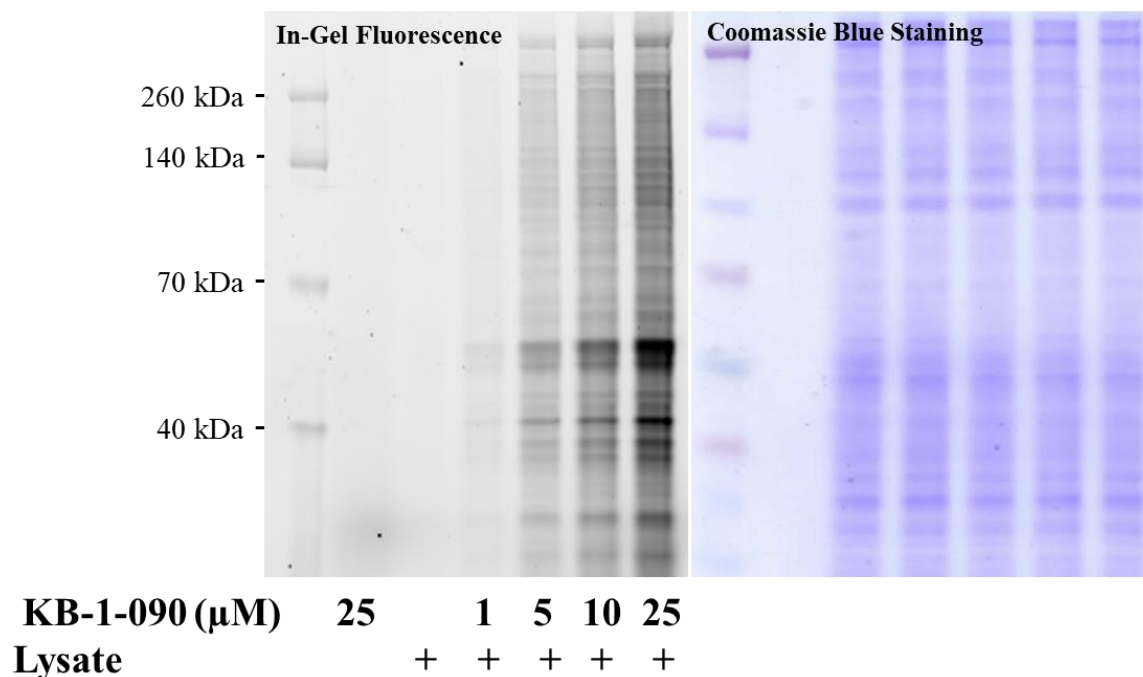GST-P1 (2 µg/µL) or SHSY-5Y cell lysates (1 µg/µL) was incubated with 1-100 µM KB-1-090 in 0.5 M sodium phosphate buffer (pH=7.4) for 5 minutes at room temperature before irradiating samples at 302 nm for 5 minutes. Additional experiments using SHSY-5Y cell lysates that were incubated with 5 µM KB-1-090 and 50 µM, 500 µM GSH or 50 µM KB-1-013. These samples were then separated by SDS-PAGE gel electrophoresis (30 µg protein/lane) and gel were immediately imaged using the GE Typhoon Trio imager (Ex/Em, 532/582 nm). The same gels were then stained with Coomasie Brilliant Blue and destained in order to measure the total amount of protein in each well.

5.6 Proteomic analysis

The digested recombinant protein samples were analyzed with an Agilent 6310 ion trap mass spectrometer (Agilent Technologies, Santa Clara, CA) coupled to Agilent 1100 series high-performance liquid chromatography (HPLC) system with electrospray ionization (ESI). The samples were separated using a Hypersil BSD reverse-phase C18 column (30 mm x 2.1 mm, 3 µm, Thermo Scientific) with a gradient of 90/10 (v/v) water/methanol, 0.1% formic acid and acetronitrile and 0.1% formic acid mobile phase at 300 µL/min flow rate. The positive mode ESI method was utilized for all of the LC-tandem mass spectrometry (MS/MS) analysis.

For the proteomic analysis of KB-1-013 treated SHSY-5Y cell lysates the protein digests with 1% formic acid were analyzed using the hybrid LTQ-FT linear ion trap mass spectrometer (LTQ FT, Thermo Electron Corp., Bremen, Germany) equipped with a nanospray ESI source and nano-HPLC with autosampler (Dionex, Sunnyvale, CA). The trapping cartridge and the

nano-column used for separation were Zorbax 300 SB-C18 (5 x 0.3 mm, 5 μm, Agilent Technologies) and Zorbax 300 SB-C18 (150 mm x 75 μm , 3.5 μm, Agilent Technologies), respectively. The separations were carried out at 250 nL/min flow rate at a gradient with the mobile phase containing 95/5 (v/v) water/acetonitrile, 0.1 % formic acid and 95/5 (v/v) acetonitrile/water, 0.1% formic acid. The RAW files from LTQ-FT-ICR mass spectrometer were converted to mzXML files and they were searched by the MassMatrix (http://www.massmatrix.net) search engine against the IPI human v3.65 database with KB-1-013 as the variable modification.

For the intact protein analysis recombinant GST-P1 (10 µM) was incubated with DMSO or 50 µM of each photoprobe for five minutes at room temperature. Samples containing the azide probe (KB-1-013) were irradiated at 302 nm for four minutes at room temperature. After photoirradiation, TCEP (50 mM) and 0.1% formic acid was added to each sample and these samples were analyzed using a hybrid LTQ-FT linear ion trap mass spectrometer (LTQ-FT).

REFERENCES

1. Oeppen, J.; Vaupel, J. W., Demography. Broken limits to life expectancy. *Science* **2002,** *296* (5570), 1029-31.

2. United Nations, D. o. E. a. S. A., Population Division (2017). World Population Prospects: The 2017 Revision, Key Findings and Advance Tables. ESA/P/WP/248.

3. Omran, A. R., The epidemiologic transition: a theory of the epidemiology of population change. 1971. *Milbank Q* **2005,** *83* (4), 731-57.

4. 2017 Alzheimer's disease facts and figures. *Alzheimer's & Dementia* **2017,** *13* (4), 325-373.

5. Skovronsky, D. M.; Lee, V. M.; Trojanowski, J. Q., Neurodegenerative diseases: new concepts of pathogenesis and their therapeutic implications. *Annu Rev Pathol* **2006,** *1*, 151-70.

6. Moller, H. J.; Graeber, M. B., The case described by Alois Alzheimer in 1911. Historical and conceptual perspectives based on the clinical record and neurohistological sections. *Eur Arch Psychiatry Clin Neurosci* **1998,** *248* (3), 111-22.

7. Soto, C., Unfolding the role of protein misfolding in neurodegenerative diseases. *Nat Rev Neurosci* **2003,** *4* (1), 49-60.

8. Martin, J. B., Molecular basis of the neurodegenerative disorders. *N Engl J Med* **1999,** *340* (25), 1970-80.

9. Hamilton, R. L., Lewy Bodies in Alzheimer's Disease: A Neuropathological Review of 145 Cases Using α-Synuclein Immunohistochemistry. *Brain Pathology* **2000,** *10* (3), 378-384.

10. Dickson, D. W., Neuropathology of Parkinson disease. *Parkinsonism Relat Disord* **2018,** *46 Suppl 1*, S30-S33.

11. Goedert, M., Alpha-synuclein and neurodegenerative diseases. *Nat Rev Neurosci* **2001,** *2* (7), 492-501.

12. Pratt, A. J.; Getzoff, E. D.; Perry, J. J., Amyotrophic lateral sclerosis: update and new developments. *Degener Neurol Neuromuscul Dis* **2012,** *2012* (2), 1-14.

13. Blokhuis, A. M.; Groen, E. J.; Koppers, M.; van den Berg, L. H.; Pasterkamp, R. J., Protein aggregation in amyotrophic lateral sclerosis. *Acta Neuropathol* **2013,** *125* (6), 777-94.

14.   Waldvogel, H. J.; Kim, E. H.; Tippett, L. J.; Vonsattel, J. P.; Faull, R. L., The Neuropathology of Huntington's Disease. *Curr Top Behav Neurosci* **2015,** *22*, 33-80.

15.   Gotz, J.; Ittner, L. M., Animal models of Alzheimer's disease and frontotemporal dementia. *Nat Rev Neurosci* **2008,** *9* (7), 532-44.

16.   Hsiao, K.; Chapman, P.; Nilsen, S.; Eckman, C.; Harigaya, Y.; Younkin, S.; Yang, F.; Cole, G., Correlative memory deficits, Abeta elevation, and amyloid plaques in transgenic mice. *Science* **1996,** *274* (5284), 99-102.

17.   Sturchler-Pierrat, C.; Abramowski, D.; Duke, M.; Wiederhold, K. H.; Mistl, C.; Rothacher, S.; Ledermann, B.; Burki, K.; Frey, P.; Paganetti, P. A.; Waridel, C.; Calhoun, M. E.; Jucker, M.; Probst, A.; Staufenbiel, M.; Sommer, B., Two amyloid precursor protein transgenic mouse models with Alzheimer disease-like pathology. *Proc Natl Acad Sci U S A* **1997,** *94* (24), 13287-92.

18.   Games, D.; Adams, D.; Alessandrini, R.; Barbour, R.; Berthelette, P.; Blackwell, C.; Carr, T.; Clemens, J.; Donaldson, T.; Gillespie, F.; et al., Alzheimer-type neuropathology in transgenic mice overexpressing V717F beta-amyloid precursor protein. *Nature* **1995,** *373* (6514), 523-7.

19.   Cheng, I. H.; Palop, J. J.; Esposito, L. A.; Bien-Ly, N.; Yan, F.; Mucke, L., Aggressive amyloidosis in mice expressing human amyloid peptides with the Arctic mutation. *Nat Med* **2004,** *10* (11), 1190-2.

20.   Mucke, L.; Masliah, E.; Yu, G. Q.; Mallory, M.; Rockenstein, E. M.; Tatsuno, G.; Hu, K.; Kholodenko, D.; Johnson-Wood, K.; McConlogue, L., High-level neuronal expression of abeta 1-42 in wild-type human amyloid protein precursor transgenic mice: synaptotoxicity without plaque formation. *J Neurosci* **2000,** *20* (11), 4050-8.

21.   Duff, K.; Eckman, C.; Zehr, C.; Yu, X.; Prada, C. M.; Perez-tur, J.; Hutton, M.; Buee, L.; Harigaya, Y.; Yager, D.; Morgan, D.; Gordon, M. N.; Holcomb, L.; Refolo, L.; Zenk, B.; Hardy, J.; Younkin, S., Increased amyloid-beta42(43) in brains of mice expressing mutant presenilin 1. *Nature* **1996,** *383* (6602), 710-3.

22.   Borchelt, D. R.; Thinakaran, G.; Eckman, C. B.; Lee, M. K.; Davenport, F.; Ratovitsky, T.; Prada, C. M.; Kim, G.; Seekins, S.; Yager, D.; Slunt, H. H.; Wang, R.; Seeger, M.; Levey, A. I.; Gandy, S. E.; Copeland, N. G.; Jenkins, N. A.; Price, D. L.; Younkin, S. G.; Sisodia, S. S., Familial Alzheimer's disease-linked presenilin 1 variants elevate Abeta1-42/1-40 ratio in vitro and in vivo. *Neuron* **1996,** *17* (5), 1005-13.

23. Casas, C.; Sergeant, N.; Itier, J. M.; Blanchard, V.; Wirths, O.; van der Kolk, N.; Vingtdeux, V.; van de Steeg, E.; Ret, G.; Canton, T.; Drobecq, H.; Clark, A.; Bonici, B.; Delacourte, A.; Benavides, J.; Schmitz, C.; Tremp, G.; Bayer, T. A.; Benoit, P.; Pradier, L., Massive CA1/2 neuronal loss with intraneuronal and N-terminal truncated Abeta42 accumulation in a novel Alzheimer transgenic model. *Am J Pathol* **2004,** *165* (4), 1289-300.

24. Gotz, J.; Probst, A.; Spillantini, M. G.; Schafer, T.; Jakes, R.; Burki, K.; Goedert, M., Somatodendritic localization and hyperphosphorylation of tau protein in transgenic mice expressing the longest human brain tau isoform. *EMBO J* **1995,** *14* (7), 1304-13.

25. Probst, A.; Gotz, J.; Wiederhold, K. H.; Tolnay, M.; Mistl, C.; Jaton, A. L.; Hong, M.; Ishihara, T.; Lee, V. M.; Trojanowski, J. Q.; Jakes, R.; Crowther, R. A.; Spillantini, M. G.; Burki, K.; Goedert, M., Axonopathy and amyotrophy in mice transgenic for human four-repeat tau protein. *Acta Neuropathol* **2000,** *99* (5), 469-81.

26. Lewis, J.; McGowan, E.; Rockwood, J.; Melrose, H.; Nacharaju, P.; Van Slegtenhorst, M.; Gwinn-Hardy, K.; Paul Murphy, M.; Baker, M.; Yu, X.; Duff, K.; Hardy, J.; Corral, A.; Lin, W. L.; Yen, S. H.; Dickson, D. W.; Davies, P.; Hutton, M., Neurofibrillary tangles, amyotrophy and progressive motor disturbance in mice expressing mutant (P301L) tau protein. *Nat Genet* **2000,** *25* (4), 402-5.

27. Dawson, H. N.; Cantillana, V.; Chen, L.; Vitek, M. P., The tau N279K exon 10 splicing mutation recapitulates frontotemporal dementia and parkinsonism linked to chromosome 17 tauopathy in a mouse model. *J Neurosci* **2007,** *27* (34), 9155-68.

28. Allen, B.; Ingram, E.; Takao, M.; Smith, M. J.; Jakes, R.; Virdee, K.; Yoshida, H.; Holzer, M.; Craxton, M.; Emson, P. C.; Atzori, C.; Migheli, A.; Crowther, R. A.; Ghetti, B.; Spillantini, M. G.; Goedert, M., Abundant tau filaments and nonapoptotic neurodegeneration in transgenic mice expressing human P301S tau protein. *J Neurosci* **2002,** *22* (21), 9340-51.

29. Yoshiyama, Y.; Higuchi, M.; Zhang, B.; Huang, S. M.; Iwata, N.; Saido, T. C.; Maeda, J.; Suhara, T.; Trojanowski, J. Q.; Lee, V. M., Synapse loss and microglial activation precede tangles in a P301S tauopathy mouse model. *Neuron* **2007,** *53* (3), 337-51.

30. Oddo, S.; Caccamo, A.; Shepherd, J. D.; Murphy, M. P.; Golde, T. E.; Kayed, R.; Metherate, R.; Mattson, M. P.; Akbari, Y.; LaFerla, F. M., Triple-transgenic model of Alzheimer's disease with plaques and tangles: intracellular Abeta and synaptic dysfunction. *Neuron* **2003,** *39* (3), 409-21.

31. Bertram, L.; Lill, C. M.; Tanzi, R. E., The genetics of Alzheimer disease: back to the future. *Neuron* **2010,** *68* (2), 270-81.

32.   Dodart, J. C.; Marr, R. A.; Koistinaho, M.; Gregersen, B. M.; Malkani, S.; Verma, I. M.; Paul, S. M., Gene delivery of human apolipoprotein E alters brain Abeta burden in a mouse model of Alzheimer's disease. *Proc Natl Acad Sci U S A* **2005,** *102* (4), 1211-6.

33.   D'Souza, Y.; Elharram, A.; Soon-Shiong, R.; Andrew, R. D.; Bennett, B. M., Characterization of Aldh2 (-/-) mice as an age-related model of cognitive impairment and Alzheimer's disease. *Mol Brain* **2015,** *8*, 27.

34.   Hao, P. P.; Chen, Y. G.; Wang, J. L.; Wang, X. L.; Zhang, Y., Meta-analysis of aldehyde dehydrogenase 2 gene polymorphism and Alzheimer's disease in East Asians. *Can J Neurol Sci* **2011,** *38* (3), 500-6.

35.   Ohsawa, I.; Nishimaki, K.; Murakami, Y.; Suzuki, Y.; Ishikawa, M.; Ohta, S., Age-dependent neurodegeneration accompanying memory loss in transgenic mice defective in mitochondrial aldehyde dehydrogenase 2 activity. *J Neurosci* **2008,** *28* (24), 6239-49.

36.   Sies, H., *Oxidative stress*. Orlando : Academic Press: London, 1985; p xv, 507 p.

37.   Floyd, R. A.; Carney, J. M., Free radical damage to protein and DNA: mechanisms involved and relevant observations on brain undergoing oxidative stress. *Ann Neurol* **1992,** *32 Suppl*, S22-7.

38.   Halliwell, B., Oxidative stress and neurodegeneration: where are we now? *J Neurochem* **2006,** *97* (6), 1634-58.

39.   Pratico, D., Oxidative stress hypothesis in Alzheimer's disease: a reappraisal. *Trends Pharmacol Sci* **2008,** *29* (12), 609-15.

40.   Slemmer, J. E.; Shacka, J. J.; Sweeney, M. I.; Weber, J. T., Antioxidants and free radical scavengers for the treatment of stroke, traumatic brain injury and aging. *Curr Med Chem* **2008,** *15* (4), 404-14.

41.   Boveris, A.; Oshino, N.; Chance, B., The cellular production of hydrogen peroxide. *Biochem J* **1972,** *128* (3), 617-30.

42.   Sies, H.; Berndt, C.; Jones, D. P., Oxidative Stress. *Annu Rev Biochem* **2017,** *86*, 715-748.

43.   Turrens, J. F., Mitochondrial formation of reactive oxygen species. *J Physiol* **2003,** *552* (Pt 2), 335-44.

44.   Lloyd, R. V.; Hanna, P. M.; Mason, R. P., The origin of the hydroxyl radical oxygen in the Fenton reaction. *Free Radic Biol Med* **1997,** *22* (5), 885-8.

45.   De Bont, R.; van Larebeke, N., Endogenous DNA damage in humans: a review of quantitative data. *Mutagenesis* **2004,** *19* (3), 169-85.

46.   Mecocci, P.; MacGarvey, U.; Beal, M. F., Oxidative damage to mitochondrial DNA is increased in Alzheimer's disease. *Ann Neurol* **1994,** *36* (5), 747-51.

47.   Sies, H., Biochemistry of Oxidative Stress. *Angewandte Chemie International Edition in English* **1986,** *25* (12), 1058-1071.

48.   Davies, M. J., Protein oxidation and peroxidation. *Biochem J* **2016,** *473* (7), 805-25.

49.   Aksenov, M. Y.; Aksenova, M. V.; Butterfield, D. A.; Geddes, J. W.; Markesbery, W. R., Protein oxidation in the brain in Alzheimer's disease. *Neuroscience* **2001,** *103* (2), 373-83.

50.   Comporti, M., Lipid peroxidation and biogenic aldehydes: from the identification of 4-hydroxynonenal to further achievements in biopathology. *Free Radic Res* **1998,** *28* (6), 623-35.

51.   Jones, D. P., Redefining oxidative stress. *Antioxid Redox Signal* **2006,** *8* (9-10), 1865-79.

52.   Pisoschi, A. M.; Pop, A., The role of antioxidants in the chemistry of oxidative stress: A review. *Eur J Med Chem* **2015,** *97*, 55-74.

53.   Esterbauer, H.; Schaur, R. J.; Zollner, H., Chemistry and biochemistry of 4-hydroxynonenal, malonaldehyde and related aldehydes. *Free Radical Biology and Medicine* **1991,** *11* (1), 81-128.

54.   Schaur, R. J., Basic aspects of the biochemical reactivity of 4-hydroxynonenal. *Molecular Aspects of Medicine* **2003,** *24* (4–5), 149-159.

55.   Ayala, A.; Mu; #xf1; oz, M. F.; Arg; #xfc; elles, S., Lipid Peroxidation: Production, Metabolism, and Signaling Mechanisms of Malondialdehyde and 4-Hydroxy-2-Nonenal. *Oxidative Medicine and Cellular Longevity* **2014,** *2014*, 31.

56.   Lin, M.-H.; Yen, J.-H.; Weng, C.-Y.; Wang, L.; Ha, C.-L.; Wu, M.-J., Lipid peroxidation end product 4-hydroxy-trans-2-nonenal triggers unfolded protein response and heme oxygenase-1 expression in PC12 cells: Roles of ROS and MAPK pathways. *Toxicology* **2014,** *315*, 24-37.

57.   West, J. D.; Marnett, L. J., Alterations in Gene Expression Induced by the Lipid Peroxidation Product, 4-Hydroxy-2-nonenal. *Chemical Research in Toxicology* **2005,** *18* (11), 1642-1653.

58.   Huang, Y.; Li, W.; Kong, A.-N. T., Anti-oxidative stress regulator NF-E2-related factor 2 mediates the adaptive induction of antioxidant and detoxifying enzymes by lipid peroxidation metabolite 4-hydroxynonenal. *Cell & Bioscience* **2012,** *2* (1), 40.

59. Markesbery, W. R.; Carney, J. M., Oxidative alterations in Alzheimer's disease. *Brain Pathol* **1999,** *9* (1), 133-46.

60. Mattson, M. P.; Fu, W.; Waeg, G.; Uchida, K., 4-Hydroxynonenal, a product of lipid peroxidation, inhibits dephosphorylation of the microtubule-associated protein tau. *NeuroReport* **1997,** *8* (9), 2275-2281.

61. Bae, E.-J.; Ho, D.-H.; Park, E.; Jung, J. W.; Cho, K.; Hong, J. H.; Lee, H.-J.; Kim, K. P.; Lee, S.-J., Lipid Peroxidation Product 4-Hydroxy-2-Nonenal Promotes Seeding-Capable Oligomer Formation and Cell-to-Cell Transfer of α-Synuclein. *Antioxidants & Redox Signaling* **2013,** *18* (7), 770-783.

62. Siegel, S. J.; Bieschke, J.; Powers, E. T.; Kelly, J. W., The Oxidative Stress Metabolite 4-Hydroxynonenal Promotes Alzheimer Protofibril Formation. *Biochemistry* **2007,** *46* (6), 1503-1510.

63. Nunomura, A.; Perry, G.; Aliev, G.; Hirai, K.; Takeda, A.; Balraj, E. K.; Jones, P. K.; Ghanbari, H.; Wataya, T.; Shimohama, S.; Chiba, S.; Atwood, C. S.; Petersen, R. B.; Smith, M. A., Oxidative damage is the earliest event in Alzheimer disease. *J Neuropathol Exp Neurol* **2001,** *60* (8), 759-67.

64. Nunomura, A.; Perry, G.; Aliev, G.; Hirai, K.; Takeda, A.; Balraj, E. K.; Jones, P. K.; Ghanbari, H.; Wataya, T.; Shimohama, S.; Chiba, S.; Atwood, C. S.; Petersen, R. B.; Smith, M. A., Oxidative damage is the earliest event in Alzheimer disease. *Journal of neuropathology and experimental neurology* **2001,** *60* (8), 759-767.

65. Markesbery, W. R.; Lovell, M. A., Four-hydroxynonenal, a product of lipid peroxidation, is increased in the brain in Alzheimer's disease. *Neurobiol Aging* **1998,** *19* (1), 33-6.

66. Lovell, M. A.; Ehmann, W. D.; Mattson, M. P.; Markesbery, W. R., Elevated 4-hydroxynonenal in ventricular fluid in Alzheimer's disease. *Neurobiol Aging* **1997,** *18* (5), 457-61.

67. Girotti, A. W., Lipid hydroperoxide generation, turnover, and effector action in biological systems. *J Lipid Res* **1998,** *39* (8), 1529-42.

68. Massey, K. A.; Nicolaou, A., Lipidomics of oxidized polyunsaturated fatty acids. *Free Radic Biol Med* **2013,** *59*, 45-55.

69. Ayala, A.; Munoz, M. F.; Arguelles, S., Lipid peroxidation: production, metabolism, and signaling mechanisms of malondialdehyde and 4-hydroxy-2-nonenal. *Oxid Med Cell Longev* **2014,** *2014*, 360438.

70. Esterbauer, H., Cytotoxicity and genotoxicity of lipid-oxidation products. *Am J Clin Nutr* **1993,** *57* (5 Suppl), 779S-785S; discussion 785S-786S.

71. Pryor, W. A.; Porter, N. A., Suggested mechanisms for the production of 4-hydroxy-2-nonenal from the autoxidation of polyunsaturated fatty acids. *Free Radic Biol Med* **1990,** *8* (6), 541-3.

72. Guéraud, F.; Atalay, M.; Bresgen, N.; Cipak, A.; Eckl, P. M.; Huc, L.; Jouanin, I.; Siems, W.; Uchida, K., Chemistry and biochemistry of lipid peroxidation products. *Free Radical Research* **2010,** *44* (10), 1098-1124.

73. Esterbauer, H.; Schaur, R. J.; Zollner, H., Chemistry and biochemistry of 4-hydroxynonenal, malonaldehyde and related aldehydes. *Free Radic Biol Med* **1991,** *11* (1), 81-128.

74. Hecker, M.; Ullrich, V., On the mechanism of prostacyclin and thromboxane A2 biosynthesis. *J Biol Chem* **1989,** *264* (1), 141-50.

75. Barrera, G., Oxidative stress and lipid peroxidation products in cancer progression and therapy. *ISRN Oncol* **2012,** *2012*, 137289.

76. Pizzimenti, S.; Toaldo, C.; Pettazzoni, P.; Dianzani, M. U.; Barrera, G., The "two-faced" effects of reactive oxygen species and the lipid peroxidation product 4-hydroxynonenal in the hallmarks of cancer. *Cancers (Basel)* **2010,** *2* (2), 338-63.

77. Kuiper, H. C.; Miranda, C. L.; Sowell, J. D.; Stevens, J. F., Mercapturic acid conjugates of 4-hydroxy-2-nonenal and 4-oxo-2-nonenal metabolites are in vivo markers of oxidative stress. *J Biol Chem* **2008,** *283* (25), 17131-8.

78. Petersen, D. R.; Doorn, J. A., Reactions of 4-hydroxynonenal with proteins and cellular targets. *Free Radic Biol Med* **2004,** *37* (7), 937-45.

79. Marnett, L. J., Oxy radicals, lipid peroxidation and DNA damage. *Toxicology* **2002,** *181-182*, 219-22.

80. Voulgaridou, G. P.; Anestopoulos, I.; Franco, R.; Panayiotidis, M. I.; Pappa, A., DNA damage induced by endogenous aldehydes: current state of knowledge. *Mutat Res* **2011,** *711* (1-2), 13-27.

81. Feng, Z.; Hu, W.; Hu, Y.; Tang, M. S., Acrolein is a major cigarette-related lung cancer agent: Preferential binding at p53 mutational hotspots and inhibition of DNA repair. *Proc Natl Acad Sci U S A* **2006,** *103* (42), 15404-9.

82. Maddukuri, L.; Eoff, R. L.; Choi, J. Y.; Rizzo, C. J.; Guengerich, F. P.; Marnett, L. J., In vitro bypass of the major malondialdehyde- and base propenal-derived DNA adduct by human Y-family DNA polymerases kappa, iota, and Rev1. *Biochemistry* **2010,** *49* (38), 8415-24.

83.   Minko, I. G.; Kozekov, I. D.; Harris, T. M.; Rizzo, C. J.; Lloyd, R. S.; Stone, M. P., Chemistry and biology of DNA containing 1,N(2)-deoxyguanosine adducts of the alpha,beta-unsaturated aldehydes acrolein, crotonaldehyde, and 4-hydroxynonenal. *Chem Res Toxicol* **2009,** *22* (5), 759-78.

84.   Chou, P. H.; Kageyama, S.; Matsuda, S.; Kanemoto, K.; Sasada, Y.; Oka, M.; Shinmura, K.; Mori, H.; Kawai, K.; Kasai, H.; Sugimura, H.; Matsuda, T., Detection of lipid peroxidation-induced DNA adducts caused by 4-oxo-2(E)-nonenal and 4-oxo-2(E)-hexenal in human autopsy tissues. *Chem Res Toxicol* **2010,** *23* (9), 1442-8.

85.   LoPachin, R. M.; Barber, D. S.; Gavin, T., Molecular mechanisms of the conjugated alpha,beta-unsaturated carbonyl derivatives: relevance to neurotoxicity and neurodegenerative diseases. *Toxicol Sci* **2008,** *104* (2), 235-49.

86.   Sayre, L. M.; Lin, D.; Yuan, Q.; Zhu, X.; Tang, X., Protein adducts generated from products of lipid oxidation: focus on HNE and one. *Drug Metab Rev* **2006,** *38* (4), 651-75.

87.   Esterbauer, H.; Cheeseman, K. H., Determination of aldehydic lipid peroxidation products: malonaldehyde and 4-hydroxynonenal. *Methods Enzymol* **1990,** *186*, 407-21.

88.   Vidal, N.; Cavaille, J. P.; Graziani, F.; Robin, M.; Ouari, O.; Pietri, S.; Stocker, P., High throughput assay for evaluation of reactive carbonyl scavenging capacity. *Redox Biol* **2014,** *2*, 590-8.

89.   Yan, L. J.; Forster, M. J., Chemical probes for analysis of carbonylated proteins: a review. *J Chromatogr B Analyt Technol Biomed Life Sci* **2011,** *879* (17-18), 1308-15.

90.   Di Domenico, F.; Pupo, G.; Tramutola, A.; Giorgi, A.; Schinina, M. E.; Coccia, R.; Head, E.; Butterfield, D. A.; Perluigi, M., Redox proteomics analysis of HNE-modified proteins in Down syndrome brain: clues for understanding the development of Alzheimer disease. *Free Radic Biol Med* **2014,** *71*, 270-80.

91.   Spickett, C. M., The lipid peroxidation product 4-hydroxy-2-nonenal: Advances in chemistry and analysis. *Redox Biol* **2013,** *1*, 145-52.

92.   Galligan, J. J.; Smathers, R. L.; Fritz, K. S.; Epperson, L. E.; Hunter, L. E.; Petersen, D. R., Protein carbonylation in a murine model for early alcoholic liver disease. *Chem Res Toxicol* **2012,** *25* (5), 1012-21.

93.   Han, B.; Hare, M.; Wickramasekara, S.; Fang, Y.; Maier, C. S., A comparative 'bottom up' proteomics strategy for the site-specific identification and quantification of protein modifications by electrophilic lipids. *J Proteomics* **2012,** *75* (18), 5724-33.

94.   Roe, M. R.; Xie, H.; Bandhakavi, S.; Griffin, T. J., Proteomic mapping of 4-hydroxynonenal protein modification sites by solid-phase hydrazide chemistry and mass spectrometry. *Anal Chem* **2007,** *79* (10), 3747-56.

95.   Vila, A.; Tallman, K. A.; Jacobs, A. T.; Liebler, D. C.; Porter, N. A.; Marnett, L. J., Identification of protein targets of 4-hydroxynonenal using click chemistry for ex vivo biotinylation of azido and alkynyl derivatives. *Chem Res Toxicol* **2008,** *21* (2), 432-44.

96.   Kim, H. Y.; Tallman, K. A.; Liebler, D. C.; Porter, N. A., An azido-biotin reagent for use in the isolation of protein adducts of lipid-derived electrophiles by streptavidin catch and photorelease. *Mol Cell Proteomics* **2009,** *8* (9), 2080-9.

97.   Codreanu, S. G.; Ullery, J. C.; Zhu, J.; Tallman, K. A.; Beavers, W. N.; Porter, N. A.; Marnett, L. J.; Zhang, B.; Liebler, D. C., Alkylation damage by lipid electrophiles targets functional protein systems. *Mol Cell Proteomics* **2014,** *13* (3), 849-59.

98.   Tzeng, S. C.; Maier, C. S., Label-Free Proteomics Assisted by Affinity Enrichment for Elucidating the Chemical Reactivity of the Liver Mitochondrial Proteome toward Adduction by the Lipid Electrophile 4-hydroxy-2-nonenal (HNE). *Front Chem* **2016,** *4*, 2.

99.   Reed, T. T.; Pierce, W. M.; Markesbery, W. R.; Butterfield, D. A., Proteomic identification of HNE-bound proteins in early Alzheimer disease: Insights into the role of lipid peroxidation in the progression of AD. *Brain Res* **2009,** *1274*, 66-76.

100.   Bevins, R. A.; Besheer, J., Object recognition in rats and mice: a one-trial non-matching-to-sample learning task to study 'recognition memory'. *Nat Protoc* **2006,** *1* (3), 1306-11.

101.   Antunes, M.; Biala, G., The novel object recognition memory: neurobiology, test procedure, and its modifications. *Cogn Process* **2012,** *13* (2), 93-110.

102.   Lin, D.; Lee, H. G.; Liu, Q.; Perry, G.; Smith, M. A.; Sayre, L. M., 4-Oxo-2-nonenal is both more neurotoxic and more protein reactive than 4-hydroxy-2-nonenal. *Chem Res Toxicol* **2005,** *18* (8), 1219-31.

103.   Doorn, J. A.; Hurley, T. D.; Petersen, D. R., Inhibition of human mitochondrial aldehyde dehydrogenase by 4-hydroxynon-2-enal and 4-oxonon-2-enal. *Chem Res Toxicol* **2006,** *19* (1), 102-10.

104.   Mitchell, D. Y.; Petersen, D. R., Inhibition of rat hepatic mitochondrial aldehyde dehydrogenase-mediated acetaldehyde oxidation by trans-4-hydroxy-2-nonenal. *Hepatology* **1991,** *13* (4), 728-34.

105.   Doorn, J. A.; Petersen, D. R., Covalent modification of amino acid nucleophiles by the lipid peroxidation products 4-hydroxy-2-nonenal and 4-oxo-2-nonenal. *Chem Res Toxicol* **2002,** *15* (11), 1445-50.

106. Mannervik, B.; Danielson, U. H., Glutathione transferases--structure and catalytic activity. *CRC Crit Rev Biochem* **1988,** *23* (3), 283-337.

107. Kano, T.; Sakai, M.; Muramatsu, M., Structure and expression of a human class pi glutathione S-transferase messenger RNA. *Cancer Res* **1987,** *47* (21), 5626-30.

108. Wang, Y.-T. T.; Piyankarage, S. C.; Williams, D. L.; Thatcher, G. R., Proteomic profiling of nitrosative stress: protein S-oxidation accompanies S-nitrosylation. *ACS chemical biology* **2014,** *9* (3), 821-830.

109. Dunlap, T.; Piyankarage, S. C.; Wijewickrama, G. T.; Abdul-Hay, S.; Vanni, M.; Litosh, V.; Luo, J.; Thatcher, G. R., Quinone-induced activation of Keap1/Nrf2 signaling by aspirin prodrugs masquerading as nitric oxide. *Chem Res Toxicol* **2012,** *25* (12), 2725-36.

110. Sinha, V.; Wijewickrama, G. T.; Chandrasena, R. E.; Xu, H.; Edirisinghe, P. D.; Schiefer, I. T.; Thatcher, G. R., Proteomic and mass spectroscopic quantitation of protein S-nitrosation differentiates NO-donors. *ACS Chem Biol* **2010,** *5* (7), 667-80.

111. Chang, M.; Shin, Y. G.; van Breemen, R. B.; Blond, S. Y.; Bolton, J. L., Structural and functional consequences of inactivation of human glutathione S-transferase P1-1 mediated by the catechol metabolite of equine estrogens, 4-hydroxyequilenin. *Biochemistry* **2001,** *40* (15), 4811-20.

112. Schaur, R. J.; Siems, W.; Bresgen, N.; Eckl, P. M., 4-Hydroxy-nonenal-A Bioactive Lipid Peroxidation Product. *Biomolecules* **2015,** *5* (4), 2247-337.

113. Speers, A. E.; Cravatt, B. F., Profiling enzyme activities in vivo using click chemistry methods. *Chem Biol* **2004,** *11* (4), 535-46.

114. Chan, T. R.; Hilgraf, R.; Sharpless, K. B.; Fokin, V. V., Polytriazoles as copper(I)-stabilizing ligands in catalysis. *Org Lett* **2004,** *6* (17), 2853-5.

115. Lu, P. J.; Wulf, G.; Zhou, X. Z.; Davies, P.; Lu, K. P., The prolyl isomerase Pin1 restores the function of Alzheimer-associated phosphorylated tau protein. *Nature* **1999,** *399* (6738), 784-8.

116. Butterfield, D. A.; Abdul, H. M.; Opii, W.; Newman, S. F.; Joshi, G.; Ansari, M. A.; Sultana, R., Pin1 in Alzheimer's disease. *J Neurochem* **2006,** *98* (6), 1697-706.

117. Liou, Y. C.; Sun, A.; Ryo, A.; Zhou, X. Z.; Yu, Z. X.; Huang, H. K.; Uchida, T.; Bronson, R.; Bing, G.; Li, X.; Hunter, T.; Lu, K. P., Role of the prolyl isomerase Pin1 in protecting against age-dependent neurodegeneration. *Nature* **2003,** *424* (6948), 556-61.

118. Pastorino, L.; Sun, A.; Lu, P. J.; Zhou, X. Z.; Balastik, M.; Finn, G.; Wulf, G.; Lim, J.; Li, S. H.; Li, X.; Xia, W.; Nicholson, L. K.; Lu, K. P., The prolyl isomerase Pin1 regulates amyloid precursor protein processing and amyloid-beta production. *Nature* **2006,** *440* (7083), 528-34.

119. Aluise, C. D.; Rose, K.; Boiani, M.; Reyzer, M. L.; Manna, J. D.; Tallman, K.; Porter, N. A.; Marnett, L. J., Peptidyl-prolyl cis/trans-isomerase A1 (Pin1) is a target for modification by lipid electrophiles. *Chem Res Toxicol* **2013,** *26* (2), 270-9.

120. Aluise, C. D.; Camarillo, J. M.; Shimozu, Y.; Galligan, J. J.; Rose, K. L.; Tallman, K. A.; Marnett, L. J., Site-specific, intramolecular cross-linking of Pin1 active site residues by the lipid electrophile 4-oxo-2-nonenal. *Chem Res Toxicol* **2015,** *28* (4), 817-27.

121. Oe, T.; Arora, J. S.; Lee, S. H.; Blair, I. A., A novel lipid hydroperoxide-derived cyclic covalent modification to histone H4. *J Biol Chem* **2003,** *278* (43), 42098-105.

122. Ashburner, M.; Ball, C. A.; Blake, J. A.; Botstein, D.; Butler, H.; Cherry, J. M.; Davis, A. P.; Dolinski, K.; Dwight, S. S.; Eppig, J. T.; Harris, M. A.; Hill, D. P.; Issel-Tarver, L.; Kasarskis, A.; Lewis, S.; Matese, J. C.; Richardson, J. E.; Ringwald, M.; Rubin, G. M.; Sherlock, G., Gene ontology: tool for the unification of biology. The Gene Ontology Consortium. *Nat Genet* **2000,** *25* (1), 25-9.

123. Karch, K. R.; Sidoli, S.; Garcia, B. A., Identification and Quantification of Histone PTMs Using High-Resolution Mass Spectrometry. *Methods Enzymol* **2016,** *574*, 3-29.

124. Burcham, P. C.; Kaminskas, L. M.; Fontaine, F. R.; Petersen, D. R.; Pyke, S. M., Aldehyde-sequestering drugs: tools for studying protein damage by lipid peroxidation products. *Toxicology* **2002,** *181-182*, 229-36.

125. Dickinson, D. A.; Forman, H. J., Glutathione in defense and signaling: lessons from a small thiol. *Ann N Y Acad Sci* **2002,** *973*, 488-504.

126. Hartley, D. P.; Ruth, J. A.; Petersen, D. R., The hepatocellular metabolism of 4-hydroxynonenal by alcohol dehydrogenase, aldehyde dehydrogenase, and glutathione S-transferase. *Arch Biochem Biophys* **1995,** *316* (1), 197-205.

127. Esterbauer, H.; Zollner, H.; Scholz, N., Reaction of glutathione with conjugated carbonyls. *Z Naturforsch C* **1975,** *30* (4), 466-73.

128. Alin, P.; Danielson, U. H.; Mannervik, B., 4-Hydroxyalk-2-enals are substrates for glutathione transferase. *FEBS Lett* **1985,** *179* (2), 267-70.

129. Hubatsch, I.; Ridderstrom, M.; Mannervik, B., Human glutathione transferase A4-4: an alpha class enzyme with high catalytic efficiency in the conjugation of 4-hydroxynonenal and other genotoxic products of lipid peroxidation. *Biochem J* **1998,** *330 (Pt 1)*, 175-9.

130. Tjalkens, R. B.; Luckey, S. W.; Kroll, D. J.; Petersen, D. R., Alpha,beta-unsaturated aldehydes increase glutathione S-transferase mRNA and protein: correlation with activation of the antioxidant response element. *Arch Biochem Biophys* **1998,** *359* (1), 42-50.

131. Raza, H.; John, A., 4-hydroxynonenal induces mitochondrial oxidative stress, apoptosis and expression of glutathione S-transferase A4-4 and cytochrome P450 2E1 in PC12 cells. *Toxicol Appl Pharmacol* **2006,** *216* (2), 309-18.

132. Yang, Y.; Yang, Y.; Trent, M. B.; He, N.; Lick, S. D.; Zimniak, P.; Awasthi, Y. C.; Boor, P. J., Glutathione-S-transferase A4-4 modulates oxidative stress in endothelium: possible role in human atherosclerosis. *Atherosclerosis* **2004,** *173* (2), 211-21.

133. Atkuri, K. R.; Mantovani, J. J.; Herzenberg, L. A.; Herzenberg, L. A., N-Acetylcysteine--a safe antidote for cysteine/glutathione deficiency. *Curr Opin Pharmacol* **2007,** *7* (4), 355-9.

134. Terneus, M. V.; Brown, J. M.; Carpenter, A. B.; Valentovic, M. A., Comparison of S-adenosyl-L-methionine (SAMe) and N-acetylcysteine (NAC) protective effects on hepatic damage when administered after acetaminophen overdose. *Toxicology* **2008,** *244* (1), 25-34.

135. Sinha-Hikim, I.; Shen, R.; Paul Lee, W. N.; Crum, A.; Vaziri, N. D.; Norris, K. C., Effects of a novel cystine-based glutathione precursor on oxidative stress in vascular smooth muscle cells. *Am J Physiol Cell Physiol* **2010,** *299* (3), C638-42.

136. Chandramani Shivalingappa, P.; Jin, H.; Anantharam, V.; Kanthasamy, A.; Kanthasamy, A., N-Acetyl Cysteine Protects against Methamphetamine-Induced Dopaminergic Neurodegeneration via Modulation of Redox Status and Autophagy in Dopaminergic Cells. *Parkinsons Dis* **2012,** *2012*, 424285.

137. de Senzi Moraes Pinto, R.; Ferretti, R.; Moraes, L. H.; Neto, H. S.; Marques, M. J.; Minatel, E., N-acetylcysteine treatment reduces TNF-alpha levels and myonecrosis in diaphragm muscle of mdx mice. *Clin Nutr* **2013,** *32* (3), 472-5.

138. Horinishi, H.; Grillo, M.; Margolis, F. L., Purification and characterization of carnosine synthetase from mouse olfactory bulbs. *J Neurochem* **1978,** *31* (4), 909-19.

139. Hipkiss, A. R.; Preston, J. E.; Himswoth, D. T.; Worthington, V. C.; Abbot, N. J., Protective effects of carnosine against malondialdehyde-induced toxicity towards cultured rat brain endothelial cells. *Neurosci Lett* **1997,** *238* (3), 135-8.

140. Guiotto, A.; Ruzza, P.; Babizhayev, M. A.; Calderan, A., Malondialdehyde scavenging and aldose-derived Schiff bases' transglycation properties of synthetic histidyl-hydrazide carnosine analogs. *Bioorg Med Chem* **2007,** *15* (18), 6158-63.

141. Hipkiss, A. R.; Worthington, V. C.; Himsworth, D. T.; Herwig, W., Protective effects of carnosine against protein modification mediated by malondialdehyde and hypochlorite. *Biochimica et biophysica acta* **1998,** *1380* (1), 46-54.

142. Carini, M.; Aldini, G.; Beretta, G.; Arlandini, E.; Facino, R. M., Acrolein-sequestering ability of endogenous dipeptides: characterization of carnosine and homocarnosine/acrolein adducts by electrospray ionization tandem mass spectrometry. *J Mass Spectrom* **2003,** *38* (9), 996-1006.

143. Bispo, V. S.; de Arruda Campos, I. P.; Di Mascio, P.; Medeiros, M. H., Structural Elucidation of a Carnosine-Acrolein Adduct and its Quantification in Human Urine Samples. *Sci Rep* **2016,** *6*, 19348.

144. Liu, Y.; Xu, G.; Sayre, L. M., Carnosine inhibits (E)-4-hydroxy-2-nonenal-induced protein cross-linking: structural characterization of carnosine-HNE adducts. *Chem Res Toxicol* **2003,** *16* (12), 1589-97.

145. Zhu, X.; Gallogly, M. M.; Mieyal, J. J.; Anderson, V. E.; Sayre, L. M., Covalent cross-linking of glutathione and carnosine to proteins by 4-oxo-2-nonenal. *Chem Res Toxicol* **2009,** *22* (6), 1050-9.

146. Guiotto, A.; Calderan, A.; Ruzza, P.; Osler, A.; Rubini, C.; Jo, D. G.; Mattson, M. P.; Borin, G., Synthesis and evaluation of neuroprotective alpha,beta-unsaturated aldehyde scavenger histidyl-containing analogues of carnosine. *J Med Chem* **2005,** *48* (19), 6156-61.

147. Aldini, G.; Carini, M.; Beretta, G.; Bradamante, S.; Facino, R. M., Carnosine is a quencher of 4-hydroxy-nonenal: through what mechanism of reaction? *Biochem Biophys Res Commun* **2002,** *298* (5), 699-706.

148. Aldini, G.; Granata, P.; Carini, M., Detoxification of cytotoxic alpha,beta-unsaturated aldehydes by carnosine: characterization of conjugated adducts by electrospray ionization tandem mass spectrometry and detection by liquid chromatography/mass spectrometry in rat skeletal muscle. *J Mass Spectrom* **2002,** *37* (12), 1219-28.

149. Tang, S. C.; Arumugam, T. V.; Cutler, R. G.; Jo, D. G.; Magnus, T.; Chan, S. L.; Mughal, M. R.; Telljohann, R. S.; Nassar, M.; Ouyang, X.; Calderan, A.; Ruzza, P.; Guiotto, A.; Mattson, M. P., Neuroprotective actions of a histidine analogue in models of ischemic stroke. *J Neurochem* **2007,** *101* (3), 729-36.

150. Burcham, P. C.; Pyke, S. M., Hydralazine inhibits rapid acrolein-induced protein oligomerization: role of aldehyde scavenging and adduct trapping in cross-link blocking and cytoprotection. *Mol Pharmacol* **2006,** *69* (3), 1056-65.

151. Liu-Snyder, P.; Borgens, R. B.; Shi, R., Hydralazine rescues PC12 cells from acrolein-mediated death. *J Neurosci Res* **2006,** *84* (1), 219-27.

152. Park, J.; Zheng, L.; Marquis, A.; Walls, M.; Duerstock, B.; Pond, A.; Vega-Alvarez, S.; Wang, H.; Ouyang, Z.; Shi, R., Neuroprotective role of hydralazine in rat spinal cord injury-attenuation of acrolein-mediated damage. *J Neurochem* **2014,** *129* (2), 339-49.

153. Hamann, K.; Nehrt, G.; Ouyang, H.; Duerstock, B.; Shi, R., Hydralazine inhibits compression and acrolein-mediated injuries in ex vivo spinal cord. *J Neurochem* **2008,** *104* (3), 708-18.

154. Chen, W. Y.; Zhang, J.; Ghare, S.; Barve, S.; McClain, C.; Joshi-Barve, S., Acrolein Is a Pathogenic Mediator of Alcoholic Liver Disease and the Scavenger Hydralazine Is Protective in Mice. *Cell Mol Gastroenterol Hepatol* **2016,** *2* (5), 685-700.

155. Yao, L.; Wu, Y. T.; Tian, G. X.; Xia, C. Q.; Zhang, F.; Zhang, W., Acrolein Scavenger Hydralazine Prevents Streptozotocin-Induced Painful Diabetic Neuropathy and Spinal Neuroinflammation in Rats. *Anat Rec (Hoboken)* **2017**.

156. Kaminskas, L. M.; Pyke, S. M.; Burcham, P. C., Strong protein adduct trapping accompanies abolition of acrolein-mediated hepatotoxicity by hydralazine in mice. *J Pharmacol Exp Ther* **2004,** *310* (3), 1003-10.

157. Maheshwari, M.; Roberts, J. K.; Desutter, B.; Duong, K. T.; Tingling, J.; Fawver, J. N.; Schall, H. E.; Kahle, M.; Murray, I. V., Hydralazine modifies Abeta fibril formation and prevents modification by lipids in vitro. *Biochemistry* **2010,** *49* (49), 10371-80.

158. Galvani, S.; Coatrieux, C.; Elbaz, M.; Grazide, M. H.; Thiers, J. C.; Parini, A.; Uchida, K.; Kamar, N.; Rostaing, L.; Baltas, M.; Salvayre, R.; Negre-Salvayre, A., Carbonyl scavenger and antiatherogenic effects of hydrazine derivatives. *Free Radic Biol Med* **2008,** *45* (10), 1457-67.

159. Cebak, J. E.; Singh, I. N.; Hill, R. L.; Wang, J. A.; Hall, E. D., Phenelzine Protects Brain Mitochondrial Function In Vitro and In Vivo following Traumatic Brain Injury by Scavenging the Reactive Carbonyls 4-Hydroxynonenal and Acrolein Leading to Cortical Histological Neuroprotection. *J Neurotrauma* **2017,** *34* (7), 1302-1317.

160. D'Souza, Y.; Kawamoto, T.; Bennett, B. M., Role of the lipid peroxidation product, 4-hydroxynonenal, in the development of nitrate tolerance. *Chem Res Toxicol* **2014,** *27* (4), 663-73.

161. Vindis, C.; Escargueil-Blanc, I.; Elbaz, M.; Marcheix, B.; Grazide, M. H.; Uchida, K.; Salvayre, R.; Negre-Salvayre, A., Desensitization of platelet-derived growth factor receptor-beta by oxidized lipids in vascular cells and atherosclerotic lesions: prevention by aldehyde scavengers. *Circ Res* **2006,** *98* (6), 785-92.

162. Iacobini, C.; Menini, S.; Blasetti Fantauzzi, C.; Pesce, C. M.; Giaccari, A.; Salomone, E.; Lapolla, A.; Orioli, M.; Aldini, G.; Pugliese, G., FL-926-16, a novel bioavailable carnosinase-resistant carnosine derivative, prevents onset and stops progression of diabetic nephropathy in db/db mice. *Br J Pharmacol* **2018,** *175* (1), 53-66.

163. Singh, I. N.; Gilmer, L. K.; Miller, D. M.; Cebak, J. E.; Wang, J. A.; Hall, E. D., Phenelzine mitochondrial functional preservation and neuroprotection after traumatic brain injury related to scavenging of the lipid peroxidation-derived aldehyde 4-hydroxy-2-nonenal. *J Cereb Blood Flow Metab* **2013,** *33* (4), 593-9.

164. Nakajima, H.; Amano, W.; Kubo, T.; Fukuhara, A.; Ihara, H.; Azuma, Y. T.; Tajima, H.; Inui, T.; Sawa, A.; Takeuchi, T., Glyceraldehyde-3-phosphate dehydrogenase aggregate formation participates in oxidative stress-induced cell death. *J Biol Chem* **2009,** *284* (49), 34331-41.

165. Nakajima, H.; Itakura, M.; Kubo, T.; Kaneshige, A.; Harada, N.; Izawa, T.; Azuma, Y. T.; Kuwamura, M.; Yamaji, R.; Takeuchi, T., Glyceraldehyde-3-phosphate Dehydrogenase (GAPDH) Aggregation Causes Mitochondrial Dysfunction during Oxidative Stress-induced Cell Death. *J Biol Chem* **2017,** *292* (11), 4727-4742.

166. Ishii, T.; Tatsuda, E.; Kumazawa, S.; Nakayama, T.; Uchida, K., Molecular basis of enzyme inactivation by an endogenous electrophile 4-hydroxy-2-nonenal: identification of modification sites in glyceraldehyde-3-phosphate dehydrogenase. *Biochemistry* **2003,** *42* (12), 3474-80.

167. Nakamura, M.; Tomitori, H.; Suzuki, T.; Sakamoto, A.; Terui, Y.; Saiki, R.; Dohmae, N.; Igarashi, K.; Kashiwagi, K., Inactivation of GAPDH as one mechanism of acrolein toxicity. *Biochem Biophys Res Commun* **2013,** *430* (4), 1265-71.

168. Ando, Y.; Brannstrom, T.; Uchida, K.; Nyhlin, N.; Nasman, B.; Suhr, O.; Yamashita, T.; Olsson, T.; El Salhy, M.; Uchino, M.; Ando, M., Histochemical detection of 4-hydroxynonenal protein in Alzheimer amyloid. *J Neurol Sci* **1998,** *156* (2), 172-6.

169. Sayre, L. M.; Zelasko, D. A.; Harris, P. L.; Perry, G.; Salomon, R. G.; Smith, M. A., 4-Hydroxynonenal-derived advanced lipid peroxidation end products are increased in Alzheimer's disease. *J Neurochem* **1997,** *68* (5), 2092-7.

170. Ellis, G.; Fang, E.; Maheshwari, M.; Roltsch, E.; Holcomb, L.; Zimmer, D.; Martinez, D.; Murray, I. V., Lipid oxidation and modification of amyloid-beta (Abeta) in vitro and in vivo. *J Alzheimers Dis* **2010,** *22* (2), 593-607.

171. Magni, F.; Galbusera, C.; Tremolada, L.; Ferrarese, C.; Kienle, M. G., Characterisation of adducts of the lipid peroxidation product 4-hydroxy-2-nonenal and amyloid beta-peptides by liquid chromatography/electrospray ionisation mass spectrometry. *Rapid Commun Mass Spectrom* **2002,** *16* (15), 1485-93.

172.	Siegel, S. J.; Bieschke, J.; Powers, E. T.; Kelly, J. W., The oxidative stress metabolite 4-hydroxynonenal promotes Alzheimer protofibril formation. *Biochemistry* **2007,** *46* (6), 1503-10.

173.	Perez, M.; Cuadros, R.; Smith, M. A.; Perry, G.; Avila, J., Phosphorylated, but not native, tau protein assembles following reaction with the lipid peroxidation product, 4-hydroxy-2-nonenal. *FEBS Lett* **2000,** *486* (3), 270-4.

174.	Wang, Q.; Woltjer, R. L.; Cimino, P. J.; Pan, C.; Montine, K. S.; Zhang, J.; Montine, T. J., Proteomic analysis of neurofibrillary tangles in Alzheimer disease identifies GAPDH as a detergent-insoluble paired helical filament tau binding protein. *FASEB J* **2005,** *19* (7), 869-71.

175.	Itakura, M.; Nakajima, H.; Kubo, T.; Semi, Y.; Kume, S.; Higashida, S.; Kaneshige, A.; Kuwamura, M.; Harada, N.; Kita, A.; Azuma, Y. T.; Yamaji, R.; Inui, T.; Takeuchi, T., Glyceraldehyde-3-phosphate Dehydrogenase Aggregates Accelerate Amyloid-beta Amyloidogenesis in Alzheimer Disease. *J Biol Chem* **2015,** *290* (43), 26072-87.

176.	Fitch, W. M., Of urfs and orfs: A primer on how to analyze derived amino acid sequences. *Cell 50* (3), 329.

177.	Grek, C. L.; Zhang, J.; Manevich, Y.; Townsend, D. M.; Tew, K. D., Causes and consequences of cysteine S-glutathionylation. *J Biol Chem* **2013,** *288* (37), 26497-504.

178.	Martinez-Ruiz, A.; Lamas, S., Signalling by NO-induced protein S-nitrosylation and S-glutathionylation: convergences and divergences. *Cardiovasc Res* **2007,** *75* (2), 220-8.

179.	Dalle-Donne, I.; Rossi, R.; Colombo, G.; Giustarini, D.; Milzani, A., Protein S-glutathionylation: a regulatory device from bacteria to humans. *Trends Biochem Sci* **2009,** *34* (2), 85-96.

180.	Dalle-Donne, I.; Rossi, R.; Giustarini, D.; Colombo, R.; Milzani, A., S-glutathionylation in protein redox regulation. *Free Radic Biol Med* **2007,** *43* (6), 883-98.

181.	Forman, H. J.; Fukuto, J. M.; Torres, M., Redox signaling: thiol chemistry defines which reactive oxygen and nitrogen species can act as second messengers. *Am J Physiol Cell Physiol* **2004,** *287* (2), C246-56.

182.	Caplan, J. F.; Filipenko, N. R.; Fitzpatrick, S. L.; Waisman, D. M., Regulation of annexin A2 by reversible glutathionylation. *J Biol Chem* **2004,** *279* (9), 7740-50.

183.	Cohen, R. A.; Adachi, T., Nitric-oxide-induced vasodilatation: regulation by physiologic s-glutathiolation and pathologic oxidation of the sarcoplasmic endoplasmic reticulum calcium ATPase. *Trends Cardiovasc Med* **2006,** *16* (4), 109-14.

184.   Adachi, T.; Weisbrod, R. M.; Pimentel, D. R.; Ying, J.; Sharov, V. S.; Schoneich, C.;
        Cohen, R. A., S-Glutathiolation by peroxynitrite activates SERCA during arterial
        relaxation by nitric oxide. *Nat Med* **2004,** *10* (11), 1200-7.

185.   Taylor, E. R.; Hurrell, F.; Shannon, R. J.; Lin, T. K.; Hirst, J.; Murphy, M. P., Reversible
        glutathionylation of complex I increases mitochondrial superoxide formation. *J Biol
        Chem* **2003,** *278* (22), 19603-10.

186.   Ghezzi, P.; Casagrande, S.; Massignan, T.; Basso, M.; Bellacchio, E.; Mollica, L.;
        Biasini, E.; Tonelli, R.; Eberini, I.; Gianazza, E.; Dai, W. W.; Fratelli, M.; Salmona, M.;
        Sherry, B.; Bonetto, V., Redox regulation of cyclophilin A by glutathionylation.
        Proteomics **2006,** *6* (3), 817-25.

187.   Sitia, R.; Molteni, S. N., Stress, protein (mis)folding, and signaling: the redox connection.
        Sci STKE **2004,** *2004* (239), pe27.

188.   Cumming, R. C.; Schubert, D., Amyloid-beta induces disulfide bonding and aggregation
        of GAPDH in Alzheimer's disease. *FASEB J* **2005,** *19* (14), 2060-2.

189.   Reed, D. J., Glutathione: toxicological implications. *Annu Rev Pharmacol Toxicol* **1990,**
        30, 603-31.

190.   Schafer, F. Q.; Buettner, G. R., Redox environment of the cell as viewed through the
        redox state of the glutathione disulfide/glutathione couple. *Free Radical Biology and
        Medicine* **2001,** *30* (11), 1191-1212.

191.   Hofmann, B.; Hecht, H. J.; Flohe, L., Peroxiredoxins. *Biol Chem* **2002,** *383* (3-4), 347-
        64.

192.   Jacob, C.; Giles, G. I.; Giles, N. M.; Sies, H., Sulfur and selenium: the role of oxidation
        state in protein structure and function. *Angew Chem Int Ed Engl* **2003,** *42* (39), 4742-58.

193.   Gilbert, H. F., Thiol/disulfide exchange equilibria and disulfide bond stability. *Methods
        Enzymol* **1995,** *251*, 8-28.

194.   Cooper, A. J.; Pinto, J. T.; Callery, P. S., Reversible and irreversible protein
        glutathionylation: biological and clinical aspects. *Expert Opin Drug Metab Toxicol* **2011,**
        7 (7), 891-910.

195.   Townsend, D. M.; Manevich, Y.; He, L.; Hutchens, S.; Pazoles, C. J.; Tew, K. D., Novel
        role for glutathione S-transferase pi. Regulator of protein S-Glutathionylation following
        oxidative and nitrosative stress. *J Biol Chem* **2009,** *284* (1), 436-45.

196.   Debarbieux, L.; Beckwith, J., The reductive enzyme thioredoxin 1 acts as an oxidant
        when it is exported to the Escherichia coli periplasm. *Proceedings of the National
        Academy of Sciences* **1998,** *95* (18), 10751-10756.

197. Ghezzi, P., Protein glutathionylation in health and disease. *Biochimica et biophysica acta* **2013,** *1830* (5), 3165-72.

198. Gallogly, M. M.; Mieyal, J. J., Mechanisms of reversible protein glutathionylation in redox signaling and oxidative stress. *Curr Opin Pharmacol* **2007,** *7* (4), 381-91.

199. Wang, J.; Boja, E. S.; Tan, W.; Tekle, E.; Fales, H. M.; English, S.; Mieyal, J. J.; Chock, P. B., Reversible glutathionylation regulates actin polymerization in A431 cells. *J Biol Chem* **2001,** *276* (51), 47763-6.

200. Adachi, T.; Pimentel, D. R.; Heibeck, T.; Hou, X.; Lee, Y. J.; Jiang, B.; Ido, Y.; Cohen, R. A., S-glutathiolation of Ras mediates redox-sensitive signaling by angiotensin II in vascular smooth muscle cells. *J Biol Chem* **2004,** *279* (28), 29857-62.

201. Hoppe, G.; Chai, Y. C.; Crabb, J. W.; Sears, J., Protein s-glutathionylation in retinal pigment epithelium converts heat shock protein 70 to an active chaperone. *Exp Eye Res* **2004,** *78* (6), 1085-92.

202. Pan, S.; Berk, B. C., Glutathiolation regulates tumor necrosis factor-alpha-induced caspase-3 cleavage and apoptosis: key role for glutaredoxin in the death pathway. *Circ Res* **2007,** *100* (2), 213-9.

203. Mohr, S.; Hallak, H.; de Boitte, A.; Lapetina, E. G.; Brune, B., Nitric oxide-induced S-glutathionylation and inactivation of glyceraldehyde-3-phosphate dehydrogenase. *J Biol Chem* **1999,** *274* (14), 9427-30.

204. Barrett, W. C.; DeGnore, J. P.; Konig, S.; Fales, H. M.; Keng, Y. F.; Zhang, Z. Y.; Yim, M. B.; Chock, P. B., Regulation of PTP1B via glutathionylation of the active site cysteine 215. *Biochemistry* **1999,** *38* (20), 6699-705.

205. Figtree, G. A.; Liu, C. C.; Bibert, S.; Hamilton, E. J.; Garcia, A.; White, C. N.; Chia, K. K.; Cornelius, F.; Geering, K.; Rasmussen, H. H., Reversible oxidative modification: a key mechanism of Na+-K+ pump regulation. *Circ Res* **2009,** *105* (2), 185-93.

206. Singh, A.; Thornton, E. R.; Westheimer, F. H., The photolysis of diazoacetylchymotrypsin. *J Biol Chem* **1962,** *237*, 3006-8.

207. Tomohiro, T., Tag-Creation Approaches for Highly Efficient Profiling of Interacting Proteins and Domains. In *Photoaffinity Labeling for Structural Probing Within Protein*, Hatanaka, Y.; Hashimoto, M., Eds. Springer Japan: Tokyo, 2017; pp 13-43.

208. Sumranjit, J.; Chung, S. J., Recent advances in target characterization and identification by photoaffinity probes. *Molecules* **2013,** *18* (9), 10425-51.

209. Wands, A. M.; Kohler, J. J., Recent Developments in Designing Compact Biological Photoprobes. In *Photoaffinity Labeling for Structural Probing Within Protein*, Hatanaka, Y.; Hashimoto, M., Eds. Springer Japan: Tokyo, 2017; pp 45-78.

210. Dubinsky, L.; Krom, B. P.; Meijler, M. M., Diazirine based photoaffinity labeling. *Bioorg Med Chem* **2012,** *20* (2), 554-70.

211. Murale, D. P.; Hong, S. C.; Haque, M. M.; Lee, J. S., Photo-affinity labeling (PAL) in chemical proteomics: a handy tool to investigate protein-protein interactions (PPIs). *Proteome Sci* **2016,** *15*, 14.

212. Board, P. G.; Menon, D., Glutathione transferases, regulators of cellular metabolism and physiology. *Biochimica et biophysica acta* **2013,** *1830* (5), 3267-88.

213. Shishido, Y.; Tomoike, F.; Kimura, Y.; Kuwata, K.; Yano, T.; Fukui, K.; Fujikawa, H.; Sekido, Y.; Murakami-Tonami, Y.; Kameda, T.; Shuto, S.; Abe, H., A covalent G-site inhibitor for glutathione S-transferase Pi (GSTP1-1). *Chem Commun (Camb)* **2017,** *53* (81), 11138-11141.

214. Oakley, A. J.; Lo Bello, M.; Battistoni, A.; Ricci, G.; Rossjohn, J.; Villar, H. O.; Parker, M. W., The structures of human glutathione transferase P1-1 in complex with glutathione and various inhibitors at high resolution. *J Mol Biol* **1997,** *274* (1), 84-100.

215. Lo Bello, M.; Oakley, A. J.; Battistoni, A.; Mazzetti, A. P.; Nuccetelli, M.; Mazzarese, G.; Rossjohn, J.; Parker, M. W.; Ricci, G., Multifunctional role of Tyr 108 in the catalytic mechanism of human glutathione transferase P1-1. Crystallographic and kinetic studies on the Y108F mutant enzyme. *Biochemistry* **1997,** *36* (20), 6207-17.

216. Crawford, L. A.; Weerapana, E., A tyrosine-reactive irreversible inhibitor for glutathione S-transferase Pi (GSTP1). *Mol Biosyst* **2016,** *12* (6), 1768-71.

217. Chang, M.; Bolton, J. L.; Blond, S. Y., Expression and purification of hexahistidine-tagged human glutathione S-transferase P1-1 in Escherichia coli. *Protein Expr Purif* **1999,** *17* (3), 443-8.

218. Habig, W. H.; Pabst, M. J.; Jakoby, W. B., Glutathione S-transferases. The first enzymatic step in mercapturic acid formation. *J Biol Chem* **1974,** *249* (22), 7130-9.

APPENDICES

APPENDIX A. IDENTIFIED PROTEINS FROM LC-MS/MS ANALSYS OF HNE TREATED SHSY-5Y CELL LYSATES

TABLE IV. LIST OF PROTEINS IDENTIFIED FROM THE ENRICHMENT OF AHNE MODIFIED PROTEINS

#	Identified Proteins (403 total)	Accession Number	Protein Identification Probability	
			S1	S2
1	Cytoplasmic dynein 1 heavy chain 1 OS=Homo sapiens GN=DYNC1H1 PE=1 SV=5	DYHC1_HUMAN	100%	100%
2	Clathrin heavy chain 1 OS=Homo sapiens GN=CLTC PE=1 SV=5	CLH1_HUMAN	100%	100%
3	Myosin-9 OS=Homo sapiens GN=MYH9 PE=1 SV=4	MYH9_HUMAN	100%	100%
4	Filamin-A OS=Homo sapiens GN=FLNA PE=1 SV=4	FLNA_HUMAN	100%	100%
5	Heat shock cognate 71 kDa protein OS=Homo sapiens GN=HSPA8 PE=1 SV=1	HSP7C_HUMAN	100%	100%
6	Transitional endoplasmic reticulum ATPase OS=Homo sapiens GN=VCP PE=1 SV=4	TERA_HUMAN	100%	100%
7	Pyruvate kinase PKM OS=Homo sapiens GN=PKM PE=1 SV=4	KPYM_HUMAN	100%	100%
8	Elongation factor 2 OS=Homo sapiens GN=EEF2 PE=1 SV=4	EF2_HUMAN	100%	100%
9	Endoplasmin OS=Homo sapiens GN=HSP90B1 PE=1 SV=1	ENPL_HUMAN	100%	100%
10	Neutral alpha-glucosidase AB OS=Homo sapiens GN=GANAB PE=1 SV=3	GANAB_HUMAN	100%	100%
11	78 kDa glucose-regulated protein OS=Homo sapiens GN=HSPA5 PE=1 SV=2	GRP78_HUMAN	100%	100%
12	Ubiquitin-like modifier-activating enzyme 1 OS=Homo sapiens GN=UBA1 PE=1 SV=3	UBA1_HUMAN	100%	100%
13	60 kDa heat shock protein, mitochondrial OS=Homo sapiens GN=HSPD1 PE=1 SV=2	CH60_HUMAN	100%	100%
14	Heterogeneous nuclear ribonucleoprotein U OS=Homo sapiens GN=HNRNPU PE=1 SV=6	HNRPU_HUMAN	100%	100%
15	Tubulin alpha-1A chain OS=Homo sapiens GN=TUBA1A PE=1 SV=1	TBA1A_HUMAN	100%	100%
16	Heat shock protein HSP 90-alpha OS=Homo sapiens GN=HSP90AA1 PE=1 SV=5	HS90A_HUMAN	100%	100%
17	Heat shock protein HSP 90-beta OS=Homo sapiens GN=HSP90AB1 PE=1 SV=4	HS90B_HUMAN	100%	100%
18	Vimentin OS=Homo sapiens GN=VIM PE=1 SV=4	VIME_HUMAN	100%	100%
19	Fatty acid synthase OS=Homo sapiens GN=FASN PE=1 SV=3	FAS_HUMAN	100%	100%
20	Interleukin enhancer-binding factor 3 OS=Homo sapiens GN=ILF3 PE=1 SV=3	ILF3_HUMAN	100%	100%
21	Keratin, type II cytoskeletal 1 OS=Homo sapiens GN=KRT1 PE=1 SV=6	K2C1_HUMAN	100%	100%
22	Leucine-rich PPR motif-containing protein, mitochondrial OS=Homo sapiens GN=LRPPRC PE=1 SV=3	LPPRC_HUMAN	100%	100%

APPENDIX A (continued)

23	Talin-1 OS=Homo sapiens GN=TLN1 PE=1 SV=3	TLN1_HUMAN	100%	100%
24	Puromycin-sensitive aminopeptidase OS=Homo sapiens GN=NPEPPS PE=1 SV=2	PSA_HUMAN	100%	100%
25	Heat shock 70 kDa protein 1A OS=Homo sapiens GN=HSPA1A PE=1 SV=1	HS71A_HUMAN (+1)	100%	100%
26	ATP-citrate synthase OS=Homo sapiens GN=ACLY PE=1 SV=3	ACLY_HUMAN	100%	100%
27	Dihydropyrimidinase-related protein 2 OS=Homo sapiens GN=DPYSL2 PE=1 SV=1	DPYL2_HUMAN	100%	100%
28	Filamin-B OS=Homo sapiens GN=FLNB PE=1 SV=2	FLNB_HUMAN	100%	100%
29	Actin, cytoplasmic 1 OS=Homo sapiens GN=ACTB PE=1 SV=1	ACTB_HUMAN (+2)	100%	100%
30	Transcription intermediary factor 1-beta OS=Homo sapiens GN=TRIM28 PE=1 SV=5	TIF1B_HUMAN	100%	100%
31	Tubulin beta-3 chain OS=Homo sapiens GN=TUBB3 PE=1 SV=2	TBB3_HUMAN	100%	100%
32	Annexin A6 OS=Homo sapiens GN=ANXA6 PE=1 SV=3	ANXA6_HUMAN	100%	100%
33	Dihydropyrimidinase-related protein 3 OS=Homo sapiens GN=DPYSL3 PE=1 SV=1	DPYL3_HUMAN	100%	100%
34	T-complex protein 1 subunit gamma OS=Homo sapiens GN=CCT3 PE=1 SV=4	TCPG_HUMAN	100%	100%
35	Alpha-actinin-1 OS=Homo sapiens GN=ACTN1 PE=1 SV=2	ACTN1_HUMAN	100%	100%
36	Stress-70 protein, mitochondrial OS=Homo sapiens GN=HSPA9 PE=1 SV=2	GRP75_HUMAN	100%	100%
37	Alpha-enolase OS=Homo sapiens GN=ENO1 PE=1 SV=2	ENOA_HUMAN	100%	100%
38	Hypoxia up-regulated protein 1 OS=Homo sapiens GN=HYOU1 PE=1 SV=1	HYOU1_HUMAN	100%	100%
39	ATP synthase subunit beta, mitochondrial OS=Homo sapiens GN=ATP5B PE=1 SV=3	ATPB_HUMAN	100%	100%
40	Kinesin-1 heavy chain OS=Homo sapiens GN=KIF5B PE=1 SV=1	KINH_HUMAN	100%	100%
41	Tubulin beta chain OS=Homo sapiens GN=TUBB PE=1 SV=2	TBB5_HUMAN	100%	100%
42	Protein disulfide-isomerase A3 OS=Homo sapiens GN=PDIA3 PE=1 SV=4	PDIA3_HUMAN	100%	100%
43	Importin subunit beta-1 OS=Homo sapiens GN=KPNB1 PE=1 SV=2	IMB1_HUMAN	100%	100%
44	Alpha-actinin-4 OS=Homo sapiens GN=ACTN4 PE=1 SV=2	ACTN4_HUMAN	100%	100%
45	26S proteasome non-ATPase regulatory subunit 2 OS=Homo sapiens GN=PSMD2 PE=1 SV=3	PSMD2_HUMAN	100%	100%
46	Spectrin beta chain, non-erythrocytic 1 OS=Homo sapiens GN=SPTBN1 PE=1 SV=2	SPTB2_HUMAN	100%	100%
47	Transketolase OS=Homo sapiens GN=TKT PE=1 SV=3	TKT_HUMAN	100%	100%
48	Heterogeneous nuclear ribonucleoprotein K OS=Homo sapiens GN=HNRNPK PE=1 SV=1	HNRPK_HUMAN	100%	100%
49	Myosin-10 OS=Homo sapiens GN=MYH10 PE=1 SV=3	MYH10_HUMAN	100%	100%
50	Eukaryotic translation initiation factor 3 subunit A OS=Homo sapiens GN=EIF3A PE=1 SV=1	EIF3A_HUMAN	100%	100%
51	Hexokinase-1 OS=Homo sapiens GN=HK1 PE=1 SV=3	HXK1_HUMAN	100%	100%
52	Staphylococcal nuclease domain-containing protein 1 OS=Homo sapiens GN=SND1 PE=1 SV=1	SND1_HUMAN	100%	100%

APPENDIX A (continued)

53	Spectrin alpha chain, non-erythrocytic 1 OS=Homo sapiens GN=SPTAN1 PE=1 SV=3	SPTN1_HUMAN	100%	100%
54	Ras GTPase-activating-like protein IQGAP1 OS=Homo sapiens GN=IQGAP1 PE=1 SV=1	IQGA1_HUMAN	100%	100%
55	Dolichyl-diphosphooligosaccharide--protein glycosyltransferase subunit 1 OS=Homo sapiens GN=RPN1 PE=1 SV=1	RPN1_HUMAN	100%	100%
56	ATP synthase subunit alpha, mitochondrial OS=Homo sapiens GN=ATP5A1 PE=1 SV=1	ATPA_HUMAN	100%	100%
57	Heat shock 70 kDa protein 4 OS=Homo sapiens GN=HSPA4 PE=1 SV=4	HSP74_HUMAN	100%	100%
58	Keratin, type I cytoskeletal 9 OS=Homo sapiens GN=KRT9 PE=1 SV=3	K1C9_HUMAN	100%	100%
59	Microtubule-associated protein 1B OS=Homo sapiens GN=MAP1B PE=1 SV=2	MAP1B_HUMAN	100%	100%
60	DNA-dependent protein kinase catalytic subunit OS=Homo sapiens GN=PRKDC PE=1 SV=3	PRKDC_HUMAN	100%	100%
61	T-complex protein 1 subunit beta OS=Homo sapiens GN=CCT2 PE=1 SV=4	TCPB_HUMAN	100%	100%
62	T-complex protein 1 subunit theta OS=Homo sapiens GN=CCT8 PE=1 SV=4	TCPQ_HUMAN	100%	100%
63	Peptidyl-prolyl cis-trans isomerase A OS=Homo sapiens GN=PPIA PE=1 SV=2	PPIA_HUMAN	100%	100%
64	Glycine--tRNA ligase OS=Homo sapiens GN=GARS PE=1 SV=3	GARS_HUMAN	100%	100%
65	T-complex protein 1 subunit epsilon OS=Homo sapiens GN=CCT5 PE=1 SV=1	TCPE_HUMAN	100%	100%
66	Bifunctional glutamate/proline--tRNA ligase OS=Homo sapiens GN=EPRS PE=1 SV=5	SYEP_HUMAN	100%	100%
67	MICOS complex subunit MIC60 OS=Homo sapiens GN=IMMT PE=1 SV=1	MIC60_HUMAN	100%	100%
68	T-complex protein 1 subunit alpha OS=Homo sapiens GN=TCP1 PE=1 SV=1	TCPA_HUMAN	100%	100%
69	Sarcoplasmic/endoplasmic reticulum calcium ATPase 2 OS=Homo sapiens GN=ATP2A2 PE=1 SV=1	AT2A2_HUMAN	100%	100%
70	Trifunctional enzyme subunit alpha, mitochondrial OS=Homo sapiens GN=HADHA PE=1 SV=2	ECHA_HUMAN	100%	100%
71	Retrotransposon-like protein 1 OS=Homo sapiens GN=RTL1 PE=3 SV=3	RTL1_HUMAN	100%	100%
72	T-complex protein 1 subunit delta OS=Homo sapiens GN=CCT4 PE=1 SV=4	TCPD_HUMAN	100%	100%
73	Calcium-binding mitochondrial carrier protein Aralar2 OS=Homo sapiens GN=SLC25A13 PE=1 SV=2	CMC2_HUMAN	100%	100%
74	Heterogeneous nuclear ribonucleoprotein M OS=Homo sapiens GN=HNRNPM PE=1 SV=3	HNRPM_HUMAN	100%	100%
75	Keratin, type II cytoskeletal 2 epidermal OS=Homo sapiens GN=KRT2 PE=1 SV=2	K22E_HUMAN	100%	100%
76	Exportin-2 OS=Homo sapiens GN=CSE1L PE=1 SV=3	XPO2_HUMAN	100%	100%
77	Cullin-associated NEDD8-dissociated protein 1 OS=Homo sapiens GN=CAND1 PE=1 SV=2	CAND1_HUMAN	100%	100%
78	Keratin, type I cytoskeletal 10 OS=Homo sapiens GN=KRT10 PE=1 SV=6	K1C10_HUMAN	100%	100%
79	T-complex protein 1 subunit zeta OS=Homo sapiens GN=CCT6A PE=1 SV=3	TCPZ_HUMAN	100%	100%

APPENDIX A (continued)

80	DNA replication licensing factor MCM7 OS=Homo sapiens GN=MCM7 PE=1 SV=4	MCM7_HUMAN	100%	100%
81	Programmed cell death 6-interacting protein OS=Homo sapiens GN=PDCD6IP PE=1 SV=1	PDC6I_HUMAN	100%	100%
82	Lon protease homolog, mitochondrial OS=Homo sapiens GN=LONP1 PE=1 SV=2	LONM_HUMAN	100%	100%
83	T-complex protein 1 subunit eta OS=Homo sapiens GN=CCT7 PE=1 SV=2	TCPH_HUMAN	100%	100%
84	Nucleolin OS=Homo sapiens GN=NCL PE=1 SV=3	NUCL_HUMAN	100%	100%
85	General vesicular transport factor p115 OS=Homo sapiens GN=USO1 PE=1 SV=2	USO1_HUMAN	100%	100%
86	Calpain-1 catalytic subunit OS=Homo sapiens GN=CAPN1 PE=1 SV=1	CAN1_HUMAN	100%	100%
87	Fascin OS=Homo sapiens GN=FSCN1 PE=1 SV=3	FSCN1_HUMAN	100%	100%
88	Putative tubulin-like protein alpha-4B OS=Homo sapiens GN=TUBA4B PE=5 SV=2	TBA4B_HUMAN	98%	100%
89	C-1-tetrahydrofolate synthase, cytoplasmic OS=Homo sapiens GN=MTHFD1 PE=1 SV=3	C1TC_HUMAN	100%	100%
90	Ubiquitin carboxyl-terminal hydrolase 5 OS=Homo sapiens GN=USP5 PE=1 SV=2	UBP5_HUMAN	100%	100%
91	Extended synaptotagmin-1 OS=Homo sapiens GN=ESYT1 PE=1 SV=1	ESYT1_HUMAN	100%	100%
92	Filamin-C OS=Homo sapiens GN=FLNC PE=1 SV=3	FLNC_HUMAN	100%	100%
93	Glucose-6-phosphate 1-dehydrogenase OS=Homo sapiens GN=G6PD PE=1 SV=4	G6PD_HUMAN	100%	100%
94	Phosphoglycerate kinase 1 OS=Homo sapiens GN=PGK1 PE=1 SV=3	PGK1_HUMAN	100%	100%
95	Isoleucine--tRNA ligase, cytoplasmic OS=Homo sapiens GN=IARS PE=1 SV=2	SYIC_HUMAN	100%	100%
96	Methionine--tRNA ligase, cytoplasmic OS=Homo sapiens GN=MARS PE=1 SV=2	SYMC_HUMAN	100%	100%
97	Protein-glutamine gamma-glutamyltransferase 2 OS=Homo sapiens GN=TGM2 PE=1 SV=2	TGM2_HUMAN	100%	100%
98	Calnexin OS=Homo sapiens GN=CANX PE=1 SV=2	CALX_HUMAN	100%	100%
99	V-type proton ATPase catalytic subunit A OS=Homo sapiens GN=ATP6V1A PE=1 SV=2	VATA_HUMAN	100%	100%
100	Cytoskeleton-associated protein 4 OS=Homo sapiens GN=CKAP4 PE=1 SV=2	CKAP4_HUMAN	100%	100%
101	Dihydropyrimidinase-related protein 1 OS=Homo sapiens GN=CRMP1 PE=1 SV=1	DPYL1_HUMAN	100%	100%
102	26S proteasome non-ATPase regulatory subunit 1 OS=Homo sapiens GN=PSMD1 PE=1 SV=2	PSMD1_HUMAN	100%	100%
103	Ubiquitin-60S ribosomal protein L40 OS=Homo sapiens GN=UBA52 PE=1 SV=2	RL40_HUMAN (+3)	100%	100%
104	Valine--tRNA ligase OS=Homo sapiens GN=VARS PE=1 SV=4	SYVC_HUMAN	100%	100%
105	X-ray repair cross-complementing protein 6 OS=Homo sapiens GN=XRCC6 PE=1 SV=2	XRCC6_HUMAN	100%	100%
106	Septin-9 OS=Homo sapiens GN=SEPT9 PE=1 SV=2	SEPT9_HUMAN	100%	100%
107	Plectin OS=Homo sapiens GN=PLEC PE=1 SV=3	PLEC_HUMAN	0%	100%

APPENDIX A (continued)

108	Serine/threonine-protein phosphatase 2A 65 kDa regulatory subunit A alpha isoform OS=Homo sapiens GN=PPP2R1A PE=1 SV=4	2AAA_HUMAN	100%	100%
109	Kinesin-like protein KIF21A OS=Homo sapiens GN=KIF21A PE=1 SV=2	KI21A_HUMAN	100%	100%
110	Poly [ADP-ribose] polymerase 1 OS=Homo sapiens GN=PARP1 PE=1 SV=4	PARP1_HUMAN	100%	100%
111	Phosphoribosylformylglycinamidine synthase OS=Homo sapiens GN=PFAS PE=1 SV=4	PUR4_HUMAN	100%	100%
112	Bifunctional purine biosynthesis protein PURH OS=Homo sapiens GN=ATIC PE=1 SV=3	PUR9_HUMAN	100%	100%
113	Lysine--tRNA ligase OS=Homo sapiens GN=KARS PE=1 SV=3	SYK_HUMAN	100%	100%
114	Vacuolar protein sorting-associated protein 35 OS=Homo sapiens GN=VPS35 PE=1 SV=2	VPS35_HUMAN	100%	100%
115	GMP synthase [glutamine-hydrolyzing] OS=Homo sapiens GN=GMPS PE=1 SV=1	GUAA_HUMAN	100%	100%
116	eIF-2-alpha kinase activator GCN1 OS=Homo sapiens GN=GCN1 PE=1 SV=6	GCN1_HUMAN	100%	100%
117	Importin-5 OS=Homo sapiens GN=IPO5 PE=1 SV=4	IPO5_HUMAN	100%	100%
118	Far upstream element-binding protein 2 OS=Homo sapiens GN=KHSRP PE=1 SV=4	FUBP2_HUMAN	100%	100%
119	Glucose-6-phosphate isomerase OS=Homo sapiens GN=GPI PE=1 SV=4	G6PI_HUMAN	100%	100%
120	Eukaryotic translation initiation factor 4 gamma 1 OS=Homo sapiens GN=EIF4G1 PE=1 SV=4	IF4G1_HUMAN	100%	100%
121	Vesicle-fusing ATPase OS=Homo sapiens GN=NSF PE=1 SV=3	NSF_HUMAN	100%	100%
122	ATP-dependent 6-phosphofructokinase, muscle type OS=Homo sapiens GN=PFKM PE=1 SV=2	PFKAM_HUMAN	100%	100%
123	Isoleucine--tRNA ligase, mitochondrial OS=Homo sapiens GN=IARS2 PE=1 SV=2	SYIM_HUMAN	100%	100%
124	Arginine--tRNA ligase, cytoplasmic OS=Homo sapiens GN=RARS PE=1 SV=2	SYRC_HUMAN	100%	100%
125	Dynactin subunit 1 OS=Homo sapiens GN=DCTN1 PE=1 SV=3	DCTN1_HUMAN	100%	100%
126	Protein disulfide-isomerase A4 OS=Homo sapiens GN=PDIA4 PE=1 SV=2	PDIA4_HUMAN	100%	100%
127	Dynamin-1-like protein OS=Homo sapiens GN=DNM1L PE=1 SV=2	DNM1L_HUMAN	98%	100%
128	Probable ATP-dependent RNA helicase DDX5 OS=Homo sapiens GN=DDX5 PE=1 SV=1	DDX5_HUMAN	100%	100%
129	Eukaryotic translation initiation factor 3 subunit C OS=Homo sapiens GN=EIF3C PE=1 SV=1	EIF3C_HUMAN (+1)	100%	100%
130	Fermitin family homolog 2 OS=Homo sapiens GN=FERMT2 PE=1 SV=1	FERM2_HUMAN	100%	100%
131	Gelsolin OS=Homo sapiens GN=GSN PE=1 SV=1	GELS_HUMAN	100%	100%
132	NAD(P) transhydrogenase, mitochondrial OS=Homo sapiens GN=NNT PE=1 SV=3	NNTM_HUMAN	100%	100%
133	Profilin-1 OS=Homo sapiens GN=PFN1 PE=1 SV=2	PROF1_HUMAN	100%	100%
134	Coatomer subunit beta' OS=Homo sapiens GN=COPB2 PE=1 SV=2	COPB2_HUMAN	100%	100%

APPENDIX A (continued)

135	Coatomer subunit alpha OS=Homo sapiens GN=COPA PE=1 SV=2	COPA_HUMAN	100%	100%
136	Calreticulin OS=Homo sapiens GN=CALR PE=1 SV=1	CALR_HUMAN	98%	100%
137	Acylamino-acid-releasing enzyme OS=Homo sapiens GN=APEH PE=1 SV=4	ACPH_HUMAN	100%	100%
138	Aminopeptidase B OS=Homo sapiens GN=RNPEP PE=1 SV=2	AMPB_HUMAN	100%	100%
139	26S proteasome non-ATPase regulatory subunit 3 OS=Homo sapiens GN=PSMD3 PE=1 SV=2	PSMD3_HUMAN	100%	100%
140	Lysosomal alpha-glucosidase OS=Homo sapiens GN=GAA PE=1 SV=4	LYAG_HUMAN	100%	100%
141	Leucine-rich repeat-containing protein 47 OS=Homo sapiens GN=LRRC47 PE=1 SV=1	LRC47_HUMAN	100%	100%
142	40S ribosomal protein SA OS=Homo sapiens GN=RPSA PE=1 SV=4	RSSA_HUMAN	100%	100%
143	Signal transducer and activator of transcription 1-alpha/beta OS=Homo sapiens GN=STAT1 PE=1 SV=2	STAT1_HUMAN	100%	100%
144	Insulin-like growth factor 2 mRNA-binding protein 3 OS=Homo sapiens GN=IGF2BP3 PE=1 SV=2	IF2B3_HUMAN	100%	100%
145	Nuclear mitotic apparatus protein 1 OS=Homo sapiens GN=NUMA1 PE=1 SV=2	NUMA1_HUMAN	99%	100%
146	ATP-dependent RNA helicase A OS=Homo sapiens GN=DHX9 PE=1 SV=4	DHX9_HUMAN	98%	100%
147	Trifunctional purine biosynthetic protein adenosine-3 OS=Homo sapiens GN=GART PE=1 SV=1	PUR2_HUMAN	85%	100%
148	Nestin OS=Homo sapiens GN=NES PE=1 SV=2	NEST_HUMAN	0%	100%
149	Far upstream element-binding protein 1 OS=Homo sapiens GN=FUBP1 PE=1 SV=3	FUBP1_HUMAN	100%	100%
150	Eukaryotic translation initiation factor 3 subunit B OS=Homo sapiens GN=EIF3B PE=1 SV=3	EIF3B_HUMAN	100%	100%
151	Eukaryotic initiation factor 4A-I OS=Homo sapiens GN=EIF4A1 PE=1 SV=1	IF4A1_HUMAN	100%	100%
152	Leucine--tRNA ligase, cytoplasmic OS=Homo sapiens GN=LARS PE=1 SV=2	SYLC_HUMAN	100%	100%
153	Vigilin OS=Homo sapiens GN=HDLBP PE=1 SV=2	VIGLN_HUMAN	98%	100%
154	Glutamine--tRNA ligase OS=Homo sapiens GN=QARS PE=1 SV=1	SYQ_HUMAN	0%	100%
155	Aconitate hydratase, mitochondrial OS=Homo sapiens GN=ACO2 PE=1 SV=2	ACON_HUMAN	100%	100%
156	Coatomer subunit beta OS=Homo sapiens GN=COPB1 PE=1 SV=3	COPB_HUMAN	100%	100%
157	Ezrin OS=Homo sapiens GN=EZR PE=1 SV=4	EZRI_HUMAN	100%	100%
158	L-lactate dehydrogenase B chain OS=Homo sapiens GN=LDHB PE=1 SV=2	LDHB_HUMAN	100%	100%
159	Glutathione S-transferase P OS=Homo sapiens GN=GSTP1 PE=1 SV=2	GSTP1_HUMAN	100%	100%
160	Cell cycle and apoptosis regulator protein 2 OS=Homo sapiens GN=CCAR2 PE=1 SV=2	CCAR2_HUMAN	100%	100%
161	Phospholipase A-2-activating protein OS=Homo sapiens GN=PLAA PE=1 SV=2	PLAP_HUMAN	100%	100%
162	CAD protein OS=Homo sapiens GN=CAD PE=1 SV=3	PYR1_HUMAN	100%	100%

APPENDIX A (continued)

163	Coatomer subunit gamma-1 OS=Homo sapiens GN=COPG1 PE=1 SV=1	COPG1_HUMAN	100%	100%
164	14-3-3 protein gamma OS=Homo sapiens GN=YWHAG PE=1 SV=2	1433G_HUMAN	100%	100%
165	Stress-induced-phosphoprotein 1 OS=Homo sapiens GN=STIP1 PE=1 SV=1	STIP1_HUMAN	100%	100%
166	Catenin alpha-1 OS=Homo sapiens GN=CTNNA1 PE=1 SV=1	CTNA1_HUMAN	100%	100%
167	Echinoderm microtubule-associated protein-like 4 OS=Homo sapiens GN=EML4 PE=1 SV=3	EMAL4_HUMAN	100%	100%
168	Fructose-bisphosphate aldolase A OS=Homo sapiens GN=ALDOA PE=1 SV=2	ALDOA_HUMAN	100%	100%
169	Sodium/potassium-transporting ATPase subunit alpha-1 OS=Homo sapiens GN=ATP1A1 PE=1 SV=1	AT1A1_HUMAN	100%	100%
170	L-lactate dehydrogenase A chain OS=Homo sapiens GN=LDHA PE=1 SV=2	LDHA_HUMAN	100%	100%
171	Dihydropyrimidinase-related protein 5 OS=Homo sapiens GN=DPYSL5 PE=1 SV=1	DPYL5_HUMAN	100%	100%
172	Importin-9 OS=Homo sapiens GN=IPO9 PE=1 SV=3	IPO9_HUMAN	100%	100%
173	Glyceraldehyde-3-phosphate dehydrogenase OS=Homo sapiens GN=GAPDH PE=1 SV=3	G3P_HUMAN	100%	100%
174	Malate dehydrogenase, mitochondrial OS=Homo sapiens GN=MDH2 PE=1 SV=3	MDHM_HUMAN	100%	100%
175	Serpin H1 OS=Homo sapiens GN=SERPINH1 PE=1 SV=2	SERPH_HUMAN	100%	100%
176	Heat shock protein 75 kDa, mitochondrial OS=Homo sapiens GN=TRAP1 PE=1 SV=3	TRAP1_HUMAN	100%	100%
177	DNA replication licensing factor MCM6 OS=Homo sapiens GN=MCM6 PE=1 SV=1	MCM6_HUMAN	100%	100%
178	Polypyrimidine tract-binding protein 1 OS=Homo sapiens GN=PTBP1 PE=1 SV=1	PTBP1_HUMAN	100%	100%
179	Protein disulfide-isomerase A6 OS=Homo sapiens GN=PDIA6 PE=1 SV=1	PDIA6_HUMAN	100%	100%
180	Sec1 family domain-containing protein 1 OS=Homo sapiens GN=SCFD1 PE=1 SV=4	SCFD1_HUMAN	100%	100%
181	Kinesin heavy chain isoform 5C OS=Homo sapiens GN=KIF5C PE=1 SV=1	KIF5C_HUMAN	100%	100%
182	Protein transport protein Sec31A OS=Homo sapiens GN=SEC31A PE=1 SV=3	SC31A_HUMAN	99%	100%
183	Importin-7 OS=Homo sapiens GN=IPO7 PE=1 SV=1	IPO7_HUMAN	98%	100%
184	Multidrug resistance protein 1 OS=Homo sapiens GN=ABCB1 PE=1 SV=3	MDR1_HUMAN	98%	100%
185	Major vault protein OS=Homo sapiens GN=MVP PE=1 SV=4	MVP_HUMAN	98%	100%
186	NADPH--cytochrome P450 reductase OS=Homo sapiens GN=POR PE=1 SV=2	NCPR_HUMAN	98%	100%
187	Elongation factor Tu, mitochondrial OS=Homo sapiens GN=TUFM PE=1 SV=2	EFTU_HUMAN	91%	100%
188	60S ribosomal protein L5 OS=Homo sapiens GN=RPL5 PE=1 SV=3	RL5_HUMAN	23%	100%
189	Rab GDP dissociation inhibitor alpha OS=Homo sapiens GN=GDI1 PE=1 SV=2	GDIA_HUMAN	100%	100%
190	Nicotinamide phosphoribosyltransferase OS=Homo sapiens GN=NAMPT PE=1 SV=1	NAMPT_HUMAN	100%	100%

APPENDIX A (continued)

191	Adenylyl cyclase-associated protein 1 OS=Homo sapiens GN=CAP1 PE=1 SV=5	CAP1_HUMAN	100%	100%
192	Synaptic vesicle membrane protein VAT-1 homolog OS=Homo sapiens GN=VAT1 PE=1 SV=2	VAT1_HUMAN	100%	100%
193	Asparagine--tRNA ligase, cytoplasmic OS=Homo sapiens GN=NARS PE=1 SV=1	SYNC_HUMAN	100%	100%
194	X-ray repair cross-complementing protein 5 OS=Homo sapiens GN=XRCC5 PE=1 SV=3	XRCC5_HUMAN	100%	100%
195	Melanoma-associated antigen D2 OS=Homo sapiens GN=MAGED2 PE=1 SV=2	MAGD2_HUMAN	100%	100%
196	Very long-chain specific acyl-CoA dehydrogenase, mitochondrial OS=Homo sapiens GN=ACADVL PE=1 SV=1	ACADV_HUMAN	100%	100%
197	DNA replication licensing factor MCM5 OS=Homo sapiens GN=MCM5 PE=1 SV=5	MCM5_HUMAN	100%	100%
198	Eukaryotic translation initiation factor 3 subunit L OS=Homo sapiens GN=EIF3L PE=1 SV=1	EIF3L_HUMAN	100%	100%
199	Protein disulfide-isomerase OS=Homo sapiens GN=P4HB PE=1 SV=3	PDIA1_HUMAN	100%	100%
200	Dipeptidyl peptidase 3 OS=Homo sapiens GN=DPP3 PE=1 SV=2	DPP3_HUMAN	100%	100%
201	Sorting nexin-2 OS=Homo sapiens GN=SNX2 PE=1 SV=2	SNX2_HUMAN	100%	100%
202	Unconventional myosin-Ib OS=Homo sapiens GN=MYO1B PE=1 SV=3	MYO1B_HUMAN	100%	100%
203	Heat shock protein 105 kDa OS=Homo sapiens GN=HSPH1 PE=1 SV=1	HS105_HUMAN	100%	100%
204	DNA replication licensing factor MCM4 OS=Homo sapiens GN=MCM4 PE=1 SV=5	MCM4_HUMAN	100%	100%
205	Heterogeneous nuclear ribonucleoprotein Q OS=Homo sapiens GN=SYNCRIP PE=1 SV=2	HNRPQ_HUMAN	100%	100%
206	Copine-1 OS=Homo sapiens GN=CPNE1 PE=1 SV=1	CPNE1_HUMAN	100%	100%
207	Exportin-1 OS=Homo sapiens GN=XPO1 PE=1 SV=1	XPO1_HUMAN	100%	100%
208	Alanine--tRNA ligase, cytoplasmic OS=Homo sapiens GN=AARS PE=1 SV=2	SYAC_HUMAN	100%	100%
209	ATP-dependent 6-phosphofructokinase, liver type OS=Homo sapiens GN=PFKL PE=1 SV=6	PFKAL_HUMAN	100%	100%
210	Catenin beta-1 OS=Homo sapiens GN=CTNNB1 PE=1 SV=1	CTNB1_HUMAN	98%	100%
211	SUMO-activating enzyme subunit 2 OS=Homo sapiens GN=UBA2 PE=1 SV=2	SAE2_HUMAN	97%	100%
212	Aspartate--tRNA ligase, cytoplasmic OS=Homo sapiens GN=DARS PE=1 SV=2	SYDC_HUMAN	100%	97%
213	AP-2 complex subunit beta OS=Homo sapiens GN=AP2B1 PE=1 SV=1	AP2B1_HUMAN	21%	100%
214	ATP-dependent RNA helicase DDX1 OS=Homo sapiens GN=DDX1 PE=1 SV=2	DDX1_HUMAN	0%	100%
215	Procollagen-lysine,2-oxoglutarate 5-dioxygenase 3 OS=Homo sapiens GN=PLOD3 PE=1 SV=1	PLOD3_HUMAN	100%	100%
216	DNA replication licensing factor MCM2 OS=Homo sapiens GN=MCM2 PE=1 SV=4	MCM2_HUMAN	100%	100%
217	Secretory carrier-associated membrane protein 3 OS=Homo sapiens GN=SCAMP3 PE=1 SV=3	SCAM3_HUMAN	100%	100%
218	Prolyl 4-hydroxylase subunit alpha-1 OS=Homo sapiens GN=P4HA1 PE=1 SV=2	P4HA1_HUMAN	100%	100%

APPENDIX A (continued)

219	Annexin A2 OS=Homo sapiens GN=ANXA2 PE=1 SV=2	ANXA2_HUMAN	100%	100%
220	Elongation factor 1-gamma OS=Homo sapiens GN=EEF1G PE=1 SV=3	EF1G_HUMAN	100%	100%
221	Actin-related protein 3 OS=Homo sapiens GN=ACTR3 PE=1 SV=3	ARP3_HUMAN	100%	100%
222	Elongation factor 1-alpha 1 OS=Homo sapiens GN=EEF1A1 PE=1 SV=1	EF1A1_HUMAN (+1)	100%	100%
223	Heterogeneous nuclear ribonucleoprotein L OS=Homo sapiens GN=HNRNPL PE=1 SV=2	HNRPL_HUMAN	100%	100%
224	Mitochondrial import receptor subunit TOM70 OS=Homo sapiens GN=TOMM70 PE=1 SV=1	TOM70_HUMAN	100%	100%
225	Squamous cell carcinoma antigen recognized by T-cells 3 OS=Homo sapiens GN=SART3 PE=1 SV=1	SART3_HUMAN	100%	100%
226	26S proteasome regulatory subunit 4 OS=Homo sapiens GN=PSMC1 PE=1 SV=1	PRS4_HUMAN	100%	100%
227	Histone H2B type 1-B OS=Homo sapiens GN=HIST1H2BB PE=1 SV=2	H2B1B_HUMAN (+12)	100%	100%
228	40S ribosomal protein S3 OS=Homo sapiens GN=RPS3 PE=1 SV=2	RS3_HUMAN	100%	100%
229	Coatomer subunit delta OS=Homo sapiens GN=ARCN1 PE=1 SV=1	COPD_HUMAN	100%	100%
230	DNA replication licensing factor MCM3 OS=Homo sapiens GN=MCM3 PE=1 SV=3	MCM3_HUMAN	99%	100%
231	Neuroblast differentiation-associated protein AHNAK OS=Homo sapiens GN=AHNAK PE=1 SV=2	AHNK_HUMAN	100%	99%
232	AP-2 complex subunit alpha-2 OS=Homo sapiens GN=AP2A2 PE=1 SV=2	AP2A2_HUMAN	98%	100%
233	DNA mismatch repair protein Msh2 OS=Homo sapiens GN=MSH2 PE=1 SV=1	MSH2_HUMAN	98%	100%
234	Catenin delta-1 OS=Homo sapiens GN=CTNND1 PE=1 SV=1	CTND1_HUMAN	98%	100%
235	Protein enabled homolog OS=Homo sapiens GN=ENAH PE=1 SV=2	ENAH_HUMAN	98%	100%
236	Peptidyl-prolyl cis-trans isomerase FKBP4 OS=Homo sapiens GN=FKBP4 PE=1 SV=3	FKBP4_HUMAN	100%	97%
237	[F-actin]-methionine sulfoxide oxidase MICAL1 OS=Homo sapiens GN=MICAL1 PE=1 SV=2	MICA1_HUMAN	96%	99%
238	Microtubule-actin cross-linking factor 1, isoforms 1/2/3/5 OS=Homo sapiens GN=MACF1 PE=1 SV=4	MACF1_HUMAN	80%	100%
239	Protein transport protein Sec23B OS=Homo sapiens GN=SEC23B PE=1 SV=2	SC23B_HUMAN	0%	100%
240	Heterogeneous nuclear ribonucleoprotein R OS=Homo sapiens GN=HNRNPR PE=1 SV=1	HNRPR_HUMAN	100%	100%
241	Golgi resident protein GCP60 OS=Homo sapiens GN=ACBD3 PE=1 SV=4	GCP60_HUMAN	100%	100%
242	1-phosphatidylinositol 4,5-bisphosphate phosphodiesterase gamma-1 OS=Homo sapiens GN=PLCG1 PE=1 SV=1	PLCG1_HUMAN	100%	100%
243	6-phosphogluconate dehydrogenase, decarboxylating OS=Homo sapiens GN=PGD PE=1 SV=3	6PGD_HUMAN	100%	100%
244	Creatine kinase B-type OS=Homo sapiens GN=CKB PE=1 SV=1	KCRB_HUMAN	100%	100%
245	Pre-mRNA-splicing factor ATP-dependent RNA helicase DHX15 OS=Homo sapiens GN=DHX15 PE=1 SV=2	DHX15_HUMAN	100%	100%

APPENDIX A (continued)

246	Heat shock protein beta-1 OS=Homo sapiens GN=HSPB1 PE=1 SV=2	HSPB1_HUMAN	100%	100%
247	Nucleosome assembly protein 1-like 1 OS=Homo sapiens GN=NAP1L1 PE=1 SV=1	NP1L1_HUMAN	100%	100%
248	D-3-phosphoglycerate dehydrogenase OS=Homo sapiens GN=PHGDH PE=1 SV=4	SERA_HUMAN	100%	100%
249	Rab GDP dissociation inhibitor beta OS=Homo sapiens GN=GDI2 PE=1 SV=2	GDIB_HUMAN	100%	100%
250	Heterogeneous nuclear ribonucleoprotein H OS=Homo sapiens GN=HNRNPH1 PE=1 SV=4	HNRH1_HUMAN	100%	100%
251	WD repeat-containing protein 1 OS=Homo sapiens GN=WDR1 PE=1 SV=4	WDR1_HUMAN	100%	100%
252	Nuclear protein localization protein 4 homolog OS=Homo sapiens GN=NPLOC4 PE=1 SV=3	NPL4_HUMAN	100%	100%
253	tRNA (cytosine(34)-C(5))-methyltransferase OS=Homo sapiens GN=NSUN2 PE=1 SV=2	NSUN2_HUMAN	100%	100%
254	Septin-7 OS=Homo sapiens GN=SEPT7 PE=1 SV=2	SEPT7_HUMAN	100%	100%
255	SEC23-interacting protein OS=Homo sapiens GN=SEC23IP PE=1 SV=1	S23IP_HUMAN	99%	100%
256	Nodal modulator 1 OS=Homo sapiens GN=NOMO1 PE=1 SV=5	NOMO1_HUMAN	99%	100%
257	Unconventional myosin-Ic OS=Homo sapiens GN=MYO1C PE=1 SV=4	MYO1C_HUMAN	100%	98%
258	Nuclear factor NF-kappa-B p100 subunit OS=Homo sapiens GN=NFKB2 PE=1 SV=4	NFKB2_HUMAN	98%	100%
259	Prolyl endopeptidase OS=Homo sapiens GN=PREP PE=1 SV=2	PPCE_HUMAN	98%	100%
260	Regulator of nonsense transcripts 1 OS=Homo sapiens GN=UPF1 PE=1 SV=2	RENT1_HUMAN	98%	100%
261	DNA damage-binding protein 1 OS=Homo sapiens GN=DDB1 PE=1 SV=1	DDB1_HUMAN	98%	100%
262	Tubulin--tyrosine ligase-like protein 12 OS=Homo sapiens GN=TTLL12 PE=1 SV=2	TTL12_HUMAN	98%	100%
263	Importin-4 OS=Homo sapiens GN=IPO4 PE=1 SV=2	IPO4_HUMAN	98%	100%
264	Tryptophan--tRNA ligase, cytoplasmic OS=Homo sapiens GN=WARS PE=1 SV=2	SYWC_HUMAN	100%	94%
265	Polyadenylate-binding protein 1 OS=Homo sapiens GN=PABPC1 PE=1 SV=2	PABP1_HUMAN	94%	100%
266	NAD-dependent malic enzyme, mitochondrial OS=Homo sapiens GN=ME2 PE=1 SV=1	MAOM_HUMAN	100%	89%
267	Cytoplasmic dynein 1 intermediate chain 2 OS=Homo sapiens GN=DYNC1I2 PE=1 SV=3	DC1I2_HUMAN	44%	100%
268	Zyxin OS=Homo sapiens GN=ZYX PE=1 SV=1	ZYX_HUMAN	40%	100%
269	Tubulin-specific chaperone D OS=Homo sapiens GN=TBCD PE=1 SV=2	TBCD_HUMAN	0%	100%
270	Coronin-7 OS=Homo sapiens GN=CORO7 PE=1 SV=2	CORO7_HUMAN	0%	100%
271	Tubulin beta-2B chain OS=Homo sapiens GN=TUBB2B PE=1 SV=1	TBB2B_HUMAN	100%	100%
272	NADH-ubiquinone oxidoreductase 75 kDa subunit, mitochondrial OS=Homo sapiens GN=NDUFS1 PE=1 SV=3	NDUS1_HUMAN	100%	100%
273	Cytoplasmic FMR1-interacting protein 1 OS=Homo sapiens GN=CYFIP1 PE=1 SV=1	CYFP1_HUMAN	100%	100%

APPENDIX A (continued)

274	Heterogeneous nuclear ribonucleoprotein U-like protein 2 OS=Homo sapiens GN=HNRNPUL2 PE=1 SV=1	HNRL2_HUMAN	100%	100%
275	Tubulin beta-6 chain OS=Homo sapiens GN=TUBB6 PE=1 SV=1	TBB6_HUMAN	100%	100%
276	Manganese-transporting ATPase 13A1 OS=Homo sapiens GN=ATP13A1 PE=1 SV=2	AT131_HUMAN	100%	100%
277	Neurosecretory protein VGF OS=Homo sapiens GN=VGF PE=1 SV=2	VGF_HUMAN	98%	100%
278	Peroxisomal multifunctional enzyme type 2 OS=Homo sapiens GN=HSD17B4 PE=1 SV=3	DHB4_HUMAN	98%	100%
279	Carnitine O-palmitoyltransferase 2, mitochondrial OS=Homo sapiens GN=CPT2 PE=1 SV=2	CPT2_HUMAN	98%	100%
280	Adenosylhomocysteinase OS=Homo sapiens GN=AHCY PE=1 SV=4	SAHH_HUMAN	100%	97%
281	Histone deacetylase 2 OS=Homo sapiens GN=HDAC2 PE=1 SV=2	HDAC2_HUMAN	97%	100%
282	E3 ubiquitin-protein ligase HUWE1 OS=Homo sapiens GN=HUWE1 PE=1 SV=3	HUWE1_HUMAN	98%	99%
283	Cold shock domain-containing protein E1 OS=Homo sapiens GN=CSDE1 PE=1 SV=2	CSDE1_HUMAN	96%	100%
284	Nucleoside diphosphate kinase A OS=Homo sapiens GN=NME1 PE=1 SV=1	NDKA_HUMAN	99%	97%
285	ATP-dependent 6-phosphofructokinase, platelet type OS=Homo sapiens GN=PFKP PE=1 SV=2	PFKAP_HUMAN	90%	100%
286	Carnitine O-palmitoyltransferase 1, liver isoform OS=Homo sapiens GN=CPT1A PE=1 SV=2	CPT1A_HUMAN	89%	100%
287	Matrin-3 OS=Homo sapiens GN=MATR3 PE=1 SV=2	MATR3_HUMAN	88%	100%
288	Citrate synthase, mitochondrial OS=Homo sapiens GN=CS PE=1 SV=2	CISY_HUMAN	99%	86%
289	Exportin-T OS=Homo sapiens GN=XPOT PE=1 SV=2	XPOT_HUMAN	80%	100%
290	SH3 and PX domain-containing protein 2B OS=Homo sapiens GN=SH3PXD2B PE=1 SV=3	SPD2B_HUMAN	71%	100%
291	Ubiquitin carboxyl-terminal hydrolase 14 OS=Homo sapiens GN=USP14 PE=1 SV=3	UBP14_HUMAN	99%	50%
292	B-cell receptor-associated protein 31 OS=Homo sapiens GN=BCAP31 PE=1 SV=3	BAP31_HUMAN	39%	100%
293	CCR4-NOT transcription complex subunit 1 OS=Homo sapiens GN=CNOT1 PE=1 SV=2	CNOT1_HUMAN	25%	99%
294	Exportin-5 OS=Homo sapiens GN=XPO5 PE=1 SV=1	XPO5_HUMAN	100%	19%
295	Bifunctional 3'-phosphoadenosine 5'-phosphosulfate synthase 1 OS=Homo sapiens GN=PAPSS1 PE=1 SV=2	PAPS1_HUMAN	13%	100%
296	Dynamin-2 OS=Homo sapiens GN=DNM2 PE=1 SV=2	DYN2_HUMAN	7%	99%
297	Dihydropyrimidinase-related protein 4 OS=Homo sapiens GN=DPYSL4 PE=1 SV=2	DPYL4_HUMAN	100%	5%
298	Glutamine--fructose-6-phosphate aminotransferase [isomerizing] 1 OS=Homo sapiens GN=GFPT1 PE=1 SV=3	GFPT1_HUMAN	0%	100%
299	Succinate dehydrogenase [ubiquinone] flavoprotein subunit, mitochondrial OS=Homo sapiens GN=SDHA PE=1 SV=2	SDHA_HUMAN	0%	100%
300	14-3-3 protein epsilon OS=Homo sapiens GN=YWHAE PE=1 SV=1	1433E_HUMAN	0%	100%
301	ATP-dependent RNA helicase DDX42 OS=Homo sapiens GN=DDX42 PE=1 SV=1	DDX42_HUMAN	0%	100%

APPENDIX A (continued)

302	Splicing factor 3B subunit 3 OS=Homo sapiens GN=SF3B3 PE=1 SV=4	SF3B3_HUMAN	0%	100%
303	N-alpha-acetyltransferase 15, NatA auxiliary subunit OS=Homo sapiens GN=NAA15 PE=1 SV=1	NAA15_HUMAN	0%	100%
304	DNA-directed RNA polymerase II subunit RPB2 OS=Homo sapiens GN=POLR2B PE=1 SV=1	RPB2_HUMAN	0%	100%
305	Kinectin OS=Homo sapiens GN=KTN1 PE=1 SV=1	KTN1_HUMAN	0%	100%
306	CTP synthase 1 OS=Homo sapiens GN=CTPS1 PE=1 SV=2	PYRG1_HUMAN	0%	100%
307	Cytoplasmic aconitate hydratase OS=Homo sapiens GN=ACO1 PE=1 SV=3	ACOC_HUMAN	0%	100%
308	26S proteasome regulatory subunit 10B OS=Homo sapiens GN=PSMC6 PE=1 SV=1	PRS10_HUMAN	100%	0%
309	Host cell factor 1 OS=Homo sapiens GN=HCFC1 PE=1 SV=2	HCFC1_HUMAN	0%	100%
310	ATP-dependent RNA helicase DDX3X OS=Homo sapiens GN=DDX3X PE=1 SV=3	DDX3X_HUMAN	100%	100%
311	Guanine nucleotide-binding protein G(i) subunit alpha-2 OS=Homo sapiens GN=GNAI2 PE=1 SV=3	GNAI2_HUMAN	100%	100%
312	Tubulin beta-4B chain OS=Homo sapiens GN=TUBB4B PE=1 SV=1	TBB4B_HUMAN	100%	100%
313	Alkyldihydroxyacetonephosphate synthase, peroxisomal OS=Homo sapiens GN=AGPS PE=1 SV=1	ADAS_HUMAN	98%	100%
314	5'-3' exoribonuclease 2 OS=Homo sapiens GN=XRN2 PE=1 SV=1	XRN2_HUMAN	98%	100%
315	Src substrate cortactin OS=Homo sapiens GN=CTTN PE=1 SV=2	SRC8_HUMAN	98%	100%
316	Threonine--tRNA ligase, cytoplasmic OS=Homo sapiens GN=TARS PE=1 SV=3	SYTC_HUMAN	98%	100%
317	Transportin-1 OS=Homo sapiens GN=TNPO1 PE=1 SV=2	TNPO1_HUMAN	98%	100%
318	Sideroflexin-1 OS=Homo sapiens GN=SFXN1 PE=1 SV=4	SFXN1_HUMAN	98%	100%
319	Actin, aortic smooth muscle OS=Homo sapiens GN=ACTA2 PE=1 SV=1	ACTA_HUMAN (+3)	97%	100%
320	Gamma-enolase OS=Homo sapiens GN=ENO2 PE=1 SV=3	ENOG_HUMAN	100%	97%
321	Dopamine beta-hydroxylase OS=Homo sapiens GN=DBH PE=1 SV=3	DOPO_HUMAN	100%	97%
322	Heterogeneous nuclear ribonucleoproteins A2/B1 OS=Homo sapiens GN=HNRNPA2B1 PE=1 SV=2	ROA2_HUMAN	100%	97%
323	26S proteasome regulatory subunit 6A OS=Homo sapiens GN=PSMC3 PE=1 SV=3	PRS6A_HUMAN	100%	97%
324	Protein unc-13 homolog D OS=Homo sapiens GN=UNC13D PE=1 SV=1	UN13D_HUMAN	98%	99%
325	Sorting nexin-1 OS=Homo sapiens GN=SNX1 PE=1 SV=3	SNX1_HUMAN	98%	99%
326	Neutral amino acid transporter B(0) OS=Homo sapiens GN=SLC1A5 PE=1 SV=2	AAAT_HUMAN	99%	97%
327	Elongation factor 1-alpha 2 OS=Homo sapiens GN=EEF1A2 PE=1 SV=1	EF1A2_HUMAN	95%	100%
328	Far upstream element-binding protein 3 OS=Homo sapiens GN=FUBP3 PE=1 SV=2	FUBP3_HUMAN	100%	88%
329	GTP-binding nuclear protein Ran OS=Homo sapiens GN=RAN PE=1 SV=3	RAN_HUMAN	83%	100%
330	Dynamin-1 OS=Homo sapiens GN=DNM1 PE=1 SV=2	DYN1_HUMAN	77%	100%

APPENDIX A (continued)

331	V-type proton ATPase subunit B, kidney isoform OS=Homo sapiens GN=ATP6V1B1 PE=1 SV=3	VATB1_HUMAN	62%	100%
332	FRAS1-related extracellular matrix protein 3 OS=Homo sapiens GN=FREM3 PE=3 SV=2	FREM3_HUMAN	60%	100%
333	Radixin OS=Homo sapiens GN=RDX PE=1 SV=1	RADI_HUMAN	34%	94%
334	E3 ubiquitin-protein ligase UBR4 OS=Homo sapiens GN=UBR4 PE=1 SV=1	UBR4_HUMAN	99%	23%
335	Kinesin-like protein KIF3A OS=Homo sapiens GN=KIF3A PE=1 SV=4	KIF3A_HUMAN	21%	100%
336	Plastin-3 OS=Homo sapiens GN=PLS3 PE=1 SV=4	PLST_HUMAN	99%	16%
337	Serine/threonine-protein kinase PAK 2 OS=Homo sapiens GN=PAK2 PE=1 SV=3	PAK2_HUMAN	100%	11%
338	Coatomer subunit gamma-2 OS=Homo sapiens GN=COPG2 PE=1 SV=1	COPG2_HUMAN	8%	100%
339	Polyadenylate-binding protein 4 OS=Homo sapiens GN=PABPC4 PE=1 SV=1	PABP4_HUMAN	7%	100%
340	Probable ATP-dependent RNA helicase DDX17 OS=Homo sapiens GN=DDX17 PE=1 SV=2	DDX17_HUMAN	0%	100%
341	ER membrane protein complex subunit 1 OS=Homo sapiens GN=EMC1 PE=1 SV=1	EMC1_HUMAN	0%	100%
342	Drebrin OS=Homo sapiens GN=DBN1 PE=1 SV=4	DREB_HUMAN	0%	100%
343	LisH domain-containing protein ARMC9 OS=Homo sapiens GN=ARMC9 PE=1 SV=2	ARMC9_HUMAN	100%	0%
344	26S proteasome regulatory subunit 7 OS=Homo sapiens GN=PSMC2 PE=1 SV=3	PRS7_HUMAN	100%	0%
345	Constitutive coactivator of PPAR-gamma-like protein 1 OS=Homo sapiens GN=FAM120A PE=1 SV=2	F120A_HUMAN	0%	100%
346	Glycogen phosphorylase, muscle form OS=Homo sapiens GN=PYGM PE=1 SV=6	PYGM_HUMAN	0%	100%
347	Cysteine--tRNA ligase, cytoplasmic OS=Homo sapiens GN=CARS PE=1 SV=3	SYCC_HUMAN	0%	100%
348	Exosome complex exonuclease RRP44 OS=Homo sapiens GN=DIS3 PE=1 SV=2	RRP44_HUMAN	0%	100%
349	AP-1 complex subunit beta-1 OS=Homo sapiens GN=AP1B1 PE=1 SV=2	AP1B1_HUMAN	0%	100%
350	ATP-binding cassette sub-family E member 1 OS=Homo sapiens GN=ABCE1 PE=1 SV=1	ABCE1_HUMAN	0%	100%
351	Serine/threonine-protein phosphatase 2B catalytic subunit alpha isoform OS=Homo sapiens GN=PPP3CA PE=1 SV=1	PP2BA_HUMAN	100%	0%
352	Protein transport protein Sec24C OS=Homo sapiens GN=SEC24C PE=1 SV=3	SC24C_HUMAN	0%	100%
353	Protein phosphatase 1F OS=Homo sapiens GN=PPM1F PE=1 SV=3	PPM1F_HUMAN	99%	0%
354	Ras GTPase-activating-like protein IQGAP2 OS=Homo sapiens GN=IQGAP2 PE=1 SV=4	IQGA2_HUMAN	54%	0%
355	Tubulin beta-2A chain OS=Homo sapiens GN=TUBB2A PE=1 SV=1	TBB2A_HUMAN	100%	100%
356	Guanine nucleotide-binding protein G(o) subunit alpha OS=Homo sapiens GN=GNAO1 PE=1 SV=4	GNAO_HUMAN	100%	100%
357	Kinesin light chain 1 OS=Homo sapiens GN=KLC1 PE=1 SV=2	KLC1_HUMAN	98%	100%

APPENDIX A (continued)

358	Tubulin alpha-3C/D chain OS=Homo sapiens GN=TUBA3C PE=1 SV=3	TBA3C_HUMAN	69%	74%
359	Sodium/potassium-transporting ATPase subunit alpha-3 OS=Homo sapiens GN=ATP1A3 PE=1 SV=3	AT1A3_HUMAN	53%	76%
360	14-3-3 protein eta OS=Homo sapiens GN=YWHAH PE=1 SV=4	1433F_HUMAN	43%	66%
361	ATP-binding cassette sub-family F member 1 OS=Homo sapiens GN=ABCF1 PE=1 SV=2	ABCF1_HUMAN	0%	100%
362	Non-syndromic hearing impairment protein 5 OS=Homo sapiens GN=DFNA5 PE=1 SV=2	DFNA5_HUMAN	100%	0%
363	Ras GTPase-activating protein-binding protein 2 OS=Homo sapiens GN=G3BP2 PE=1 SV=2	G3BP2_HUMAN	0%	100%
364	Dihydrolipoyllysine-residue acetyltransferase component of pyruvate dehydrogenase complex, mitochondrial OS=Homo sapiens GN=DLAT PE=1 SV=3	ODP2_HUMAN	0%	100%
365	2',5'-phosphodiesterase 12 OS=Homo sapiens GN=PDE12 PE=1 SV=2	PDE12_HUMAN	100%	0%
366	4F2 cell-surface antigen heavy chain OS=Homo sapiens GN=SLC3A2 PE=1 SV=3	4F2_HUMAN	0%	100%
367	Intercellular adhesion molecule 1 OS=Homo sapiens GN=ICAM1 PE=1 SV=2	ICAM1_HUMAN	0%	100%
368	Rab3 GTPase-activating protein catalytic subunit OS=Homo sapiens GN=RAB3GAP1 PE=1 SV=3	RB3GP_HUMAN	0%	100%
369	60S ribosomal protein L8 OS=Homo sapiens GN=RPL8 PE=1 SV=2	RL8_HUMAN	0%	100%
370	Eukaryotic translation initiation factor 3 subunit F OS=Homo sapiens GN=EIF3F PE=1 SV=1	EIF3F_HUMAN	100%	0%
371	Proto-oncogene tyrosine-protein kinase receptor Ret OS=Homo sapiens GN=RET PE=1 SV=3	RET_HUMAN	0%	100%
372	Transgelin-2 OS=Homo sapiens GN=TAGLN2 PE=1 SV=3	TAGL2_HUMAN	100%	0%
373	Eukaryotic translation initiation factor 4 gamma 2 OS=Homo sapiens GN=EIF4G2 PE=1 SV=1	IF4G2_HUMAN	0%	100%
374	14-3-3 protein theta OS=Homo sapiens GN=YWHAQ PE=1 SV=1	1433T_HUMAN	97%	0%
375	Dolichyl-diphosphooligosaccharide--protein glycosyltransferase subunit 2 OS=Homo sapiens GN=RPN2 PE=1 SV=3	RPN2_HUMAN	0%	100%
376	Nck-associated protein 1 OS=Homo sapiens GN=NCKAP1 PE=1 SV=1	NCKP1_HUMAN	0%	100%
377	Receptor of activated protein C kinase 1 OS=Homo sapiens GN=RACK1 PE=1 SV=3	RACK1_HUMAN	99%	0%
378	Cytoplasmic dynein 1 light intermediate chain 2 OS=Homo sapiens GN=DYNC1LI2 PE=1 SV=1	DC1L2_HUMAN	99%	0%
379	Signal recognition particle subunit SRP68 OS=Homo sapiens GN=SRP68 PE=1 SV=2	SRP68_HUMAN	0%	99%
380	Nuclear pore complex protein Nup155 OS=Homo sapiens GN=NUP155 PE=1 SV=1	NU155_HUMAN	99%	0%
381	Niban-like protein 1 OS=Homo sapiens GN=FAM129B PE=1 SV=3	NIBL1_HUMAN	99%	0%
382	Kinesin-like protein KIF7 OS=Homo sapiens GN=KIF7 PE=1 SV=2	KIF7_HUMAN	99%	0%
383	Annexin A7 OS=Homo sapiens GN=ANXA7 PE=1 SV=3	ANXA7_HUMAN	99%	0%

APPENDIX A (continued)

| 384	Prolow-density lipoprotein receptor-related protein 1 OS=Homo sapiens GN=LRP1 PE=1 SV=2	LRP1_HUMAN	0%	99%
385	Prolyl 3-hydroxylase 3 OS=Homo sapiens GN=P3H3 PE=1 SV=1	P3H3_HUMAN	0%	99%
386	Phosphate carrier protein, mitochondrial OS=Homo sapiens GN=SLC25A3 PE=1 SV=2	MPCP_HUMAN	0%	99%
387	Signal recognition particle receptor subunit alpha OS=Homo sapiens GN=SRPRA PE=1 SV=2	SRPRA_HUMAN	0%	99%
388	Potassium-transporting ATPase alpha chain 2 OS=Homo sapiens GN=ATP12A PE=1 SV=3	AT12A_HUMAN	0%	64%
389	Tubulin beta-4A chain OS=Homo sapiens GN=TUBB4A PE=1 SV=2	TBB4A_HUMAN	88%	100%
390	Heterogeneous nuclear ribonucleoprotein F OS=Homo sapiens GN=HNRNPF PE=1 SV=3	HNRPF_HUMAN	56%	100%
391	Heat shock-related 70 kDa protein 2 OS=Homo sapiens GN=HSPA2 PE=1 SV=1	HSP72_HUMAN	28%	100%
392	Tubulin beta-8 chain OS=Homo sapiens GN=TUBB8 PE=1 SV=2	TBB8_HUMAN	40%	80%
393	14-3-3 protein beta/alpha OS=Homo sapiens GN=YWHAB PE=1 SV=3	1433B_HUMAN	100%	0%
394	Guanine nucleotide-binding protein G(s) subunit alpha isoforms XLas OS=Homo sapiens GN=GNAS PE=1 SV=2	GNAS1_HUMAN (+1)	100%	0%
395	Plasma membrane calcium-transporting ATPase 4 OS=Homo sapiens GN=ATP2B4 PE=1 SV=2	AT2B4_HUMAN	0%	100%
396	Heat shock protein HSP 90-alpha A2 OS=Homo sapiens GN=HSP90AA2P PE=1 SV=2	HS902_HUMAN	0%	95%
397	T-complex protein 1 subunit zeta-2 OS=Homo sapiens GN=CCT6B PE=1 SV=5	TCPW_HUMAN	91%	0%
398	ATP-dependent RNA helicase DDX3Y OS=Homo sapiens GN=DDX3Y PE=1 SV=2	DDX3Y_HUMAN	0%	68%
399	Putative heat shock protein HSP 90-alpha A4 OS=Homo sapiens GN=HSP90AA4P PE=5 SV=1	HS904_HUMAN	70%	0%
400	Plasma membrane calcium-transporting ATPase 3 OS=Homo sapiens GN=ATP2B3 PE=1 SV=3	AT2B3_HUMAN	0%	67%
401	Putative heat shock protein HSP 90-alpha A5 OS=Homo sapiens GN=HSP90AA5P PE=2 SV=1	HS905_HUMAN	0%	54%
402	POTE ankyrin domain family member E OS=Homo sapiens GN=POTEE PE=2 SV=3	POTEE_HUMAN (+1)	35%	0%
403	Neurofilament light polypeptide OS=Homo sapiens GN=NEFL PE=1 SV=3	NFL_HUMAN	0%	29%

# APPENDIX B. PROTEIN CRYSTAL STRUCTRUES FROM RCSB PROTEIN DATA BANK WITH GSH OR GSH-CONJUGATE LINGANDS

TABLE V. LIST OF CRYSTAL STRUCTURES WITH GSH OR GSH-CONJUGATE LIGANDS IN THE RCBS PDB

PDB ID	Ligand	Protein	Resolution
10GS	Phenyl GSH	GST P1-1	2.2
18GS	Dinitrobezene GSH	GST P1-1	1.9
1AQV	Bromobenzene GSH	GST P1-1	1.94
1AQW	GSH	GST P1-1	1.8
1AQX	Trinitrobenzene GSH	GST P1-1	2
1EEM	GSH	GST O1-1	2
1FRO	Phenyl GSH	Glyoxalase I	2.2
1FW1	GSH	Maleylacetoacetate Isomerase/GST Z	1.9
1GRA	GSH	Glutathione Reductase	2
1GUH	Phenyl GSH	GST A1-1	2.6
1HNB	Dinitrobezene GSH	GST M2-2	3.5
1HNL	GSH	Lysozyme	1.8
1K0N	GSH	Chloride Intracellular Channel Protein I	1.8
1KCG	GSH	NKG2D	2.6
1LJR	GSH	GST T2-2	3.2
1MC5	Hydroxymethyl GSH	Formaldehyde Dehydrogenase	2.6
1PL1	Methoxybenzyl GSH	GST A1-1	1.75
1Q8M	GSH	TREM-1	2.6
1QH5	N-Hydroxyl-N-bromophenylcarbamoyl GSH	Glyoxalase II	1.45
1QIN	N-Hydroxyl-N-bromophenylcarbamoyl GSH	Glyoxalase I	2
1TDI	GSH	GST A3-3	2.4
1XWK	Dinitrobezene GSH	GST M1-1	2.3
1Y1A	GSH	Calcium and Integrin Binding I	2.3
1YZX	Sulfino GSH	GST K	1.93
2A2R	Nitro GSH	GST P1-1	1.4
2A2S	Nitro GSH	GST P1-1	1.7
2BRQ	GSH	Filamin A and Intefrin B 7-subunit	2.1
2F3M	Trinitrobenzene GSH	GST M1-1	2.7
2FLS	GSH	Glutaredoxin 2	2.05
2GRT	Oxidized GSH	Glutatione Reductase	2.7
2HGS	GSH	Glutathione Synthase	2.1
2HT9	GSH	Glutaredoxin 2	1.9
2PGT	Dihydrophenanthrene GSH	GST P1-1	1.9

APPENDIX B (continued)

2PNO	GSH	Leukotriene C4 Synthase	3.3
2R4V	GSH	Chloride Intracellular Channel Protein 2	1.85
2UUH	GSH	Leukotriene C4 Synthase	2.15
2VCQ	GSH	Prostaglandin D Synthase	1.95
2VCV	GSH	GST A3	1.8
2WJU	GSH	GST A2-2	2.3
2WUL	GSH	Glutaredoxin Related Protein 5	2.4
2XPY	GSH	Leukotriene A-4 Hydrolase	2.73
2ZK2	GSH	PPAR gamma	2.26
3B29	GSH	Leukotriene C4 Synthase	3.2
3BHJ	GSH	Carbonyl Reductase I	1.77
3BHM	Methoxy GSH	Carbonyl Reductase I	1.8
3 E73	GSH	LanC-like Protein I	2.8
3EE2	GSH	Prostaglandin D Synthase	1.91
3GUR	GSH	GST Mu2	2.5
3HKK	GSH Sulfonic Acid	Leukotriene C4 Synthase	2.9
3KMO	GSH	GST P	2.6
3KXO	GSH	Prostaglandin D Synthase	2.1
3LEO	GSH	Leukotriene C4 Synthase	2.1
3LJR	Menaphthyl GSH	GST T2-2	3.3
3LFL	GSH	GST O1	1.8
3OB7	GSH	GST 1-1	2
3P8F	GSH	Matriptase	1.2
3P8G	GSH	Matriptase	1.9
3PCV	GSH	Leukotriene C4 Synthase	1.9
3Q19	GSH	GST O2	1.9
3RPN	S-Hexyl GSH	GST K1	2
3VI7	GSH	Prostaglandin D Synthase	2.1
4ACS	GSH	GST A2-2	1.16
4AL0	GSH	Prostaglandin E Synthase	1.72
4EDY	GSH	Prostaglandin D Synthase	2
4EE0	Solfino GSH	Prostaglandin D Synthase	1.75
1QIP	Nitrobenzyloxycarbonyl GSH	Lactoylglutathione Lyase	1.72
1HNA	Dinitrobezene GSH	GST M2-2	1.85

APPENDIX C. SELECT REPLICATES OF IN-GEL IMAGES

Figure 75. Replicate of GST-P1 treated with aHNE and aONE.
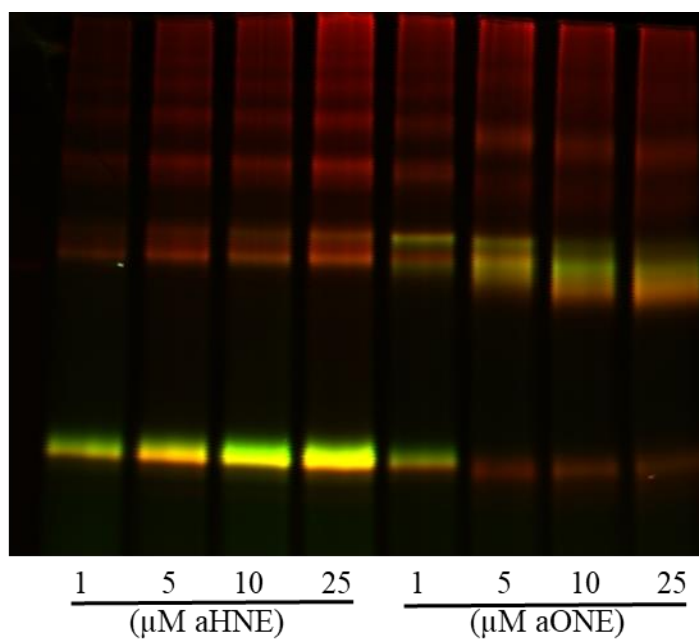
Figure 76. Replicate of Pin1 treated with aHNE and aONE
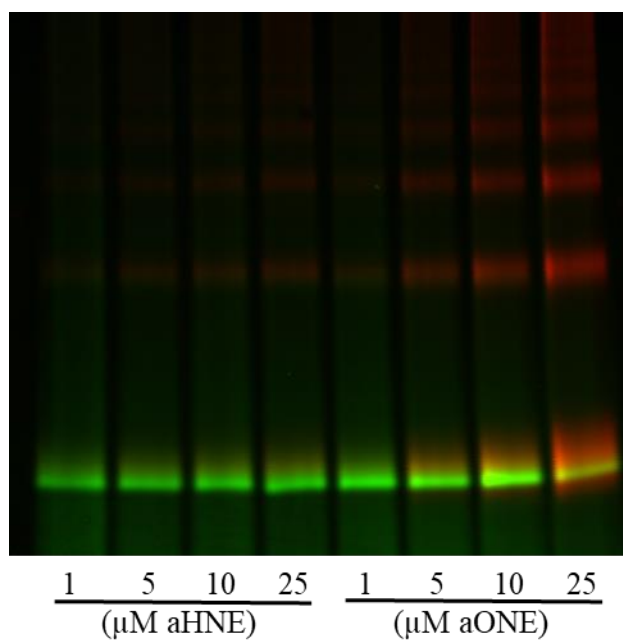
APPENDIX C (continued)

Figure 77. Replicate of SHSY-5Y cell lysates treated with aHNE and aONE
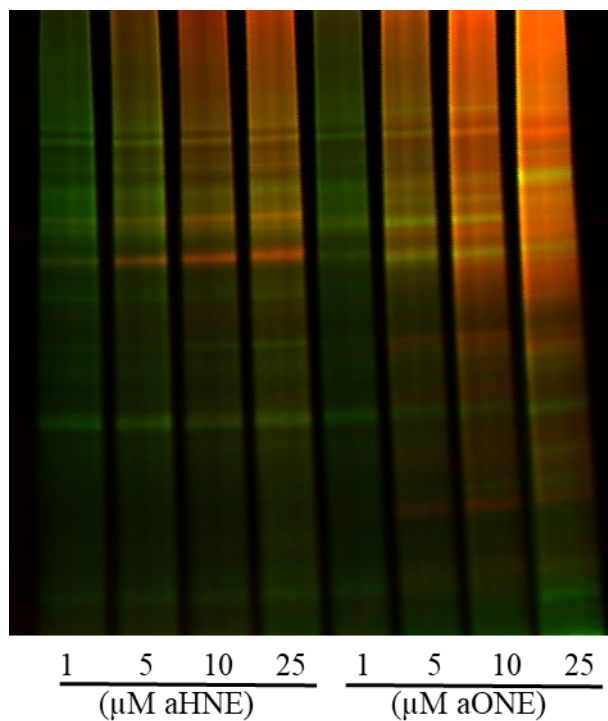
APPENDIX C (continued)

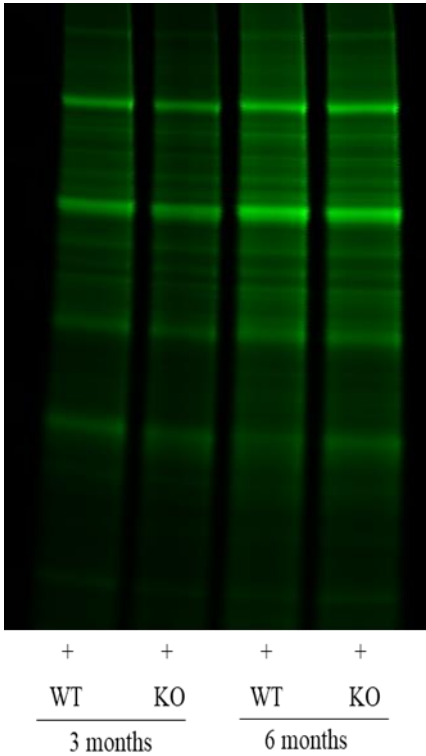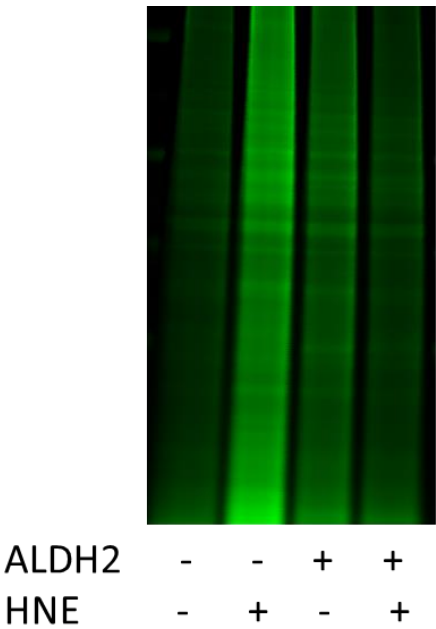**Figure 78**. Replicate of ALDH2(-/-) and WT brain samples

Figure 79. Replicate of PC12 WT and ALDH2(-/-) cells treated with HNE

APPENDIX C (continued)

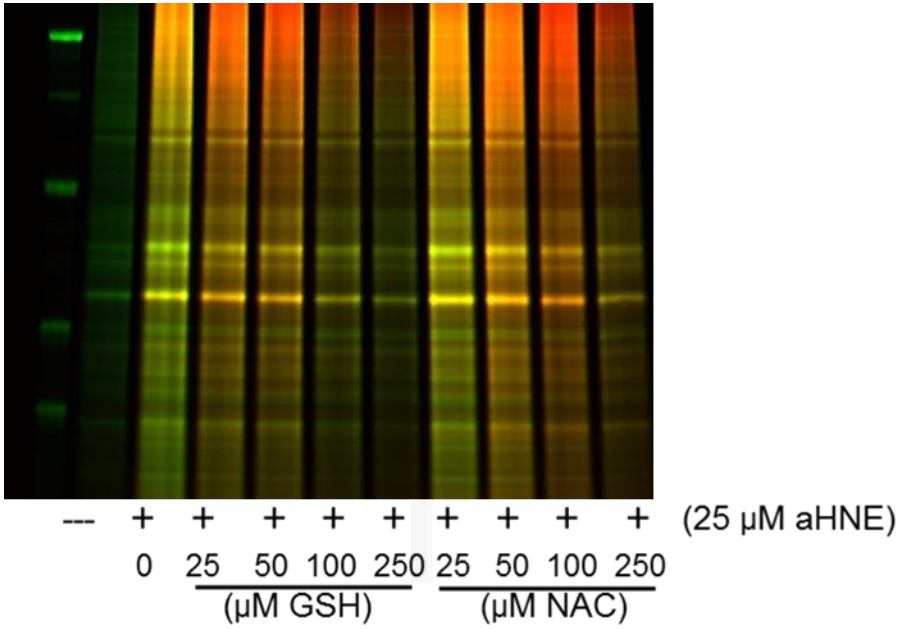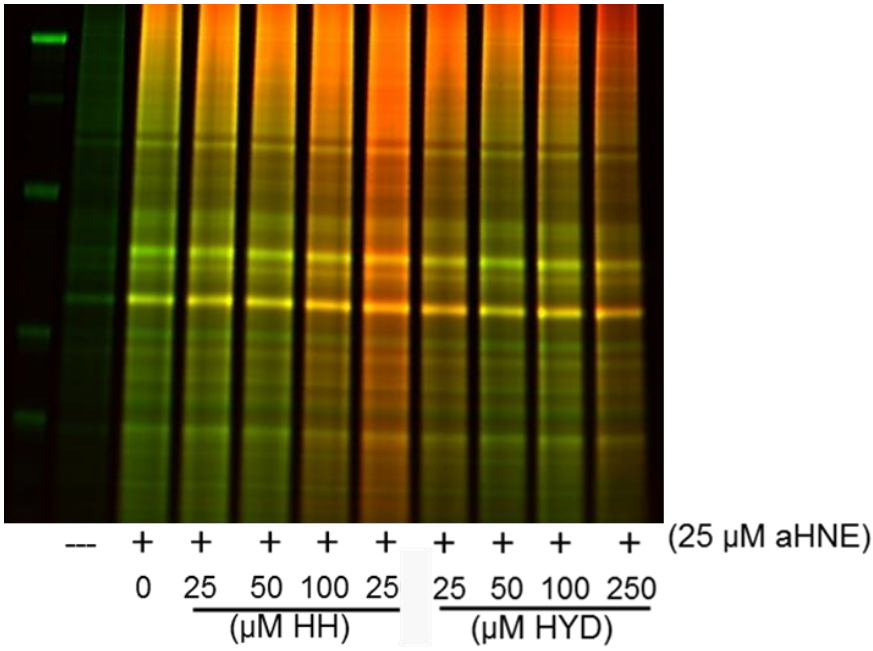**Figure 80**. Replicate of SHSY-5Y lysates treated with GSH, NAC, and aHNE

Figure 81. Replicate of SHSY-5Y lysates treated with HH, HYD, and aHNE

APPENDIX C (continued)

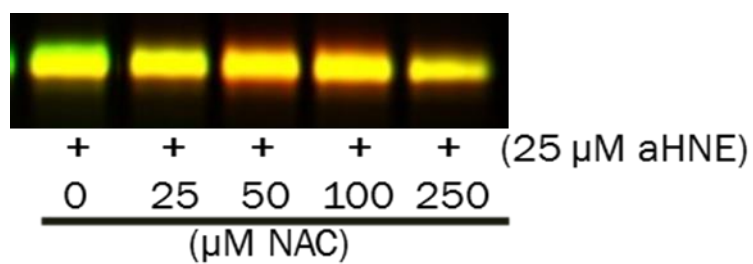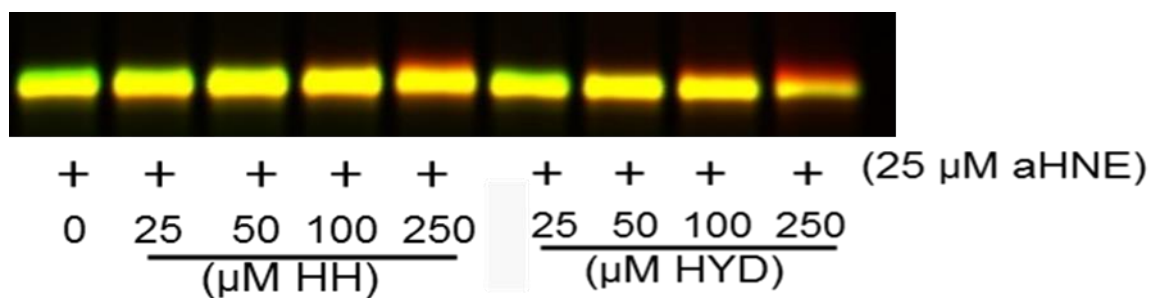**Figure 82**. Replicate of GST-P1 treated with NAC and aHNE

Figure 83. Replicate of GST-P1 treated with HH, HYD, and aHNE

VITA

Emily N. Pierce (nee Thayer)

Education	**PhD Candidate, Medicinal Chemistry** **Aug. 2012-Present** University of Illinois-Chicago, Chicago, IL. **B.S., Chemistry** **2008-2012** Benedictine College, Atchison, KS.
Research Experience and skills	**Graduate Student**, University of Illinois Chicago **Aug. 2012-Present** Laboratory of Dr. Thatcher

- Characterize the role of lipid peroxidation products and protein carbonylation in age-dependent dementia
- Evaluate the reactivity of electrophilic aldehydes with small molecule trapping agents using HPLC and LC-MS/MS
- Quantify and characterize protein adducts using chemical biology techniques and quantitative bottom-up proteomics
- Optimize enzyme assays used to screen libraries of novel small molecules
- **Skills**: design and optimization of enzyme assays, recombinant protein expression, protein purification, western blot, in-gel imaging (near-IR, fluorescent), bottom-up proteomics (experimental design, sample preparation, and data analysis), HPLC , ion trap MS, Biomek 3000 liquid handling automation workstation

Internship, Abbvie
June 2017 - Aug. 2017

- Worked during a 12 week internship to characterize the *in vitro* and *in vivo* aggregation of antibody-drug conjugates (ADCs)
- Isolated and quantified aggregation by radiolabeled ADCs using immunoprecipitation and size exclusion chromatography (SEC)
- Identified the components of these protein aggregates and ADC PTMs by shotgun proteomics

- Presented data from this project at an internal department meeting
- **Skills**: experience with Thermo QE plus MS and Thermo Orbitrap Elite MS, SEC, immunoprecipitation, native gel electrophoresis, TopCount scintillation counter, PyMOL,

Undergraduate Research Internship, Atchison KS
Sept. 2010 - May 2012

- Paid research internship
  Worked 10-15 hrs/week during the 2010-2011 and 2011-2012 academic years and full time for the intervening summer
- Developed a process for the extraction of protein from the spent grains of ethanol production which can serve as a starting material for biodegradable polymers
- Collaborated with researchers at MGP Ingredients, Kansas State University, and Pittsburg State University through a grant provided by the US Small Business Administration

Publications Kent, C. R.; Bryja, M.; Gustafson, H. A.; Kawarski, M. Y.; Lenti, G.; **Pierce, E. N.**; Knopp, R. C.; Ceja, V.; Pati, B.; Walters, D. E.; Karver, C. E.*, Variation of the aryl substituent on the piperazine ring within the 4-(piperazin-1-yl)-2,6-di(pyrrolidin-1-yl)pyrimidine scaffold unveils potent, non-competitive inhibitors of the inflammatory caspases. *Bioorg Med Chem Lett* **2016,** *26* (22), 5476-5480.

Pierce, E. N.; Piyankarage, S. C.; Dunlap, T.; Litosh, V.; Siklos, M. I.; Wang, Y. T.; Thatcher, G. R.* Prodrugs Bioactivated to Quinones Target NF-kappaB and Multiple Protein Networks: Identification of the Quinonome. *Chem Res Toxicol.* **2016,** *29* (7), 1151-9.

Kastrati I., Siklos M.I., El-Shannawy L., **Thayer E.N.**, Thatcher, G.R.J., Frasor, J. Dimethyl Fumarate Inhibits the Nuclear Factor kB Pathway in Breast Cancer Cells by Covalent Modification of p65 Protein. *J Biol Chem.* **2016,** *291* (7), 3639-47.

Madhubhani, L.P., Hemachandra, P., Patel H., Esala, R., Chandrasena, P., Choi, J., Wang, S., Wang, Y., **Thayer, E.N.**, Scism, R., Michalsen, B.T., Bolton, J.L., Thatcher, G.R.J.* Benzothiophene SERMs act as breast cancer chemopreventive agents by modulating estrogen oxidative

metabolism in human mammary epithelial cells. *Cancer Prev Res (Phila)*. **2014,** 7(5):505-515.

Teaching Experience	**Teaching Assistant**, University of Illinois Chicago **Aug. 2012 – Dec. 2014**

Chemistry Tutor, Benedictine College
Aug. 2010 – May 2012

- Tutored students enrolled in general and organic chemistry

Teaching Assistant, Benedictine College
Aug. 2011 – May 2012

- Guided classes of 15-20 students through experiments designed for organic chemistry and quantitative analysis lab courses

Presentations

"Evaluation of Neuroprotective Scavengers to Prevent Formation of Aldehyde Protein Adducts", Emily Pierce, 54th MIKI Meeting, Minneapolis MN, April 7-9 2017

"Chemoproteomic Approach to Characterizing the Role of 4-HNE in Accelerated Cognitive Impairment and Traumatic Brain Injury", Emily Pierce, Sue Lee, Manel Benaissa, Emily Nepomuceno, Dr. Gregory Thatcher, 53th MIKI Meeting, Iowa City IA, April 10-12 2016

"Evaluation of Photoactivatable Chemical Probes for the Identification of Glutationylating Proteins" Emily Thayer, Yue-Ting Wang, Bhargava Karumudi, Emma Mendonca, Vy Pham, Dr. Gregory Thatcher, 52st MIKI Meeting, Chicago IL, April 11-13 2014

"Design, Synthesis and Evaluation of Photoactivatable Probes for Photoaffinity Labeling", Emily Thayer, Yue-Ting Wang, Bhargava Karumudi, Emma Mendonca, Vy Pham, Dr. Gregory Thatcher, 246th ACS National Meeting, Indianapolis IN, September 8-12 2013

"Design, Synthesis and Evaluation of Photoactivatable Probes for Photoaffinity Labeling", Emily Thayer, Yue-Ting Wang, Bhargava Karumudi, Emma Mendonca, Vy Pham, Dr. Gregory Thatcher, 51st MIKI Meeting, Minneapolis MN, April 12-14 2013

"*Exploring New Methods for Extraction Zein from Corn*", Emily Thayer, Sarah Laskares, Dr. Aileen Beard, 243rd ACS National Meeting, San Diego CA, March 2012

"*Extraction of Zein from DDGS for Commercial Applications*", Emily Thayer, Sarah Laskares, Dr. Aileen Beard, 242nd ACS National Meeting, Denver CO, Aug. 28-Sept. 1, 2011

"*Extraction of Zein from DDGS for Commercial Applications*", Emily Thayer, Sarah Laskares, Dr. Aileen Beard, Wakarusa Valley ACS Student Research Symposium, Oct. 8, 2011

Leadership Experience	**Medicinal Chemistry and Pharmacognosy Graduate Student Association**

- Served as President during 2015-2016 academic year
- Organized annual lectureships for the Medicinal Chemistry and Pharmacognosy department
- Responsible for fundraising and organizing the student run 2014 MIKI conference

Awards	**Myron Goldsmith Scholarship** **Feb. 2016**

Professor Ludwig Bauer Award
Feb. 2013

Presidential Scholarship
Aug. 2008 – May 2012

- Full academic scholarship for undergraduate degree